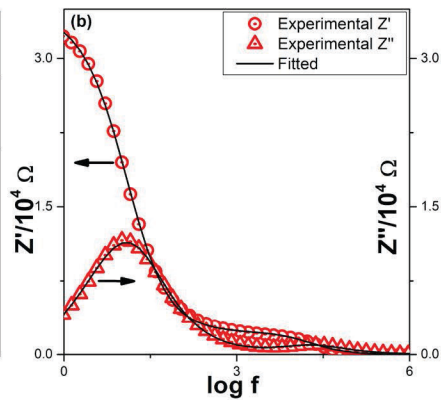
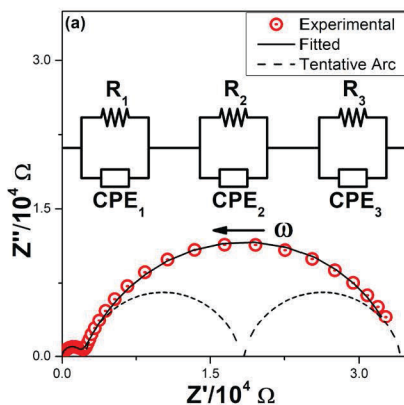


ANALYTICAL IMPEDANCE SPECTROSCOPY

BASICS AND APPLICATIONS

Lakshman Pandey, Devendra Kumar,
Om Parkash and Shukdev Pandey



CRC Press
Taylor & Francis Group

Analytical Impedance Spectroscopy

This book introduces the subject of impedance spectroscopy starting from fundamentals through to latest applications in areas such as ceramics, piezoelectric, sensors, agriculture, food quality control, medical diagnostics, cancer research and so forth. Within the ambit of impedance spectroscopy, plots simulated for useful equivalent circuit models, design of sample holder, necessary precautions to be taken during measurement are described. It further discusses development of softwares for analysis of experimental data and choice of the most appropriate equivalent circuit model. All the materials are supported by problems, answers, appendices and references.

Features:

- Includes fundamentals, equivalent circuit modeling and analysis of data related to impedance spectroscopy.
- Presents experimental measurements in a nuts-and-bolts approach.
- Includes derivation of expressions for some selected models and values of immittance functions as frequency of measurements tend to zero and to infinity.
- Provides clear recipe for beginners for proceeding toward developing equivalent circuit models.
- Describes computer program for complex nonlinear least squares fitting with example of program IMPSPEC.BAS

This book is aimed at senior undergraduate/graduate students and researchers in materials engineering, mechanical engineering, electrical engineering, chemical engineering, biomedical engineering, construction engineering, physics, chemistry, medical diagnostics, agriculture and dairy.



Taylor & Francis

Taylor & Francis Group

<http://taylorandfrancis.com>

Analytical Impedance Spectroscopy

Basics and Applications

Lakshman Pandey, Devendra Kumar,
Om Parkash and Shukdev Pandey



CRC Press

Taylor & Francis Group
Boca Raton London New York

CRC Press is an imprint of the
Taylor & Francis Group, an **informa** business

Cover image: Lakshman Pandey

First edition published 2024

by CRC Press

6000 Broken Sound Parkway NW, Suite 300, Boca Raton, FL 33487-2742

and by CRC Press

4 Park Square, Milton Park, Abingdon, Oxon, OX14 4RN

CRC Press is an imprint of Taylor & Francis Group, LLC

© 2024 Lakshman Pandey, Devendra Kumar, Om Parkash and Shukdev Pandey

Reasonable efforts have been made to publish reliable data and information, but the author and publisher cannot assume responsibility for the validity of all materials or the consequences of their use. The authors and publishers have attempted to trace the copyright holders of all material reproduced in this publication and apologize to copyright holders if permission to publish in this form has not been obtained. If any copyright material has not been acknowledged please write and let us know so we may rectify in any future reprint.

Except as permitted under U.S. Copyright Law, no part of this book may be reprinted, reproduced, transmitted, or utilized in any form by any electronic, mechanical, or other means, now known or hereafter invented, including photocopying, microfilming, and recording, or in any information storage or retrieval system, without written permission from the publishers.

For permission to photocopy or use material electronically from this work, access www.copyright.com or contact the Copyright Clearance Center, Inc. (CCC), 222 Rosewood Drive, Danvers, MA 01923, 978-750-8400. For works that are not available on CCC please contact mpkbookspermissions@tandf.co.uk

Trademark notice: Product or corporate names may be trademarks or registered trademarks and are used only for identification and explanation without intent to infringe.

ISBN: 978-0-367-54964-0 (hbk)

ISBN: 978-0-367-54970-1 (pbk)

ISBN: 978-1-003-09138-7 (ebk)

DOI: 10.1201/9781003091387

Typeset in Times

by Newgen Publishing UK

Contents

Preface.....	vii
About the Authors.....	ix
Chapter 1 Basic Ideas.....	1
1.1 Ohm's Law.....	1
1.2 Charging and Discharging of a Capacitor and Inductor	3
1.3 Basics of Electrical Impedance and Phase Difference (AC Response)	8
1.4 Electrical Behavior of RC and RL Circuits	18
Summary	26
Chapter 2 Concept of Impedance Spectroscopy, Various Immittance Functions and Equivalent Circuit Representation	28
2.1 Concept of Impedance Spectroscopy and Various Immittance Functions.....	28
2.2 Representation of Electrical Behavior of Materials by Equivalent Circuit Model.....	30
Summary	39
Chapter 3 Experimental Measurements	41
3.1 Experimental Measurements and Plotting the Data.....	41
Summary	47
Chapter 4 Equivalent Circuit Models and Their Simulated Immittance Behaviors.....	49
4.1 Model Involving Resistance R and Capacitance C in Parallel	50
4.2 Model Involving Resistance R and Capacitance C in Series.....	53
4.3 Parallel Combination R_1C_1 in Series with C_2	55
4.4 Parallel Combination R_1C_1 in Series with R_2	57
4.5 Two Parallel RC Networks Connected in Series.....	59
4.6 Series R_1C_1 in Parallel to R_2	64
4.7 Three Parallel RC Networks Connected in Series	66
4.8 Parallel Combination of Resistance R and Constant Phase Angle Element	70
4.9 Series Combination of R and CPE.....	75

4.10	Series Combination of Parallel R_1 -CPE ₁ and Parallel R_2 -CPE ₂	79
4.11	Series Combination of Parallel R_1C_1 , Parallel R_2C_2 and CPE	83
4.12	Series Combination of Parallel R_1 -CPE ₁ , R_2 and CPE ₂	85
4.13	Parallel Combination of R_1 , C_1 and CPE ₁ in Series with Parallel R_2C_2	88
4.14	A Parallel Combination of Resistance R and Inductor L	92
4.15	A Series Combination of R and L	95
4.16	A Parallel Combination R_1L_1 Connected in Series with R_2 and L_2	97
4.17	Series R_1C_1 in Parallel with Series R_2C_2 and R_3	99
4.18	A Series Combination R_1 - L_1 - C_1 Connected in Parallel with C_2	101
	Summary	108
Chapter 5	Analysis of Experimental Data	109
5.1	Equivalent Circuit Modeling and Data Analysis.....	109
5.2	Complex Nonlinear Least Squares Procedure	115
5.3	Electrode Effects	116
	Summary	119
Chapter 6	Applications	121
6.1	Ceramics and Glass Ceramics.....	121
6.2	Ferroelectrics and Piezoelectrics.....	130
6.3	Magnetic Systems	139
6.4	Corrosion and Electrochemistry	144
6.5	Polymers and Composites.....	152
6.6	Biological Systems and Medical Diagnostics.....	162
6.7	Agriculture, Food Quality and Dairy	173
6.8	Fuel Cells, Solar Cells and Miscellaneous Systems	180
	Summary	202
	Answers to Problems	205
	Appendix A1: GW BASIC Program	217
	Appendix A2: Linear and Nonlinear Least Squares	219
	References	229
	Index	247

Preface

This book has been written to serve as a source book for an introductory course on impedance spectroscopy for graduate students and researchers proceeding to use this technique in their studies. This technique essentially involves measurement of electrical impedance as function of frequency of the applied voltage and interpretation of the data by using suitable equivalent circuit model representing the charge transfer processes possibly present in the system under investigation. Due to ready availability of commercial impedance analyzers capable of impedance measurements over wide frequency ranges (sub millihertz to several tens of megahertz), ease of measurement and portability, the application of impedance spectroscopy has witnessed tremendous expansion from ceramics to electrochemistry to corrosion to agriculture and dairy to biological sciences to medical diagnostics, etc. in recent years. The users groups comprise workers coming from highly diverse academic backgrounds of science and technology disciplines including medical and agricultural. The authors have experienced that, though the measurements are straightforward, the users raise some basic queries that need to be addressed so as to enable them to acquire some feel of the technique specially regarding development of equivalent circuit models for their systems. This book does not aim to give a comprehensive treatment of the technique of impedance spectroscopy. The purpose of this book is to give an exposure to the users from diverse backgrounds about some basic description of the circuit elements, experimental measurements, equivalent circuit modeling and few applications. The equivalent circuit models involve series and parallel combinations of common circuit elements, such as resistance R , capacitance C , inductance L and another so-called constant phase angle element (CPE). A CPE is mathematical realization of an element, in which the phase angle between applied ac voltage and the resulting current is a constant, independent of frequency. As the prospective users of impedance spectroscopy come from highly diverse backgrounds, it was considered appropriate to describe the impedance of these elements by obtaining various necessary expressions. When current flows through a sample having regions of different electrical properties such as conductivity or dielectric permittivity, accumulation of charge may occur inside those regions as well as at the interfaces, and this accumulation would occur with some rate. Such a process may be described by representing the region/interface by RC circuit having time constant RC . Different types of regions/interfaces would have different time constants and thus would respond to the applied ac voltage at different frequencies. Charging and discharging of a capacitor/inductor, concept of impedance and phase difference and electrical behavior of RC circuit are described in Chapter 1. How to combine the circuit elements representing those regions/interfaces having charge transfer processes is what gives rise to the development of equivalent circuit model. How to obtain the values of the circuit elements used in the model by utilizing the frequency response of impedance Z and other related functions and correlate with the charge transfers occurring in the real system under study is called impedance spectroscopy. Concept of impedance spectroscopy and representation of electrical behavior of materials by equivalent circuit model are described in Chapter 2. Basics of impedance

measurement arrangements are given in Chapter 3. The search of a suitable circuit model is greatly facilitated by comparing the experimentally observed responses with simulated behavior of some model circuits. Therefore, few useful circuit models with their simulated impedance patterns are described in Chapter 4. Though the values of circuit elements can usually be estimated by such comparisons, their values can be obtained more accurately by fitting the data to the chosen models. This is done by resorting to least squares procedure. As the parameters to be evaluated, such as R 's and C 's, appear in nonlinear way in the expression for Z for the models and two sets of experimental data (real part of complex impedance Z vs frequency and imaginary part of complex impedance Z vs frequency) are to be simultaneously fitted, the procedure is called complex nonlinear least squares (CNLS). A simple description of this is the subject matter of Chapter 5. A qualitative exposure to applications of impedance spectroscopy is given in Chapter 6 in the fields of ceramics and glass ceramics, ferroelectrics and piezoelectrics, magnetic systems, corrosion and electrochemistry, polymers and composites, biological systems and medical diagnostics, agriculture, food quality and dairy, fuel cells, solar cells and miscellaneous systems (gas sensors, petroleum, battery, Covid-19). A few problems with solution are also given here and there for illustration purposes. Solutions of the differential equations, basics of least square procedure, etc. are given as appendices, wherever required.

The work is dedicated to The ALMIGHTY, to our Guruji Swami Narayan Tirtha Ji Maharaj and Swami Atmanand Tirtha Ji Maharaj, without whose grace and blessings this work would have never been completed, and to our honorable teachers and guides, colleagues, friends and family members, who have inspired and supported us throughout the years. The authors are grateful to Dr. Gagandeep Singh of Taylor & Francis Publishing for his untiring support during completion of the manuscript.

**Lakshman Pandey, Devendra Kumar
Om Parkash and Shukdev Pandey**

About the Authors

Lakshman Pandey, a physicist, has his BSc and MSc degrees from Banaras Hindu University, Varanasi and PhD from IIT Kanpur (1980). He has worked as Postdoctoral Fellow at Department of Physics, University of Alberta, Edmonton, Canada (1980–1983), Visiting Scientist and Visiting Professor at Department of Physics, University of Alberta, Edmonton, Canada (1984, 1986, 1990), Third World Academy of Sciences (TWAS) Associate Members at Brazilian Center for Physical Research, Rio de Janeiro, Brazil (2000, 2002), UGC Research Scientist at School of Materials Science & Technology, IIT(BHU) (1984–1989), Associate Professor (1989–1998) and Professor (1998–2018) at Department of Post Graduate Studies & Research in Physics and Electronics, Rani Durgavati University, Jabalpur, India. He has offered various courses in Physics, Electronics and Materials Science to MSc, MPhil, MTech, BTech and PhD students at Rani Durgavati University Jabalpur, School of Materials & Technology, IIT(BHU), and Indian Institute of Information Technology-Design and Manufacturing (IIIT-DM), Jabalpur. He has been Head of Department of Physics and Electronics (2002–2005), Dean of Faculty of Science of Rani Durgavati University (2005–2007), Member of Executive Council of Rani Durgavati University (2005–2007, 2013–2016), Chairman of Board of Studies in Physics and in Electronics (2002–2006), Prof-in-charge of University Science Instrumentation Centre (1999–2000), Member of Academic Senate of Indian Institute of Information Technology Design and Manufacturing (PDPM-IIITDM), Jabalpur (2005–2011). During his about 45 years of teaching and research career, he has worked on problems of theoretical and experimental nature including instrumentation and software development. He has worked in the areas of NMR in solids and gases (experiment, theory), NMR instrumentation, ferroelectrics, impedance spectroscopy, electronic ceramics, solidification, development of computer software, science concepts in ancient Sanskrit texts. He has been Associate Member of TWAS (2000–2006) and is Life Member of Materials Research Society of India (MRSI), Indian Institute of Metals (IIM), Indian Physics Association (IPA) and Luminescence Society of India (LSI). He is a founder member of a scientific organization “Mahakoshal Vigyan Parishad, Jabalpur”. He has supervised 8 PhD students (including three on impedance spectroscopy), 12 MPhil, 4 MTech, 15 MSc dissertations and has contributed over 100 research articles. He designed and developed NMR sample probes for gaseous samples in IIT Kanpur and for piezoelectric solids in Canada. He has developed the computer software IMPSPEC.BAS for complex nonlinear least squares (CNLS) and equivalent circuit modeling in impedance spectroscopy being widely used by his group.

Devendra Kumar, a physicist and materials scientist (PhD from IIT Kanpur), was Professor and Head, Department of Ceramic Engineering, Indian Institute of Technology (Banaras Hindu University) Varanasi, India. During his 35 years of Teaching and Research Career, he taught various courses on glass and ceramic technology and fabrication and characterization of advanced materials and developed many UG and PG Laboratories. His research areas include electroceramics (microwave

dielectrics, glass ceramics dielectrics, varistors, solid oxide fuel cells), bioceramics (structural and spectroscopic characterization), metal matrix composites (structural and mechanical and electrochemical characterization). Prof. Devendra Kumar has published more than 300 research articles with good citations. He guided 28 PhD and 87 MTech students. He is a fellow of Institution of Engineers and Indian Institute of Ceramics. He has served at various national-level committees and has connection with various glass and ceramic industries. He is Member Research Council, CSIR-Central Glass & Ceramic Research Institute, Kolkata, Chairman, Advisory Committee, CSIR-Central Glass & Ceramic Research Institute, Khurja Centre, Khurja (UP), Member, Expert Committee; Mining, Minerals, Metals and Materials (4M), Council of Scientific and Industrial Research (CSIR), New Delhi, Convener, Flat and Coated Glass Subcommittee, CHD 10:6 of Glass, Glassware and Laboratory Ware Sectional Committee, Bureau of Indian Standards (BIS), New Delhi and Member Governing Council, Center for Development for Glass Industries, Firozabad (UP).

Om Parkash, a physical chemist and materials scientist (PhD from IIT Kanpur), was Professor and Head of Department of Ceramic Engineering, Indian Institute of Technology (Banaras Hindu University), Varanasi. He was a research associate in Lehigh University (USA) for one year (1988–1989). During his 39 years of teaching and research career behavior, he has published more than 250 papers, which are well cited. He has guided 20 PhD and 60 MTech students. He developed and taught various UG and PG courses on synthesis, characterization and electrical, magnetic, dielectric and corrosion behavior of metals, ceramics and polymers. His research areas include electronic ceramics (electrical, dielectric and magnetic properties of rare earth transition metal oxide perovskites, varistors, glass ceramics, polymer matrix ceramic composites and dielectrics), solid electrolyte for intermediate and low-temperature solid oxide fuel cells, metal-matrix composites (structural, mechanical and electrochemical behavior). He was a member of Advisory Committees (Materials, Mining and Mineral Engineering; Physics and Mathematical Sciences for Women Scientists Scheme) of Department of Science and Technology, Government of India for 15 years. He is a fellow of Indian Institute of Ceramics and life member of Materials Research Society of India. He has been using impedance spectroscopy extensively for development of ceramics.

Shukdev Pandey did his Bachelor of Engineering in Electronics & Telecommunication from Rajeev Gandhi Technical University, Bhopal in 2010. He did his Master of Technology in Ceramic Engineering from IIT (BHU), Varanasi in 2012. Thereafter, he completed his Doctor of Philosophy in Ceramic Engineering from IIT (BHU), Varanasi in 2018. His PhD thesis title is “Structural, Electrical and Impedance Spectroscopic Studies on Sr^{2+} , Fe^{3+} and Sn^{4+} doped BaTiO_3 Ceramics”. His research areas include preparation and structural, electrical and magnetic characterization of electronic ceramic materials, microwave dielectric measurements, applications of electronic materials in development of microwave components, analytical modeling, design and simulation of rectangular dielectric resonator antenna (RDRA), equivalent circuit modeling and impedance spectroscopy. He has published seven research papers

and contributed an invited book chapter titled “Impedance Spectroscopy: A Powerful Technique for Study of Electronic Ceramics” in *Ceramic Materials – Synthesis, Characterization, Applications and Recycling*, Dolores Eliche Quesada, Luis Perez Villarejo and Pedro Sánchez Soto (eds).

He has extensively worked with Prof. Devendra Kumar, Prof. Om Parkash and Prof. L. Pandey on impedance spectroscopy and equivalent circuit modeling. Presently he is working as a research scientist, Industrial Research and Consultancy Centre, Department of Biosciences and Bioengineering, IIT Bombay, Powai, Mumbai, India.



Taylor & Francis

Taylor & Francis Group


<http://taylorandfrancis.com>

1 Basic Ideas

1.1 OHM'S LAW

Imagine a conductor through which current I (amperes, A) is flowing and the potential difference between its ends is V (volts). If all the physical conditions, such as temperature, are kept constant, then by increasing V , I also increases in the same ratio. This is Ohm's law. The ratio of V to I is called the resistance R of the conductor. According to Ohm's law, we have (Simpson 1974, p 6)

$$V = RI \text{ or } R = \frac{V}{I} \quad (1.1)$$

Resistance R is expressed in volt/ampere or ohms ($1 \Omega = 1 \text{ V/A}$), sketched as  and represented by the symbol Ω . The inverse of resistance is called conductance G . Resistance means opposition to current flow. Equation (1.1) is empirically true for many different kinds of circuit elements. If the conductor is in the form of a rectangular slab with area of cross section A_{cross} (square meters) and length l (meters) as shown in Figure 1.1, then we have

$$R = \rho \frac{l}{A_{\text{cross}}} \quad (1.2)$$

where ρ (expressed in ohm.meter, $\Omega.m$) is resistivity and R is in ohms (NCERT 2009, Physics XII part I, p 96).

Equation (1.1) can be written as

$$\frac{V}{I} = \rho \frac{l}{A_{\text{cross}}} \quad (1.3)$$

Or

$$\frac{I}{A_{\text{cross}}} = \frac{1}{\rho} \frac{V}{l} \quad (1.4)$$

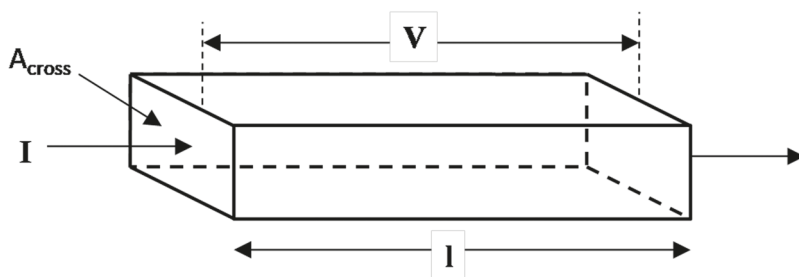


FIGURE 1.1 A rectangular slab of a material of resistivity ρ with area of cross section A_{cross} and length l . The applied voltage V creates a current I .

Or

$$\mathbf{J} = \sigma \mathbf{E} \quad (1.5)$$

The current per unit area I/A_{cross} , with area taken normal to the direction of current, is called the current density \mathbf{J} (A/m^2). The quantity σ is electrical conductivity and is measured in $(\Omega \cdot \text{m})^{-1}$, i.e. mho/m, also called Siemens per meter $\text{S} \cdot \text{m}^{-1}$; 1 mho being equal to 1 S. The entity \mathbf{E} ($= V/l$) is the electric field (volts/meter) acting at the slab along the length and normal to the area of cross section A_{cross} . In vector form Eq. (1.4) can be written, in general, as (NCERT 2009 Physics XII part I, p 97)

$$\mathbf{J} = \sigma \mathbf{E} \quad (1.6)$$

For an isotropic material, such as an as-prepared glass or ceramic, σ would be a scalar (i.e. has only one component and can be expressed by using a single number), whereas for usual anisotropic material (such as a single crystal with non-cubic crystal structure), σ would be a second-rank tensor having, in general, six nonzero components in three-dimensional Cartesian laboratory coordinate frame (the number of independent components depend upon the symmetry of the crystal structure) (Nye 1985).

A material or circuit element is called ohmic if it obeys Ohm's law. A material is said to obey Ohm's law if its I vs V graph is linear, i.e. if R is independent of V and I , or its \mathbf{J} vs \mathbf{E} graph is linear and conductivity σ is independent of \mathbf{E} and current density \mathbf{J} . The relation $R = V/I$ is the general definition of resistance whether or not the conductor obeys Ohm's law. There are several circuit elements, including devices, that do not obey Ohm's law. A p-n junction is an example of a non-ohmic device where the current does not vary linearly with the voltage. Ohm's law is a material property (Halliday et al. 1992, p 703).

One ampere of current is the flow of 1 C of charge (i.e. 6.25×10^{18} electrons) per second. Charge in motion is what is called current. Here we are concerned with the net charge that is transported and not with the entities acting as charge carriers. Charge carriers may be particles like electrons or protons which may or may not be

attached to atoms, molecules or larger objects. Current at a point is given by the rate of change of electric charge at that point and its direction is taken by convention to be the direction of flow of effective positive charge. Thus the direction of current would be taken in the direction opposite to the direction of flow of electrons. If the direction of flow of charge is always the same as time passes, the current is called direct current (dc). If the charge flows back and forth alternatively, then the current is called alternating current (ac). When charge is transported through a resistance R , energy is dissipated, and the rate of energy dissipation is called power lost. Power dissipated in a resistor R is given by

$$P = \frac{V^2}{R} \text{ volt} - \text{ampere (called watts)} \quad (1.7)$$

The electrical potential (or voltage) at a certain point in a circuit is defined as the potential energy of a charge at that point divided by the charge. The potential energy of a positive charge is the work done in bringing it from infinity to that point. It is assumed that potential energy of the charge at infinity is zero and therefore it is taken as a reference point. Any point in the circuit where we can say that energy of all charges is zero can be taken as a reference point. This point is called “ground” or “earth”. A “ground” point is that which has constant and unvarying potential not affected by charge (current) going into it or coming out of it and by convention this potential being set equal to zero. So practically, metal chassis, metal box containing the circuit, a large metal piece kept in the box enclosing the circuit can be taken as ground. The earth is a good conductor and is so large that its total charge (voltage) would not get affected by adding or taking out some charge from it. Therefore, a circuit ground connected to the earth makes a good ground and the voltage of all the points in the circuit are measured with respect to that ground point. In a measurement setup all the necessary wires to be connected to the ground should be connected to the same ground point to avoid effects from ground loops. The ground loops are created by long conductor loops in which all points are supposed to be at ground potential, but due to various reasons it is not so. The ground point physically not connected to the earth is called floating ground. Voltage at a given point has no absolute meaning; it only means potential energy per unit charge relative to ground. If 1 J of energy is needed to bring 1 C of charge from ground point to some point in the circuit, then the voltage at that point is said to be 1 V (Simpson 1974, p 2). Things move/adjust in such a way that potential energy is minimized and therefore positive charges would move from high potential points to low potential points and negative charges the other way.

1.2 CHARGING AND DISCHARGING OF A CAPACITOR AND INDUCTOR

The charging and discharging of a capacitor and inductor is now described by considering series RC and series RL circuits. This is very helpful in impedance spectroscopic work when interpretation of the components of an equivalent circuit model is undertaken.

1.2.1 CHARGING AND DISCHARGING OF A CAPACITOR (DC RESPONSE OF A SERIES RC CIRCUIT)

The charging of a capacitor can be illustrated by considering a circuit involving a resistor R , capacitor C , a dc voltage source V_0 and a switch, all connected in series as schematically shown in Figure 1.2.

When the switch is thrown toward the terminal “a”, current i flows into the circuit and charge $q(t)$ starts accumulating at the capacitor plates. If during a time interval dt , a charge $dq (= idt)$ moves through the circuit, then energy conservation yields

$$V_0 dq = i^2 R dt + d\left(\frac{q^2}{2C}\right) \quad (1.8)$$

Or

$$V_0 dq = i^2 R dt + \frac{q}{C} dq \quad (1.9)$$

By dividing by dt , using $i = dq/dt$ and rearranging the terms, we get

$$R \frac{dq}{dt} + \frac{q}{C} = V_0 \quad (1.10)$$

The solution of this equation for initial condition that $q = 0$ at $t = 0$ is given as

$$q = CV_0 \left(1 - e^{-\frac{t}{RC}}\right) \quad (1.11)$$

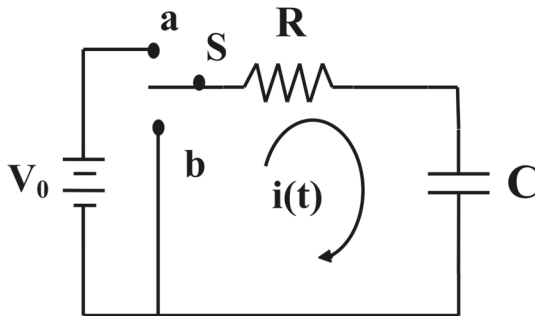


FIGURE 1.2 When the switch S is thrown to “a”, the capacitor starts getting charged by the current i . When the switch is thrown to “b”, the capacitor discharges through R .

As the exponent is dimensionless, the quantity RC has dimensions of t (time, seconds) and is called the time constant denoted by τ . When R is in ohms, C is in farads, then τ is in seconds ($1 \Omega \times 1 \text{ F} = 1 \text{ second}$). Equation (1.11) tells that at $t = 0$, the value of charge stored at the capacitor is zero. As $t \rightarrow \infty$, charge stored approaches the value CV_0 . The charging process is exponential indicating that the capacitor would practically never get fully charged. At $t = RC$, the charge stored is equal to $CV_0(1 - e^{-1})$, i.e. $0.6321 CV_0$, i.e. the voltage V_C across C is $0.632V_0$. It means that in a time duration equal to the time constant τ , a capacitor gets charged up to 63.2% of the final value. The charging is 86.47% at $t = 2\tau$, 95% at $t = 3\tau$, 98.2% at $t = 4\tau$, 99.3% at $t = 5\tau$. It means that V_C is equal to $0.632V_0$ at $t = \tau$, $0.865V_0$ at $t = 2\tau$, $0.950V_0$ at $t = 3\tau$, $0.982V_0$ at $t = 4\tau$, $0.993V_0$ at $t = 5\tau$. After $t = 5\tau$, the capacitor is assumed to have become fully charged and that the voltage across the capacitor has become equal to that of the power source. The region from $t = 0$ to 5τ is called the transient region. The region after $t = 5\tau$ is called steady-state region. The voltage across the capacitor as function of time during charging is shown in Figure 1.3.

In Figure 1.2 when the switch, after remaining connected to “a” for long time, is thrown to the terminal “b”, the battery is disconnected and the plates of the capacitor get connected through the resistor which provides a path for current to flow. This leads to the discharge of the capacitor. The discharge current dq/dt and the charge q on the capacitor at an instant t are given by Eq. (1.12)

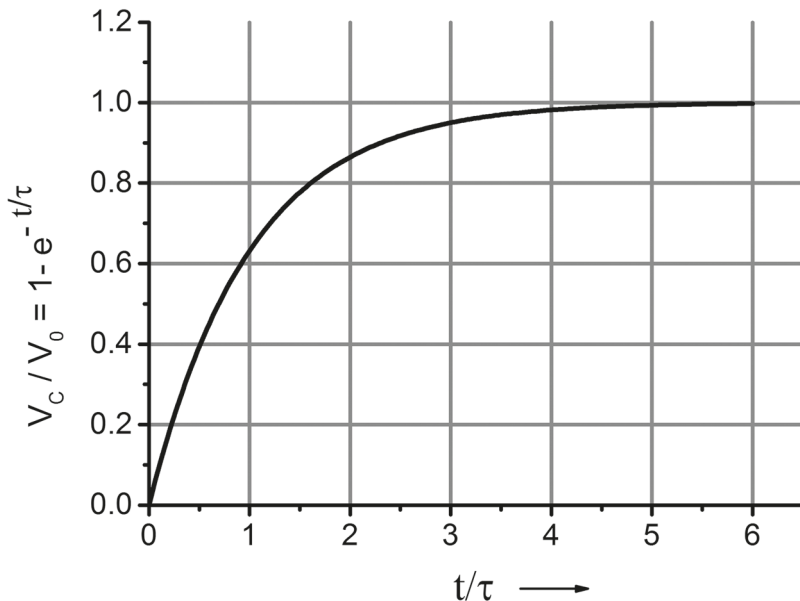


FIGURE 1.3 The voltage V_C across the capacitor as function of time during charging. After the duration of 5τ , the capacitor gets charged up to $0.993V_0$ and is considered as fully charged. For $R = 1000 \Omega$ and $C = 1 \mu\text{F}$, the time constant τ is equal to 1 ms, and the capacitor is almost fully charged in 5 ms.

$$R \frac{dq}{dt} + \frac{q}{C} = 0 \quad (1.12)$$

The solution of this equation is

$$q = q_0 e^{-\frac{t}{RC}} \quad (1.13)$$

where $q_0 (= CV_0)$ is the charge at $t = 0$ assuming that the switch was connected to b after the capacitor had got fully charged. The time constant τ for discharge is RC . At $t = RC$, the charge remaining at the capacitor would be $q_0 e^{-1}$, i.e. 37% of the initial value q_0 . At $t = 5\tau$, q would have reduced to 0.7%. The values of V_c will be $0.37V_0$ at $t = \tau$, $0.14V_0$ at $t = 2\tau$, $0.05V_0$ at $t = 3\tau$, $0.02V_0$ at $t = 4\tau$, $0.007V_0$ at $t = 5\tau$, etc. After the lapse of time equal to 5τ after the switch is thrown to “b”, the capacitor is treated as fully discharged. The discharging is shown in Figure 1.4.

It may be mentioned that in the treatment presented above the power source was considered to be ideal. For a real dc source, such as a battery, its internal resistance r would also appear in series with R during charging process. However, for the

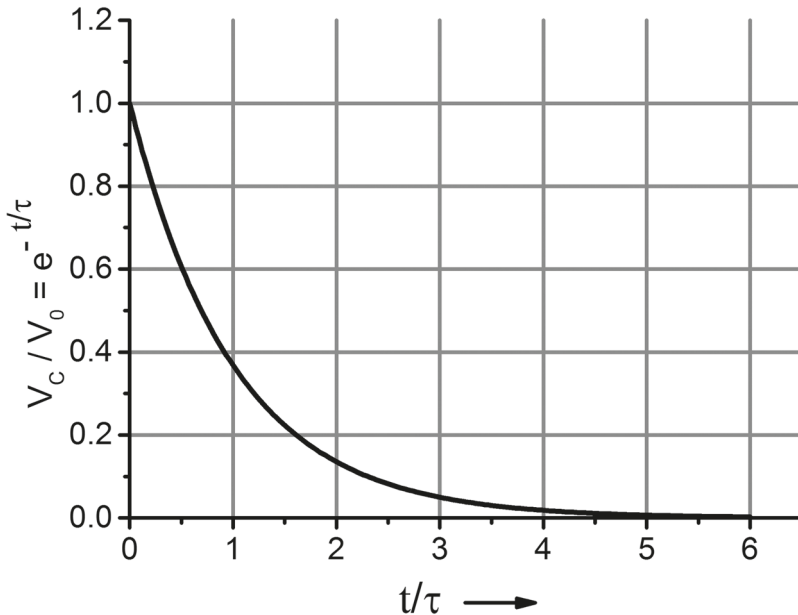


FIGURE 1.4 Discharging of a capacitor (the voltage V_c across the capacitor as function of time during discharging). The voltage across the capacitor drops to $0.37V_0$ at $t = \tau$, and to $0.007V_0$ at $t = 5\tau$, after which the capacitor is assumed to be completely discharged. For $R = 1000 \Omega$ and $C = 1 \mu\text{F}$, the time constant τ is equal to 1 ms and the capacitor is almost fully discharged in 5 ms.

discharging when the switch is thrown to “b”, the internal resistance would not appear and time constants would be different.

1.2.2 CHARGING AND DISCHARGING OF AN INDUCTOR (DC RESPONSE OF A SERIES RL CIRCUIT)

An inductor having inductance L connected in series with a resistance R is shown in Figure 1.5. When the switch is closed to terminal “a”, current $i(t)$ begins to build up. A time-varying current induces an emf given by Ldi/dt across the inductor.

Kirchoff’s voltage law yields

$$Ri + L \frac{di}{dt} = V_0 \quad (1.14)$$

Or

$$\frac{di}{dt} + \frac{R}{L}i = \frac{V_0}{L} \quad (1.15)$$

The solution of this equation for initial condition that $i(t) = 0$ at $t = 0$, is given as

$$i(t) = \frac{V_0}{R} \left(1 - e^{-\frac{t}{L/R}} \right) \quad (1.16)$$

As the exponential of a function is always dimensionless, the quantity L/R has the dimensions of time and is called the time constant τ of the RL circuit. The current is zero at $t = 0$, rises exponentially and, after a long time, becomes equal to V_0/R . It means that after a long time the circuit behaves as if L were absent. The time constant L/R is equal to the duration after which the current has built up to $V_0(1-e^{-1})/R$, i.e. 63% of the final value. At $t = 5 L/R$, the current would have built to 99.3%.

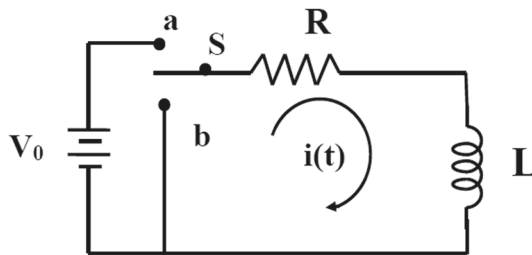


FIGURE 1.5 Series RL circuit with a dc voltage source V_0 .

The duration from $t = 0$ to $5 L/R$ is the transient period after which it is assumed that steady state has been achieved.

After the steady state, if the switch is thrown to the position “b”, the series combination of L and R gets shorted and the current flowing in the circuit is described by

$$Ri + L \frac{di}{dt} = 0 \quad (1.17)$$

By using the initial condition that at $t = 0$, $i(0) = V/R$, the solution of this equation is obtained as

$$i(t) = \frac{V}{R} e^{-\frac{t}{L/R}} \quad (1.18)$$

Current decays to zero exponentially with a time constant L/R . Here the time $t = 0$ refers to the moment when the switch is thrown to “b”. The charging and discharging graphs will be similar to those shown in Figures 1.3 and 1.4, respectively.

It may be noted that if larger time constants are involved, then such circuits would take long times to get discharged. This is why it is advised not to touch the circuit parts immediately after opening the equipment chassis if the system is operated at high voltages. It is a general practice to discharge the circuit components by shorting them using long screwdrivers after the power to the equipment had been switched off and chassis is opened for repair or some other purposes.

1.3 BASICS OF ELECTRICAL IMPEDANCE AND PHASE DIFFERENCE (AC RESPONSE)

In the discussion presented in the above sections, dc sources were used. In the present section the dc is replaced by an ac source. In the case of dc, the quantity given by voltage divided by current was called resistance R (ohms); for ac this is called impedance Z (ohms). In order to get a feel of the subject, it is worthwhile to get some general ideas about ac.

1.3.1 ALTERNATING CURRENT WAVEFORMS

In impedance spectroscopic measurements an alternating voltage source is used. The current in which the charge flows back and forth alternatively is called ac. The back and forth flow of charge in ac can be of any shape, but the most common type is that where this motion is sinusoidal, i.e. the current (or voltage) versus time plot is a sine function. Also, since a waveform having nonsinusoidal bounded shapes can be represented as superposition of sinusoidal functions (Fourier’s theorem; Simpson 1974, pp 84–89; Kreyszig 1992, p 462; Arfken 1985, pp 760–810), study of ac having sinusoidal nature and response of systems to such signals is of great importance.

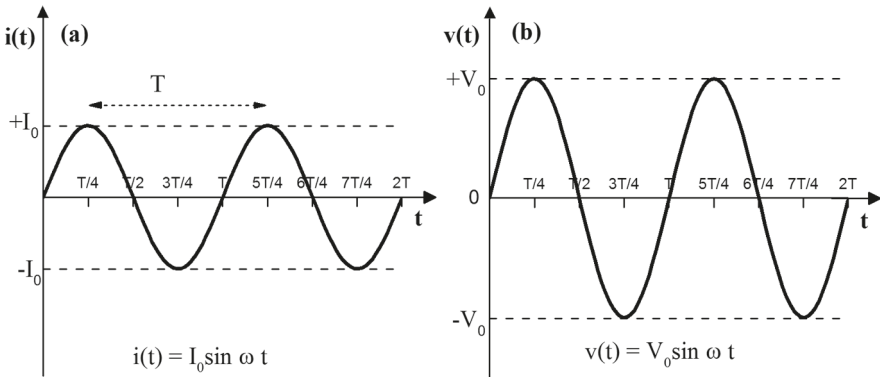
An ac voltage source may be specified by stating its peak amplitude or root mean square amplitude. An ac current $i(t)$ and ac voltage $v(t)$ of frequency f can be mathematically expressed as

$$i(t) = I_0 \sin \omega t \tag{1.19}$$

$$v(t) = V_0 \sin \omega t \tag{1.20}$$

where $\omega (= 2\pi f)$ is called angular frequency (ω has units of radians/second; 2π radians = 360° , 1 radian = $360/2\pi = 57.3^\circ$, $\pi = 3.14159$). I_0 is the amplitude of current and V_0 is the amplitude of voltage. The plots of $v(t)$ and $i(t)$ as function of time t are shown in Figures 1.6(a) and 1.6(b), respectively (Simpson 1974, p 35). The time duration between two consecutive maxima (or minima) is called the period and is usually denoted by T (seconds). The number of times charge flows back and forth in 1 second (i.e. current changes polarity in 1 second) is called frequency (denoted by f). Thus, f is equal to number of complete cycles occurring in 1 second and is expressed in cycles/second (also called Hertz denoted as Hz). Since T is the time duration of one cycle, frequency f is equal to $1/T$ and $T = 1/f$.

Now, let us consider a sinusoidal voltage (voltage signal) of angular frequency ω_1 , i.e. $v(t) = A_1 \sin \omega_1 t$. A plot of amplitude versus angular frequency ω will possess only a single point at $\omega = \omega_1$ as shown in Figure 1.7(a). Similarly, for a voltage represented as $v(t) = A_1 \sin \omega_1 t + A_2 \sin \omega_2 t + A_3 \sin \omega_3 t$, the amplitude versus ω plot would have three points each at $\omega = \omega_1, \omega_2$ and ω_3 as shown in Figure 1.7(b) where the amplitudes are customarily shown as bars. For a signal composed of n number of sine waves, the



$f = \text{frequency}$	$\omega = \text{angular frequency}$	$T = \text{time period}$
$f = 1/T = \omega / 2\pi$	$\omega = 2\pi f = 2\pi/T$	$T = 1/f = 2\pi/\omega \quad T/2 = \pi/\omega$

FIGURE 1.6 Sketch showing (a) sinusoidal current $i(t) = I_0 \sin \omega t$ and (b) sinusoidal voltage $v(t) = V_0 \sin \omega t$.

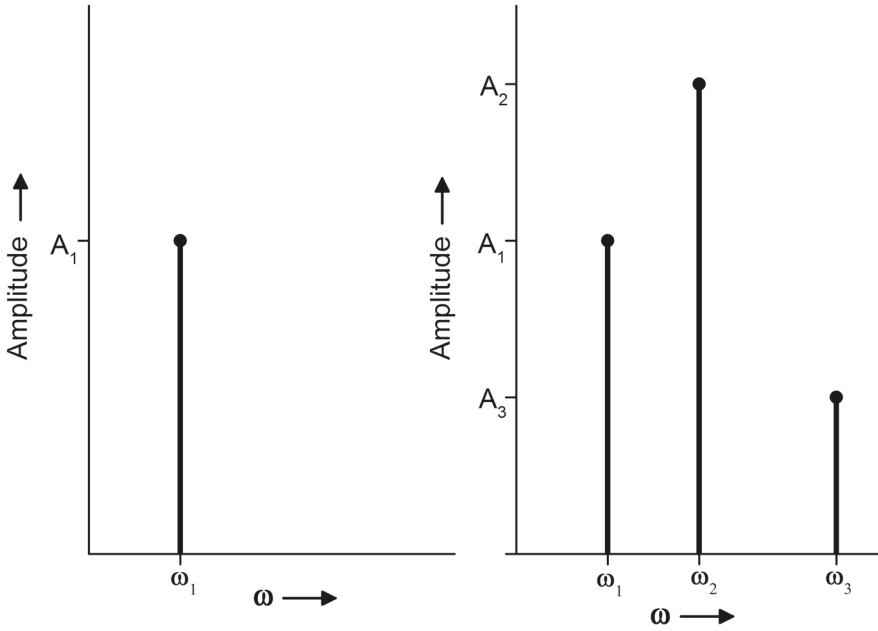


FIGURE 1.7 Amplitude spectrum of (a) $v(t) = A_1 \sin \omega_1 t$ and (b) $v(t) = A_1 \sin \omega_1 t + A_2 \sin \omega_2 t + A_3 \sin \omega_3 t$.

plot would contain n bars. Such plots are called amplitude spectrum of the voltage signal.

If a voltage $v(t) = V_0 \sin \omega t$ is applied to a pure resistance R , then current flowing through the resistance would be $i(t) = I_0 \sin \omega t$, where $I_0 = V_0/R$. In one cycle the instantaneous values of current would be positive and negative, both in equal amounts. Thus, sum of instantaneous values of current is zero, and the average current over one complete cycle is zero. However, the power (given by $v(t) i(t) = V_0 \sin \omega t (V_0/R) \sin \omega t$) varies as $\sin^2 \omega t$. Sometimes, it is convenient to use a cosine function for voltage, i.e. $v(t) = V_0 \cos \omega t$, so that when $\omega \rightarrow 0$, $v(t)$ becomes equal to V_0 and represents a dc source. Therefore, average power over one cycle would involve average of the functions $\cos^2 \omega t$ or $\sin^2 \omega t$. Power dissipated in a resistor R by a dc source of voltage V_0 giving rise to a current I_0 is given by (see Problem 1.1).

$$P = V_0 I_0 = I_0 R R = I_0^2 R = \frac{V_0^2}{R} \text{ volt-ampere (watts)} \quad (1.21)$$

If the voltage applied is ac given by

$$v(t) = V_0 \cos \omega t \quad (1.22)$$

then the current is $v(t)/R$ and is given by

$$i(t) = \frac{v_0 \cos \omega t}{R} = I_0 \cos \omega t \quad (1.23)$$

where $I_0 (= V_0/R)$ is the peak value (amplitude) of the current. The power delivered to the resistance at any instant is

$$P(t) = v(t)i(t) = V_0 \cos \omega t \left(\frac{V_0 \cos \omega t}{R} \right) = \frac{V_0^2}{R} (\cos \omega t)^2 \quad (1.24)$$

It is seen that, as $i(t)$ is a cosine function of time, the average current in the resistor over one cycle (period) (or many cycles) is zero. The power, however, varies as $\cos^2 \omega t$ from instant to instant. So, average power over one cycle is given by

$$\begin{aligned} P_{\text{average}} &= \frac{1}{T} \int_0^T v(t)i(t) dt = \frac{1}{T} \int_0^T \frac{V_0^2}{R} (\cos \omega t)^2 dt \\ &= \frac{1}{T} \int_0^T \frac{V_0^2}{R} \left(\frac{1 + \cos 2\omega t}{2} \right) dt = \frac{V_0^2}{2R} \end{aligned} \quad (1.25)$$

The expression for ac power can be written in the same form as that for dc power, viz V_0^2/R , or $I_0^2 R$ by using quantities called root-mean-square (rms) amplitude, V_{rms} , for ac voltage, and as root-mean-square (rms) amplitude, I_{rms} , for ac current, as described below.

The expression (1.25) can be rewritten in terms of voltage as

$$\begin{aligned} P_{\text{average}} &= \frac{1}{T} \int_0^T v(t)i(t) dt = \frac{1}{T} \int_0^T \frac{V_0^2}{R} (\cos \omega t)^2 dt \\ &= \frac{1}{R} \left(\frac{1}{T} \int_0^T V_0^2 \cos^2 \omega t dt \right) = \frac{V_{\text{rms}}^2}{R} \end{aligned} \quad (1.26)$$

where

$$\begin{aligned} V_{\text{rms}} &= \left(\frac{1}{T} \int_0^T [v(t)]^2 dt \right)^{1/2} = \left(\frac{1}{T} \int_0^T [V_0 \cos \omega t]^2 dt \right)^{1/2} \\ &= \frac{V_0}{\sqrt{2}} = 0.707 V_0 \end{aligned} \quad (1.27)$$

Thus, we have

$$\text{Peak value of applied voltage } v(t) = V_0 = \sqrt{2}V_{\text{rms}}, P_{\text{average}} = \frac{V_{\text{rms}}^2}{R} \quad (1.28)$$

As is seen from Eq. (1.27), V_{rms} is obtained by taking the root of the mean of square of voltage, hence the name subscript rms is used.

Similarly, the expression (1.26) can be written in terms of current as

$$\begin{aligned} P_{\text{average}} &= \frac{1}{T} \int_0^T v(t)i(t) dt = \frac{1}{T} \int_0^T I_0^2 R (\cos \omega t)^2 dt \\ &= R \left(\frac{1}{T} \int_0^T I_0^2 \cos^2 \omega t dt \right) = \frac{I_{\text{rms}}^2}{R} \end{aligned} \quad (1.29)$$

where

$$\begin{aligned} I_{\text{rms}} &= \left(\frac{1}{T} \int_0^T [i(t)]^2 dt \right)^{1/2} = \left(\frac{1}{T} \int_0^T [I_0 \cos \omega t]^2 dt \right)^{1/2} \\ &= \frac{I_0}{\sqrt{2}} = 0.707 I_0 \end{aligned} \quad (1.30)$$

Thus, we have

$$\text{Peak value of } i(t) = I_0 = \sqrt{2}I_{\text{rms}} \quad (1.31)$$

Therefore,

$$P_{\text{average}} = I_{\text{rms}}^2 R = \frac{V_{\text{rms}}^2}{R} \quad (1.32)$$

Thus, V_0^2/R or $I_0^2 R$ used for power in dc case are replaced by V_{rms}^2/R or $I_{\text{rms}}^2 R$ when ac is used (Simpson 1974).

An ac signal (or source) can be described by giving its peak amplitude and frequency or its rms amplitude and frequency. Usually household supply lines are specified by mentioning the rms values. Thus a 110-V, 60-Hz power supply line has peak value of $(\sqrt{2}) \times 110$ V, i.e. 154 V and peak-to-peak value of 308 V and frequency of 60 Hz. A 220-V, 50-Hz household electricity supply line will have peak voltage of $(\sqrt{2}) \times 220$ V, i.e. 308 V and peak-to-peak voltage of 616 V and frequency of 50

Hz. An additional phrase “phase” is also used to specify ac signals. The phase of a single supply line does not carry much meaning, however, in three-phase supplies, phase difference between two lines is 120° . The term “phase” is described in the next section.

1.3.2 PHASE

The term “phase” used in the context of waves and of materials have different meanings. In the context of materials, chemically distinct and mechanically separable regions of a sample are identified as “phase”. Thus a glass-ceramic sample in which all the crystallites have the same crystal structure would be called a two-phase system: phase one comprising crystalline regions and the phase two comprising uncrystallized glass. An oil-water mixture is a two-phase system. The concept of phase is quite different for waves. The term “phase” is used to express the time gap between the occurrences of maxima of waves of same frequency in a period (Simpson 1974, p 38). Two waves of same frequency are said to be in phase if they reach their peak values at exactly the same time. If the maximum values are not reached at the same time, the waves are said to be out of phase. The phase difference is also expressed in terms of angle as one complete cycle of duration T corresponds to 360° or 2π radians. A feel of phase difference can be obtained by watching two identical swings in a garden. If the swings are reaching their peak (maximum displacement) in the same direction simultaneously, then they are in phase. If one is traversing its peak while the other one is somewhere else, then they are out of phase. If both are swinging in the same direction, one being at its maximum extent and the other one being still at the middle at that moment, then the second one is out of phase and lags the first one by a duration $T/4$ (equivalent to 90°) or the first one is leading by phase angle 90° , where T is the time duration the swing takes to complete one cycle (period). If one is at its maximum displacement while the other one is at its maximum displacement on the opposite side, then they are out of phase by 180° . Such waves are graphically shown in Figure 1.8. Also, since $\sin \omega t = \sin(\omega t + 2\pi) = \sin(\omega t + 4\pi) = \dots$, in the graphical representation, points such as A and B in Figure 1.8 for a single wave, separated by $T, 2T, 3T$ (i.e. separated by $2\pi, 4\pi, 6\pi, \dots$), are said to represent same phase.

An ac voltage is expressed, in general, by including the phase θ in its mathematical presentation as $v(t) = V_0 \sin(\omega t + \theta)$. The phase difference between waves is beautifully displayed by an instrument called cathode-ray oscilloscope (CRO). For cases where more than two frequencies are involved, measurement of phases are with respect to the wave of lowest frequency (The Radio Amateur 1968).

1.3.3 AC RESPONSE OF AN IDEAL CAPACITOR

Assume that a voltage source $v(t)$ given by

$$v(t) = V_0 \cos \omega t \quad (1.33)$$

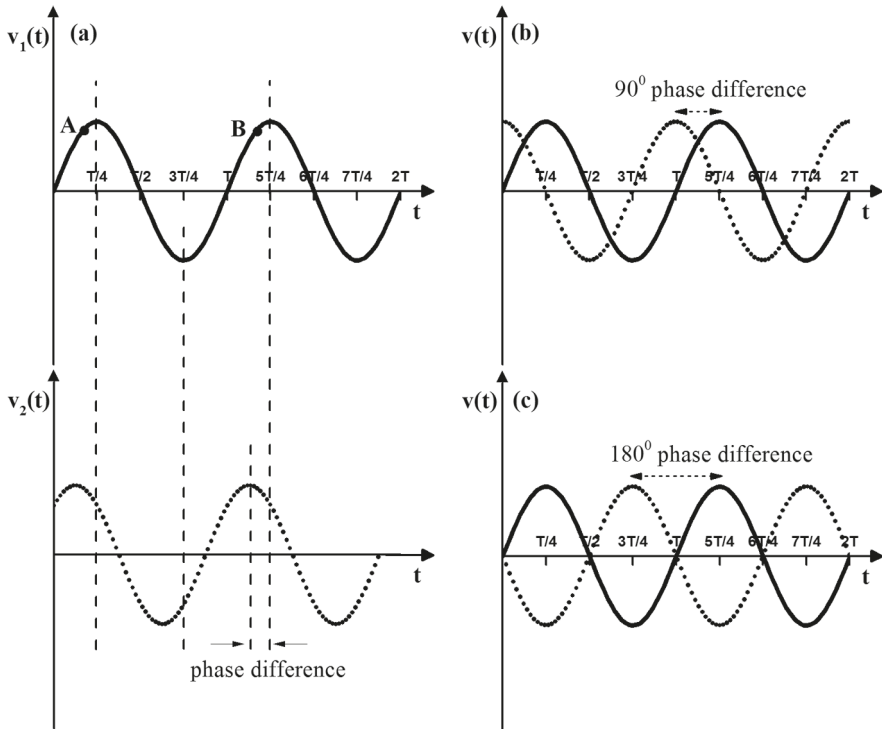


FIGURE 1.8 Two ac voltages $v_1(t)$ and $v_2(t)$ (a) out of phase. Points A and B represent the same phase (b) with 90° phase difference and (c) with 180° phase difference.

is applied across a capacitor having capacitance C . The charge q accumulated at an instant is given as (Simpson 1974, p 46)

$$q = Cv = CV_0 \cos \omega t \quad (1.34)$$

The current i is given by

$$i = dq/dt = \frac{d}{dt}(CV_0 \cos \omega t) \quad (1.35)$$

Or

$$i(t) = -\omega CV_0 \sin \omega t = \omega CV_0 \cos(\omega t + \pi/2) \quad (1.36)$$

Equation (1.36) reveals that the current $i(t)$ leads the applied voltage by a phase angle of $\pi/2$ radian ($= 90^\circ$ or $(\pi/2)/\omega = (\pi/2)/(2\pi/T) = T/4$ seconds). We encounter here with a situation where we have to deal with quantities having magnitude as well as phase. If we have combinations of several capacitors and other elements, phase differences arising in the currents emerging from those elements would combine in a complicated way. The treatment of ac response of systems is greatly simplified and made easier to handle by representing ac voltages and currents as complex quantities. A complex number is expressed as $z = x + j y$, where x is called the real part and y the imaginary part, $j = \sqrt{-1}$, $x = \text{Re}[z]$, $y = \text{Im}[z]$. The magnitude of z , written as $|z|$, is given by $\sqrt{(x^2 + y^2)}$. The quantity z is graphically represented by using Cartesian coordinates with $\text{Re}[z]$ as X-axis and $\text{Im}[z]$ as Y-axis, where z is pointed in a direction making an angle $\theta = \tan^{-1}(y/x)$ with the real axis. This X-Y plane is called the complex plane. Thus we can visualize a complex quantity z as a quantity that has a magnitude $|z|$ and has a phase angle of θ measured counterclockwise with respect to real axis. Thus, by using the relation (de Moivre's theorem)

$$e^{j\theta} = \cos\theta + j\sin\theta \quad (1.37)$$

voltage given by Eq. (1.33) is expressed as

$$v(t) = V_0 \cos\omega t = \text{Re}\left[V_0 e^{j\omega t}\right] = \text{Re}\left[V_0 (\cos\omega t + j\sin\omega t)\right] \quad (1.38)$$

The voltage $V_0 e^{j\omega t}$ can be represented by a point which is rotating at an angular frequency ω counterclockwise in the complex plane on a circle of radius V_0 . The vector drawn from origin to this point is called the voltage vector which makes an angle of ωt with respect to the real axis at any instant t . The time taken to traverse a whole circle is the period T where $\omega T = 2\pi$. The components of this vector are $V_0 \cos\omega t$ (along the real axis, X-axis) and $V_0 \sin\omega t$ (along the imaginary axis, Y-axis).

The expression for current, as given in Eq. (1.36), then becomes

$$i(t) = -\omega CV_0 \sin\omega t = \omega CV_0 \cos\left(\omega t + \frac{\pi}{2}\right) = \text{Re}\left[\omega CV_0 e^{j\left(\omega t + \frac{\pi}{2}\right)}\right] \quad (1.39)$$

This can be obtained directly from Eq. (1.35) by using the relation $j = e^{j\pi/2}$ as shown below

$$i(t) = \frac{dq}{dt} = \frac{d}{dt}\left(C\text{Re}\left[V_0 e^{j\omega t}\right]\right) = \text{Re}\left[j\omega CV_0 e^{j\omega t}\right] = \text{Re}\left[\omega CV_0 e^{j\left(\omega t + \frac{\pi}{2}\right)}\right] \quad (1.40)$$

Here, we see that

$$i(t) = \operatorname{Re} \left[j\omega C V_0 e^{j\omega t} \right] = \operatorname{Re} \left[\frac{V_0 e^{j\omega t}}{\frac{1}{j\omega C}} \right] \quad (1.41)$$

The “Re” is not explicitly written by convention and $i(t)$ is written as

$$i(t) = \left[\frac{v(t)}{\frac{1}{j\omega C}} \right] = j\omega C v(t) \quad (1.42)$$

We know from Ohm’s law that current is equal to applied voltage divided by resistance. Therefore, we find that the effective resistance of a capacitor of capacitance C to the current flow at frequency ω is $1/(j\omega C)$. This quantity is called capacitive reactance (generally denoted by X_c) or, in general, “impedance” of a capacitor. It has units of ohm. The appearance of “ j ” ($j = e^{j\pi/2}$) in the impedance $1/(j\omega C)$ takes into account the fact that an ac voltage applied to such a system will give rise to a current which will lead the applied voltage by a phase difference of 90° [see Eq. (1.40)]. The impedance of a capacitor tends to infinity (i.e. very large) as $\omega \rightarrow 0$ (i.e. for dc) indicating that it behaves as an open circuit for dc. The impedance goes to zero (very small value) as $\omega \rightarrow \infty$ indicating that a capacitor starts behaving as a short circuit as the frequency of the applied voltage is raised. These features are highly useful in impedance spectroscopic equivalent circuit modelling.

Power dissipated in one cycle is given by

$$P_{\text{average}} = \frac{1}{T} \int_0^T v(t)i(t)dt = \frac{1}{T} \int_0^T V_0 \cos \omega t \left[-\omega C V_0 \sin \omega t \right] dt = 0 \quad (1.43)$$

1.3.4 AC RESPONSE OF AN IDEAL INDUCTOR

The current flowing through an inductor having inductance L when a voltage $v(t) = V_0 \cos \omega t$ is applied across it is given by (Simpson 1974, p 54)

$$v(t) = L \frac{di}{dt} \quad (1.44)$$

Or

$$L di = v(t) dt = V_0 \cos \omega t dt \quad (1.45)$$

Integrating we get

$$L[i(t) - i(0)] = \frac{V_0}{\omega} \sin \omega t = \frac{V_0}{\omega} \cos \left(\omega t - \frac{\pi}{2} \right) \quad (1.46)$$

where $i(0)$ is the value of current at $t = 0$. Assuming that there is no current in the inductor coil in the beginning we get

$$i(t) = \frac{V_0}{L\omega} \cos \left(\omega t - \frac{\pi}{2} \right) \quad (1.47)$$

It indicates that the current lags the applied voltage by 90° ($\pi/2$ radians). The effective resistance (or impedance) of the inductor has magnitude equal to $L\omega$, which becomes negligible at low frequencies and increases as frequency is raised. So, at low frequencies an inductor behaves as a short circuit, and at high frequencies it behaves as an open circuit.

By using complex notation, $v(t)$ may be written as

$$v(t) = V_0 \cos \omega t = \text{Re} [V_0 e^{j\omega t}] \quad (1.48)$$

Equation (1.45) then becomes

$$Ldi = v(t)dt = \text{Re} [V_0 e^{j\omega t}] dt \quad (1.49)$$

On integrating and assuming that current is equal to zero at $t = 0$, we get

$$\begin{aligned} i(t) &= \frac{1}{L} \text{Re} \left[\frac{V_0 e^{j\omega t}}{j\omega} \right] = \text{Re} \left[\frac{V_0 e^{j\omega t}}{\omega L} e^{-j\pi/2} \right] = \text{Re} \left[\frac{V_0 e^{j\left(\omega t - \frac{\pi}{2}\right)}}{\omega L} \right] \\ &= \frac{V_0}{L\omega} \cos \left(\omega t - \frac{\pi}{2} \right) \end{aligned} \quad (1.50)$$

As done in the earlier section, by convention “Re” is not mentioned and we write

$$i(t) = \frac{V_0 e^{j\omega t}}{j\omega L} = \frac{v(t)}{j\omega L} \quad (1.51)$$

Thus, it is seen that “ $j\omega L$ ” is the effective resistance (or impedance) of an ideal inductor. It is called inductive reactance denoted by X_L . It also indicates that the

magnitude of the inductive reactance is equal to ωL and appearance of “j” in denominator in the above equation carries the information that the current produced in such a system would lag the applied voltage by 90° , since $1/j = e^{-j\pi/2}$ [see Eq. (1.50)]. Writing the impedance in complex form carries all the information about amplitude and phase of the current. It can be shown here also that power dissipated in one cycle (or over many cycles) is zero.

1.4 ELECTRICAL BEHAVIOR OF RC AND RL CIRCUITS

Equivalent circuit models for impedance spectroscopic studies generally involve combinations of resistive (R), capacitive (C) and inductive (L) elements. In what follows, series and parallel combinations of RC and RL are discussed.

1.4.1 IMPEDANCE OF A SERIES RC CIRCUIT

A series RC circuit connected to an ac voltage source, $v(t) = V_0 \cos \omega t$, is shown in Figure 1.9. When the switch is closed, the system would experience a transient state before achieving steady state. Study of the transient behavior is useful in several applications (Dubey et al. 2009; Saxena et al. 2019a) and, therefore, is also presented here. The treatment involves differential equations which can be elegantly solved by using Laplace transforms (Kreyszig 1992). However, keeping the diverse backgrounds of the workers in the field of impedance spectroscopy, only the elementary methods are used here.

The relation between applied voltage and current i in the circuit can, by using Kirchoff’s law, be written as (Chakrabarti 2019, p 350; Chakrabarti 2008, p 8.14)

$$Ri + \frac{1}{c} \int i \, dt = V_0 \cos \omega t \quad (1.52)$$

Differentiating we get

$$R \frac{di}{dt} + \frac{1}{c} i = -\omega V_0 \sin \omega t \quad (1.53)$$

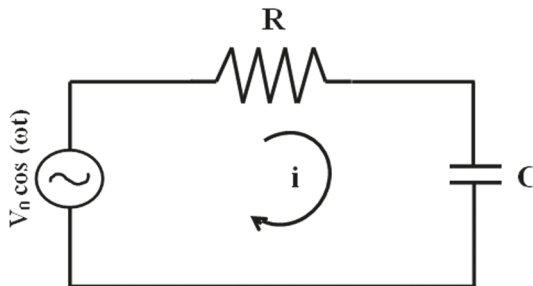


FIGURE 1.9 A series RC circuit connected to a voltage source $v = V_0 \cos \omega t$.

or

$$\frac{di}{dt} + \frac{1}{RC}i = -\frac{\omega V_0}{R} \sin \omega t \quad (1.54)$$

By using the initial condition that at $t = 0$, the initial current is given as $i = i_0 = V_0/R$, the solution is obtained as (see Problem 1.2)

$$i(t) = e^{-t/RC} \left[\frac{V_0}{R} - \frac{V_0}{\sqrt{\left(\frac{1}{\omega C}\right)^2 + R^2}} \cos \theta \right] + \frac{V_0}{\sqrt{\left(\frac{1}{\omega C}\right)^2 + R^2}} \cos(\omega t + \theta) \quad (1.55)$$

where the angle θ is given by

$$\tan \theta = \frac{1}{\omega CR} = \frac{1/\omega C}{R} \quad (1.56)$$

The first term in Eq. (1.55), called the transient response, fades away in time $\sim 5 RC$ (as $e^{-5} = 0.007$ thus negligible), and the second term, called the steady-state response, persists. It suggests that when applied ac voltage is switched to different frequencies for impedance measurement, a gap of $\sim 5 RC$ should be given between consecutive voltages to avoid transient effects. In the steady state, the current has amplitude given by $V_0/\sqrt{[(1/\omega C)^2 + R^2]}$ and leads the applied voltage by an angle θ given by $\tan \theta = (1/\omega C)/R$. The magnitude of the impedance Z is given by $\sqrt{[(1/\omega C)^2 + R^2]}$. This may be represented by a vector of magnitude $\sqrt{[(1/\omega C)^2 + R^2]}$ with X component equal to R and Y component equal to $1/(\omega C)$.

Expression for impedance is obtained more conveniently by using the complex notations. The impedances of resistor and capacitor are, respectively, R and $1/(j\omega C)$. The total impedance of the series RC combination is equal to $R + 1/(j\omega C)$. The current $i(t)$ in the circuit is given by

$$\begin{aligned} i(t) &= \frac{\text{applied voltage}}{\text{impedance}} = \frac{V_0 e^{j\omega t}}{R + \frac{1}{j\omega C}}, \quad i(t) = \text{Re} \left[\frac{V_0}{\sqrt{R^2 + \left(\frac{1}{\omega C}\right)^2}} e^{j(\omega t + \theta)} \right] \\ &= \frac{V_0}{\sqrt{R^2 + \left(\frac{1}{\omega C}\right)^2}} \cos(\omega t + \theta) \end{aligned} \quad (1.57)$$

It indicates that when a voltage $V_0 e^{j\omega t}$ is applied to a series RC circuit, then the current produced has magnitude equal to $V_0 / \sqrt{[(1/\omega C)^2 + R^2]}$ and leads the applied voltage by an angle θ given by $\tan \theta = (1/\omega C)/R$. This is also depicted pictorially by a vector diagram where the resistance R is shown along the real axis (X-axis) and the capacitive reactance $1/(\omega C)$ is shown along the imaginary axis (Y-axis), so that the length of the vector representing the value of impedance becomes $\sqrt{[(1/(\omega C))^2 + R^2]}$. Writing the impedance in complex form carries all the information about the current $i(t)$, i.e. its amplitude and phase. Expression for impedance of a circuit model possessing different components connected in series would be given by adding their individual complex impedances.

1.4.2 IMPEDANCE OF A SERIES RL CIRCUIT

A series RL circuit connected to an ac voltage source is schematically shown in Figure 1.10.

Kirchoff's law gives (Chakrabarti 2019, p 346)

$$Ri + L \frac{di}{dt} = V_0 \cos \omega t \quad (1.58)$$

$$\frac{di}{dt} + \frac{R}{L} i = \frac{V_0}{L} \cos \omega t \quad (1.59)$$

By using the initial condition that at $t = 0$, $i(t) = 0$, the solution is obtained as

$$i(t) = e^{-\frac{R}{L}t} \left[-\frac{V_0}{\sqrt{\omega^2 L^2 + R^2}} \cos \theta \right] + \frac{V_0}{\sqrt{\omega^2 L^2 + R^2}} \cos(\omega t - \theta) \quad (1.60)$$

where $\tan \theta = \omega L/R$.

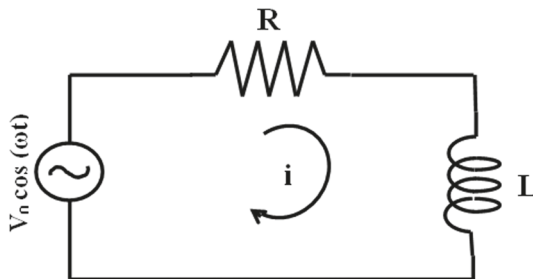


FIGURE 1.10 A series RL circuit connected to a voltage source $v = V_0 \cos \omega t$.

The first term is the transient term which fades away after a duration approximately equal to $5L/R$ [see Section 1.2.2]. The value of impedance is $\sqrt{[(\omega L)^2 + R^2]}$ and the current lags the applied voltage by an angle θ .

Using complex notations, the impedance of a series combination of a resistor and an inductor is given by $R + j\omega L$. The current $i(t)$ in the circuit is given by

$$i(t) = \text{Re} \left[\frac{v(t)}{R + j\omega L} \right] = \text{Re} \left[\frac{V_0 e^{j\omega t}}{R + j\omega L} \right] = \frac{V_0}{\sqrt{R^2 + (\omega L)^2}} \cos(\omega t - \theta) \quad (1.61)$$

where θ is given by $\tan \theta = \omega L/R$. It indicates that current $i(t)$ has a phase difference of θ with the applied voltage where $\tan \theta = \omega L/R$ and has amplitude given by

$$i_0 = \frac{V_0}{\sqrt{R^2 + (\omega L)^2}} \quad (1.62)$$

The impedance is given by $\sqrt{[R^2 + (\omega L)^2]}$. This may be depicted pictorially by a vector diagram where the resistance R is shown along the real axis (X-axis) and the inductive reactance ωL is shown along the imaginary axis (Y-axis), so that the length of the vector representing the value of impedance becomes $\sqrt{[(\omega L)^2 + R^2]}$.

1.4.3 DC RESPONSE OF A PARALLEL RC CIRCUIT

Electrical response of a parallel circuit may be conveniently described by using a current source. Consider the circuit shown in Figure 1.11, where the current source has been represented by a source giving a current $I(=i)$. Currents flowing through resistor R and capacitor C are i_R and i_C , respectively (Chakrabarti 2008, 2019).

As the voltages across R and C are equal, by using Kirchoff's law we get

$$R i_R - \frac{1}{C} \int i_C dt = 0 \quad (1.63)$$

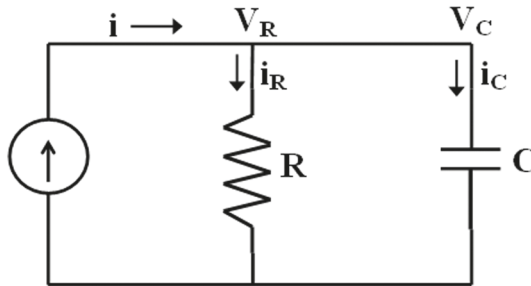


FIGURE 1.11 A parallel RC circuit connected to a dc current source.

$$i_R = I - i_C \quad (1.64)$$

The charge q accumulated at the capacitor is given by

$$q = C v_C = \int_0^t i_C dt \quad (1.65)$$

At $t = 0$, the integral is zero which gives $v_C = 0$ and $q = 0$.

By using this initial condition, the solution of Eqs. (1.63) and (1.64) are obtained as

$$i_C = I e^{-t/RC} \quad (1.66)$$

and

$$i_R = I \left(1 - e^{-\frac{t}{RC}} \right) \quad (1.67)$$

Also, it can be seen that

$$v_R = R i_R = IR \left(1 - e^{-\frac{t}{RC}} \right) = v_C \quad (1.68)$$

The charge on the capacitor accumulates exponentially with time constant RC . The value of v_C for a fully charged capacitor is IR and current $i_C = 0$ and $i_R = I$. The capacitor is treated as fully charged after a duration of $5RC$. When the source is detached, the capacitor discharges through R . The discharging process can be described by the equation

$$R i_R - \frac{q}{C} = 0 \quad (1.69)$$

By differentiating we get

$$R \frac{di_R}{dt} - \frac{1}{C} i_R = 0 \quad (1.70)$$

After integration we get

$$i_R = K_3 e^{-t/RC} \quad (1.71)$$

where K_3 is a constant. At $t = 0$, $i_R = I$, which gives $K_3 = I$ and we get

$$v_R = Ri_R = IRe^{-t/RC} = v_C \quad (1.72)$$

The capacitor is treated as fully discharged after a duration of $5 RC$.

1.4.4 AC RESPONSE OF A PARALLEL RC CIRCUIT

For analyzing the behavior of a parallel RC circuit when an ac signal is fed to it, let us consider the circuit shown in Figure 1.11 again. The analysis is similar to that given in previous section but the dc current source is replaced by an ac current source.

Thus

$$I = I_0 \cos \omega t \quad (1.73)$$

Now, we can write the equations, related to voltages and currents, as

$$v_R = v_C \quad (1.74)$$

$$Ri_R = \frac{q_C}{C} = \frac{1}{C} \int_0^t i_C dt, \quad i_R = I - i_C \quad (1.75)$$

Therefore, we get

$$R(I - i_C) = \frac{1}{C} \int i_C dt \quad (1.76)$$

Differentiation with respect to t yields

$$\frac{d_i C}{dt} + \frac{1}{RC} i_C = -I_0 \omega \sin \omega t \quad (1.77)$$

The solution is obtained by noting that initially at $t = 0$, Eq. (1.80) gives $q_C = 0$ which indicates that $i_R = 0$ and hence $i_C = I_0$. Current i_C is given by

$$i_C = \left[I_0 - \frac{I_0 \omega RC}{\sqrt{1 + (\omega RC)^2}} \cos \theta \right] e^{-t/RC} + \frac{I_0 \omega RC}{\sqrt{1 + (\omega RC)^2}} \cos(\omega t + \theta) \quad (1.78)$$

Or,

$$i_C = [I_0 \sin^2 \theta] e^{-\frac{t}{RC}} + I_0 \cos \theta \cos(\omega t + \theta) \quad (1.79)$$

where $\tan \theta = 1/(\omega RC)$. The first term corresponds to the transient state while the second term represents the steady state. The voltage across the capacitor is given by

$$V_C = \frac{qC}{C} = \frac{1}{C} \int_0^t i_C dt \quad (1.80)$$

$$v_C = -I_0 R \frac{1}{1+(\omega RC)^2} e^{-\frac{t}{RC}} + \frac{I_0 R}{\sqrt{1+(\omega RC)^2}} \sin(\omega t + \theta) \quad (1.81)$$

The value of i_R is given as

$$i_R = I - i_C = I_0 \cos \omega t - \left[I_0 \sin^2 \theta e^{-\frac{t}{RC}} + I_0 \cos \theta \cos(\omega t + \theta) \right] \quad (1.82)$$

$$= -I_0 \frac{1}{1+(\omega RC)^2} e^{-\frac{t}{RC}} + \frac{I_0}{\sqrt{1+(\omega RC)^2}} \sin(\omega t + \theta) \quad (1.83)$$

Thus, v_R is given as

$$v_R = i_R R = -I_0 R \frac{1}{1+(\omega RC)^2} e^{-\frac{t}{RC}} + \frac{I_0 R}{\sqrt{1+(\omega RC)^2}} \sin(\omega t + \theta) \quad (1.84)$$

which is same as v_C as expected since R and C are connected in parallel.

The first term in the expressions for i_C , v_C , i_R and v_R [Eqs. (1.79), (1.81), (1.83) and (1.84)] is the transient term which fades away in time duration beyond $5 RC$. This indicates that when the frequency of the applied ac source is switched to other values during impedance measurements, a time gap of $\sim 5 RC$ should be given between consecutive changes so that no charges remain on the sample and steady state has been achieved for each measurement. The steady-state values of i_C , i_R , v_C and v_R are given as

$$i_C (\text{steady state}) = I_0 \frac{\omega RC}{\sqrt{1+(\omega RC)^2}} \cos(\omega t + \theta) \quad (1.85)$$

$$i_R \text{ (steady state)} = I_0 \frac{1}{\sqrt{1 + (\omega RC)^2}} \cos(\omega t + \theta - \pi/2) \quad (1.86)$$

$$v_R = v_C = I_0 R \frac{1}{\sqrt{1 + (\omega RC)^2}} \sin(\omega t + \theta) \quad (1.87)$$

The impedance of the parallel RC combination is given by the ratio of the magnitudes of v_C and input current I as given below

$$\begin{aligned} \text{Impedance} &= \frac{\text{magnitude of } v_C}{\text{magnitude of } I} = \frac{I_0 R \frac{1}{\sqrt{1 + (\omega RC)^2}}}{I_0} \\ &= R \frac{1}{\sqrt{1 + (\omega RC)^2}} = \frac{1}{\sqrt{\left(\frac{1}{R}\right)^2 + (\omega C)^2}} \end{aligned} \quad (1.88)$$

All this information is elegantly expressed by using complex notations. Impedance, Z , of a circuit comprising a resistor R with a capacitor C connected in parallel to it would be given as

$$\frac{1}{Z} = \frac{1}{R} + \frac{1}{\frac{1}{j\omega C}} = \frac{1}{R} + j\omega C = \frac{1 + j\omega CR}{R} \quad (1.89)$$

or

$$\begin{aligned} Z &= \frac{R}{1 + j\omega CR} = \frac{R}{1 + j\omega CR} \frac{1 - j\omega CR}{1 - j\omega CR} = \frac{R(1 - j\omega CR)}{1 + (\omega CR)^2} \\ &= \frac{R}{1 + (\omega CR)^2} - j \frac{R\omega CR}{1 + (\omega CR)^2} = |Z|e^{-j\theta} \end{aligned} \quad (1.90)$$

where

$$|Z| = \frac{1}{\sqrt{\left(\frac{1}{R}\right)^2 + (\omega C)^2}} \quad (1.91)$$

is the magnitude of the impedance and

$$\tan \theta = -\omega CR \quad (1.92)$$

When a voltage $v(t) = v_0 e^{j\omega t}$ is applied, the resulting current $i(t)$ would be given by

$$i(t) = \frac{v(t)}{z} = \frac{v(t)}{|z|e^{-j\theta}} = \frac{V_0}{|z|} e^{j(\omega t + \theta)} \quad (1.93)$$

SUMMARY

1. For many systems, when applied voltage (V) is increased, resulting current (I) also increases in the same ratio. This is Ohm's law. The ratio of voltage to current is called the resistance R (more generally impedance Z) of the system. Thus, from Ohm's law, we have $V = IR$ or $V = IZ$. Systems obeying Ohm's law are called ohmic. Devices such as a pn junction are non-ohmic.
2. The time constant of a RC circuit is the time duration $\tau = RC$ (measured in seconds) required for the voltage across the capacitor to reach up to $1/e$, i.e. 63% of the applied voltage in the charging process. In the discharging process, the time constant RC is the time duration in which the capacitor would lose 63% of its voltage (i.e. the capacitor voltage will fall to 37% of its initial value). A capacitor is treated as fully charged in 5τ seconds after connecting to the voltage source. Similarly, a capacitor is assumed to be completely discharged in 5τ seconds after its beginning of discharge. This indicates that during impedance measurements, a time gap of $\sim 5 RC$ should be given between consecutive ac input changes so that no charges remain on the sample before each measurement, and zero initial conditions have been established.
3. The time constant for a series RL circuit is L/R . It is the time duration in which current builds up to 63% of the maximum value. It is assumed that, after the lapse of time of the order of five times the time constant, the transients are over and the system has achieved steady state.
4. In an ac of frequency f , the current flows forward and backward f times per second. A complete forward and backward traversal is called a cycle, and time taken for a complete cycle is called period T ($T = 1/f$). T is measured in seconds and frequency in cycles/second or Hz.
5. The phase difference between two ac signals (voltage or current), say sinusoidal voltages v_1 and v_2 , of same frequency is the time gap between the occurrence of their maxima within one period (one cycle). One cycle corresponds to 360° or 2π radians. If v_2 achieves its maximum after t_1 seconds with respect to the occurrence of maximum of v_1 , then the phase difference is $2\pi(t_1/T)$ radians. For example, if $t_1 = T/4$, then v_2 lags v_1 by 90° or v_1 leads v_2 by 90° .
6. When a circuit involves resistance and some other component such as capacitance or inductance, the opposition offered by the circuit to the flow of ac

current is expressed by a general term called impedance, denoted by Z . The current $i(t)$ produced in such a circuit by an applied voltage $v(t)$ is given by $v(t)/Z$.

7. The magnitudes of impedance for individual resistor (of value R ohms), capacitor (of value C Farads) and inductor (of value L Henrys) for an ac voltage of frequency ω are R , $1/(\omega C)$ and ωL , respectively. All these quantities are expressed in ohms. ω is equal to $2\pi f$ and is called angular frequency expressed in radians/second.
8. The impedances for parallel RC and parallel RL circuits are $1/\sqrt{[(1/R)^2 + (\omega C)^2]}$ and $1/\sqrt{[1/(R)^2 + 1/(\omega L)^2]}$, respectively. Calculations about magnitude and phase of signals in such circuits and other complicated circuits become very easy and convenient by expressing ac voltage as a complex function, viz $v(t) = V_0 e^{j\omega t}$, where $j = \sqrt{-1}$. The values of impedance Z for resistor R , capacitor C and inductor L are, then, given by R , $1/(j\omega C)$ and $j\omega L$, respectively. The appearance of j accounts for phase difference of 90° between the current and applied voltage. For capacitor, $i(t) = v(t)/Z = j\omega C V_0 e^{j\omega t} = \omega C V_0 e^{j(\omega t + \pi/2)}$, as $j = e^{j\pi/2}$, i.e. current will lead the voltage by 90° . For inductor, $i(t) = v(t)/Z = V_0 e^{j\omega t}/(j\omega L) = -j V_0 e^{j\omega t}/(\omega L) = [1/(\omega L)]V_0 e^{j(\omega t - \pi/2)}$, as $-j = e^{-j\pi/2}$, i.e., current lags the applied voltage by 90° .
9. The impedances for series RC and series RL circuits are $\sqrt{[R^2 + 1/(\omega C)^2]}$ and $\sqrt{[R^2 + (\omega L)^2]}$, respectively. The phase difference θ between current and applied voltage for series RC circuit is given by $\tan \theta = 1/(\omega CR)$, and for a series RL circuit is given by $\tan \theta = \omega L/R$.

PROBLEMS

- Problem 1.1 Calculate the power dissipated in a resistor R when a dc voltage V is applied.
- Problem 1.2 Consider a series RC circuit being connected to an ac voltage source $v(t) = V_0 \cos \omega t$. Solve the related equations to find the current in the circuit.
- Problem 1.3 Obtain the units of the product RC .
- Problem 1.4 Obtain the units of L/R .
- Problem 1.5 Find the magnitude of Z' and Z'' for a series RL circuit when the applied frequency is such that $\omega L/R = 1$.
- Problem 1.6 Obtain the units of ωRC .

2 Concept of Impedance Spectroscopy, Various Immittance Functions and Equivalent Circuit Representation

2.1 CONCEPT OF IMPEDANCE SPECTROSCOPY AND VARIOUS IMMITTANCE FUNCTIONS

Spectroscopy deals with measuring and interpreting spectra that arise from the interaction of electromagnetic radiation (a form of energy propagated as electromagnetic waves) with matter. The basic method used is shining a beam of electromagnetic radiation onto the sample placed in an environment of our choice and recording its response as function of radiation frequency (wavelength). A plot of the response as function of frequency (wavelength) is called spectrum. The response could be chosen to be the amplitude (intensity) or phase of the resulting radiation or any other property, say “A”, of the sample. Thus, plot of amplitude as function of frequency would lead to the so-called amplitude spectrum; plot of phase versus frequency would give a phase spectrum; and plot of the property “A” would yield an “A” spectrum. For example, the most familiar visible light spectrum is nothing but display of intensity versus frequency. Analysis of the experimentally observed spectrum with a view to extract information about different statics (structure) and dynamics possibly present in the sample is what is known as spectroscopy. Depending on various frequency regions employed in the measurements, different names are normally prefixed with the word spectroscopy. For example, in infrared (IR) spectroscopy the incident radiation used is in the infrared region; nuclear magnetic resonance (NMR) spectroscopy involves electromagnetic waves in radiofrequency region where the sample is usually placed in an external magnetic field. Plot of impedance of the sample as function of frequency of the incident electromagnetic wave is termed as impedance spectrum, and the analysis is called impedance spectroscopy. Impedance spectroscopy yields information about all the charge transfer processes going on in the interior of the sample that contribute to the overall impedance of the system in the applied frequency range. Impedance spectroscopy is also called as complex impedance analysis and electrical impedance spectroscopy.

Impedance spectroscopy essentially involves measurement of real and imaginary parts of electrical impedance ($Z = Z' - jZ''$, $j = \sqrt{-1}$) of a system as function of

frequency ($\omega = 2\pi f$) for various parameters of interest such as composition, temperature, etc.^{1,2} The values of Z' and Z'' are plotted as function of frequency (Z' , Z'' vs $\log f$) for the frequency range, say f_1 to f_2 , used in the experiment giving rise to the so-called spectroscopic plots and also in complex plane (i.e. Z'' vs Z') giving the complex plane plot (also called Nyquist plot). All the information about the response of the sample to the ac stimulus in this frequency range is contained in these plots. Usually, impedance measurements are carried out by placing the sample (say, in the form of a pellet) between two electrodes which are further connected to impedance meter. Due to ready availability of versatile impedance analyzers working in extended frequency ranges and ease of measurements, impedance spectroscopy has emerged as an ever expanding, very popular and powerful tool in recent years and is being widely used in various fields encompassing materials technology, electrochemistry, biology, medical diagnostics, agriculture, dairy and fruit production, etc.

The electrical behavior of a system can be expressed in terms of interrelated functions known as impedance ($Z = Z' - jZ''$), admittance ($Y = 1/Z = Y' + jY''$), permittivity ($\epsilon = 1/(j\omega C_0 Z) = \epsilon' - j\epsilon''$) and modulus ($M = 1/\epsilon = j\omega C_0 Z = M' + jM''$), C_0 being the capacitance of the empty cell used to house the sample. These are broadly termed as immittance functions (immittance is a term derived from impedance and admittance combined together; Macdonald 2005; Pandey et al. 1995). These relations are given as

$$Z = Z' - jZ'', \quad j = \sqrt{-1} \quad (2.1)$$

$$Y = \frac{1}{Z} = \frac{1}{Z' - jZ''} = \frac{Z' + jZ''}{Z'^2 + Z''^2} = Y' + jY'';$$

$$Y' = \frac{Z'}{Z'^2 + Z''^2}, \quad Y'' = \frac{Z''}{Z'^2 + Z''^2} \quad (2.2)$$

$$\epsilon = \frac{1}{j\omega C_0 Z} = \frac{1}{j\omega C_0 (Z' - jZ'')} = \frac{1}{j\omega C_0} \frac{Z' + jZ''}{Z'^2 + Z''^2}$$

$$= \frac{1}{\omega C_0} \frac{Z'' - jZ'}{Z'^2 + Z''^2} = \epsilon' - j\epsilon'' \quad (2.3)$$

$$\epsilon' = \frac{1}{\omega C_0} \frac{Z''}{Z'^2 + Z''^2}, \quad \epsilon'' = \frac{1}{\omega C_0} \frac{Z'}{Z'^2 + Z''^2} \quad (2.4)$$

$$M = \frac{1}{\epsilon} = j\omega C_0 Z = j\omega C_0 (Z' - jZ'') = \omega C_0 (Z'' + jZ') = M' + jM'' \quad (2.5)$$

$$M' = \omega C_0 Z'', \quad M'' = \omega C_0 Z' \quad (2.6)$$

The ratio of applied ac voltage to the resulting ac current is the impedance of the system. As the various immittance functions are inversely related as well, these are conveniently used in the analysis of the impedance data. Due to inverse relations among these, certain features not so visible in plots using certain formalisms may get clearly revealed in some other formalisms. Therefore, impedance spectroscopy is also termed as immittance spectroscopy. All charge transfer processes active in the system under that voltage contribute to the overall current and impedance. A charge transfer process would have a certain time constant and would give its maximum response when the frequency of the applied voltage approaches a value given by inverse of the time constant. A process having low value of time constant would respond in higher-frequency region, whereas the process having larger value of time constant would respond at lower frequencies.

2.2 REPRESENTATION OF ELECTRICAL BEHAVIOR OF MATERIALS BY EQUIVALENT CIRCUIT MODEL

When electrical voltage is applied to a device, certain amount of current flows through it. The electrical power is not always turned directly into heat. For example, power supplied to a loud speaker, to a running motor or to a radio transmitter is largely converted to sound waves, to mechanical motion and to radio waves, respectively. In all these cases the applied energy is completely consumed, it cannot be recovered. Since there is consumption of energy, it can be said that any device that consumes power has a definite value of resistance. This general concept of resistance as something that absorbs/dissipates power is highly useful in modeling, design and development efforts. By applying this concept, the power consuming part (the so-called load) of the device can be substituted by a simple resistance. This approach provides considerable simplification to calculations and helps in development of equivalent circuit models that are highly useful in understanding the functioning of the device. It may be noted that every electrical device possesses some resistance of its own as well, e.g. wire resistance in windings, into which a part of the energy supplied is dissipated as heat (Joule heating) and the remaining may get converted to another form. The power consumed by the resistance R would be equal to the product of applied voltage and resulting current. As the current arising in a resistor is in phase with the voltage across it, it is said that the power consumed is given by product of applied voltage and in-phase current and is numerically equal to i^2R , where i is the current and R is the resistance (The Radio Amateur's Handbook 1968).

Similarly, as a capacitor stores electrical energy, a capacitor may be imagined to be present to represent all parts/processes that store energy as electrical energy. This stored energy is given by $\frac{1}{2} Cv^2$, where C is the capacitance and v the applied voltage. Likewise, parts/processes that store energy in magnetic form can be substituted by an inductor. This energy is given by $\frac{1}{2} Li^2$, where L is the value of inductance and i is the current flowing through the inductor. In general, in a device, there would exist some loss and some storing/use of energy in the form of electric and magnetic fields. Thus, it may be not so unreasonable to represent the behavior of a passive device in terms of lumped components: resistance (R), capacitor (C) and inductor (L). An electrical

circuit involving components such as R, C and L would be called a model. A model circuit comprising such lumped components and capable of showing the same impedance behavior as experimentally observed for a system would be called a lumped equivalent circuit model. In such models, all resistive parts present here and there in the sample are collected (lumped) in a single R, all energy-storing regions such as interfaces at phase boundaries in the sample are represented by a C, etc. Such models are not unique as it is quite likely that more than one model may be developed giving the same behavior (this is further described in Chapter 4). This makes the choice of an equivalent circuit model a challenging task. Equivalent circuit models not only greatly simplify the study of materials and effects of external variables but also found very useful in design and development efforts for integration of the components with the larger system and related simulations (presence of inductive elements may be invoked to describe magnetic and piezoelectric systems which would be described later on in Chapter 4).

In order to proceed further on these lines, we now revisit the situation when an ac voltage source

$$v(t) = v_0 e^{j\omega t} \quad (2.7)$$

is connected to an ideal capacitor (see Section 1.3.3). The charging current i_c is given by

$$i_c(t) = \frac{dq}{dt} = \frac{d(C_0 v)}{dt} = j\omega C_0 v = \omega C_0 e^{j\left(\omega t + \frac{\pi}{2}\right)} \quad (2.8)$$

where C_0 is the capacitance of the condenser with vacuum as dielectric and leads the applied voltage by 90° . Since current is 90° out of phase, no power loss occurs. When some material is filled in the condenser, its capacitance increases to

$$C = C_0 \frac{\epsilon'}{\epsilon_0} = C_0 k' \quad (2.9)$$

where ϵ' and ϵ_0 are real permittivities (or dielectric constants) of the dielectric material and of vacuum, respectively, and the ratio ϵ'/ϵ_0 is the relative dielectric constant k' of the dielectric (Von Hippel 1954).

In real capacitors, as discussed earlier, there might be some power loss (energy dissipation) due to various types of movement of charges inside the dielectric. That may be accounted for by stating that, in addition to the charging current i_c , there may simultaneously appear a loss current component i_l given by

$$i_l = Gv \quad (2.10)$$

and flowing in phase with the applied voltage. G is the conductance of the dielectric material whose value is numerically equal to inverse of resistance and represents all energy-consuming processes present in the dielectric. The total current through the condenser is, thus, given as

$$i = i_c + i_l = j\omega Cv + Gv = (G + j\omega C)v \quad (2.11)$$

In vector diagram representation, the above relationship is expressed by plotting the loss current, Gv , along the axis showing v (X-axis in Figure 2.1) and the charging current $j\omega Cv$ along an axis at right angles to it (Y-axis in Figure 2.1). The total current i is shown as a vector inclined to the horizontal line by an angle θ given by

$$\tan \theta = \frac{\text{charging current } i_c \text{ (90° out of phase)}}{\text{loss current } i_l \text{ (in phase)}} = \frac{\omega C}{G} \quad (2.12)$$

Had there been no loss, the current i would have been along the $j\omega C$ axis, i.e. 90° out of phase with the applied voltage (the ideal situation). The presence of loss term Gv makes the current inclined by an angle δ away from the vertical $j\omega C$ axis. This so-called loss angle δ , representing the deviation from ideality, is equal to $90-\theta$ and carries information about the losses present in the dielectric filling the condenser. This is broadly expressed in the terms of loss tangent ($\tan \delta$) or dissipation factor (D) as given below

$$D \equiv \tan \delta = \cot \theta = \frac{i_l \text{ (in phase)}}{i_c \text{ (90° out of phase)}} = \frac{G}{\omega C} \quad (2.13)$$

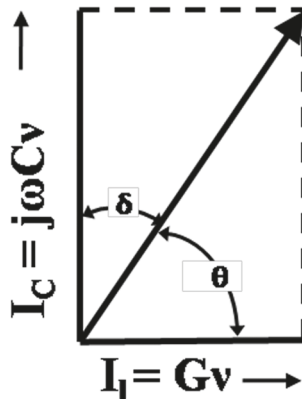


FIGURE 2.1 Charging and loss currents in a capacitor.

Thus, the current through an arbitrary condenser of capacitance C given by $j\omega Cv$ should possess both real and imaginary parts. This quantity can be made to possess a real term as well if it is assumed that the capacitance C is a complex quantity. C will become so only if permittivity and dielectric constant are considered as complex quantities. This real part of the current must arise due to the presence of losses. Therefore, the existence of loss current in addition to charging current is customarily taken care of by introducing a complex permittivity given by

$$\varepsilon = \varepsilon' - j\varepsilon'' \quad (2.14)$$

so that C now becomes complex. The total current i given in Eq. (2.11) can, now, be written as

$$\begin{aligned} i &= j\omega Cv = j\omega C_0 \frac{\varepsilon' - j\varepsilon''}{\varepsilon_0} v = (j\omega\varepsilon' + \omega\varepsilon'') \frac{C_0}{\varepsilon_0} v \\ &= j\omega C_0 \left(\frac{\varepsilon'}{\varepsilon_0} - j \frac{\varepsilon''}{\varepsilon_0} \right) v = j\omega C_0 kv \end{aligned} \quad (2.15)$$

where

$$k \equiv \frac{\varepsilon}{\varepsilon_0} = k' - jk'' \quad (2.16)$$

is the complex relative permittivity or complex dielectric constant of the material.

The loss tangent given by Eq. (2.13) then becomes

$$\tan \delta = \frac{\text{in-phase component}}{90^\circ \text{ out-of-phase component}} = \frac{\varepsilon''}{\varepsilon'} = \frac{k''}{k'} \quad (2.17)$$

Now, if the condenser used in our discussion is a parallel plate capacitor of plate area A and separation d , then the value of the capacitance, C_0 , with vacuum as dielectric, is given by

$$C_0 = \varepsilon_0 \frac{A}{d} \quad (2.18)$$

Equation (2.15) then becomes

$$i = (j\omega\varepsilon' + \omega\varepsilon'') \frac{C_0}{\varepsilon_0} v = (j\omega\varepsilon' + \omega\varepsilon'') \frac{1}{\varepsilon_0} \left(\varepsilon_0 \frac{A}{d} \right) v \quad (2.19)$$

which gives

$$\frac{i}{A} = (j\omega\epsilon' + \omega\epsilon'') \frac{v}{d} \quad (2.20)$$

Now, i/A is the current per unit area, i.e. the current density J , and v/d is voltage per unit distance, i.e. electric field E . Thus Eq. (2.20) can be written as

$$J = (j\omega\epsilon' + \omega\epsilon'')E = j\omega(\epsilon' - j\epsilon'')E = \epsilon \frac{dE}{dt} \quad (2.21)$$

where the following relation has been used

$$\frac{v}{d} = E = \frac{v_0 e^{j\omega t}}{d}, \quad \frac{dE}{dt} = \frac{v_0 e^{j\omega t} j\omega}{d} = j\omega \frac{v}{d} = j\omega E \quad (2.22)$$

Comparing Eq. (2.21) with the relation $J = \sigma E$, we see that the factor $\omega\epsilon'' + j\omega\epsilon'$ corresponds to the conductivity of the dielectric filling the condenser. The factor $\omega\epsilon''$, i.e. the product of angular frequency and the loss factor, is equivalent to dielectric conductivity. As it is the real part in Eq. (2.21), it would represent the in-phase current, and hence dissipation of energy. It may be noted that in the treatment presented earlier, nothing has been assumed regarding specific sources of energy-consuming processes for which the loss current was introduced in Eqs. (2.10) and (2.11). Therefore, this dielectric conductivity corresponds to the sum of all dissipative effects present in the dielectric. It may represent, as well, an actual ohmic conductivity caused by charge transfers due to migrating charge carriers. It may also include energy loss associated with the frequency dependence (dispersion) of ϵ' due to frictions experienced by electric dipoles trying to reorient at pace with the applied electric field.

It may be mentioned that current density J and electric field E are vector quantities. Vector quantities are those which have both magnitude and direction (i.e. can be represented by three components in a three-dimensional coordinate frame). Therefore, in the relation $J = \sigma E$, σ is a tensor quantity and, in general, would have nine components. However, keeping in mind the widely different backgrounds of readers wishing to pursue impedance spectroscopy, the tensor presentation has been avoided. The advanced reader may look at the book by Nye for details (Nye 1985).

The discussion presented earlier quickly reminds us of an ideal capacitor C having a resistance R connected in parallel. In this so-called parallel RC circuit, resistance R would provide a path for flow of some current always in phase with the applied voltage and the capacitor C would allow storage of electrical energy. Thus, based on discussions made so far, electrical behavior of a dielectric on which an ac electric field is applied may be represented, to start with, by a simple circuit having a condenser C (representing all energy-storing processes) and a parallel resistance R that

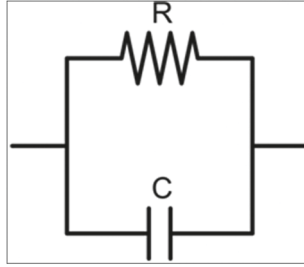


FIGURE 2.2 A parallel RC circuit.

allows a current to flow in phase with the applied voltage so as to represent all losses present.

A parallel RC circuit is schematically shown in Figure 2.2. The impedance between the terminals is given as

$$\frac{1}{Z} = \frac{1}{R} + \frac{1}{\frac{1}{j\omega C}} = \frac{1}{R} + j\omega C = \frac{1 + j\omega CR}{R} \quad (2.23)$$

or

$$Z = \frac{R}{1 + j\omega CR} = \frac{R}{1 + j\omega CR} \frac{1 - j\omega CR}{1 - j\omega CR} = \frac{R(1 - j\omega CR)}{1 + (\omega CR)^2} = \frac{R}{1 + (\omega CR)^2} - j \frac{R\omega CR}{1 + (\omega CR)^2} = Z' - jZ'' \quad (2.24)$$

From this we get

$$Z' = \frac{R}{1 + (\omega CR)^2} \quad (2.25)$$

$$Z'' = \frac{R\omega CR}{1 + (\omega CR)^2} \quad (2.26)$$

When an ac voltage is applied, the resulting current vector will be inclined at an angle θ given by

$$\tan \theta = \frac{Z''}{Z'} = \omega CR \quad (2.27)$$

and the loss tangent is given by

$$\tan \delta = \tan(90 - \theta) = \cot \theta = \frac{1}{\omega CR} \tag{2.28}$$

The limiting values at $\omega \rightarrow 0$ and $\omega \rightarrow \infty$ are given below

$$Z'|_{\omega \rightarrow 0} = R, Z'|_{\omega \rightarrow \infty} = 0, Z''|_{\omega \rightarrow 0} = 0, Z''|_{\omega \rightarrow \infty} = 0 \tag{2.29}$$

Also at $\omega = 1/CR$, i.e. when $\omega CR = 1$, we get $Z' = R/2$ and $Z'' = R/2$.

Typical plots of Z' and Z'' as function of frequency are shown in Figure 2.3(a,b). Also, it is found that Z' and Z'' satisfy the relation

$$\left(Z' - \frac{R}{2} \right)^2 + Z''^2 = \left(\frac{R}{2} \right)^2 \tag{2.30}$$

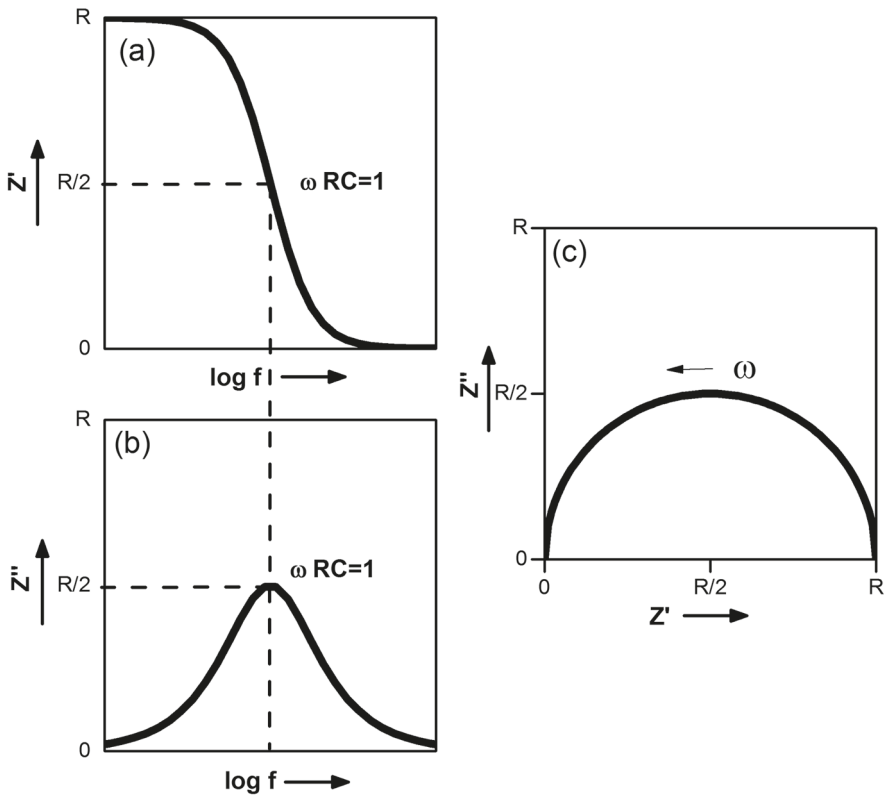


FIGURE 2.3 Plots of (a) Z' versus $\log f$, (b) Z'' versus $\log f$ and (c) Z'' versus Z' for a parallel RC circuit.

This equation is similar to the relation

$$(x - a)^2 + (y - b)^2 = r^2 \quad (2.31)$$

which is the equation of a circle having radius r and center at the point (a,b) in a X-Y Cartesian plot. Comparing Eq. (2.30) with Eq. (2.31) reveals that we have Z' in the place of x , Z'' in the place of y , $a = R/2$, $b = 0$ and $r = R/2$. This indicates that Eq. (2.30) represents a circle on a Z'' versus Z' plot. Its radius is equal to $R/2$ and the center is at the point $(R/2,0)$, which lies on the Z' axis. At $\omega = 0$, Z' is equal to R and Z'' is equal to zero, and at $\omega = \infty$, $Z' = 0$ and $Z'' = 0$, indicating that the circle would traverse from right to left as frequency is increased, pass through origin and will have an intercept equal to R on the Z' axis at the low-frequency side. As seen from Eqs. (2.25) and (2.26), the values of Z' and Z'' are positive in the whole-frequency range. Thus, the Z'' versus Z' plot for a parallel RC circuit would be a semicircle with center at point $(R/2,0)$ lying on Z' axis, would have a low-frequency intercept equal to R , would be traversing from right to left as the frequency is increased and would pass through the origin. A typical plot is shown in Figure 2.3(c). It may be noted that the peak point on the semicircle lying just above the point $(R/2,0)$ (i.e. where $Z' =$ half of the intercept R) corresponds to the frequency where ω is such that $\omega CR = 1$, i.e. this value of ω corresponds to inverse of time constant RC, i.e. the relaxation frequency.

Plots (a) and (b) are called spectroscopic plots, and plot (c) is called complex plane plot. Since frequency spans several decades, $\log(\omega)$ or $\log f$ is used on the X-axis in the spectroscopic plots.

If, for a dielectric material, Z' and Z'' are experimentally measured and Z'' versus Z' plot appears to be a clear semicircular arc, then as a first step, we can represent the behavior of the dielectric by a parallel RC circuit (an equivalent circuit model) and infer the presence of one charge transfer process. A typical experimental plot might look as shown in Figure 2.4 where stars show the experimental values. The value of R can be obtained by drawing a semicircular arc through these points and origin and extrapolating the curve to meet the Z' axis on the right low-frequency side. Using this value of R and noting the frequency where Z'' peaks value of C can be calculated from the relation $\omega CR = 1$. This value of R can be used to obtain dc conductivity. In this way, value of dc conductivity could be obtained by performing ac measurements followed by equivalent circuit modeling. This is one of the very useful applications of impedance spectroscopy.

It is cautioned that it may be misleading to jump to conclusion about the presence of a single charge transfer process just by observing the appearance of a semicircular arc in experimental Z'' versus Z' plot only. For final conclusions, other plots such as M'' versus M' need to be looked at. These points would be further discussed later in Chapter 4.

The complex plane plots, in general, might possess a single distorted semicircular type arc, depressed looking arc (i.e. a semicircular arc having its center below the Z' axis), an arc having more than one bump, an arc having a steeply rising low-frequency branch, an arc where the high-frequency side intercept point is shifted toward right on Z' axis, etc. Such plots may arise due to the presence of more than

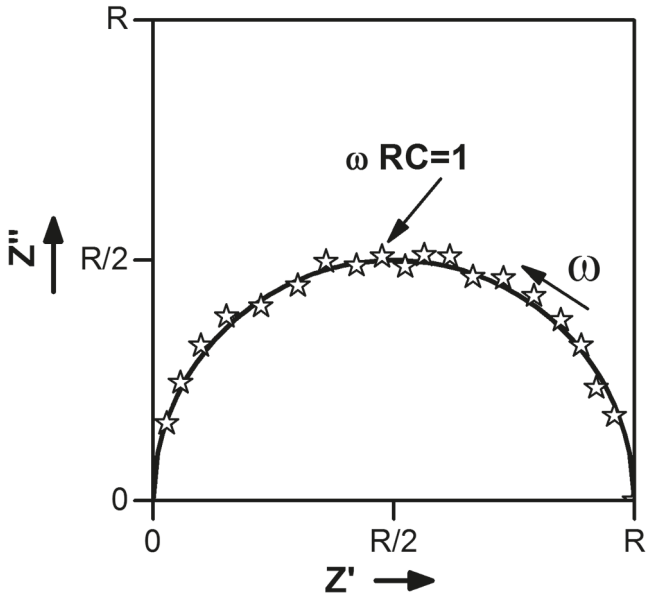


FIGURE 2.4 Plot of Z'' versus Z' . The stars (*) represent the experimental values.

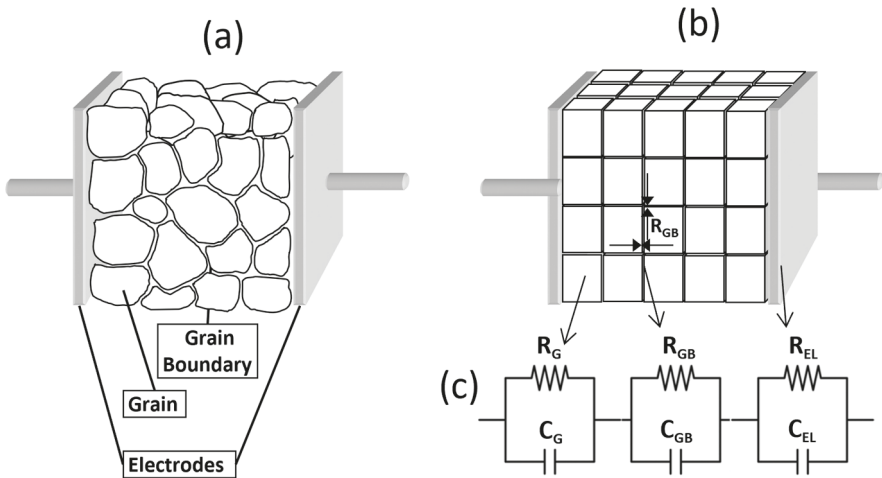


FIGURE 2.5 (a) Schematic showing ceramic grain, grain boundary and electrodes, (b) brick wall model for the same, (c) equivalent circuit model involving resistive (R) and capacitive (C) components. Indices: G, grain; GB, grain boundary; EL, ceramic–electrode interface.

one charge transfer processes in the system and can be simulated by using equivalent circuit representations for those processes. For example, a single-phase ceramic pellet placed between two parallel electrodes may be schematically shown as given in Figure 2.5(a) (Waser and Hagenbeck 2000).

A ceramic may be easily prepared by using a solid-state reaction route where the initial compounds are grinded and heated at higher temperature to yield the required material in the form of a powder. This powder is pressed to form a pellet which is further sintered, polished and electroded. Thus, the ceramic pellet placed between two electrodes to form a parallel plate capacitor for impedance measurements can be visualized as aggregate of randomly oriented small grains (small crystallites) and electrodes. The joining regions between the grains, called the grain boundary, have strained bonds due to mismatch in crystallite orientations and, therefore, possess properties different from those of grains. These so-called grain–grain boundary interfaces and the contact region of the pellet with the electrodes provide areas for charges to accumulate. Charges moving from one electrode may be thought, in a naive way, to be passing through all these regions to arrive at the other electrode. Said in a simpler way, charges get two paths to reach the other electrode: one is through the continuous grain boundary phase and the other via a path going through grain, grain boundary and grain chain. Thus, the ceramic system may be visualized as a grain–grain boundary–electrode system as shown in Figure 2.5(a). This is further simplified by using the so-called brick wall model (Figure 2.5(b)) and may be represented by three RC circuits ($R_G C_G$, $R_{GB} C_{GB}$ and $R_{EL} C_{EL}$ corresponding to grain, grain boundary and sample–electrode contact, respectively) connected in series, further connected with another parallel RC corresponding to the overall continuous grain boundary. Usually, the grain boundaries are more resistive than grains. Therefore, the overall parallel RC branch is left out and the model gets simplified to as shown in Figure 2.5(c) (Waser and Hagenbeck 2000; Macdonald 2005; Wang 2001).

The experimental immittance plots for such a system would usually possess a distorted arc (overlap of the three contributions) having clearly visible bumps if the three time constants, $R_G C_G$, $R_{GB} C_{GB}$ and $R_{EL} C_{EL}$, are widely separated. Similar approach is applied for developing equivalent circuit models for a system keeping in mind various charge transfer processes that might be possibly present in the system. For example, a possible equivalent circuit model for a wet ceramic pellet placed between two electrodes would be a circuit comprising three parallel RC's connected in series where other RC combinations may be connected in parallel across the series combination, representing the shorting path provided by the water layer (Katare et al 2005). The choice of a model is greatly facilitated by comparing the experimental plots with those simulated for various models. This subject matter would be taken up in later chapters.

SUMMARY

Plot of impedance of the sample as function of frequency of the incident electromagnetic wave is termed as impedance spectrum and the analysis is called impedance spectroscopy. Impedance spectroscopy yields information about all the charge transfer processes going on in the interior of the sample that contribute to the overall

impedance of the system in the applied frequency range. Impedance spectroscopy is also called as complex impedance analysis and electrical impedance spectroscopy. The plots of Z' or Z'' versus frequency are called spectroscopic plots and Z'' versus Z' plots are called complex plane plots or Nyquist plots. The electrical behavior of a system may be expressed by using interrelated functions (formalisms), collectively called immittance functions: impedance $Z = Z' - jZ''$, admittance $Y = 1/Z = Y' + jY''$, modulus $M = 1/\varepsilon = M' + jM''$ and relative permittivity $\varepsilon = 1/(j\omega C_0 Z) = \varepsilon' - j\varepsilon''$. Due to inverse relations among these certain features, not so visible in plots, using certain formalisms may get clearly revealed in some other formalisms. A parallel RC circuit may be used to represent a charge transfer process. The Z'' versus Z' plot for this model is a semicircular arc passing through origin and intercepting the Z' axis at the low-frequency side where $Z' = R$. The peak of the plot occurs when applied frequency ω and time constant RC of the model satisfy the relation $\omega RC = 1$. When Z'' versus Z' experimental plot for a system is such a semicircular arc, a parallel RC circuit model may be chosen to represent the system. The value of R may be obtained by noting the intercept and that of C by noting the frequency where the peak occurs. The value of R may be used to obtain the value of dc conductivity of the system. This is one of the great advantages of impedance spectroscopy that dc conductivity can be obtained by using ac measurements.

NOTES

- 1 Actually notations f (cycles per second or hertz) and ω (radians per second), respectively, represent the frequency and angular frequency. However, these are interchangeably used keeping in mind that ω is equal to $2\pi f$.
- 2 A complex quantity z is written as $z = x + jy$, where x is the real part, written as $\text{Re}(z)$, and y is the imaginary part, $\text{Im}(z)$. However, keeping in mind the earlier notations used in literature, the impedance has been expressed as $Z = Z' - jZ''$. At present both notations, i.e. $Z = Z' - jZ''$ and $Z = Z' + jZ''$, are being used in literature. When $Z = Z' - jZ''$ is used, the plots will be labeled as Z' versus $\log f$, Z'' versus $\log f$ and Z'' versus Z' . When $Z = Z' + jZ''$ is used, the plots will be labeled as Z' versus $\log f$, $-Z''$ versus $\log f$ and $-Z''$ versus Z' . Throughout this book $Z = Z' - jZ''$ has been used.

3 Experimental Measurements

3.1 EXPERIMENTAL MEASUREMENTS AND PLOTTING THE DATA

Experimental measurement essentially involves applying a small alternating voltage at the sample and measuring the resulting current and its phase difference with respect to the voltage as function of frequency ω ($\omega = 2\pi f$). This may be readily performed by sandwiching the sample between two parallel plates made of a conductor. Thus, a parallel plate capacitor is formed to which connecting leads are attached, which are further connected to the measuring setup, such as a commercially available impedance analyzer. This is the so-called two-probe method as is schematically shown in Figure 3.1. The impedance $Z(\omega)$ is calculated, from the values of the magnitude of ac voltage $v(\omega, t)$ applied and magnitude and phase of the resulting current $i(\omega, t)$ that flows through the sample, as $Z(\omega) = v(\omega, t)/i(\omega, t)$.

As an example, the method is now described for a ceramic sample. The ceramic sample is prepared in the form of a pellet by pressing and sintering the as-prepared ceramic powder. Its dimensions (diameter and thickness d) are measured, say by Vernier calipers. The two parallel faces are coated with some conducting paint (or vacuum coated) and slightly heated (cured) for making proper contact. The pellet is then placed between the two electrodes, so that a parallel plate capacitor is formed with the ceramic material as its dielectric. These electrodes are further connected to the impedance meter. Easy availability of commercial versatile impedance meters interfaced to computer has made impedance measurement a straightforward experimental work rendering impedance spectroscopy a very popular and fast-growing tool. In order to study the behavior of the sample under various external parameters such as temperature, atmosphere, etc., suitable arrangements for heating/cooling, flow of inert gas, etc. are made. For measurements at room and lower temperatures for ceramic samples, usually electrodes made of copper suffice. For higher temperatures, electrodes made of brass or steel may be used.

The two-probe method is straightforward and easy to use. However, as the current coming out from the meter would pass through various parts coming in its path from terminal A_1 to A_2 (i.e. A_1 - A_3 - A_6 -sample- A_5 - A_4 - A_2), the meter would measure the total impedance between the two terminals A_1 and A_2 including that of leads, connecting wires, sample-electrode contact and sample. Therefore, when the impedance of the

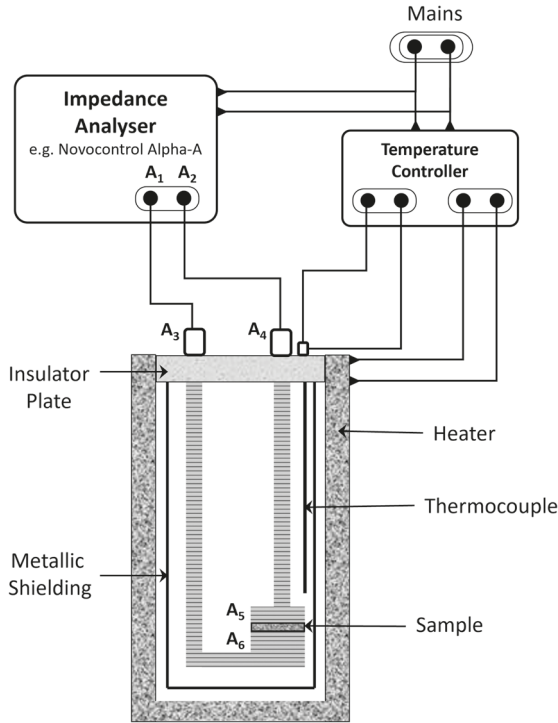


FIGURE 3.1 Two-probe setup for impedance measurements.

sample is large, lead impedances can be ignored and the values displayed by the meter would be very close to that of the sample. For samples having low impedances, the measured values would be quite erroneous. This problem is solved by adopting the four-probe technique. In four-probe method, four terminals are used as schematically shown in Figure 3.2, in which known amount of current is passed through outer electrodes 1 and 4, and voltage appearing across the middle terminals 2 and 3 is measured. The impedance is obtained by using the values of voltage and current. The advantage of this technique is that since the voltage measuring device has a high-input impedance, negligible current flows through the electrode–sample contacts at points 2 and 3, and contact effects are minimized. This technique is preferred for materials having low resistance such as semiconductors (Runyan 1975; Lark-Horovitz 1959). Sometimes, the available equipment provides only four-probe facility. Then, the terminals 1 and 2 are joined, and terminals 3 and 4 are joined, so as to use it as a two-probe setup, compromising with the benefits of the four-probe technique. For samples having impedances beyond the measuring range of the available meter, a high-quality resistor, R , of known value may be connected in parallel to the sample, i.e. across the points A_3 and A_4 in Figure 3.1. The contribution is suitably subtracted from the measured impedance values by using the formula $1/Z_{\text{sample}} = 1/Z_{\text{measured}} - 1/R$ (Mishra et al. 2013).

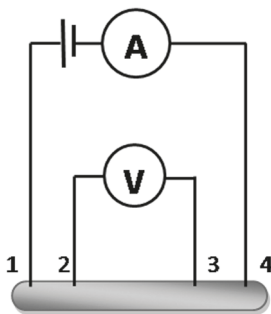


FIGURE 3.2 Schematic diagram of a four-probe setup.

The sample holder is an extremely important component of impedance spectroscopic measurements. Few points of precaution are worth mentioning. In two-probe setups, the electrodes should make good contact with the sample, otherwise small air gaps might act as air capacitors coming in series with the pellet, causing a lowered capacitance value. As shown in Figure 3.1, the two leads at A_3 and A_4 come out through an insulator plate. For high-impedance samples, this insulator plate should be suitably chosen such that its impedance is much larger than that of the sample, and remains so at elevated temperatures too, otherwise erroneous readings would be obtained due to shorting action of the insulator. That sample holder design should be preferred where the pellet is accommodated with the parallel faces lying horizontally, so as to prevent it from falling, which is quite likely when it is vertically placed. The pellets should be suitably polished to provide good contact with the electrodes, otherwise capacitances formed in the tiny gaps with air dielectric and coming in series with the pellet would severely deteriorate the observed values. Also, the part of the assembly holding the sample must be enclosed in a metallic container/faraday shield (as shown in Figure 3.1) to isolate it from outside interferences arising due to power line and other radiations. Suitable space should be provided between leads connected to the sample and the walls of the shield to avoid the capacitive shorting effects at high frequencies (Simpson 1974).

The impedance data can be collected in various forms such as absolute value of the impedance $|Z|$ and phase angle θ , real part of impedance (Z') and imaginary part (Z''), etc. The data are collected by the computer and may be displayed in desired tabular form.

For usual dielectrics, parallel RC mode may be chosen and the frequency region typically employed ranges from about 100 Hz to 1 MHz. However, depending on the requirements, this range may be extended, for which sometimes the sample holders might need some modifications to minimize effects of stray capacitances arising due to presence of conductors in the vicinity of the sample/electrodes and value of inductance appearing due to long connecting leads. The effect of connecting leads may be minimized by performing calibration procedures prescribed in the impedance meter manuals, or by using a repeated measurement with a known parallel resistance (Pandey et al. 1996; Macdonald 2005). In this method, impedance measurements

are carried out for empty sample holder, and an equivalent circuit model is obtained, which is further used to subtract the empty sample contributions from the impedance values measured with sample in place.

The value of the empty cell capacitor with vacuum as dielectric, C_0 , is obtained by using the formula

$$C_0 = \epsilon_0 \frac{A}{d} \quad (3.1)$$

where A is the area of one of the parallel faces of the sample and d is its thickness. This is used to obtain values of real and imaginary parts of other immittance functions, viz Y , M and ϵ , by using Eqs. (2.2), (2.4) and (2.5). These data are plotted as function of frequency as well as in complex plane. One such hypothetical plot has already been shown in Figure 2.4. By looking at the shape of the plots and the processes thought to be possibly present in the system under investigation, a suitable equivalent circuit model is chosen to represent the data. The values of the components in model are obtained graphically, which are further used to obtain more accurate values by using complex nonlinear least squares procedure (see Appendix A2). The choice of the most appropriate model is greatly facilitated by comparing the experimental plots with simulated plots. Some useful models and their simulated plots are described in Chapter 4.

The commercial impedance meters at present come with computer interfacing and are equipped with softwares for automatic data acquisition, plotting and fitting of the data to a suitable model. However, in order to get the feel of the procedures, plotting and analysis of the data separately is worth pursuing and is very useful for the young workers.

For carrying out measurements for magnetic materials, the sample may be put inside a coil whose ends are connected to the impedance meter. This would be described later on in Section 6.3.

It is worth noting that several pellets for the same ceramic system may be used in an experiment. The diameter of the pellets are almost same if they are prepared in the same die. However, their thickness might have little variations, which would affect the observed values. In order to make the data consistent, these values have to be normalized to same size (dimensions). In general, during measurements with different samples of the same material, values of thickness d and area of cross section A may not be exactly equal. Such situations may also arise while performing impedance measurements for liquid samples. The data so obtained, therefore, need to be normalized so that it conforms to the same A and d . This may be needed when impedance values are compared for different systems. The procedure for such a correction is presented in the following examples.

Example 3.1 Impedance measurements have been done by using three pellets: P_1 , P_2 and P_3 of a material. These pellets have thicknesses d_1 , d_2 and d_3 , respectively, and the surface area of one of the parallel faces of the pellets is $A \text{ cm}^2$. Assuming that the pellets were prepared under identical conditions, obtain expressions for normalized impedance values that should be used for comparison and other data processing.

Solution:

Let the measured resistances of the pellets be R_1 , R_2 and R_3 , respectively, which can be written as

$$R_1 = \rho \frac{d_1}{A}, R_2 = \rho \frac{d_2}{A}, R_3 = \rho \frac{d_3}{A} \quad (3.2)$$

where ρ is the resistivity (inverse of the conductivity) of the material. The values of R_2 and R_3 , modified to correspond to thickness d_1 , and written as R_2' and R_3' , would be given as

$$R_2' = \rho \frac{d_1}{A} = \left(\rho \frac{d_2}{A} \right) \frac{d_1}{d_2} = R_2 \frac{d_1}{d_2} \quad (3.3)$$

Similarly

$$R_3' = R_3 \frac{d_1}{d_3} \quad (3.4)$$

The treatment has been presented for taking resistances only. Thus, measured values of impedances have to be multiplied by (d_1/d_2) for pellet P_2 and by (d_1/d_3) for pellet P_3 .

Example 3.2 Impedance measurements have been done for a material by using three pellets: P_1 , P_2 and P_3 , having surface areas of one of the parallel faces equal to A_1 cm², A_2 cm² and A_3 cm² and thicknesses d_1 , d_2 and d_3 , respectively. Obtain expressions for impedance values normalized to thickness d_1 and area A_1 to be used for comparison and other data processing.

Solution:

Let the measured resistance values for pellets P_1 , P_2 and P_3 be R_1 , R_2 and R_3 , respectively. Also, let the resistance values for pellets P_2 and P_3 normalized to surface area A_1 and thickness d_1 be R_2' and R_3' , respectively.

R_1 , R_2 and R_3 can be written as

$$R_1 = \rho \frac{d_1}{A_1}, R_2 = \rho \frac{d_2}{A_2}, R_3 = \rho \frac{d_3}{A_3} \quad (3.5)$$

where ρ is the resistivity.

Now,

$$R_2' = \rho \frac{d_1}{A_1} = \left(\rho \frac{d_2}{A_2} \right) \frac{d_1}{d_2} \frac{A_2}{A_1} = R_2 \frac{d_1}{d_2} \frac{A_2}{A_1} \quad (3.6)$$

Similarly

$$R'_3 = R_3 \frac{d_1}{d_3} \frac{A_3}{A_1} \quad (3.7)$$

Therefore, the measured values have to be multiplied by $(d_1/d_2)(A_2/A_1)$ for pellet P_2 and by $(d_1/d_3)(A_3/A_1)$ for pellet P_3 .

Example 3.3 Impedance measurements for the same material have been done by using two setups: one having electrodes of area A_1 separated by distance d and the other having electrodes of area A_2 separated by the same distance d . Assume that the material completely fills the space between the electrodes. Obtain expressions for normalized impedance values to be used for comparison and other data processing (such a situation arises in impedance spectroscopic measurements involving liquid cells/electrolytes).

Solution:

Let the measured resistances by using first and second setups for the same material be R_1 and R_2 , respectively, which can be written as

$$R_1 = \rho \frac{d}{A_1}, R_2 = \rho \frac{d}{A_2} \quad (3.8)$$

where ρ is the resistivity.

R_2 can be rewritten as

$$R_2 = \rho \frac{d}{A_2} = \left(\rho \frac{d}{A_1} \right) \frac{A_1}{A_2} = (R'_2) \frac{A_1}{A_2}, R'_2 = R_2 \frac{A_2}{A_1} \quad (3.9)$$

where R'_2 would be the value of the resistance that would be observed when the surface area of the electrode is altered to A_1 .

Here we note that Eq. (3.8) can be written as

$$R_1 A_1 = \rho \frac{d}{1}, R_2 A_2 = \rho \frac{d}{1} \quad (3.10)$$

i.e. measured resistance multiplied by the area of the electrode is equivalent to the resistance that would be observed when measurement is done using electrode having unit area (1 cm^2).

Also

$$R_1 A_1 = \rho d = R_2 A_2 \quad (3.11)$$

i.e. since ρd is constant, electrodes of larger area would yield a lower resistance and that with smaller area would give larger resistance. For two different materials/electrolytes, value of ρ would be different.

Therefore, in order to avoid these calculations, measured impedance values are multiplied by surface area of the electrodes (inside area of one of the faces of the two parallel electrodes). It has become a general practice to use these new values in the impedance plots and write the labels as Z' (ohm.cm²) and Z'' (ohm.cm²) on X- and Y-axes, respectively, in the complex plane impedance plots. In using such notations, one has to keep in mind that units of Z' and Z'' are ohms only. So, the X- and Y-axes may be labeled as Z' (ohm) and Z'' (ohm), respectively, as usual, and it should be stated in the captions or in the text that the values have been normalized to unit area. This is further illustrated by taking a numerical example.

Let $A = 4 \text{ cm}^2$ and $R_1 = 100 \ \Omega$. Then we have

$$100 \text{ (in ohms)} = \rho \frac{d}{4 \text{ cm}^2} = \rho \frac{d}{4 \times (1 \text{ cm}^2)} \quad (3.12)$$

Multiplying both sides by 4 (just the number), we get

$$400 \text{ (in ohms)} = \rho \frac{d}{1 \text{ cm}^2}$$

The value of resistance corresponding to unit area is 400 Ω , not 400 $\Omega \cdot \text{cm}^2$.

Example 3.4 Calculate the value of C_0 for an empty sample holder used to house a pellet of thickness 2 mm and diameter 1.1 cm.

Solution:

$$\epsilon_0 = 8.85 \times 10^{-12} \text{ F/m}, A = \pi \times (0.55 \times 10^{-2} \text{ m})^2 = 9.5033 \times 10^{-5} \text{ m}^2, d = 2 \times 10^{-3} \text{ m}$$

$$\begin{aligned} C_0 &= \epsilon_0 \frac{A}{d} = \left(8.85 \times 10^{-12} \frac{\text{F}}{\text{m}} \right) \times \frac{9.5033 \times 10^{-5} \text{ m}^2}{2 \times 10^{-3} \text{ m}} \\ &= 4.2052 \times 10^{-13} \text{ F} = 0.42 \text{ pF} \end{aligned}$$

SUMMARY

Impedance measurements on solid samples may be performed by sandwiching the sample between two parallel plates made of a conductor. A parallel plate capacitor is formed to which connecting leads are attached, which are further connected to the measuring setup, such as a commercially available impedance analyzer. This is the so-called two-probe method. For low-impedance materials, four-probe method is used where current is passed through the outer electrodes, and the ratio between voltage measured across the middle electrodes and the current gives the value of

impedance. Impedance of very high resistivity systems, Z_{actual} , may be measured by connecting a high-quality resistance, R , in parallel to the sample and using the relation $1/Z_{\text{actual}} = 1/Z_{\text{measured}} - 1/R$. For solid samples, preference should be given to sample holders where the sample is placed, with its parallel surfaces lying horizontally to avoid its slipping down during measurements. Also, the sample holders should have sufficient inner space around the sample inside, so that stray capacitance effects are minimized. The contributions from leads, connectors, etc., may be removed either by following the calibration procedures provided by the instrument manufacturer or by repeating the measurements with empty sample holder, having the gap between the parallel electrodes same as the sample thickness and suitably subtracting this from the measurements done with sample in place. It is a good practice to perform a test run by using some standard sample before commencing work on new systems to ensure that the equipment is working well.

4 Equivalent Circuit Models and Their Simulated Immittance Behaviors

Impedance spectroscopic studies are carried out by representing the system under observation by a suitable equivalent circuit model that represents the observed impedance behavior best. Choice of a suitable model is a difficult process and this becomes much more so as there may be several models that would produce the same impedance versus frequency behavior. The development of the model is greatly facilitated by comparing the experimental plots with those simulated for various models, and keeping in mind the possible charge transfer processes that might be present in the system or may be dormant and would start contributing when certain external parameters, such as temperature, are changed. A specific feature of the complex plane plots is the appearance of semicircular arcs whose centers may or may not lie on the real axis. The cases where the center lies on the real axis may be modeled by utilizing usual components such as R and C. For modeling the systems showing arcs having centers below the real axis, a component known as constant phase angle element (CPE) is utilized. Usually, the phase angle between applied voltage and the resulting current in a system depends on the frequency of the applied voltage. However, there may occur certain situations where this phase difference is constant (independent of frequency), arising due to different reasons, e.g. distribution of time constant in the system. Such systems are modeled by invoking the concept of the so-called CPE. CPE is a mathematical function that yields a constant phase difference between current and applied voltage and has been more or less accepted as a convenient tool to represent experimental data that yield depressed complex plane plots.

In this chapter, some simple model circuits involving resistive, capacitive and inductive components are considered, expressions for real and imaginary parts of immittance functions are derived and their simulated patterns are presented. Simulated behavior of few models involving CPE is also given. For brevity, only the complex plane plots are shown. The presentation $Z = Z' - jZ''$ has been used. Other immittance functions are obtained by using relations impedance ($Z = Z' - jZ''$), admittance ($Y = 1/Z = Y' + jY''$), permittivity ($\epsilon = 1/(j\omega C_0 Z) = \epsilon' - j\epsilon''$) and modulus ($M = 1/\epsilon = j\omega C_0 Z = M' + jM''$), C_0 being the capacitance of the empty cell used to house the sample.

Mathematical expressions for real and imaginary parts of immittance functions and their limiting values for $\omega \rightarrow 0$ and $\omega \rightarrow \infty$ are obtained. The complex plane plots are also called Nyquist plots. It may be mentioned that some immittance functions

are inversely related, so plots using certain formalisms may not clearly display the low-frequency or high-frequency behavior, whereas those features may get clearly revealed in other formalisms. Therefore, plots of all the four immittance functions are given. The immittance values are normalized and the values of the ratios of components are suitably chosen such that the variations are clearly displayed. For brevity, the spectroscopic plots, i.e. variations of the immittance values as function of frequency, are not given (Macdonald 2005; Pandey et al. 1995, 1998; Katare 1997; Katare et al. 1999; Chaitanya 2008; Chaitanya et al. 2014; Pandey et al. 2017, 2019a).

4.1 MODEL INVOLVING RESISTANCE R AND CAPACITANCE C IN PARALLEL

This has already been described in Section 2.2. However, for the sake of completeness it is briefly presented here. This is the most useful model widely used to represent a charge transfer process in vast variety of systems and also is readily used to introduce the subject of impedance spectroscopy. A parallel RC circuit is shown schematically in Figure 4.1(a).

Expressions for immittance functions are given as

$$Z = Z' - jZ'' = \frac{R_1}{1 + j\omega C_1 R_1} = \frac{R_1}{1 + (\omega C_1 R_1)^2} - j \frac{R\omega C_1 R_1}{1 + (\omega C_1 R_1)^2} \quad (4.1)$$

$$Z' = \frac{R_1}{1 + (\omega C_1 R_1)^2}, Z'' = \frac{R\omega C_1 R_1}{1 + (\omega C_1 R_1)^2} \quad (4.2)$$

$$M' = \omega C_0 Z'' = \frac{C_0}{C_1} \frac{(\omega C_2 R_1)^2}{1 + (\omega C_1 R_1)^2}, M'' = \omega C_0 Z' = \frac{C_0}{C_1} \frac{\omega C_1 R_1}{1 + (\omega C_1 R_1)^2} \quad (4.3)$$

$$Y' = \frac{1}{R_1}, Y'' = \omega C_1 \quad (4.4)$$

$$\varepsilon' = \frac{1}{\omega C_0} Y'' = \frac{C_1}{C_0}, \varepsilon'' = \frac{1}{\omega C_0} Y' = \frac{C_1}{C_0} \frac{1}{\omega C_1 R_1} \quad (4.5)$$

The limiting values of these functions at $\omega \rightarrow 0$ and $\omega \rightarrow \infty$ are given below

$$Z'|_{\omega \rightarrow 0} = R_1, Z'|_{\omega \rightarrow \infty} = 0, Z''|_{\omega \rightarrow 0} = 0, Z''|_{\omega \rightarrow \infty} = 0 \quad (4.6)$$

$$M' \Big|_{\omega \rightarrow 0} = 0, M' \Big|_{\omega \rightarrow \infty} = \frac{C_0}{C_1}, M'' \Big|_{\omega \rightarrow 0} = 0, M'' \Big|_{\omega \rightarrow \infty} = 0 \quad (4.7)$$

$$Y' \Big|_{\omega \rightarrow 0} = \frac{1}{R_1}, Y' \Big|_{\omega \rightarrow \infty} = \frac{1}{R_1}, Y'' \Big|_{\omega \rightarrow 0} = 0, Y'' \Big|_{\omega \rightarrow \infty} = \infty \quad (4.8)$$

$$e' \Big|_{\omega \rightarrow 0} = \frac{C_1}{C_0}, e' \Big|_{\omega \rightarrow \infty} = \frac{C_1}{C_0}, e'' \Big|_{\omega \rightarrow 0} = \infty, e'' \Big|_{\omega \rightarrow \infty} = 0 \quad (4.9)$$

Z' and Z'' satisfy the relation

$$\left(Z' - \frac{R_1}{2} \right)^2 + (Z'')^2 = \left(\frac{R_1}{2} \right)^2 \quad (4.10)$$

indicating that Z'' versus Z' plot will be a semicircle of radius $R_1/2$ with center at the point $(R_1/2, 0)$ on the Z' axis. The arc will traverse from right to left as the frequency increases, pass through the origin and will have an intercept on the Z' axis at point $(R_1, 0)$ at the low-frequency end. Also, at the frequency where $\omega C_1 R_1 = 1$, we have $Z' = R_1/2$ and $Z'' = R_1/2$. The point $(R_1/2, R_1/2)$ corresponds to the top of the semicircular arc in Figure 4.1(b).

Similarly, M' and M'' satisfy the relation

$$\left(M' - \frac{C_0}{2C_1} \right)^2 + (M'')^2 = \left(\frac{C_0}{2C_1} \right)^2 \quad (4.11)$$

indicating that M'' versus M' plot will be a semicircle of radius $C_0/(2C_1)$ with center at the point $(C_0/(2C_1), 0)$ on the M' axis. The arc will traverse from left to right as the frequency increases, pass through the origin and will have an intercept on the M' axis at point $(C_0/C_1, 0)$ at the high-frequency end. Also at the frequency where $\omega C_1 R_1 = 1$, we have $M' = C_0/(2C_1)$ and $M'' = C_0/(2C_1)$. The point $(C_0/(2C_1), C_0/(2C_1))$ corresponds to the top of the semicircular arc in Figure 4.1(c). Thus, if this model is chosen to represent the system, the values of the components R_1 and C_1 can be obtained by noting the low-frequency side intercept on the Z' axis ($R_1 =$ this intercept) in the Z'' versus Z' plot and the frequency ω_1 corresponding to the top of the arc giving $C_1 = 1/(\omega_1 R_1)$. The values of the components can be obtained from M'' versus M' plot as well. The high-frequency intercept on the M' axis gives C_0/C_1 , i.e. C_1 and the frequency corresponding to the top of the plot gives R_1 from the relation $\omega C_1 R_1 = 1$.

Normalized complex plane immittance plots are shown in Figures 4.1(b–e).

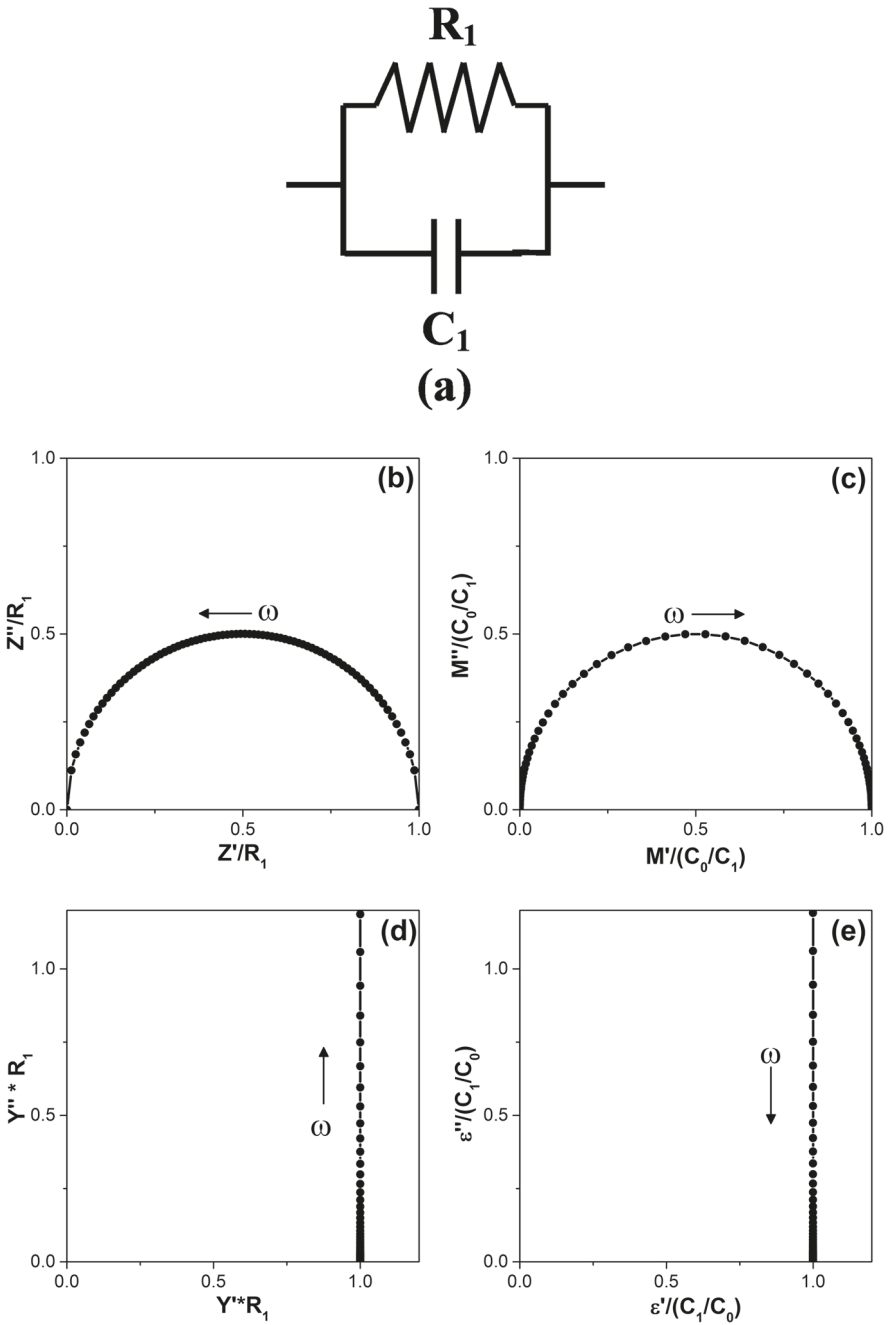


FIGURE 4.1 (a) A parallel RC circuit. Normalized plots of (b) Z''/R_1 versus Z'/R_1 , (c) $M''/(C_0/C_1)$ versus $M'/(C_0/C_1)$, (d) $Y''*R_1$ versus $Y'*R_1$ and (e) $\varepsilon''/(C_1/C_0)$ versus $\varepsilon'/(C_1/C_0)$.

4.2 MODEL INVOLVING RESISTANCE R AND CAPACITANCE C IN SERIES

Figure 4.2(a) shows a series combination of resistor and capacitor.

A series RC circuit has time constant equal to RC and may be used to represent a process. Impedance ($Z = Z' - jZ''$) of this model is given by

$$Z = R_1 - j \left(\frac{1}{\omega C_1} \right) \quad (4.12)$$

Real and imaginary parts of Z are given in Eq. (4.13), which are used to obtain other immittance functions.

$$Z' = R_1, Z'' = \frac{1}{\omega C_1} \quad (4.13)$$

The limiting values at $\omega \rightarrow 0$ and $\omega \rightarrow \infty$ are given below

$$Z' \Big|_{\omega \rightarrow 0} = R_1, Z' \Big|_{\omega \rightarrow \infty} = R_1, Z'' \Big|_{\omega \rightarrow 0} = \infty, Z'' \Big|_{\omega \rightarrow \infty} = 0 \quad (4.14)$$

$$M' \Big|_{\omega \rightarrow 0} = \frac{C_0}{C_1}, M' \Big|_{\omega \rightarrow \infty} = \frac{C_0}{C_1}, M'' \Big|_{\omega \rightarrow 0} = 0, M'' \Big|_{\omega \rightarrow \infty} = \infty \quad (4.15)$$

$$Y' \Big|_{\omega \rightarrow 0} = 0, Y' \Big|_{\omega \rightarrow \infty} = \frac{1}{R_1}, Y'' \Big|_{\omega \rightarrow 0} = 0, Y'' \Big|_{\omega \rightarrow \infty} = 0 \quad (4.16)$$

$$\varepsilon' \Big|_{\omega \rightarrow 0} = \frac{C_1}{C_0}, \varepsilon' \Big|_{\omega \rightarrow \infty} = 0, \varepsilon'' \Big|_{\omega \rightarrow 0} = 0, \varepsilon'' \Big|_{\omega \rightarrow \infty} = 0 \quad (4.17)$$

Y' and Y'' are given by

$$Y' = \frac{1}{R_1} \frac{(\omega C_1 R_1)^2}{1 + (\omega C_1 R_1)^2}, Y'' = \frac{1}{R_1} \frac{\omega C_1 R_1}{1 + (\omega C_1 R_1)^2} \quad (4.18)$$

and satisfy the relation

$$\left(Y' - \frac{1}{2R_1} \right)^2 + (Y'')^2 = \left(\frac{1}{2R_1} \right)^2 \quad (4.19)$$

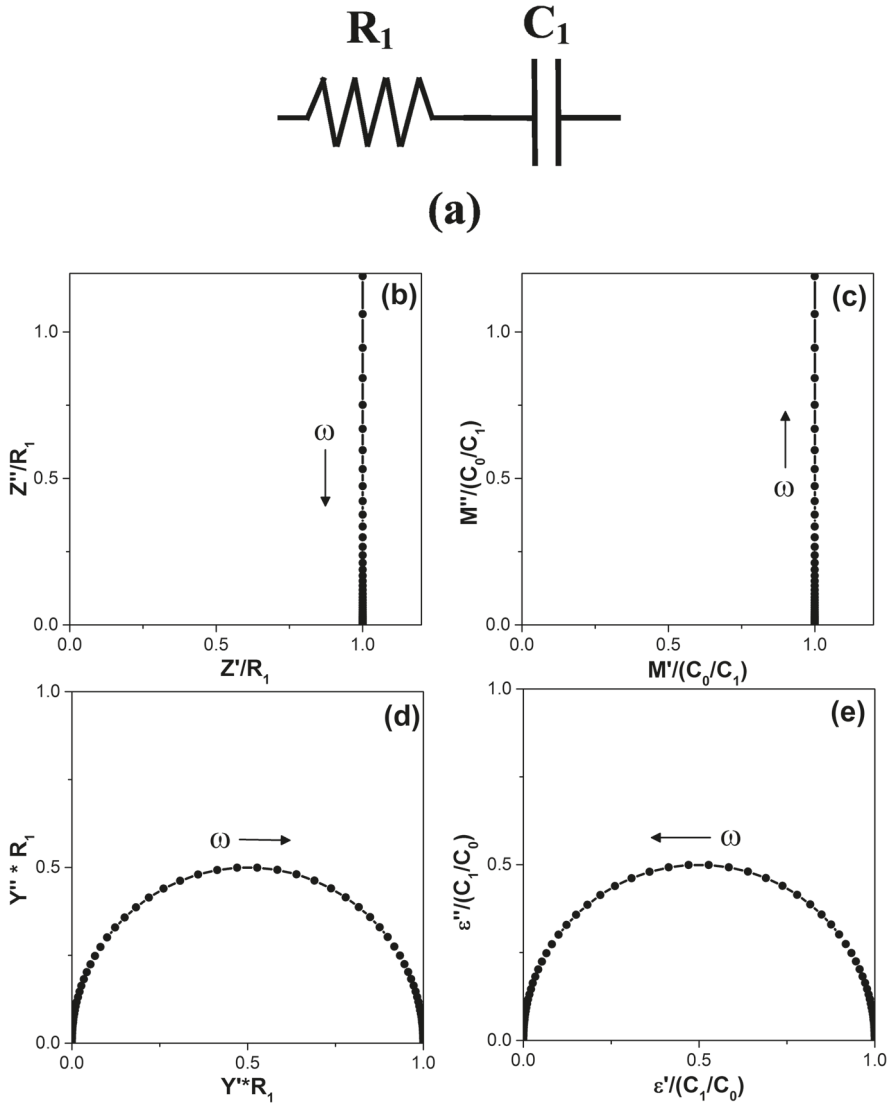


FIGURE 4.2 (a) Series RC circuit. Normalized plots of (b) Z''/R_1 versus Z'/R_1 , (c) $M''/(C_0/C_1)$ versus $M'/(C_0/C_1)$, (d) $Y''R_1$ versus $Y'R_1$ and (e) $\epsilon''/(C_1/C_0)$ versus $\epsilon'/(C_1/C_0)$.

indicating that Y'' versus Y' plot will be a semicircle of radius $1/(2R_1)$ with center at the point $(1/(2R_1), 0)$ on the Y' axis. The arc will traverse from left to right as the frequency increases, pass through the origin and will have an intercept on the Y' axis at point $(1/R_1, 0)$ at the high-frequency end. At the frequency where $\omega C_1 R_1 = 1$, we get $Y' = 1/(2R_1)$ and $Y'' = 1/(2R_1)$, i.e. frequency corresponds to the top of the arc.

Similarly, ε' and ε'' are given by

$$\varepsilon' = \frac{C_1}{C_0} \frac{1}{1 + (\omega C_1 R_1)^2}, \varepsilon'' = \frac{C_1}{C_0} \frac{\omega C_1 R_1}{1 + (\omega C_1 R_1)^2} \quad (4.20)$$

satisfy the relation

$$\left(\varepsilon' - \frac{C_1}{2C_0} \right)^2 + (\varepsilon'')^2 = \left(\frac{C_1}{2C_0} \right)^2 \quad (4.21)$$

indicating that ε'' versus ε' plot will be a semicircle of radius $C_1/(2C_0)$, center at the point $(C_1/(2C_0), 0)$ on the ε' axis. The arc will traverse from right to left as the frequency increases, pass through the origin and will have an intercept on the ε' axis at point $(C_1/C_0, 0)$ at the low-frequency end. Also at the frequency where $\omega C_1 R_1 = 1$, we have $\varepsilon' = C_1/(2C_0)$ and $\varepsilon'' = C_1/(2C_0)$, i.e. frequency corresponds to the top of the arc.

Thus, if this model is chosen to represent the experimental data, values of the components can be obtained from the high-frequency side intercept ($= C_1/C_0$) and the frequency corresponding to the top of the arc in ε'' versus ε' plot by using $\omega C_1 R_1 = 1$. These values can be obtained from the Z and M plots as well.

Normalized complex plane plots of the immittance functions are shown in Figure 4.2(b–e).

It may be mentioned that a parallel $R_p C_p$ circuit can be transformed into an equivalent series $R_s C_s$ circuit and vice versa (The Radio Amateur Handbook 1968). But with R_p and C_p frequency independent, the values of R_s and C_s obtained from the transformation come out to be frequency dependent. Similarly, if R_s and C_s are frequency independent, R_p and C_p obtained from transformation are frequency dependent. However, in impedance spectroscopic modeling in beginning, we seek models comprising lumped components, which are usually frequency independent. Therefore, study of simulated immittance behavior of parallel and series circuit separately is worth looking at. If in an experiment Z'' versus Z' gives a semicircular arc, the model would be a parallel RC circuit, and if Y'' versus Y' is a semicircular arc, the model would be a series RC circuit.

4.3 PARALLEL COMBINATION $R_1 C_1$ IN SERIES WITH C_2

Figure 4.3(a) shows a parallel combination of R_1, C_1 in series with C_2 .

Impedance of this model is given by

$$Z = \frac{R_1}{1 + (\omega C_1 R_1)^2} - j \left[\frac{\omega C_1 R_1^2}{1 + (\omega C_1 R_1)^2} + \frac{1}{\omega C_2} \right] = Z' - jZ'' \quad (4.22)$$

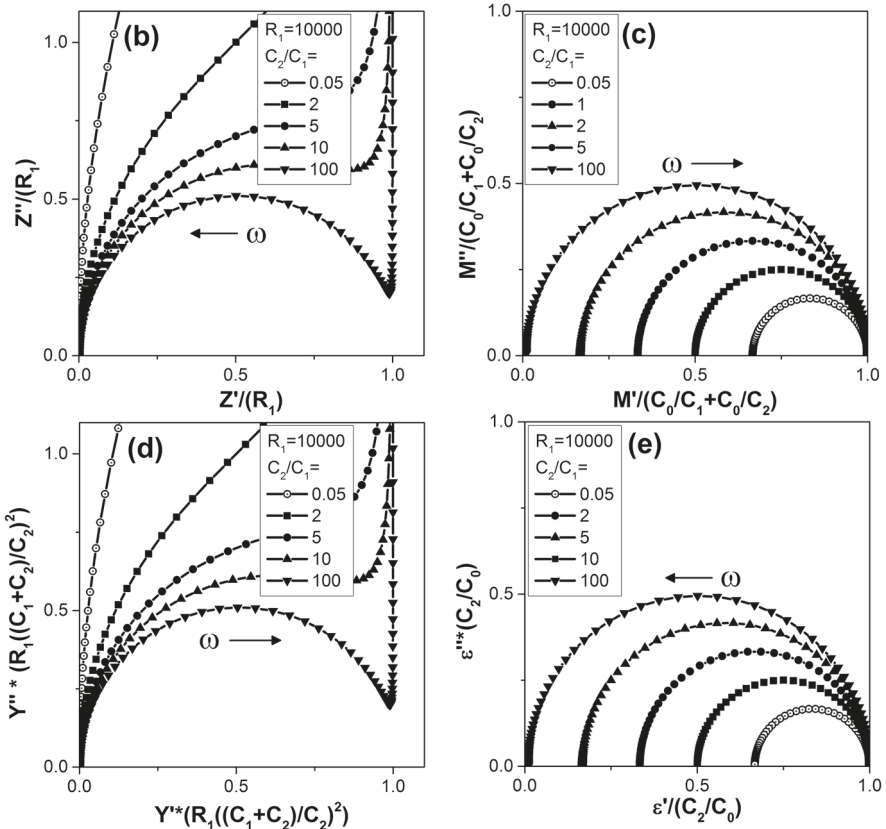
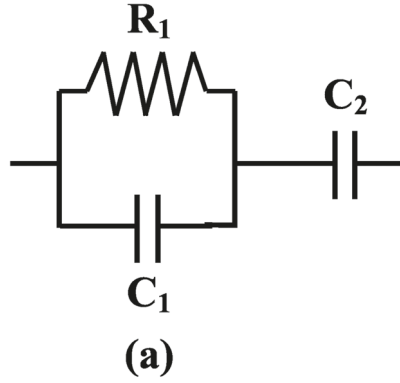


FIGURE 4.3 (a) A parallel combination of R_1 and C_1 in series with C_2 . Normalized plots of (b) Z''/R_1 versus Z'/R_1 , (c) $M''/(C_0/C_1 + C_0/C_2)$ versus $M'/(C_0/C_1 + C_0/C_2)$, (d) $Y'' R_1 ((C_1 + C_2)/C_2)^2$ versus $Y' R_1 ((C_1 + C_2)/C_2)^2$ and (e) $\epsilon''/(C_2/C_0)$ versus $\epsilon'/(C_2/C_0)$.

Real and imaginary parts of Z are given as

$$Z' = \frac{R_1}{1 + (\omega C_1 R_1)^2} \quad (4.23)$$

$$Z'' = \frac{\omega C_1 R_1^2}{1 + (\omega C_1 R_1)^2} + \frac{1}{\omega C_2} \quad (4.24)$$

Other immittance functions are obtained by using the expressions given in Chapter 2.

The limiting values at $\omega \rightarrow 0$ and $\omega \rightarrow \infty$ are given below

$$Z'|_{\omega \rightarrow 0} = R_1, Z'|_{\omega \rightarrow \infty} = 0, Z''|_{\omega \rightarrow 0} = \infty, Z''|_{\omega \rightarrow \infty} = 0 \quad (4.25)$$

$$M'|_{\omega \rightarrow 0} = \frac{C_0}{C_2}, M'|_{\omega \rightarrow \infty} = \frac{C_0}{C_1} + \frac{C_0}{C_2}, M''|_{\omega \rightarrow 0} = 0, M''|_{\omega \rightarrow \infty} = 0 \quad (4.26)$$

$$Y'|_{\omega \rightarrow 0} = 0, Y'|_{\omega \rightarrow \infty} = \frac{1}{R_1} \left(\frac{C_2}{C_1 + C_2} \right)^2, Y''|_{\omega \rightarrow 0} = 0, Y''|_{\omega \rightarrow \infty} = \infty \quad (4.27)$$

$$\varepsilon'|_{\omega \rightarrow 0} = \frac{C_2}{C_0}, \varepsilon'|_{\omega \rightarrow \infty} = \frac{1}{\left(\frac{C_0}{C_1} + \frac{C_0}{C_2} \right)}, \varepsilon''|_{\omega \rightarrow 0} = 0, \varepsilon''|_{\omega \rightarrow \infty} = 0 \quad (4.28)$$

Normalized plots of immittance functions are shown in Figure 4.3(b–e).

The two useful features of this model are (i) the Z'' versus Z' plot has a steeply rising branch at low-frequency side as frequency is lowered and (ii) the M'' versus M' plot is shifted toward right. If in an experiment such behavior is observed, presence of a series capacitor in the equivalent circuit model may be inferred.

4.4 PARALLEL COMBINATION R_1, C_1 IN SERIES WITH R_2

Figure 4.4(a) shows a parallel combination of R_1, C_1 in series with R_2 .

Real and imaginary parts of Z ($= Z' - jZ''$) are given by Eqs. (4.29) and (4.30)

$$Z' = R_2 + \frac{R_1}{1 + (\omega C_1 R_1)^2} \quad (4.29)$$

$$Z'' = \frac{\omega C_1 R_1^2}{1 + (\omega C_1 R_1)^2} \quad (4.30)$$

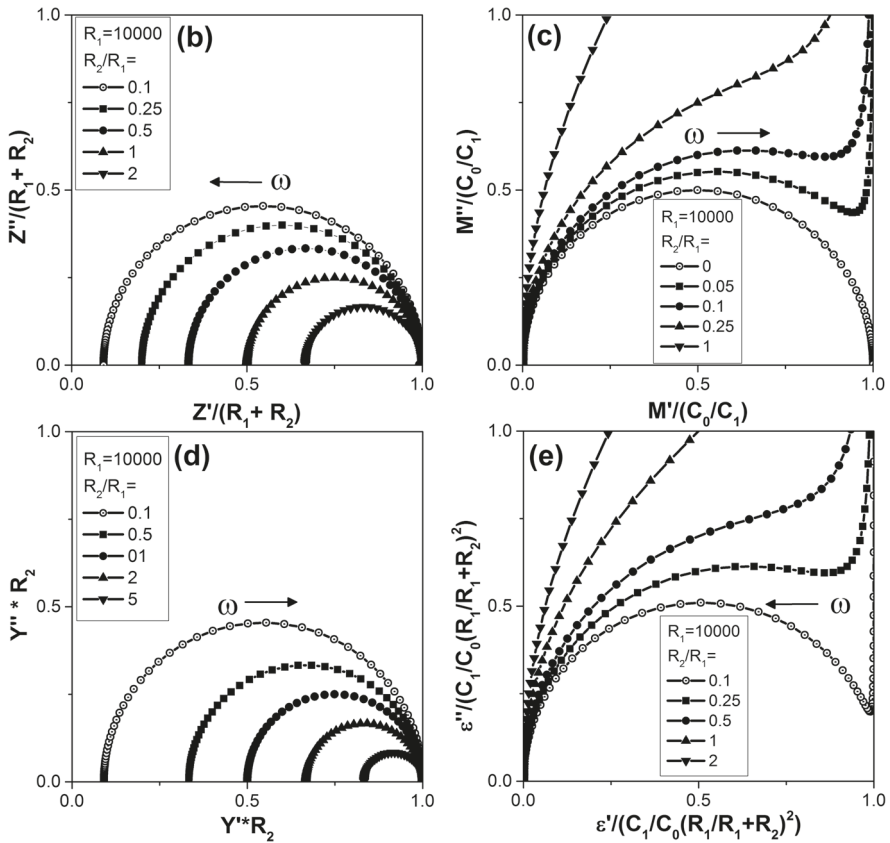
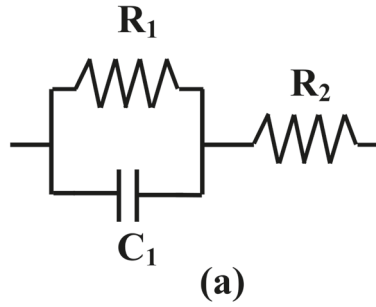


FIGURE 4.4 (a) A parallel combination of R_1 and C_1 in series with R_2 . Normalized plots of (b) $Z''/(R_1+R_2)$ versus $Z'/(R_1+R_2)$, (c) $M''/(C_0/C_1)$ versus $M'/(C_0/C_1)$, (d) $Y'' R_2$ versus $Y' R_2$ and (e) $\epsilon''/((C_1/C_0)(R_1/(R_1+R_2))^2)$ versus $\epsilon'/((C_1/C_0)(R_1/(R_1+R_2))^2)$.

The limiting values at $\omega \rightarrow 0$ and $\omega \rightarrow \infty$ are given below

$$Z'|_{\omega \rightarrow 0} = R_1 + R_2, Z'|_{\omega \rightarrow \infty} = R_2, Z''|_{\omega \rightarrow 0} = \infty, Z''|_{\omega \rightarrow \infty} = 0 \quad (4.31)$$

$$M'|_{\omega \rightarrow 0} = 0, M'|_{\omega \rightarrow \infty} = \frac{C_0}{C_1}, M''|_{\omega \rightarrow 0} = 0, M''|_{\omega \rightarrow \infty} = \infty \quad (4.32)$$

$$Y'|_{\omega \rightarrow 0} = \frac{1}{R_1 + R_2}, Y'|_{\omega \rightarrow \infty} = \frac{1}{R_2}, Y''|_{\omega \rightarrow 0} = 0, Y''|_{\omega \rightarrow \infty} = 0 \quad (4.33)$$

$$\varepsilon'|_{\omega \rightarrow 0} = \frac{C_1}{C_0} \left(\frac{R_1}{R_1 + R_2} \right)^2, \varepsilon'|_{\omega \rightarrow \infty} = 0, \varepsilon''|_{\omega \rightarrow 0} = \infty, \varepsilon''|_{\omega \rightarrow \infty} = 0 \quad (4.34)$$

Normalized complex plane immittance plots of this model are shown in Figures 4.4(c–e).

The useful features of this model are (i) the M'' versus M' plot has a steeply rising branch at high-frequency side and (ii) the Z'' versus Z' plot is shifted toward right. If in an experiment such behavior is observed, presence of a series resistance in the equivalent circuit model may be inferred.

4.5 TWO PARALLEL RC NETWORKS CONNECTED IN SERIES

Figure 4.5(a) shows two parallel RC networks connected in series.

Impedance of this model is given by

$$Z = \frac{R_1}{\frac{1}{R_1} + j\omega C_1} + \frac{R_2}{\frac{1}{R_2} + j\omega C_2} \quad (4.35)$$

Real and imaginary parts of Z are given by Eqs. (4.36) and (4.37)

$$Z' = \frac{R_1}{1 + (\omega R_1 C_1)^2} + \frac{R_2}{1 + (\omega R_2 C_2)^2} \quad (4.36)$$

$$Z'' = \frac{\omega C_1 R_1^2}{1 + (\omega R_1 C_1)^2} + \frac{\omega C_2 R_2^2}{1 + (\omega R_2 C_2)^2} \quad (4.37)$$

The limiting values of the real and imaginary parts of the immittance functions at $\omega \rightarrow 0$ and $\omega \rightarrow \infty$ are given below

$$Z'_{|\omega \rightarrow 0} = R_1 + R_2, Z'_{|\omega \rightarrow \infty} = 0, Z''_{|\omega \rightarrow 0} = 0, Z''_{|\omega \rightarrow \infty} = 0 \quad (4.38)$$

$$M'_{|\omega \rightarrow 0} = 0, M'_{|\omega \rightarrow \infty} = \frac{C_0}{C_1} + \frac{C_0}{C_2}, M''_{|\omega \rightarrow 0} = 0, M''_{|\omega \rightarrow \infty} = 0 \quad (4.39)$$

$$Y'_{|\omega \rightarrow 0} = \frac{1}{R_1 + R_2}, Y'_{|\omega \rightarrow \infty} = \frac{1}{R_1} \left(\frac{C_2}{C_1 + C_2} \right)^2 + \frac{1}{R_2} \left(\frac{C_1}{C_1 + C_2} \right)^2, \\ Y''_{|\omega \rightarrow 0} = 0, Y''_{|\omega \rightarrow \infty} = \infty \quad (4.40)$$

$$\varepsilon'_{|\omega \rightarrow 0} = \frac{C_1}{C_0} \left(\frac{R_1}{R_1 + R_2} \right)^2 + \frac{C_2}{C_0} \left(\frac{R_2}{R_1 + R_2} \right)^2, \varepsilon'_{|\omega \rightarrow \infty} = \frac{C_1 C_2}{C_0 (C_1 + C_2)} \\ \varepsilon''_{|\omega \rightarrow 0} = \infty, \varepsilon''_{|\omega \rightarrow \infty} = 0 \quad (4.41)$$

Arcs of different shapes are observed in the complex plane plots depending on the ratios of R_1 and R_2 and of the time constants $R_1 C_1$ and $R_2 C_2$. These plots are shown for $R_2/R_1 = 1$, $R_2/R_1 = 2$, $R_2/R_1 = 3$ and $R_2/R_1 = 100$, in Figures 4.5(b–q) for different values of $R_2 C_2/R_1 C_1$.

Now, let us observe the Z'' versus Z' plots. It is seen from these plots for different values of R_2/R_1 and $R_2 C_2/R_1 C_1$ that when the time constants $R_2 C_2$ and $R_1 C_1$ are quite different from one another, two well-resolved arcs appear. Therefore, if a Z'' versus Z' plot of experimental data shows such a behavior, it may be inferred that two charge transfer processes are present, and this equivalent circuit model may be considered to represent the system. The relative values of R_1 , R_2 , $R_2 C_2$ and $R_1 C_1$ can be estimated by comparing the plots with the simulated ones shown here. It is also seen, for $R_2/R_1 = 1$, that when the ratio of time constants $R_2 C_2/R_1 C_1$ is within 5, the overall arc appears to be like a depressed semicircular arc. It indicates that when slightly depressed looking arc is experimentally observed, two processes having time constant close to each other within a factor of 5 are present. It is further found that the overall Z'' versus Z' arc appears symmetrically placed when R_2 and R_1 are equal and becomes skewed depending on the ratio R_2/R_1 , the bigger portion corresponds to R_2 if $R_2/R_1 > 1$. The smaller portion (arc) corresponding to R_1 becomes smaller and smaller as R_2 becomes larger and larger. When R_2 is much larger than R_1 , the smaller arc that corresponds to R_1 gets completely masked by the bigger arc. This is shown in Figure 4.5 (n) for $R_2/R_1 = 100$. Thus, for the case when $R_2/R_1 = 100$ (i.e. $R_2 \gg R_1$), the Z'' versus Z' plot appears to be almost a clear semicircular arc similar to that obtained for a single parallel RC circuit. Therefore, if experimentally measured values of Z' and Z'' give a semicircular arc in the Z'' versus Z' plot, one would be prompted to decide that there is a single charge transfer process present in the system, and a parallel RC circuit may be accepted as an equivalent circuit model. However, as indicated above, this might be a wrong conclusion. This problem can be solved by looking at other immittance plots. For $R_2/R_1 = 100$, Figure 4.5(o) shows M'' versus M' plots for different values of $R_2 C_2/R_1 C_1$.

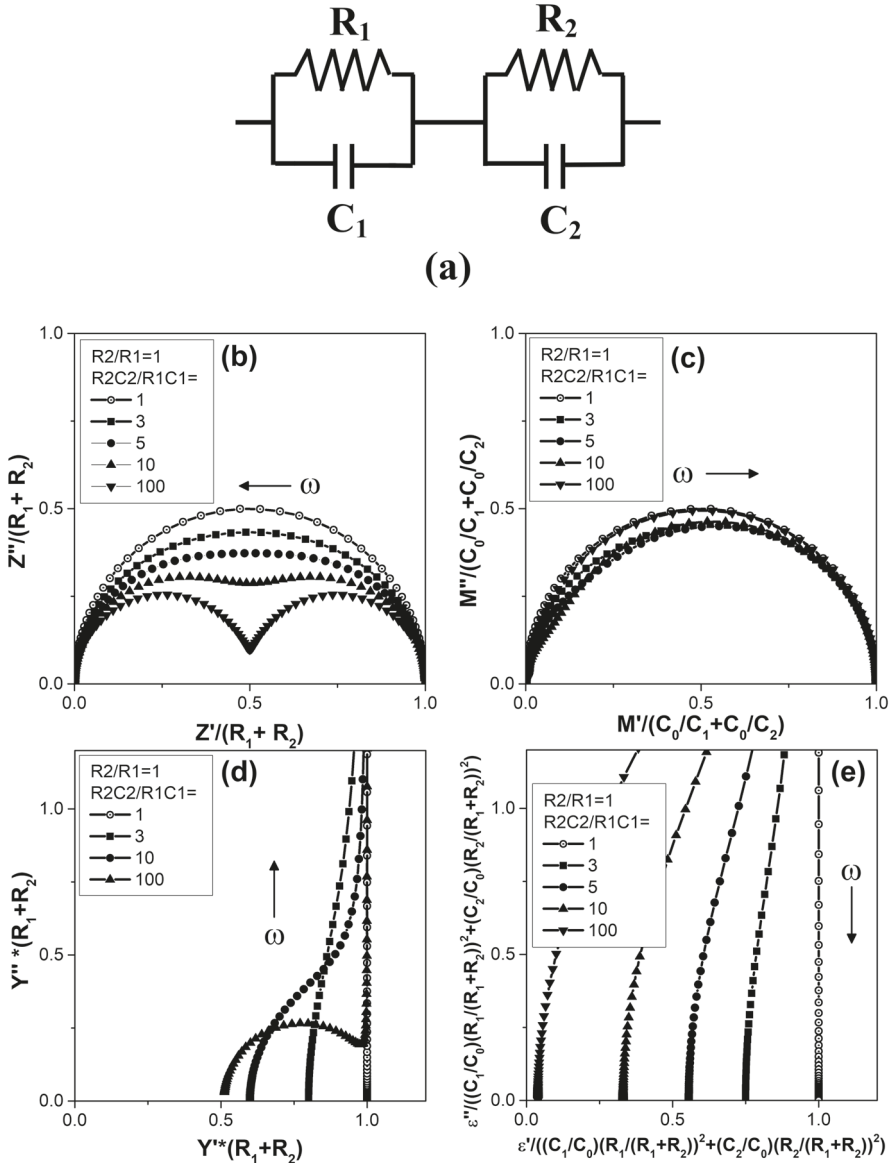


FIGURE 4.5 (a) Two parallel RC networks connected in series. Normalized plots for various ratios R_2/R_1 and $R_2C_2/(R_1C_1)$ for (b,f,i,j,n) $Z''/(R_1 + R_2)$ versus $Z'/(R_1 + R_2)$ and (c,g,k,o) $M''/(C_0/C_1 + C_0/C_2)$ versus $M'/(C_0/C_1 + C_0/C_2)$ (d,h,l,p) $Y''^*(R_1 + R_2)$ versus $Y'*(R_1 + R_2)$ (e,i,m,q) $\epsilon''/((C_1/C_0)(R_1/(R_1 + R_2))^2 + (C_2/C_0)(R_2/(R_1 + R_2))^2)$ versus $\epsilon'/((C_1/C_0)(R_1/(R_1 + R_2))^2 + (C_2/C_0)(R_2/(R_1 + R_2))^2)$ (Reproduced with permission from Springer Nature, Pandey et al. 1995, Figure 1, Equivalent Circuit Models for Electronic Ceramics, Bull. Mater. Sci., 18(5): 563–576.)

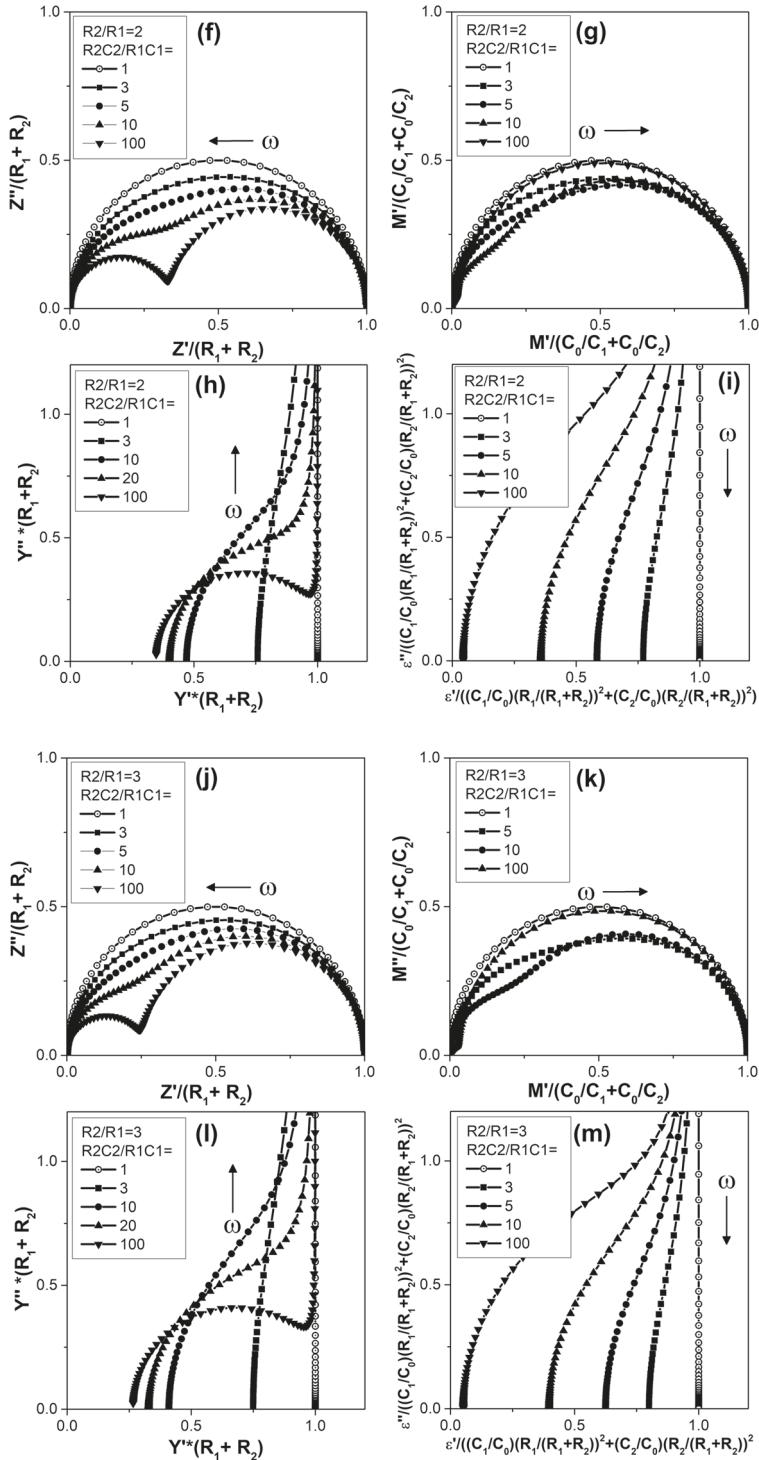


FIGURE 4.5 (Continued)

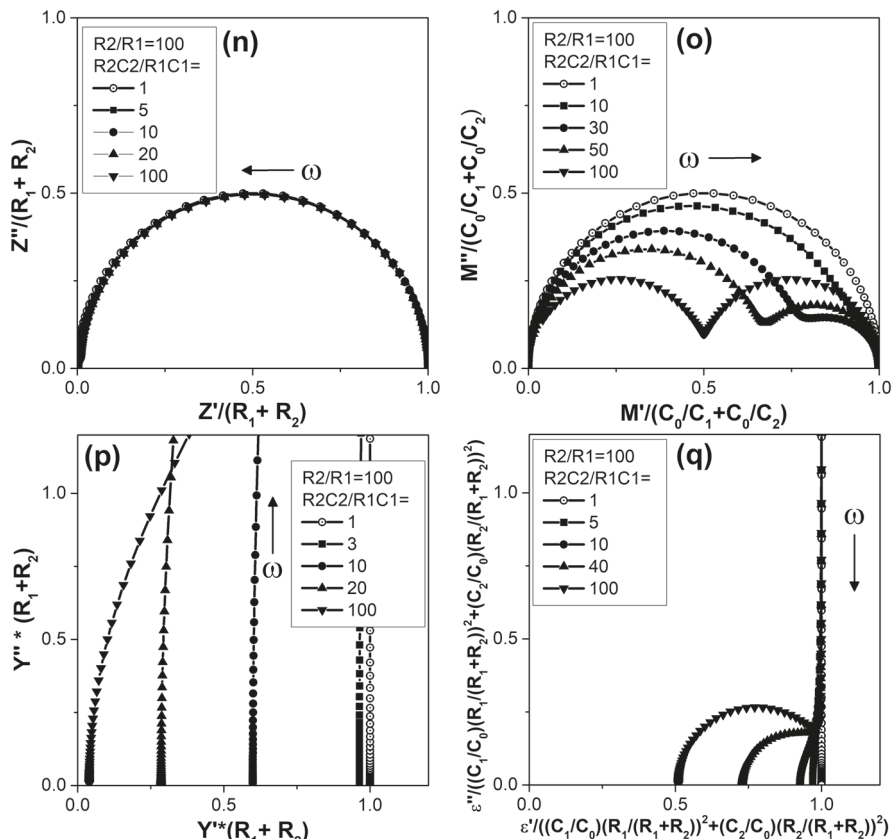


FIGURE 4.5 (Continued)

R_1C_1 revealing the presence of two arcs and hence two processes. Thus, when a clear semicircular arc is seen in Z'' versus Z' plot, it is advisable to look at other immittance plots also. A particular value of R_2C_2/R_1C_1 can be obtained by several combinations of R_2/R_1 and C_2/C_1 . If R_2C_2/R_1C_1 is a large number, say 100, two interesting cases arise: (i) $R_2/R_1 = 1$ and $C_2/C_1 = 100$ and (ii) $R_2/R_1 = 100$ and $C_2/C_1 = 1$. In case (i), Z'' versus Z' plot, showing two arcs, would be useful whereas for case (ii) M'' versus M' plot, showing two arcs, would be useful (Sinclair and West 1989). Z plots will yield information about resistive nature and M plots about capacitive nature of the material (Pandey et al. 1995).

This is perhaps the most important model applicable to various systems and useful for developing some insight about impedance spectroscopic equivalent circuit modeling. A simple model representing number of charge transfer processes in a system may be a circuit comprising parallel RC circuits connected in series, the number of RC's being equal to number of processes. If their time constants are well separated, distinct arcs appear, and when their time constants are close to each other within a factor of 5, a depressed looking single semicircular arc would appear in immittance

complex plane plots. Therefore, when a depressed looking semicircular arc is obtained in an experiment, presence of at least two processes having time constants close to each other is inferred. An usual practice is to represent such systems by a parallel RC circuit and say that there exists a distribution of time constants centered around the mean value equal to RC. This situation is more elegantly handled by using a CPE that is capable of producing a depressed arc (Macdonald 1987; Jonscher 1983; Pandey et al.

2017; Pandey 2018; Pandey et al. 1995). This will be described later.

4.6 SERIES R_1C_1 IN PARALLEL TO R_2

This model is schematically shown in Figure 4.6(a).

The admittance of this model is given as

$$Y = \left(\frac{1}{R_2} + \frac{(\omega C_1)^2 R_1}{1 + (\omega C_1 R_1)^2} \right) + j \left(\frac{\omega C_1}{1 + (\omega C_1 R_1)^2} \right) = Y' + jY'' \quad (4.42)$$

which gives

$$Y' = \frac{1}{R_2} + \frac{1}{R_1} \frac{(\omega C_1 R_1)^2}{1 + (\omega C_1 R_1)^2} \quad (4.43)$$

$$Y'' = \frac{1}{R_1} \left(\frac{\omega C_1 R_1}{1 + (\omega C_1 R_1)^2} \right) \quad (4.44)$$

The limiting values are given in Eqs. (4.45–4.48)

$$Z'|_{\omega \rightarrow 0} = R_2, Z'|_{\omega \rightarrow \infty} = \frac{R_1 R_2}{R_1 + R_2}, Z''|_{\omega \rightarrow 0} = 0, Z''|_{\omega \rightarrow \infty} = 0 \quad (4.45)$$

$$M'|_{\omega \rightarrow 0} = 0, M'|_{\omega \rightarrow \infty} = \frac{C_0}{C_1} \left(\frac{R_2}{R_1 + R_2} \right)^2, M''|_{\omega \rightarrow 0} = 0, M''|_{\omega \rightarrow \infty} = \infty \quad (4.46)$$

$$Y'|_{\omega \rightarrow 0} = \frac{1}{R_2}, Y'|_{\omega \rightarrow \infty} = \frac{1}{R_1} + \frac{1}{R_2}, Y''|_{\omega \rightarrow 0} = 0, Y''|_{\omega \rightarrow \infty} = 0 \quad (4.47)$$

$$\varepsilon'|_{\omega \rightarrow 0} = \frac{C_1}{C_0}, \varepsilon'|_{\omega \rightarrow \infty} = 0, \varepsilon''|_{\omega \rightarrow 0} = \infty, \varepsilon''|_{\omega \rightarrow \infty} = 0 \quad (4.48)$$

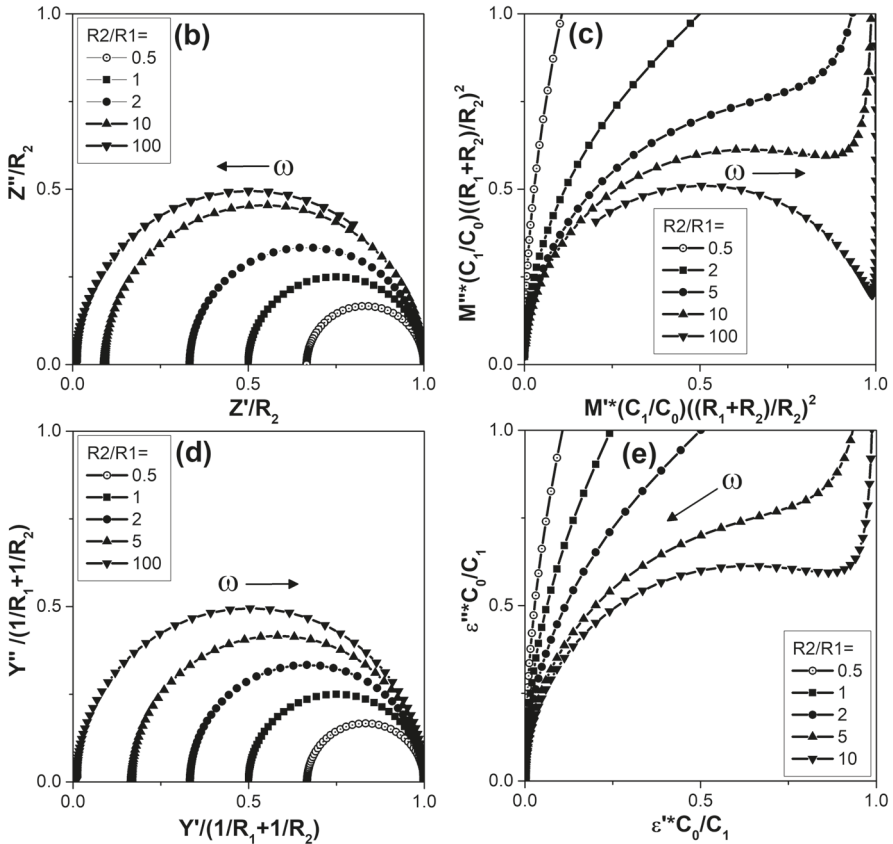
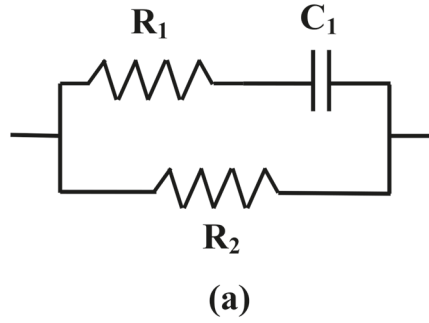


FIGURE 4.6 (a) Series R_1C_1 in parallel to R_2 . Normalized plots for various ratios of R_2/R_1 for (b) Z''/R_2 versus Z'/R_2 and (c) $M''/(C_0/C_1) (R_2/(R_1+R_2))^2$ versus $M'/(C_0/C_1) (R_2/(R_1+R_2))^2$ (d) $Y''/(1/R_1+1/R_2)$ versus $Y'/(1/R_1+1/R_2)$ (e) $\epsilon''/(C_1/C_0)$ versus $\epsilon'/(C_1/C_0)$.

The complex plane plots are shown in Figures 4.6(b–e) for various ratios of R_2/R_1 .

Equations (4.43) and (4.44) can be written as

$$Y' - \frac{1}{R_2} = \frac{1}{R_1} \frac{(\omega C_1 R_1)^2}{1 + (\omega C_1 R_1)^2}, Y'' = \frac{1}{R_1} \left(\frac{\omega C_1 R_1}{1 + (\omega C_1 R_1)^2} \right) \quad (4.49)$$

and $Y' - 1/R_2$ and Y'' satisfy the relation

$$\left(Y' - \frac{1}{R_2} - \frac{1}{2R_1} \right)^2 + Y''^2 = \left(\frac{1}{2R_1} \right)^2 \quad (4.50)$$

which is a circle having center at the point $(1/R_2 + 1/(2R_1), 0)$ and radius equal to $1/(2R_1)$. As Y' and Y'' are positive, this is a semicircular arc traversing from left to right as frequency increases, not passing through the origin but shifted to the right by $1/R_2$ and intercepting the Y' axis at the point $1/R_2 + 1/R_1$ at high-frequency side. At frequency given by $\omega C_1 R_1 = 1$, we get $Y' - 1/R_2 = 1/(2R_1)$ and $Y'' = 1/(2R_1)$, which corresponds to the top of the arc. Thus, if experimental Y'' versus Y' plot is a right-shifted semicircular arc, this model may be chosen to represent the data. The value of R_2 can be obtained by noting the value of shift, value of R_1 from the high-frequency intercept and C_1 from the relation $\omega C_1 R_1 = 1$, where ω is the frequency corresponding to the top of the arc.

This model has been used for study of biological tissues where the series $R_1 C_1$ part is used to represent the current path through the cell, and the parallel resistor represents the direct path through the intercellular material bypassing the cell. The capacitor C_1 represents the cell membrane. At higher frequencies, the impedance of the cell membrane ($\sim 1/\omega C_1$) decreases, and the current would flow through the cell as well as through the intercellular material.

4.7 THREE PARALLEL RC NETWORKS CONNECTED IN SERIES

Figure 4.7(a) shows three parallel RC networks connected in series.

Impedance of this model is given by

$$Z = \frac{1}{\frac{1}{R_1} + j\omega C_1} + \frac{1}{\frac{1}{R_2} + j\omega C_2} + \frac{1}{\frac{1}{R_3} + j\omega C_3} \quad (4.51)$$

Real and imaginary parts of Z are given by Eqs. (4.52) and (4.53)

$$Z' = \frac{R_1}{1 + (\omega R_1 C_1)^2} + \frac{R_2}{1 + (\omega R_2 C_2)^2} + \frac{R_3}{1 + (\omega R_3 C_3)^2} \quad (4.52)$$

$$Z'' = \frac{\omega C_1 R_1^2}{1 + (\omega R_1 C_1)^2} + \frac{\omega C_2 R_2^2}{1 + (\omega R_2 C_2)^2} + \frac{\omega C_3 R_3^2}{1 + (\omega R_3 C_3)^2} \quad (4.53)$$

The limiting values of real and imaginary parts of immittance functions are given by Eqs. (4.54)–(4.58).

$$Z'|_{\omega \rightarrow 0} = R_1 + R_2 + R_3, Z'|_{\omega \rightarrow \infty} = 0, Z''|_{\omega \rightarrow 0} = 0, Z''|_{\omega \rightarrow \infty} = 0 \quad (4.54)$$

$$M'|_{\omega \rightarrow 0} = 0, M'|_{\omega \rightarrow \infty} = \frac{C_0}{C_1} + \frac{C_0}{C_2} + \frac{C_0}{C_3}, M''|_{\omega \rightarrow 0} = 0, M''|_{\omega \rightarrow \infty} = 0 \quad (4.55)$$

$$Y'|_{\omega \rightarrow 0} = \frac{1}{R_1 + R_2 + R_3}$$

$$Y'|_{\omega \rightarrow \infty} = \frac{1}{R_1} \left(\frac{\frac{1}{C_1}}{\frac{1}{C_1} + \frac{1}{C_2} + \frac{1}{C_3}} \right)^2 + \frac{1}{R_2} \left(\frac{\frac{1}{C_2}}{\frac{1}{C_1} + \frac{1}{C_2} + \frac{1}{C_3}} \right)^2 + \frac{1}{R_3} \left(\frac{\frac{1}{C_3}}{\frac{1}{C_1} + \frac{1}{C_2} + \frac{1}{C_3}} \right)^2 \quad (4.56)$$

$$Y''|_{\omega \rightarrow 0} = 0, Y''|_{\omega \rightarrow \infty} = \infty \quad (4.57)$$

$$\varepsilon'|_{\omega \rightarrow 0} = \frac{C_1}{C_0} \left(\frac{R_1}{R_1 + R_2 + R_3} \right)^2 + \frac{C_2}{C_0} \left(\frac{R_2}{R_1 + R_2 + R_3} \right)^2 + \frac{C_3}{C_0} \left(\frac{R_3}{R_1 + R_2 + R_3} \right)^2, \varepsilon'|_{\omega \rightarrow \infty} = \frac{1}{\frac{C_0}{C_1} + \frac{C_0}{C_2} + \frac{C_0}{C_3}}, \quad (4.58)$$

$$\varepsilon''|_{\omega \rightarrow 0} = \infty, \varepsilon''|_{\omega \rightarrow \infty} = 0$$

Complex plane plots for immittance functions for different ratios of R_1, R_2 and R_3 and of time constants $R_1 C_1, R_2 C_2$ and $R_3 C_3$ are shown in Figures 4.7(b–i).

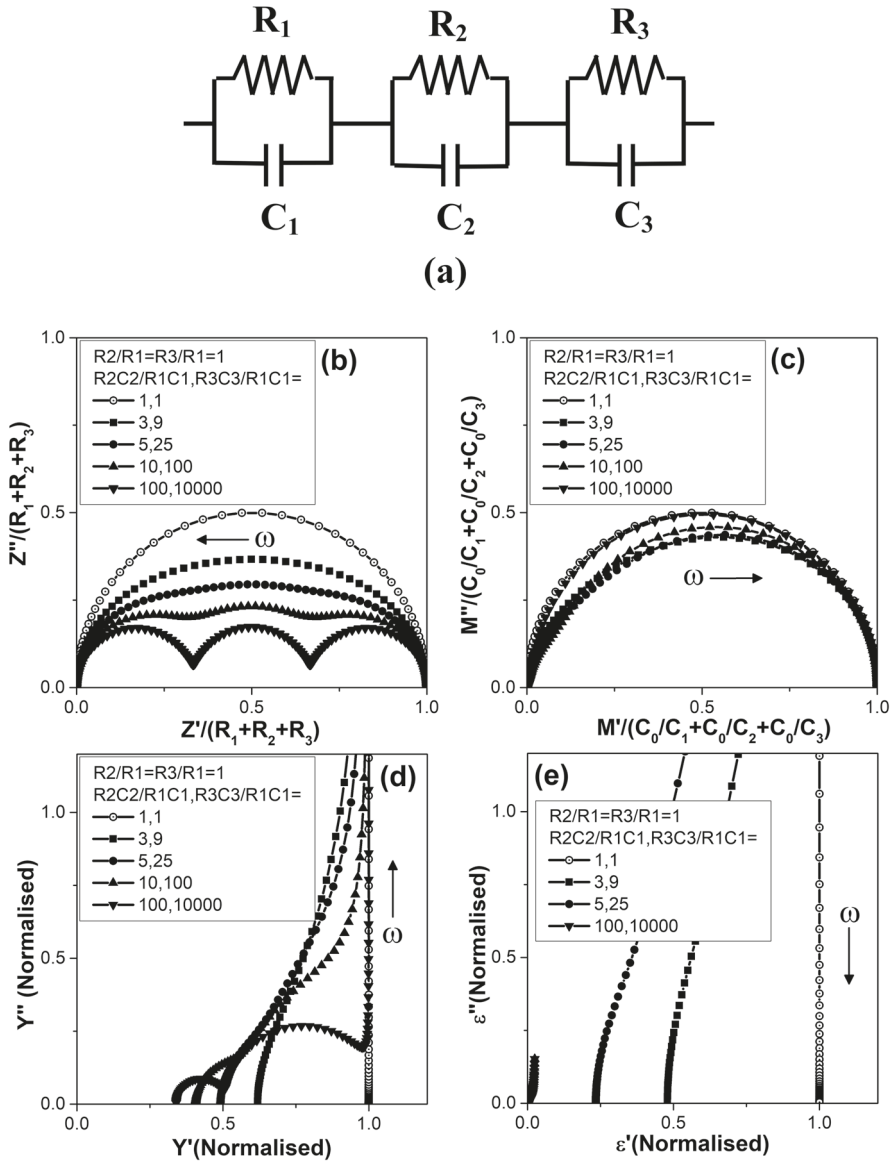


FIGURE 4.7 (a) Three parallel RC networks connected in series. Normalized plots for various ratios of resistances and time constants as given in insets. (b,f) $Z''/(R_1 + R_2 + R_3)$ versus $Z'/(R_1 + R_2 + R_3)$, (c,g) $M''/(C_0/C_1 + C_0/C_2 + C_0/C_3)$ versus $M'/(C_0/C_1 + C_0/C_2 + C_0/C_3)$, (d,h) Y'' (normalized) versus Y' (normalized), where Y' (normalized) = $Y'/(Y'$ at $\omega = \infty$) and Y'' (normalized) = $Y''/(Y''$ at $\omega = \infty$) and (e,i) ϵ'' (normalized) versus ϵ' (normalized), where ϵ' (normalized) = $\epsilon'/(\epsilon'$ at $\omega = 0$) and ϵ'' (normalized) = $\epsilon''/(\epsilon''$ at $\omega = 0$).

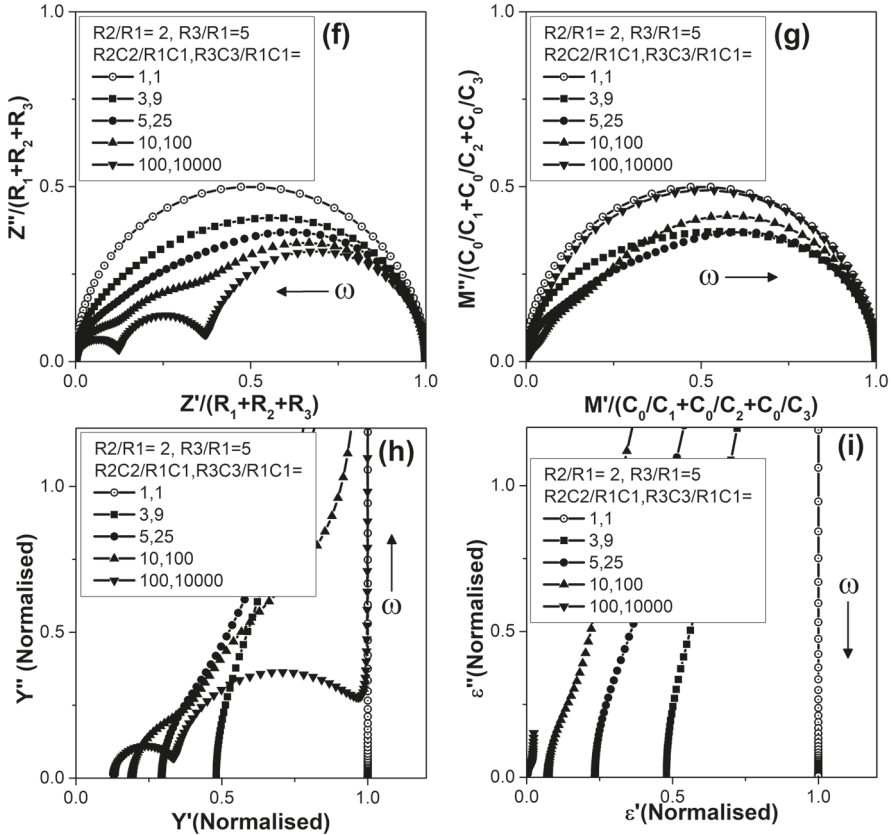


FIGURE 4.7 (Continued)

This model is an extension of the model discussed in Section 4.5 and is a quite general model widely used to represent three processes such as grain, grain boundary and sample–electrode interface in polycrystalline ceramics. Depending on the ratios of three time constants and resistances, various shapes are displayed. A comparison of the experimental plots with these plots helps in getting approximate values of the circuit elements. When the three time constants R_1C_1 , R_2C_2 and R_3C_3 are widely separated, three clear semicircular arcs are obtained. If $R_1C_1 < R_2C_2 < R_3C_3$, then in the Z'' versus Z' plot, the high-frequency arc at extreme left would correspond to R_1C_1 , the lowest-frequency arc at extreme right would correspond to R_3C_3 and the middle arc would correspond to R_2C_2 . The intercepts of these arcs with the Z' axis are at $Z' = R_1$, $Z' = R_1 + R_2$ and $Z' = R_1 + R_2 + R_3$ when traversing from left to right and are used to obtain the values of R_1 , R_2 and R_3 . If the top of these arcs occur at frequencies ω_1 , ω_2 and ω_3 , then the values of C_1 , C_2 and C_3 are obtained by using $\omega_1C_1R_1 = 1$, $\omega_2C_2R_2 = 1$ and $\omega_3C_3R_3 = 1$. In the M'' versus M' plot, the lowest-frequency arc corresponding to R_3C_3 would appear at the extreme left and the highest-frequency

arc corresponding to R_1C_1 will appear at the extreme right, and the intercepts of the arcs with M' axis will occur at $M' = C_0/C_3$, $M' = C_0/C_3 + C_0/C_2$ and $M' = C_0/C_3 + C_0/C_2 + C_0/C_1$. The values of C_1 , C_2 and C_3 may be obtained from these using the value of C_0 . If the top of the arcs occur at frequencies ω_3 , ω_2 and ω_1 , the values of R_1 , R_2 and R_3 are obtained by using $\omega_1C_1R_1 = 1$, $\omega_2C_2R_2 = 1$ and $\omega_3C_3R_3 = 1$.

4.8 PARALLEL COMBINATION OF RESISTANCE R AND CONSTANT PHASE ANGLE ELEMENT

The impedance behavior of material–electrode system can usually be represented by equivalent circuit models involving resistive (R), capacitive (C) and inductive (L) lumped components (Barsoukov and Macdonald 2005; Pandey et al. 1995; Katare et al. 1999; Katare 1997; Chaitanya 2008; Chaitanya et al. 2011, 2014). Complex plane plots (such as Z'' vs Z') possessing slightly depressed looking semicircular arcs also can be modeled by using a combination of at least two parallel RC circuits where the ratio of their time constants are within a factor of 5 (Pandey et al. 1995). For the cases where the depression is large or when the experimental immittance data cannot be represented by equivalent circuit model based on R, C and L (i.e. CNLS program does not show a good fit), the so-called CPE are introduced. One or more CPEs are suitably connected to resistive or reactive components for developing the model. It was discussed earlier that an ac voltage $v(t)$ applied across a resistor R gives rise to a current given by $v(t)/R$, which is always in phase with the voltage and independent of frequency. Current arising in a reactive component, C (or L), is given by $v(t)/(1/j\omega C)$ (or $v(t)/j\omega L$) and is 90° out of phase with the voltage. A CPE is a mathematical realization of a system in which the phase angle between applied ac voltage and the resulting current remains independent of the frequency. The impedance of a CPE, $Z_{CPE} = Z' - jZ''$, is given as (Barsoukov and Macdonald 2005)

$$Z_{CPE} = \frac{1}{Y_{CPE}} = \frac{1}{A_0(j\omega)^n} = \frac{1}{A_0(e^{j\pi/2}\omega)^n} = \frac{e^{-jn\pi/2}}{A_0\omega^n} \quad (4.59)$$

or

$$Z_{CPE} = \frac{1}{A_0\omega^n} \cos\left(\frac{n\pi}{2}\right) - j \frac{1}{A_0\omega^n} \sin\left(\frac{n\pi}{2}\right) \quad (4.60)$$

The Z'' versus Z' plot is a straight line with slope $\tan(n\pi/2)$. For $n = 0$, the imaginary part becomes zero and $Z_{CPE} = 1/A_0 \Omega$, and the CPE behaves like an ideal resistor of value $1/A_0$. For $n = 1$, the real part becomes zero and $Z_{CPE} = 1/(j\omega A_0)$ and the CPE behaves like an ideal capacitor of capacitance A_0 farad. The value of n lies between 0 and 1 when combination of CPE with R is considered for fitting an experimental data. It can be seen that when $n = -1$, the value of impedance will be $(j\omega)/A_0$, and the CPE will behave like an inductor of value $1/A_0$ H (Orazem and

Tribollet 2008, p 236). Thus, it may be conjectured that a negative value of n in the CNLS fit might also be considered as an indication for need of inclusion of inductance in the model.

The importance of a constant phase response was probably first emphasized by Fricke (1932) and was further explicitly used by Cole and Cole (1941). Its importance has been emphasized in recent times by Johnschner (1983) and Macdonald (2005).

Models comprising CPEs and R and C combinations have been developed and successfully used in analysis and interpretation of experimental impedance behavior for various sample–electrode systems by achieving excellent fits. Number of equivalent circuit models involving CPE are available in literature and ever-increasing trend is being witnessed for the application of impedance spectroscopy in diverse fields, including agriculture and medical diagnostics, by using CPE (Pandey et al. 2017).

There are various viewpoints regarding the possible sources of such a CPE behavior. However, larger consensus leans toward the belief that the CPE behavior arises due to the presence of distribution in time constants in the material–electrode systems. Therefore, when good fits are achieved by using models involving CPE, it is inferred that the system at hand possesses distribution in certain properties (such as interfaces, composition, etc.). This has led to a general practice for a liberal use of CPEs in equivalent circuit models for representing data showing distorted arcs or arcs depressed by even a little. Appearance of a distributed behavior can be vaguely visualized by considering a series combination of a large number of parallel RC circuits having their time constants close to each other and distributed in some way around some mean value.

Now, some simple models involving CPE are considered and their complex plane immittance plots are given that may be useful for selecting suitable models for representing experimental data by comparison. Their spectroscopic plots are not shown for brevity and only complex plane plots are shown (Barsoukov and Macdonald 2005; Pandey et al. 2017; Katare 1997).

A parallel combination of resistance R and CPE is shown in Figure 4.8(a).

The admittance $Y (= Y' + jY'')$ of this model is given as

$$Y = Y' + jY'' = \frac{1}{R} + A_0(j\omega)^n, \quad Y' = \frac{1}{R} + A_0\omega^n \cos\left(\frac{n\pi}{2}\right),$$

$$Y'' = A_0\omega^n \sin\left(\frac{n\pi}{2}\right) \quad (4.61)$$

It can be shown that Y' and Y'' satisfy the equation

$$Y'' = Y' \tan\left(\frac{n\pi}{2}\right) - \frac{1}{R} \tan\left(\frac{n\pi}{2}\right) \quad (4.62)$$

This shows that Y'' versus Y' plot would be a straight line having slope equal to $\tan(n\pi/2)$ and intercepting the Y' axis at the point having coordinates $(1/R, 0)$.

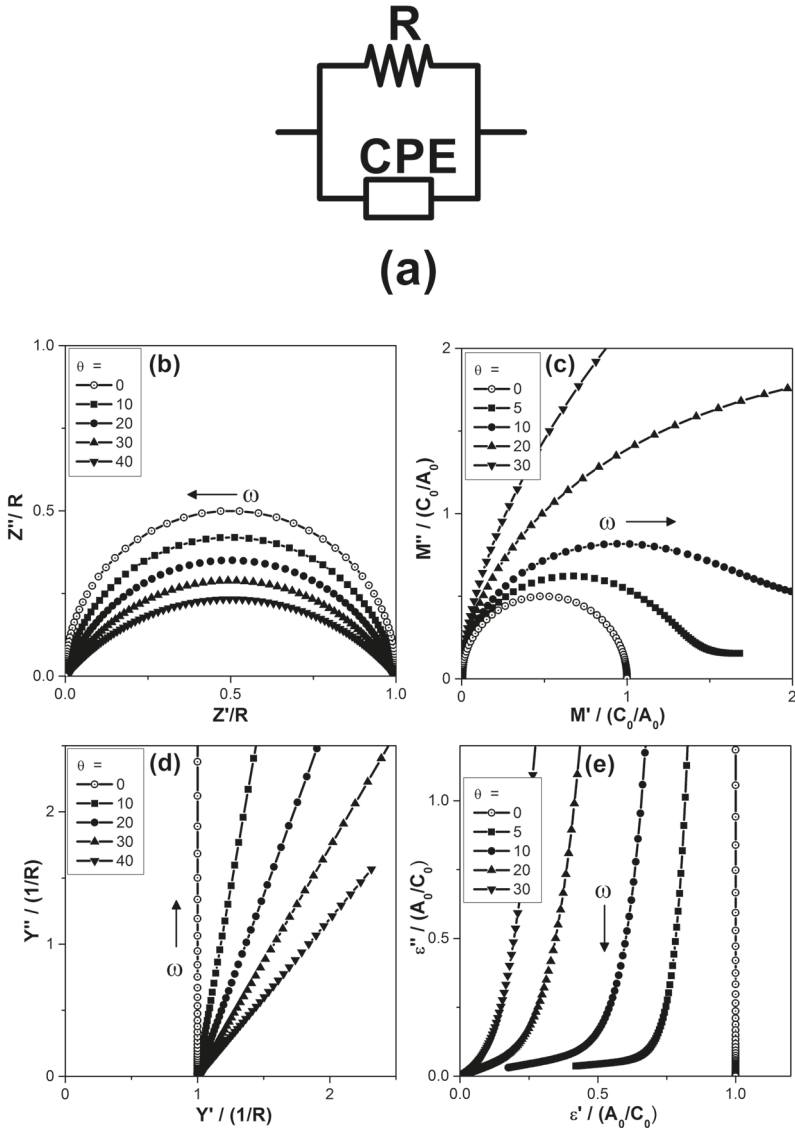


FIGURE 4.8 (a) Equivalent circuit model containing a parallel combination of resistance R and CPE. (b) Plot of Z''/R versus Z'/R for various values of θ , where θ is the angle between the Z' axis and the line joining the center of the arc to the origin. The centers for the arcs for $\theta=10, 20, 30$ and 40° in the figure are at $(0.5, -0.009), (0.5, -0.182), (0.5, -0.289), (0.5, -0.419)$, respectively. (c) Plot of $M''/(C_0/A_0)$ versus $M'/(C_0/A_0)$. (d) Plot of $Y''/(1/R)$ versus $Y'/(1/R)$. (e) Plot of $\epsilon''/(A_0/C_0)$ versus $\epsilon'/(A_0/C_0)$. Values used for calculations are $R = 5 \text{ k}\Omega$, $A_0 = 6.014 \times 10^{-4}$ and $C_0 = 1.6 \times 10^{-12} \text{ F}$. (Reproduced with Permission from Taylor & Francis, Pandey et al. 2017, Figure 1, Equivalent Circuit Models Using CPE for Impedance Spectroscopy of Electronic Ceramics, Integrated Ferroelectrics, 183: 141–162.)

The expression for impedance is

$$\begin{aligned} Z &= Z' - jZ'' = \frac{1}{Y} = \frac{1}{\frac{1}{R} + A_0(j\omega)^n} = \frac{R}{1 + RA_0(j\omega)^n} \\ &= \frac{R}{1 + RA_0(e^{j\pi/2}\omega)^n} \end{aligned} \quad (4.63)$$

$$= \frac{R}{1 + RA_0\omega^n \left(\cos \frac{n\pi}{2} + j \sin \frac{n\pi}{2} \right)} \quad (4.64)$$

$$= \frac{R}{\left(1 + RA_0\omega^n \cos \frac{n\pi}{2} \right) + j \left(RA_0\omega^n \sin \frac{n\pi}{2} \right)} \quad (4.65)$$

$$= R \frac{\left[\left(1 + RA_0\omega^n \cos \frac{n\pi}{2} \right) - j \left(RA_0\omega^n \sin \frac{n\pi}{2} \right) \right]}{\left(1 + RA_0\omega^n \cos \frac{n\pi}{2} \right)^2 + \left(RA_0\omega^n \sin \frac{n\pi}{2} \right)^2} \quad (4.66)$$

$$Z' = R \frac{\left(1 + RA_0\omega^n \cos \frac{n\pi}{2} \right)}{\left(1 + RA_0\omega^n \cos \frac{n\pi}{2} \right)^2 + \left(RA_0\omega^n \sin \frac{n\pi}{2} \right)^2} \quad (4.67)$$

$$Z'' = R \frac{\left(RA_0\omega^n \sin \frac{n\pi}{2} \right)}{\left(1 + RA_0\omega^n \cos \frac{n\pi}{2} \right)^2 + \left(RA_0\omega^n \sin \frac{n\pi}{2} \right)^2} \quad (4.68)$$

Other immittance functions are obtained by using the relations given in Chapter 2.

The values of real and imaginary parts of immittance functions for $n = 1$ as $\omega \rightarrow 0$ and $\omega \rightarrow \infty$ are

$$Z'|_{\omega \rightarrow 0} = R, Z'|_{\omega \rightarrow \infty} = 0, Z''|_{\omega \rightarrow 0} = 0, Z''|_{\omega \rightarrow \infty} = 0 \quad (4.69)$$

$$Y'|_{\omega \rightarrow 0} = \frac{1}{R}, Y'|_{\omega \rightarrow \infty} = +\infty, Y''|_{\omega \rightarrow 0} = 0, Y''|_{\omega \rightarrow \infty} = +\infty \quad (4.70)$$

$$M' \Big|_{\omega \rightarrow 0} = 0, M' \Big|_{\omega \rightarrow \infty} = \frac{C_0}{A_0}, M'' \Big|_{\omega \rightarrow 0} = 0, M'' \Big|_{\omega \rightarrow \infty} = +\infty \quad (4.71)$$

$$\varepsilon' \Big|_{\omega \rightarrow 0} = \frac{A_0}{C_0}, \varepsilon' \Big|_{\omega \rightarrow \infty} = \frac{A_0}{C_0}, \varepsilon'' \Big|_{\omega \rightarrow 0} = +\infty, \varepsilon'' \Big|_{\omega \rightarrow \infty} = 0 \quad (4.72)$$

From Eq. (4.62) it is seen that when $n = 1$, the circuit impedance is given by

$$Z = \frac{1}{Y} = \frac{1}{\frac{1}{R} + A_0(j\omega)^n} = \frac{R}{1 + RA_0(j\omega)^n} = \frac{R}{1 + j\omega RA_0} \quad (4.73)$$

For a parallel RC circuit, Z is given by

$$\frac{1}{Z} = \frac{1}{R} + \frac{1}{\frac{1}{j\omega C}} = \frac{1}{R} + j\omega C = \frac{1 + j\omega CR}{R} \quad (4.74)$$

or

$$Z = \frac{R}{1 + j\omega RC} = \frac{R}{1 + (j\omega\tau)} \quad (4.75)$$

and the time constant is $\tau = RC$. Comparison of Eqs. (4.73) and (4.75) reveals that the parallel R-CPE circuit behaves as a parallel RC circuit for $n = 1$, where the capacitor is given by A_0 . The time constant RC becomes RA_0 . For $0 < n < 1$, Z can be written by using Eq. (4.73) as

$$Z = \frac{R}{1 + RA_0(j\omega)^n} = \frac{R}{1 + (j\omega\tau)^n} \quad (4.76)$$

and its dimensions are ohms. Therefore, the time constant τ can be written as

$$\tau = (A_0 R)^{\frac{1}{n}} \quad \text{or} \quad A_0 R = \tau^n \quad (4.77)$$

It is difficult to visualize the dimensions of A_0 for this situation. However, the dimensions of A_0 are such that $\omega\tau$ is dimensionless, i.e.

$$\omega\tau = \omega(A_0 R)^{\frac{1}{n}} = 1 \text{ or } RA_0(\omega)^n = 1 \quad (4.78)$$

Dimensions of A_0 are $[1/\Omega][1/(\text{rad/s})^n]$ i.e. $\Omega^{-1}(\text{rad/s})^{-n}$.

It can be further shown that the parallel R-CPE model gives rise to a depressed Z'' versus Z' semicircular arc (Wang 2001) (see Problem 4.2). Z' and Z'' satisfy the relation

$$\left(Z' - \frac{R}{2}\right)^2 + \left(Z'' + \frac{R}{2} \tan \theta\right)^2 = \left(\frac{R}{2}\right)^2 [1 + (\tan \theta)^2] \quad (4.79)$$

where θ is given by

$$n = 1 - \alpha = 1 - \frac{\theta}{\pi/2}, \theta = \frac{\alpha\pi}{2}, (0 < n < 1, 0 < \alpha < 1) \quad (4.80)$$

Thus

$$n \frac{\pi}{2} = \frac{\pi}{2} - \theta \text{ and } \cot \frac{n\pi}{2} = \cot \left(\frac{\pi}{2} - \theta\right) = \tan \theta \quad (4.81)$$

Equation (4.79) is the equation of a circle having center at the point $(R/2, -(R/2) \tan \theta)$ and radius equal to $(R/2)\sqrt{1 + \tan^2 \theta}$ i.e. $(R/2)/\cos \theta$. The ordinate of the center is $-(R/2) \tan \theta$ i.e. it lies below the Z' axis (i.e. in the fourth quadrant). The value of Z'' is zero when $Z' = 0$ or $Z' = R$ and the values of Z' and Z'' are positive as indicated by Eqs. (4.67) and (4.68). Also, from Eq. (4.69) it is seen that $Z' = R$ and $Z'' = 0$ when $\omega \rightarrow 0$ and $Z' = 0$ and $Z'' = 0$ when $\omega \rightarrow \infty$. Thus the parallel R-CPE circuit yields a depressed semicircular arc in the Z'' versus Z' plot, traversing from right to left as the frequency increases. The angle θ is the angle between the line joining the origin to the center $(R/2, -(R/2) \tan \theta)$ and the Z' axis. Lower values of θ would correspond to less depression and higher values of n . For $n = 1$, value of θ becomes zero, coordinates of the center of the arc become $(R/2, 0)$, parallel R-CPE circuit reduces to parallel RC circuit and the Z'' versus Z' plot is a semicircular arc with its center lying on the Z' axis. Normalized complex plane plots are shown in Figures 4.8(b–e) for different values of θ , i.e. n . Larger the value of θ , larger the depression.

4.9 SERIES COMBINATION OF R AND CPE

A series combination of R and CPE is schematically shown in Figure 4.9(a).

Expressions for real and imaginary parts of immittance functions and their limiting values are given below.

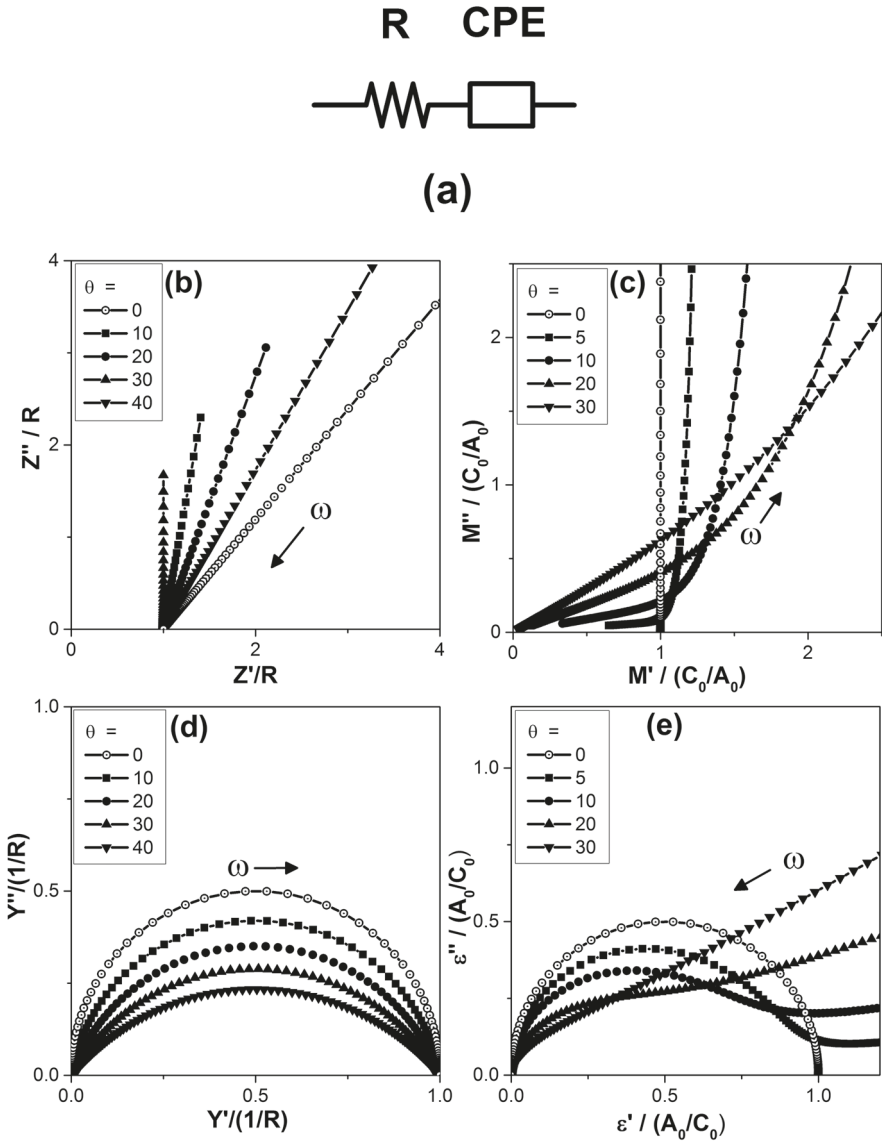


FIGURE 4.9 (a) Equivalent circuit model containing a series combination of resistance R and CPE. (b) Z''/R versus Z'/R plots, (c) $M''/(C_0/A_0)$ versus $M'/(C_0/A_0)$ plots, (d) $Y''R$ versus $Y'/(1/R)$ plots, (e) $\epsilon''/(A_0/C_0)$ versus $\epsilon'/(A_0/C_0)$ plots for various values of parameters. Values used for calculations are $R = 5 \text{ k}\Omega$, $A_0 = 6.014 \times 10^{-6}$ and $C_0 = 1.6 \times 10^{-12} \text{ F}$. (Reproduced with Permission from Taylor & Francis, Pandey et al. 2017, Figure 2, Equivalent Circuit Models Using CPE for Impedance Spectroscopy of Electronic Ceramics, Integrated Ferroelectrics, 183: 141–162.)

$$Z = Z' - jZ'' = R + \frac{1}{A_0(j\omega)^n} = R + \frac{1}{A_0\omega^n} \cos\left(\frac{n\pi}{2}\right) - j \frac{1}{A_0\omega^n} \sin\left(\frac{n\pi}{2}\right) \quad (4.82)$$

$$Z' = R + \frac{1}{A_0\omega^n} \cos\left(\frac{n\pi}{2}\right), Z'' = \frac{1}{A_0\omega^n} \sin\left(\frac{n\pi}{2}\right) \quad (4.83)$$

For $n = 1$, we get $Z' = R$ and $Z'' = 1/(A_0\omega)$, and the circuit becomes like a series RC circuit in which the capacitance is A_0 .

$$M' = \omega C_0 \left[\frac{1}{A_0\omega^n} \sin\left(\frac{n\pi}{2}\right) \right] \quad (4.84)$$

$$M'' = \omega C_0 \left[R + \frac{1}{A_0\omega^n} \cos\left(\frac{n\pi}{2}\right) \right] \quad (4.85)$$

$$Y' = \frac{R + \frac{1}{A_0\omega^n} \cos\left(\frac{n\pi}{2}\right)}{\left[R + \frac{1}{A_0\omega^n} \cos\left(\frac{n\pi}{2}\right) \right]^2 + \left[\frac{1}{A_0\omega^n} \sin\left(\frac{n\pi}{2}\right) \right]^2} \quad (4.86)$$

$$Y'' = \frac{\frac{1}{A_0\omega^n} \sin\left(\frac{n\pi}{2}\right)}{\left[R + \frac{1}{A_0\omega^n} \cos\left(\frac{n\pi}{2}\right) \right]^2 + \left[\frac{1}{A_0\omega^n} \sin\left(\frac{n\pi}{2}\right) \right]^2} \quad (4.87)$$

$$\varepsilon' = \frac{Y''}{\omega C_0}, \varepsilon'' = \frac{Y'}{\omega C_0} \quad (4.88)$$

Limiting values for $n = 1$ are given below

$$Z'|_{\omega \rightarrow 0} = +\infty, Z'|_{\omega \rightarrow \infty} = R, Z''|_{\omega \rightarrow 0} = +\infty, Z''|_{\omega \rightarrow \infty} = 0 \quad (4.89)$$

$$Y'|_{\omega \rightarrow 0} = 0, Y'|_{\omega \rightarrow \infty} = \frac{1}{R}, Y''|_{\omega \rightarrow 0} = 0, Y''|_{\omega \rightarrow \infty} = 0 \quad (4.90)$$

$$M' \Big|_{\omega \rightarrow 0} = \frac{C_0}{A_0}, M' \Big|_{\omega \rightarrow \infty} = \frac{C_0}{A_0}, M'' \Big|_{\omega \rightarrow \infty} = 0, M'' \Big|_{\omega \rightarrow \infty} = +\infty \quad (4.91)$$

$$\varepsilon' \Big|_{\omega \rightarrow 0} = \frac{A_0}{C_0}, \varepsilon' \Big|_{\omega \rightarrow \infty} = 0, \varepsilon'' \Big|_{\omega \rightarrow 0} = 0, \varepsilon'' \Big|_{\omega \rightarrow \infty} = 0 \quad (4.92)$$

It is found that Z' and Z'' satisfy the relation

$$Z'' = Z' \tan\left(\frac{n\pi}{2}\right) - R \tan\left(\frac{n\pi}{2}\right) \quad (4.93)$$

which is the equation of a straight line indicating that Z'' versus Z' plot would be a straight line having slope equal to $\tan(n\pi/2)$, passing through the point $(R,0)$ and having intercept equal to R at the Z' axis. This intercept would occur at the high-frequency side as indicated by the limiting value of Z' as $\omega \rightarrow \infty$. The straight line makes an angle $n\pi/2$ with the Z' axis. Following the definition of angle θ used earlier in Eq. (4.81), this angle is given by $n\pi/2 = (\pi/2 - \theta)$.

Also, it can be shown that Y' and Y'' satisfy the equation

$$\left(Y' - \frac{1}{2R}\right)^2 + \left(Y'' + \frac{1}{2R} \cot \frac{n\pi}{2}\right)^2 = \left(\frac{1}{2R}\right)^2 \left[1 + \left(\cot \frac{n\pi}{2}\right)^2\right] \quad (4.94)$$

or

$$\left(Y' - \frac{1}{2R}\right)^2 + \left(Y'' + \frac{1}{2R} \tan \theta\right)^2 = \left(\frac{1}{2R}\right)^2 [1 + (\tan \theta)^2] \quad (4.95)$$

This is the equation of a circle on Y'' versus Y' plot having its center at the point having coordinates $(1/(2R), -1/(2R) \tan \theta)$ and radius equal to $(1/(2R)) \sqrt{1 + \tan^2 \theta}$. From Eq. (4.95) it is seen that when $Y'' = 0$, the values of Y' are 0 or $1/R$, i.e. the circle would pass through the origin and the point $(1/R,0)$. As the limiting value of Y' is $1/R$ as $\omega \rightarrow \infty$, the arc would intercept the Y' axis at the point $(1/R,0)$ at the high-frequency side. As the y-coordinate of the center is $-1/(2R) \tan \theta$, the center of the circle lies below the Y' axis. The Y'' versus Y' plot would, thus, be a depressed semicircular arc traversing from left to right.

Simulated plots of the immittance functions for various values of θ are shown in Figures 4.9(b–e). The values have been normalized by using limiting values of the respective immittance functions for easy visualization and comparison.

Here, the Z'' versus Z' plot and Y'' versus Y' plot are easier to understand and more revealing as compared to complex plane M and ε plots. These plots indicate that if experimental Z'' versus Z' plot looks like a straight line tilted away from the Z'' axis, and Y'' versus Y' plot is a depressed semicircular arc passing through the

origin, a series R-CPE model may be used to represent the system. The unknown parameters of the model are R , A_0 and n . Value of R can be estimated by noting the intercept (which is equal to R) of the straight line on the Z'' versus Z' plot or the intercept (which is equal to $1/R$) of the Y'' versus Y' arc on the Y' axis in the high-frequency side. The value of n is obtained by noting the slope of the straight line on the Z'' versus Z' plot or by noting the angle between the Y' axis and the line joining the origin to the center $(1/(2R), -1/(2R) \tan \theta)$ of the arc and using the relation $n\pi/2 = (\pi/2 - \theta)$. The value of A_0 may be estimated by using the relation $\omega\tau = 1$ and the frequency at the peak of the Y'' versus Y' plot, or by using experimental value of Z' or Z'' , value of n and frequency and substituting them in expressions for Z' or Z'' .

4.10 SERIES COMBINATION OF PARALLEL R_1 -CPE₁ AND PARALLEL R_2 -CPE₂

A series combination of parallel R_1 -CPE₁ and parallel R_2 -CPE₂ is shown schematically in Figure 4.10(a). The CPE₁ is characterized by A_{01} and n_1 and CPE₂ by A_{02} and n_2 .

Expressions for real and imaginary parts of immittance functions are given below

$$Z = \frac{R_1}{1 + A_{01}R_1(j\omega)^{n_1}} + \frac{R_2}{1 + A_{02}R_2(j\omega)^{n_2}} \tag{4.96}$$

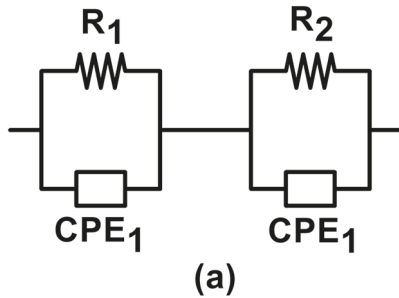


FIGURE 4.10 (a) Equivalent circuit model containing series combination of parallel R_1 -CPE₁ and parallel R_2 -CPE₂. (b–d) Plot of $Z''/(R_1 + R_2)$ versus $Z'/(R_1 + R_2)$ for various values of R_2/R_1 , τ_2/τ_1 , k ($\theta_2 = k\theta_1$) and θ_1 , where θ_1 is the angle between Z' axis and the line joining the origin to the center $(R_1/2, -R_1/2 \tan \theta_1)$ of the arc corresponding to the parallel combination R_1 -CPE₁. θ_2 is the angle between Z' axis and the line joining the point $(R_1, 0)$ to the center $(R_2/2, -(R_2/2) \tan \theta_2)$ of the arc corresponding to the parallel combination R_2 -CPE₂. (e–g) Plots of $M''/(C_0/A_{01} + C_0/A_{02})$ versus $M'/(C_0/A_{01} + C_0/A_{02})$ for various values of R_2/R_1 , τ_2/τ_1 , k ($\theta_2 = k\theta_1$) and θ_1 . (h–j) Plots of $Y''(R_1 + R_2)$ vs versus $Y'(R_1 + R_2)$ for various values of R_2/R_1 , τ_2/τ_1 , k ($\theta_2 = k\theta_1$) and θ_1 . (k) Plot of $\epsilon''/[(1/C_0)\{A_{01}(R_1/(R_1 + R_2))^2 + A_{02}(R_2/(R_1 + R_2))^2\}]$ versus $\epsilon'/[(1/C_0)\{A_{01}(R_1/(R_1 + R_2))^2 + A_{02}(R_2/(R_1 + R_2))^2\}]$ for various values of R_2/R_1 , τ_2/τ_1 , k ($\theta_2 = k\theta_1$) and θ_1 . Values used for calculations are $R = 5 \text{ k}\Omega$, $A_0 = 6.014 \times 10^{-6}$ and $C_0 = 1.6 \times 10^{-12} \text{ F}$. (Reproduced with Permission from Taylor & Francis, Pandey et al. 2017, Figure 3, Equivalent Circuit Models Using CPE for Impedance Spectroscopy of Electronic Ceramics, Integrated Ferroelectrics, 183: 141–162.)

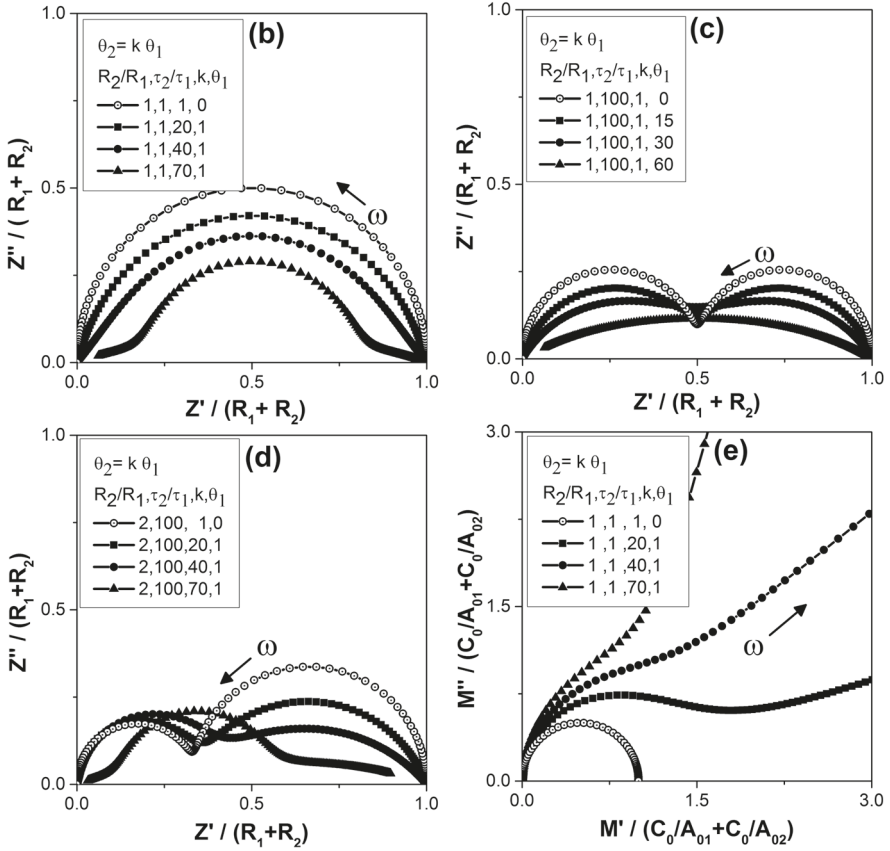


FIGURE 4.10 (Continued)

$$= \frac{R_1}{1+(j\omega\tau_1)^{n_1}} + \frac{R_2}{1+(j\omega\tau_1)^{n_1}} \quad (4.97)$$

where time constants τ_1 and τ_2 are defined as

$$\tau_1 = (A_{01}R_1)^{(1/n_1)}, \quad n_1 = 1 - \frac{\theta_1}{\pi/2} = 1 - \alpha_1, \quad \alpha_1 = \frac{\theta_1}{\pi/2} \quad (4.98)$$

$$\tau_2 = (A_{02}R_2)^{(1/n_2)}, \quad n_2 = 1 - \frac{\theta_2}{\pi/2} = 1 - \alpha_2, \quad \alpha_2 = \frac{\theta_2}{\pi/2} \quad (4.99)$$

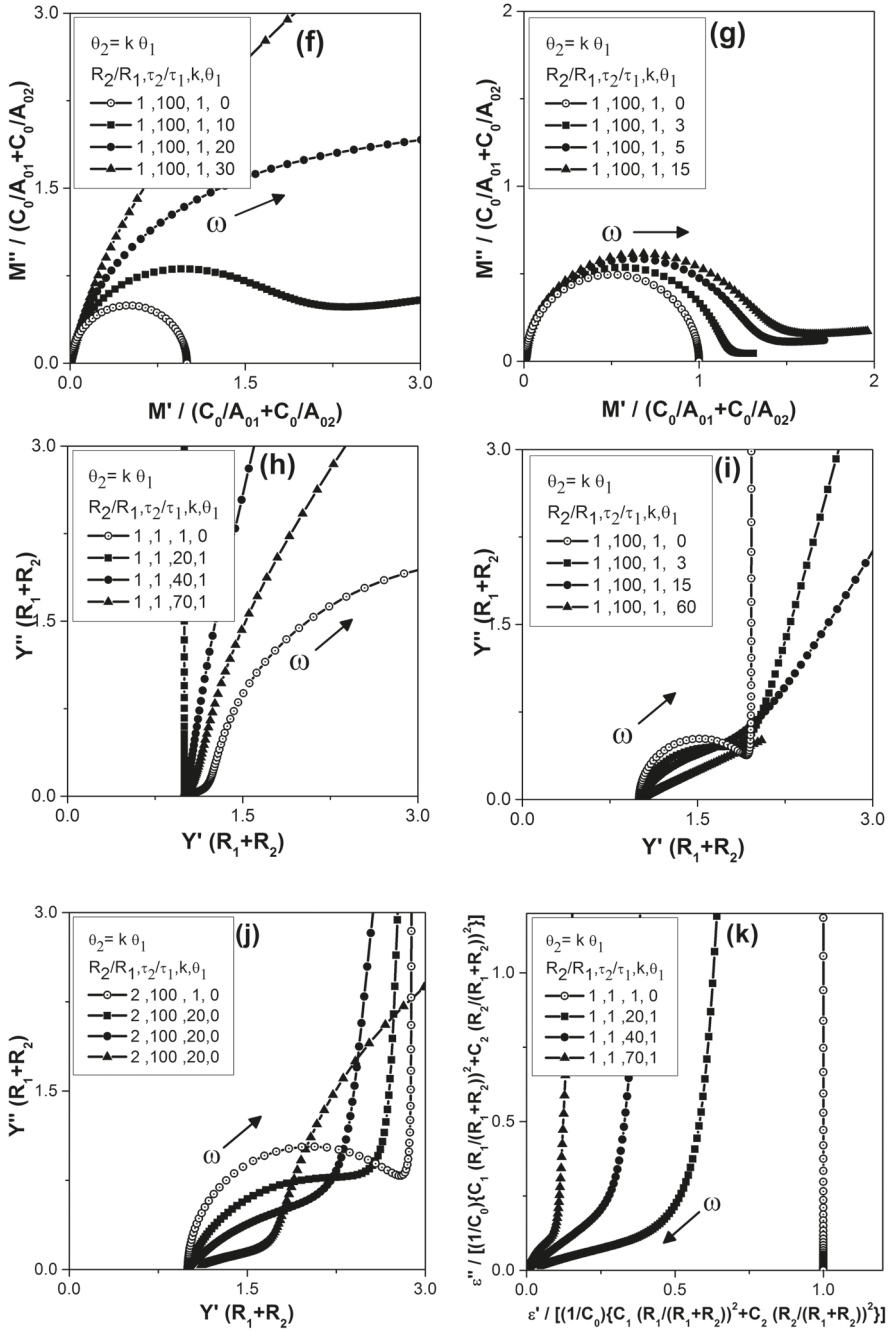


FIGURE 4.10 (Continued)

$$Z' = \frac{R_1 \left(1 + A_{01} R_1 \omega^{n_1} \cos \left(\frac{n_1 \pi}{2} \right) \right)}{\left(1 + A_{01} R_1 \omega^{n_1} \cos \left(\frac{n_1 \pi}{2} \right) \right)^2 + \left(A_{01} R_1 \omega^{n_1} \sin \left(\frac{n_1 \pi}{2} \right) \right)^2} + \frac{R_2 \left(1 + A_{02} R_2 \omega^{n_2} \cos \left(\frac{n_2 \pi}{2} \right) \right)}{\left(1 + A_{02} R_2 \omega^{n_2} \cos \left(\frac{n_2 \pi}{2} \right) \right)^2 + \left(A_{02} R_2 \omega^{n_2} \sin \left(\frac{n_2 \pi}{2} \right) \right)^2} \quad (4.100)$$

$$Z'' = \frac{R_1 A_{01} R_1 \omega^{n_1} \sin \left(\frac{n_1 \pi}{2} \right)}{\left(1 + A_{01} R_1 \omega^{n_1} \cos \left(\frac{n_1 \pi}{2} \right) \right)^2 + \left(A_{01} R_1 \omega^{n_1} \sin \left(\frac{n_1 \pi}{2} \right) \right)^2} + \frac{R_2 A_{02} R_2 \omega^{n_2} \sin \left(\frac{n_2 \pi}{2} \right)}{\left(1 + A_{02} R_2 \omega^{n_2} \cos \left(\frac{n_2 \pi}{2} \right) \right)^2 + \left(A_{02} R_2 \omega^{n_2} \sin \left(\frac{n_2 \pi}{2} \right) \right)^2} \quad (4.101)$$

Other immittance functions can be obtained by using their interrelationships. The limiting values for $n_1=1$ and $n_2=1$ are given below

$$Z'|_{\omega \rightarrow 0} = R_1 + R_2, Z'|_{\omega \rightarrow \infty} = 0, Z''|_{\omega \rightarrow 0} = 0, Z''|_{\omega \rightarrow \infty} = 0 \quad (4.102)$$

$$Y'|_{\omega \rightarrow 0} = \frac{1}{R_1 + R_2}, Y'|_{\omega \rightarrow \infty} = \frac{1}{R_2} \left(\frac{A_{02}}{A_{01} + A_{02}} \right)^2 + \frac{1}{R_2} \left(\frac{A_{01}}{A_{01} + A_{02}} \right)^2, \\ Y''|_{\omega \rightarrow 0} = 0, Y''|_{\omega \rightarrow \infty} = \infty \quad (4.103)$$

$$M'|_{\omega \rightarrow 0} = 0, M'|_{\omega \rightarrow \infty} = C_0 \left(\frac{1}{A_{01}} + \frac{1}{A_{02}} \right), M''|_{\omega \rightarrow 0} = 0, M''|_{\omega \rightarrow \infty} = 0 \quad (4.104)$$

$$\varepsilon'|_{\omega \rightarrow 0} = \frac{A_{01}}{C_0} \left(\frac{R_1}{R_1 + R_2} \right)^2 + \frac{A_{02}}{C_0} \left(\frac{R_2}{R_1 + R_2} \right)^2, \\ \varepsilon'|_{\omega \rightarrow \infty} = \frac{A_{01}}{C_0} \left(\frac{A_{02}}{A_{01} + A_{02}} \right), \varepsilon''|_{\omega \rightarrow 0} = +\infty, \varepsilon''|_{\omega \rightarrow \infty} = 0 \quad (4.105)$$

Simulated plots for different ratios of component values are shown in Figures 4.10(b–k).

It may be mentioned that this model contains two parallel R-CPE circuits and the two processes should be visible in the plots. However, it is seen from Figures 4.10(b, c) that when the resistance values and time constants of both processes are equal, a single hump type Z'' versus Z' plot appears, which acquires a peculiar shape when the depressions represented by angles θ_1 and θ_2 are quite different. When the resistances R_1 and R_2 are equal but the time constants are quite different ($\tau_2/\tau_1 = 100$), distinct depressed arcs may appear. Since τ_1 is less than τ_2 , the arc on high-frequency side would correspond to R_1 -CPE₁. The arc would intercept the Z' axis at points (0, 0) and (R_1 , 0) and would have its center at the point ($R_1/2$, $-(R_1/2) \tan \theta_1$), where θ_1 is the angle between the line joining the origin to the center and the Z' axis. The arc on low-frequency side would correspond to R_2 -CPE₂. This arc would intercept the Z' axis at points ($R_1, 0$) and ($R_1 + R_2, 0$) and would have its center at the point ($(R_1 + R_2)/2$, $-(R_2/2) \tan \theta_2$), where θ_2 is the angle between the line joining the point ($R_1, 0$) to the center and the Z' axis.

4.11 SERIES COMBINATION OF PARALLEL R_1C_1 , PARALLEL R_2C_2 AND CPE

A series combination of parallel R_1C_1 , parallel R_2C_2 and a CPE is shown schematically in Figure 4.11(a). Expressions for Z' and Z'' are given in Eqs. (4.106) and (4.107).

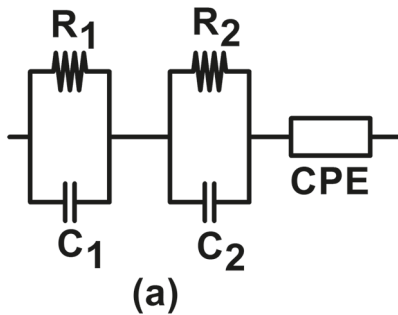


FIGURE 4.11 (a) Equivalent circuit model containing series combination of parallel R_1C_1 , parallel R_2C_2 and CPE. Plots of (b, c) $Z''/(R_1 + R_2)$ versus $Z'/(R_1 + R_2)$ for various values of R_2/R_1 , R_2C_2/R_1C_1 , A_0 and θ , where θ is the angle between Z' axis and the line showing the low-frequency linear part corresponding to CPE and passing through the point ($R_1 + R_2$, 0) (d) $M''/(C_0/C_1 + C_0/C_2)$ versus $M'/(C_0/C_1 + C_0/C_2)$ (e) $Y''(R_1 + R_2)$ versus $Y'(R_1 + R_2)$, and (f) $\epsilon''/[(1/C_0)\{C_1(R_1/(R_1 + R_2))^2 + C_2(R_2/(R_1 + R_2))^2\}]$ versus $\epsilon'/[(1/C_0)\{C_1(R_1/(R_1 + R_2))^2 + C_2(R_2/(R_1 + R_2))^2\}]$ for various values of R_2/R_1 , R_2C_2/R_1C_1 , A_0 and θ . (Reproduced with Permission from Taylor & Francis, Pandey et al. 2017, Figure 4, Equivalent Circuit Models Using CPE for Impedance Spectroscopy of Electronic Ceramics, Integrated Ferroelectrics, 183: 141–162.)

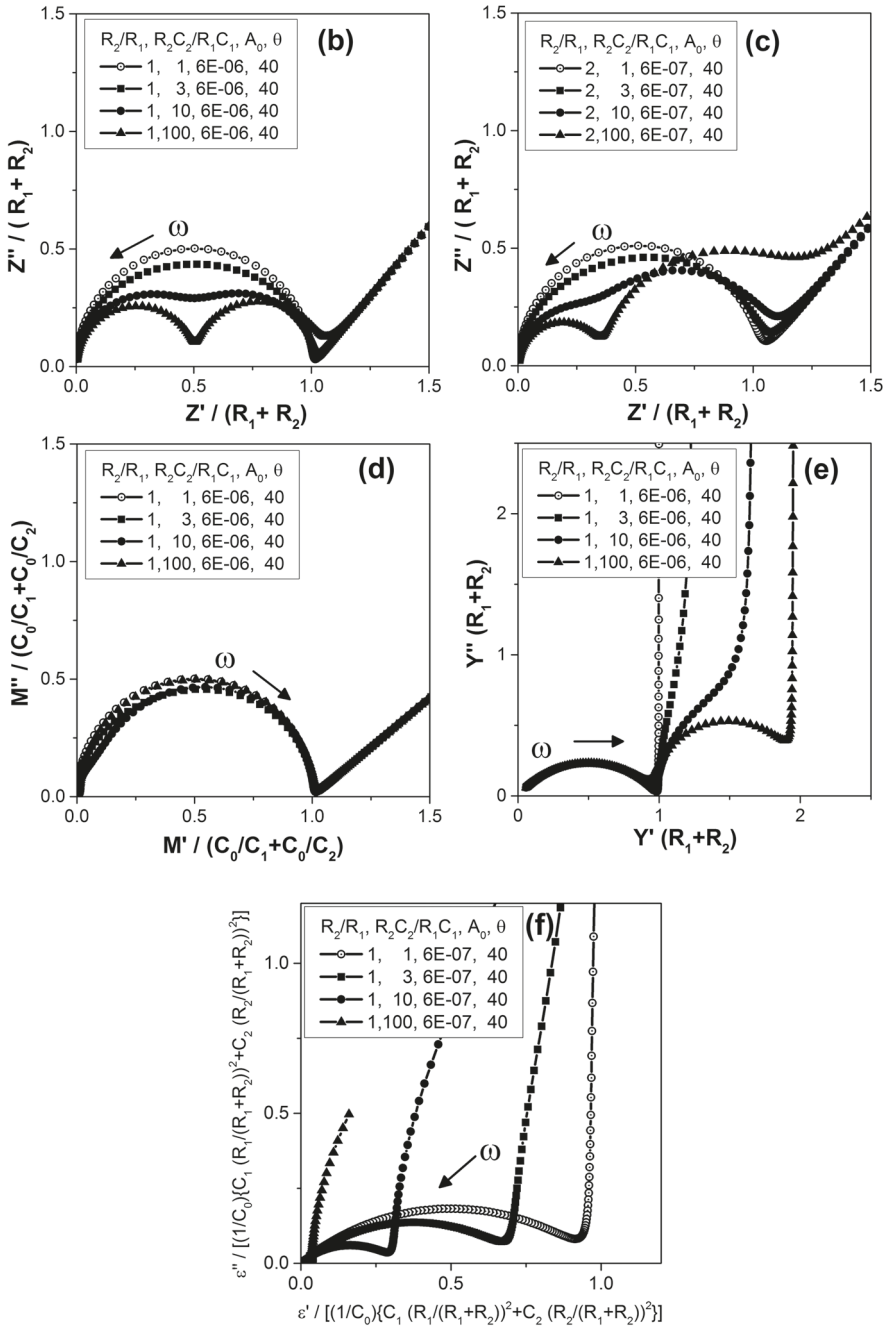


FIGURE 4.11 (Continued)

$$Z' = \frac{R_1}{1 + (\omega R_1 C_1)^2} + \frac{R_2}{1 + (\omega R_2 C_2)^2} + \left(\frac{1}{A_0 \omega^n} \right) \cos\left(\frac{n\pi}{2}\right) \quad (4.106)$$

$$Z'' = \omega R_1 C_1 \frac{R_1}{1 + (\omega R_1 C_1)^2} + \omega R_2 C_2 \frac{R_2}{1 + (\omega R_2 C_2)^2} + \left(\frac{1}{A_0 \omega^n} \right) \sin\left(\frac{n\pi}{2}\right) \quad (4.107)$$

The limiting values for $n = 1$ for various immittance functions are given below

$$Z' \Big|_{\omega \rightarrow 0} = R_1 + R_2, Z' \Big|_{\omega \rightarrow \infty} = 0, Z'' \Big|_{\omega \rightarrow 0} = \infty, Z'' \Big|_{\omega \rightarrow \infty} = 0 \quad (4.108)$$

$$Y' \Big|_{\omega \rightarrow 0} = 0, Y' \Big|_{\omega \rightarrow \infty} = \frac{1}{R_1 R_2} \left[\frac{A_0^2 (C_1^2 R_1 + C_2^2 R_2)}{(C_1 C_2 + A_0 (C_1 + C_2))^2} \right], \quad (4.109)$$

$$Y'' \Big|_{\omega \rightarrow 0} = 0, Y'' \Big|_{\omega \rightarrow \infty} = 0$$

$$M' \Big|_{\omega \rightarrow 0} = \frac{C_0}{A_0}, M' \Big|_{\omega \rightarrow \infty} = C_0 \left(\frac{1}{C_1} + \frac{1}{C_2} + \frac{1}{A_0} \right), M'' \Big|_{\omega \rightarrow 0} = 0, M'' \Big|_{\omega \rightarrow \infty} = 0 \quad (4.110)$$

$$\varepsilon' \Big|_{\omega \rightarrow 0} = \frac{A_0}{C_0}, \varepsilon' \Big|_{\omega \rightarrow \infty} = \frac{A_0}{C_0} \left(\frac{C_1 C_2}{A_0 C_1 + A_0 C_2 + C_1 C_2} \right), \varepsilon'' \Big|_{\omega \rightarrow 0} = 0, \varepsilon'' \Big|_{\omega \rightarrow \infty} = 0 \quad (4.111)$$

Plots of the immittance functions are shown in Figures 4.11(b–f).

4.12 SERIES COMBINATION OF PARALLEL R_1 -CPE₁, R_2 AND CPE₂

The model is schematically shown in Figure 4.12(a). Expressions for Z' and Z'' are given in Eqs (4.112) and (4.113).

$$Z = \frac{R_1}{1 + A_{01} R_1 (j\omega)^{n_1}} + R_2 + \frac{1}{A_{02} (j\omega)^{n_2}} \quad (4.112)$$

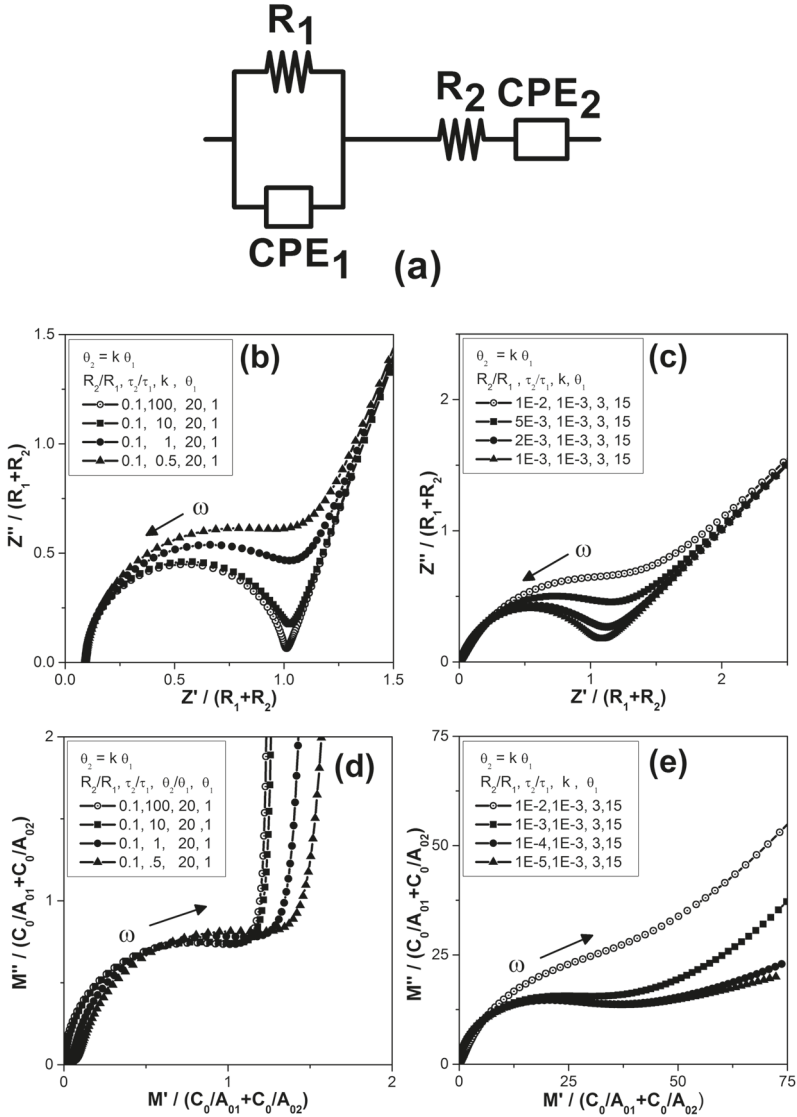


FIGURE 4.12 (a) Equivalent circuit model having series combination of parallel R_1 - CPE_1 , R_2 and CPE_2 . (b, c) Plot of $Z''/(R_1 + R_2)$ versus $Z'/(R_1 + R_2)$ for various values of R_2/R_1 , τ_2/τ_1 , θ_2/θ_1 and θ_1 . Where θ_1 is the angle between Z' axis and the line joining the highest-frequency intercept point ($R_2, 0$) to the point $(R_2 + 0.5 R_1, -0.5 R_1 \tan \theta_1)$, the center of the semicircular arc corresponding to parallel R_1 - CPE_1 . (d,e) Plot of $M''/(C_0/A_{01} + C_0/A_{02})$ versus $M'/(C_0/A_{01} + C_0/A_{02})$ (f, g, h) Plot of $Y''/(1/R_2)$ versus $Y'/(1/R_2)$. (i) Plot of $\epsilon''/(A_{02}/C_0)$ versus $\epsilon'/(A_{02}/C_0)$. Values used for calculations are $R_1 = 5 \text{ k}\Omega$ and $A_{01} = 2 \times 10^{-11}$. (Reproduced with Permission from Taylor & Francis, Pandey et al. 2017, Figure 5, Equivalent Circuit Models Using CPE for Impedance Spectroscopy of Electronic Ceramics, Integrated Ferroelectrics, 183: 141–162.)

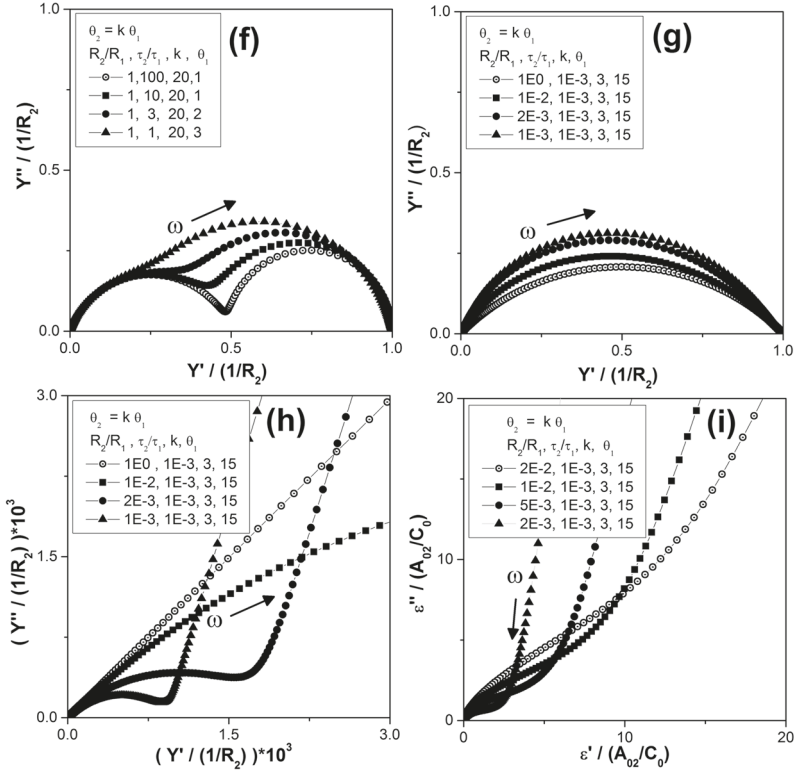


FIGURE 4.12 (Continued)

$$Z' = \frac{R_1 \left(1 + A_{01} R_1 \omega^{n_1} \cos \left(\frac{n_1 \pi}{2} \right) \right)}{\left(1 + A_{01} R_1 \omega^{n_1} \cos \left(\frac{n_1 \pi}{2} \right) \right)^2 + \left(A_{01} R_1 \omega^{n_1} \sin \left(\frac{n_1 \pi}{2} \right) \right)^2} + R_2 + \frac{1}{A_{02} \omega^{n_2}} \cos \left(\frac{n_2 \pi}{2} \right) \quad (4.113)$$

$$Z'' = \frac{R_1 \left(A_{01} R_1 \omega^{n_1} \sin \left(\frac{n_1 \pi}{2} \right) \right)}{\left(1 + A_{01} R_1 \omega^{n_1} \cos \left(\frac{n_1 \pi}{2} \right) \right)^2 + \left(A_{01} R_1 \omega^{n_1} \sin \left(\frac{n_1 \pi}{2} \right) \right)^2} + \frac{1}{A_{02} \omega^{n_2}} \sin \left(\frac{n_2 \pi}{2} \right) \quad (4.114)$$

The limiting values of immittance functions for $n_1 = 1$ and $n_2 = 1$ are given in Eqs. (4.115)–(4.118).

$$Z' \Big|_{\omega \rightarrow 0} = R_1 + R_2, Z' \Big|_{\omega \rightarrow \infty} = R_2, Z'' \Big|_{\omega \rightarrow 0} = \infty, Z'' \Big|_{\omega \rightarrow \infty} = 0 \quad (4.115)$$

$$Y' \Big|_{\omega \rightarrow 0} = 0, Y' \Big|_{\omega \rightarrow \infty} = \frac{1}{R_2}, Y'' \Big|_{\omega \rightarrow 0} = 0, Y'' \Big|_{\omega \rightarrow \infty} = 0 \quad (4.116)$$

$$M' \Big|_{\omega \rightarrow 0} = \frac{C_0}{A_{02}}, M' \Big|_{\omega \rightarrow \infty} = C_0 \left(\frac{1}{A_{01}} + \frac{1}{A_{02}} \right), M'' \Big|_{\omega \rightarrow 0} = 0, \quad (4.117)$$

$$M'' \Big|_{\omega \rightarrow \infty} = \infty$$

$$\varepsilon' \Big|_{\omega \rightarrow 0} = \frac{A_{02}}{C_0}, \varepsilon' \Big|_{\omega \rightarrow \infty} = 0, \varepsilon'' \Big|_{\omega \rightarrow 0} = 0, \varepsilon'' \Big|_{\omega \rightarrow \infty} = 0 \quad (4.118)$$

Complex plane plots are shown in Figures 4.12(b–i).

It is interesting to note that features of individual segments of the model are nicely displayed in the Z'' versus Z' plots. The right shift in the Z'' versus Z' plot corresponds to resistance R_2 . A parallel R-CPE circuit would give a depressed arc and a series CPE would give a tilted straight line in this plot.

4.13 PARALLEL COMBINATION OF R_1 , C_1 AND CPE₁ IN SERIES WITH PARALLEL R_2C_2

This model is schematically shown in Figure 4.13(a).

Expressions for Z' and Z'' are now given

$$Z' = \frac{R_1 \left(1 + R_1 A_{01} \omega^{n_1} \cos \left(\frac{n_1 \pi}{2} \right) \right)}{\left(1 + R_1 A_{01} \omega^{n_1} \cos \left(\frac{n_1 \pi}{2} \right) \right)^2 + \left(R_1 A_{01} \omega^{n_1} \sin \left(\frac{n_1 \pi}{2} \right) + \omega C_1 R_1 \right)^2} + \frac{R_2}{1 + (\omega C_2 R_2)^2} \quad (4.119)$$

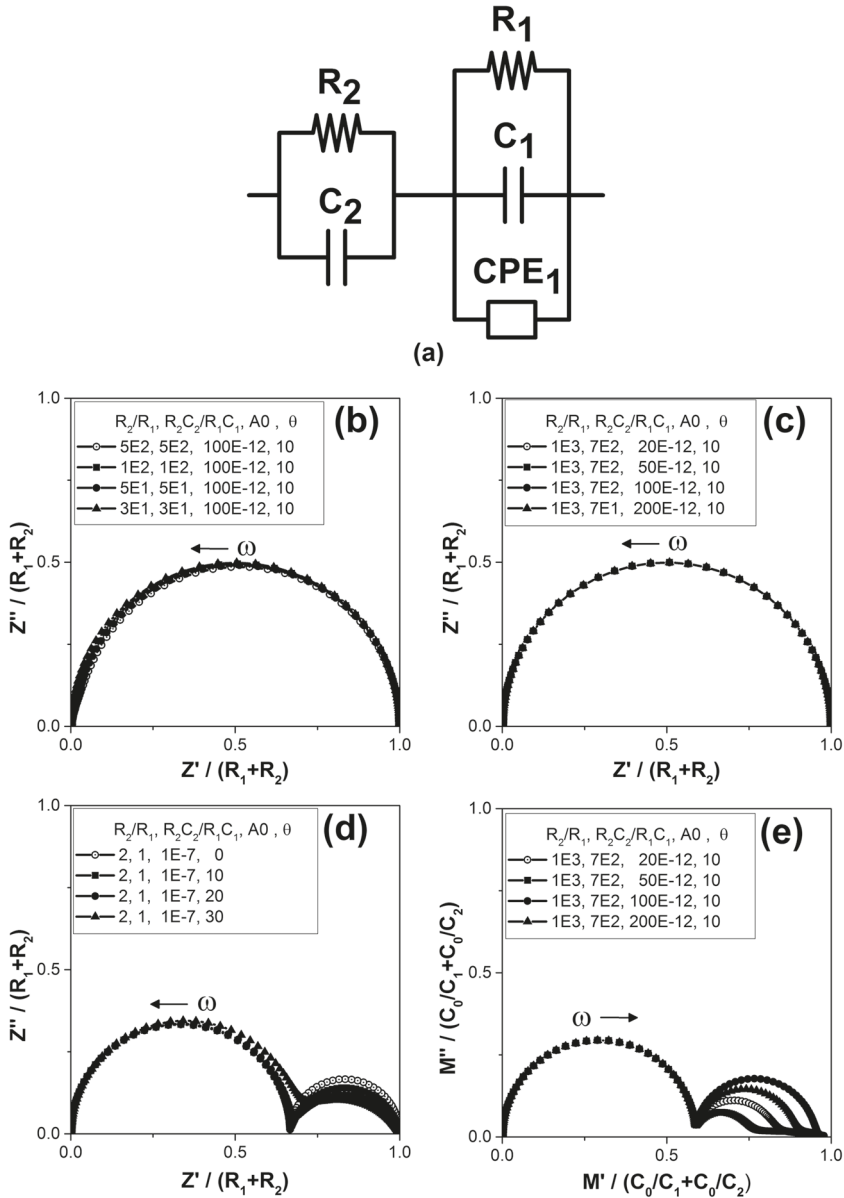


FIGURE 4.13 (a) Equivalent circuit model having a parallel combination R_2C_2 connected in series with parallel combination of R_1, C_1 and CPE_1 . Plots of (b–d) $Z''/(R_1 + R_2)$ versus $Z'/(R_1 + R_2)$ for various values of $R_2/R_1, R_2C_2/R_1C_1, A_0$ and θ . (e, f) $M''/(C_0/C_1 + C_0/C_2)$ versus $M'/(C_0/C_1 + C_0/C_2)$. (g, h) $Y''(R_1 + R_2)$ versus $Y'(R_1 + R_2)$. and (i, j) $\epsilon''/[(C_1/C_0)(R_1/(R_1 + R_2))^2 + (C_2/C_0)(R_2/(R_1 + R_2))^2]$ versus $\epsilon'/[(C_1/C_0)(R_1/(R_1 + R_2))^2 + (C_2/C_0)(R_2/(R_1 + R_2))^2]$ for various values of $R_2/R_1, R_2C_2/R_1C_1, A_0$ and θ ; where θ is the angle between Z' axis and the line joining the point $(R_2, 0)$ to the point $(R_2 + 0.5 R_1, -0.5 R_1 \tan \theta)$ (centre of the depressed arc). (Reproduced with Permission from Taylor & Francis, Pandey et al. 2017, Figure 6, Equivalent Circuit Models Using CPE for Impedance Spectroscopy of Electronic Ceramics, Integrated Ferroelectrics, 183: 141–162.)

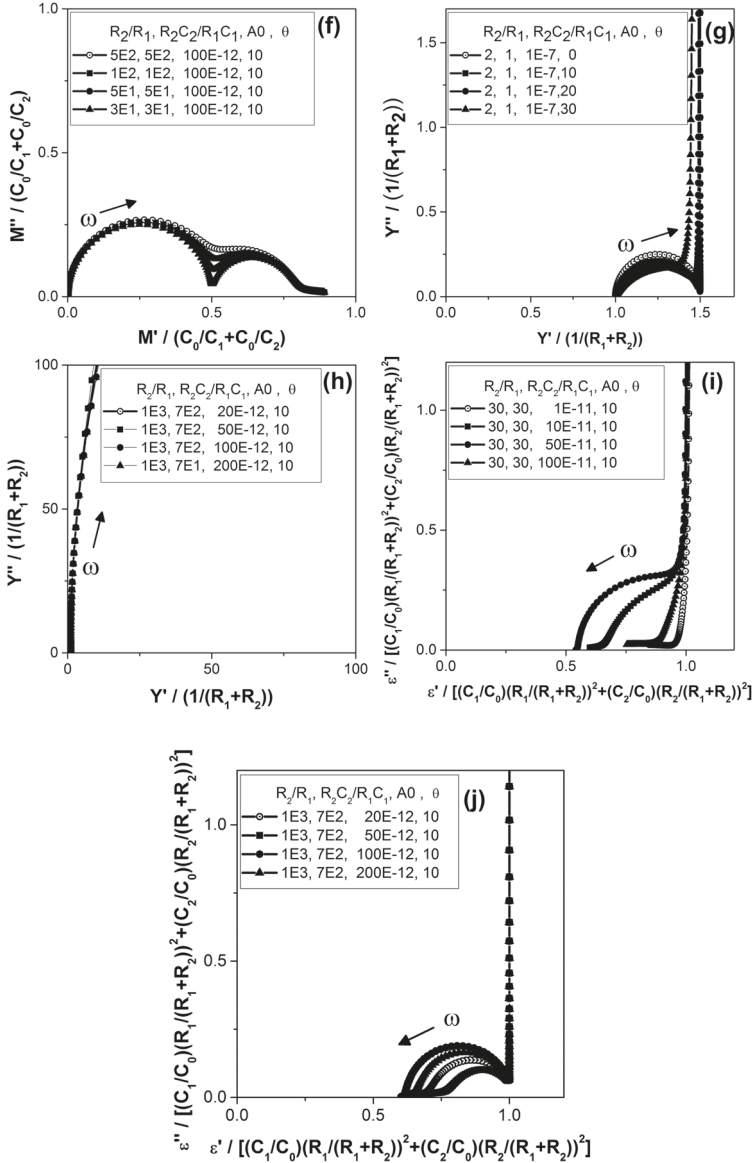


FIGURE 4.13 (Continued)

$$Z'' = \frac{R_1 \left(R_1 A_{01} \omega^{n_1} \sin \left(\frac{n_1 \pi}{2} \right) + \omega C_1 R_1 \right)}{\left(1 + R_1 A_{01} \omega^{n_1} \cos \left(\frac{n_1 \pi}{2} \right) \right)^2 + \left(R_1 A_{01} \omega^{n_1} \sin \left(\frac{n_1 \pi}{2} \right) + \omega C_1 R_1 \right)^2} + \frac{R_2 \omega C_2 R_2}{1 + (\omega C_2 R_2)^2} \quad (4.120)$$

where the impedance of CPE_1 is given by

$$Z_{CPE_1} = \frac{1}{Y_{CPE_1}} = \frac{1}{A_{01} (j\omega)^{n_1}} = \frac{1}{A_{01} \omega^{n_1}} \cos \left(\frac{n_1 \pi}{2} \right) - j \frac{1}{A_{01} \omega^{n_1}} \sin \left(\frac{n_1 \pi}{2} \right) \quad (4.121)$$

The limiting values, corresponding to $n_1 = 1$, are given below

$$Z'_{|\omega \rightarrow 0} = R_1 + R_2, Z'_{|\omega \rightarrow \infty} = 0, Z''_{|\omega \rightarrow 0} = 0, Z''_{|\omega \rightarrow \infty} = 0 \quad (4.122)$$

$$Y''_{|\omega \rightarrow 0} = \frac{1}{R_1 + R_2}, Y''_{|\omega \rightarrow \infty} = \frac{1}{R_1} \left(\frac{C_2}{C_1 + A_{01} + C_2} \right)^2 + \frac{1}{R_2} \left(\frac{C_1 + A_{01}}{C_1 + A_{01} + C_2} \right)^2 Y''_{|\omega \rightarrow 0} = 0, Y''_{|\omega \rightarrow \infty} = \infty \quad (4.123)$$

$$M'_{|\omega \rightarrow 0} = 0, M'_{|\omega \rightarrow \infty} = \frac{C_0}{C_1 + A_{01}} + \frac{C_0}{C_2}, M''_{|\omega \rightarrow 0} = 0, M''_{|\omega \rightarrow \infty} = 0 \quad (4.124)$$

$$\varepsilon'_{|\omega \rightarrow 0} = \frac{C_1 + A_{01}}{C_0} \left(\frac{R_1}{R_1 + R_2} \right)^2 + \frac{C_2}{C_0} \left(\frac{R_2}{R_1 + R_2} \right)^2, \varepsilon'_{|\omega \rightarrow \infty} = \frac{C_2}{C_0} \left(\frac{C_1 + A_{01}}{C_1 + A_{01} + C_2} \right), \varepsilon''_{|\omega \rightarrow 0} = \infty, \varepsilon''_{|\omega \rightarrow \infty} = 0 \quad (4.125)$$

Plots are shown in Figures 4.13(b–j).

4.14 A PARALLEL COMBINATION OF RESISTANCE R AND INDUCTOR L

Just as a dielectric system can store electrical energy, a magnetic system can store magnetic energy. In analogy to the dielectric case, magnetic systems may be modeled by invoking presence of inductive elements in the equivalent circuit model (von Hippel 1954). For dielectrics we talk about dielectric permittivity ϵ and for magnetic systems we have magnetic permeability μ . When a sample is placed in the magnetic field of a coil of inductance L and a voltage v is applied, a magnetization current flows which is given by

$$v = L \frac{di}{dt} \quad (4.126)$$

We proceed by considering a model comprising an inductor connected in parallel to a resistor as schematically shown in Figure 4.14(a).

The impedance Z is given by (Katare 1997, Katare et al. 1999)

$$Z = Z' - jZ'' = \frac{(\omega L)^2 R + j\omega L R^2}{R^2 + (\omega L)^2} \quad (4.127)$$

which gives

$$Z' = \frac{\left(\frac{\omega L}{R}\right)^2 R}{1 + \left(\frac{\omega L}{R}\right)^2}, Z'' = -\frac{\left(\frac{\omega L}{R}\right) R}{1 + \left(\frac{\omega L}{R}\right)^2} \quad (4.128)$$

The admittance is given as

$$Y = \frac{1}{Z} = \frac{z' + jz''}{z'^2 + z''^2} = Y' + jY'' = \frac{1}{R} + \frac{1}{j\omega L} \quad (4.129)$$

$$Y' = \frac{1}{R}, Y'' = -\frac{1}{\omega L} \quad (4.130)$$

If this model is chosen to represent the material, we may write

$$Z = j\omega L_0 \mu \quad (4.131)$$

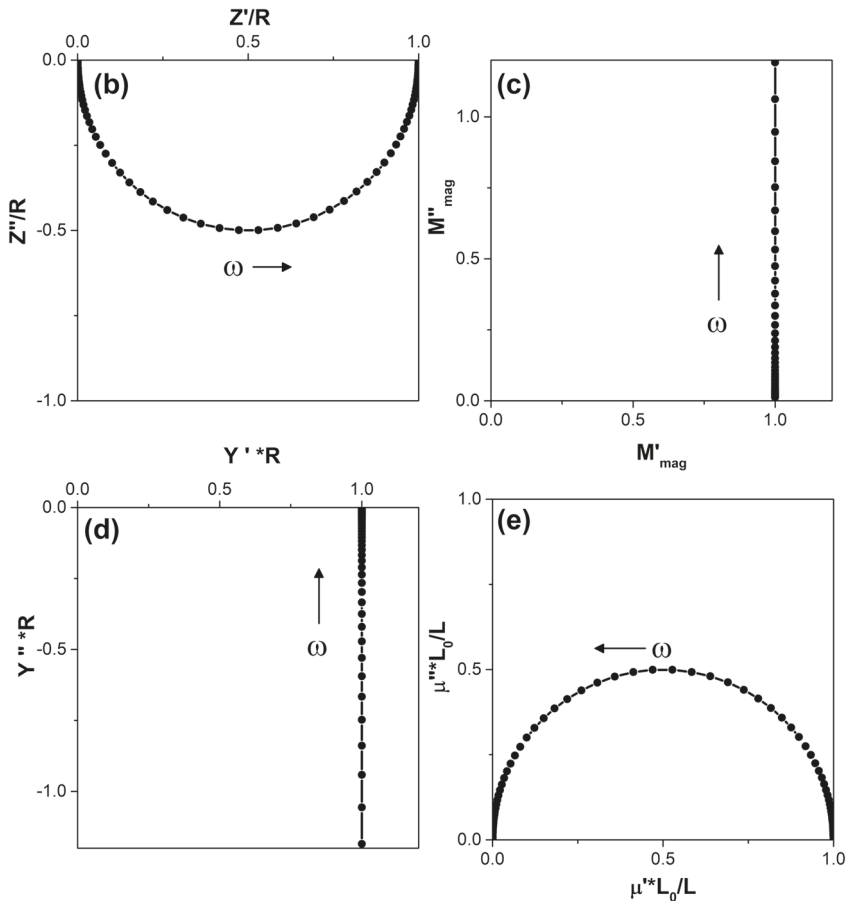
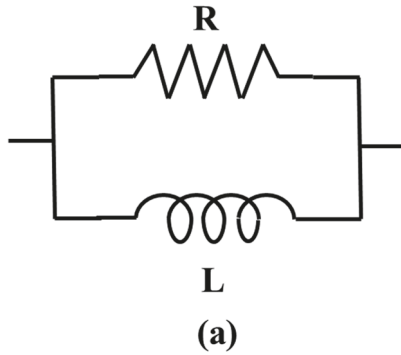


FIGURE 4.14 (a) A parallel combination of R and L. Plots of (b) Z''/R versus Z'/R , (c) $M''_{mag}/(L_0/L)$ versus $M'_{mag}/(L_0/L)$. (d) $Y''*R$ versus $Y'*R$. (e) $\mu''*L_0/L$ versus $\mu'*L_0/L$. (Reproduced with Permission from CSIR-NIScPR Delhi, Katare et al. 1999, Figure 1, A Novel Approach Based on Impedance Spectroscopy for Measurement of Magnetic Permeability of Ceramics, Indian Journal of Engineering and Materials Sciences, 6: 34–42.)

$$\mu = \frac{z}{j\omega L_0} = \frac{z' - jz''}{j\omega L_0} = \mu' - j\mu'' \quad (4.132)$$

where L_0 is the inductance of the coil with no sample inside, and μ is the magnetic permeability of the material. (Note: the quantity μ has been expressed as $\mu = \mu' - j\mu''$ as done by von Hippel 1954).

From these equations we get

$$\mu' = -\frac{z''}{\omega L_0} = \frac{1}{\omega L_0} \frac{\omega L R^2}{R^2 + (\omega L)^2} = \frac{1}{L_0} \frac{L R^2}{R^2 + (\omega L)^2} = \frac{L}{L_0} \frac{1}{1 + \left(\frac{\omega L}{R}\right)^2} \quad (4.133)$$

$$\mu'' = \frac{z'}{\omega L_0} = \frac{1}{\omega L_0} \frac{(\omega L)^2 R}{R^2 + (\omega L)^2} = \frac{L}{L_0} \frac{\left(\frac{\omega L}{R}\right)}{1 + \left(\frac{\omega L}{R}\right)^2} \quad (4.134)$$

In analogy with the dielectric case, a magnetic modulus can be defined as

$$\begin{aligned} \text{Magnetic modulus } M_{\text{mag}} &= (\mu)^{-1} = \frac{1}{\frac{z}{j\omega L_0}} = \frac{j\omega L_0}{z} \\ &= j\omega L_0 Y = j\omega L_0 \left(\frac{1}{R} + \frac{1}{j\omega L} \right) \end{aligned} \quad (4.135)$$

$$= \frac{L_0}{L} + j \frac{\omega L_0}{R} = M'_{\text{mag}} + jM''_{\text{mag}} \quad (4.136)$$

which gives

$$M'_{\text{mag}} = \frac{L_0}{L}, M''_{\text{mag}} = \frac{\omega L_0}{R} \quad (4.137)$$

The limiting values of the immittance functions as $\omega \rightarrow 0$ and $\omega \rightarrow \infty$ are given by

$$Z'|_{\omega \rightarrow 0} = 0, Z'|_{\omega \rightarrow \infty} = R, Z''|_{\omega \rightarrow 0} = 0, Z''|_{\omega \rightarrow \infty} = 0 \quad (4.138)$$

$$Y'|_{\omega \rightarrow 0} = \frac{1}{R}, Y'|_{\omega \rightarrow \infty} = \frac{1}{R}, Y''|_{\omega \rightarrow 0} = -\infty, Y''|_{\omega \rightarrow \infty} = -0 \quad (4.139)$$

$$\mu' \Big|_{\omega \rightarrow 0} = \frac{L}{L_0}, \mu' \Big|_{\omega \rightarrow \infty} = 0, \mu'' \Big|_{\omega \rightarrow 0} = 0, \mu'' \Big|_{\omega \rightarrow \infty} = 0 \quad (4.140)$$

$$M'_{mag} \Big|_{\omega \rightarrow 0} = \frac{L_0}{L}, M'_{mag} \Big|_{\omega \rightarrow \infty} = \frac{L_0}{L}, M''_{mag} \Big|_{\omega \rightarrow 0} = 0, M''_{mag} \Big|_{\omega \rightarrow \infty} = \infty \quad (4.141)$$

Also, μ' and μ'' satisfy the relation

$$\mu'^2 + \mu''^2 = \left(\frac{1}{L_0} \frac{LR^2}{R^2 + (\omega L)^2} \right)^2 + \left(\frac{1}{\omega L_0} \frac{(\omega L)^2 R}{R^2 + (\omega L)^2} \right)^2 \quad (4.142)$$

$$\begin{aligned} &= \frac{1}{L_0^2} \frac{1}{(R^2 + (\omega L)^2)^2} (L^2 R^4 + \omega^2 L^4 R^2) \\ &= \frac{1}{L_0^2} \frac{1}{(R^2 + (\omega L)^2)^2} (L^2 R^2)(R^2 + (\omega L)^2) \end{aligned} \quad (4.143)$$

$$= \frac{1}{L_0^2} \frac{1}{R^2 + (\omega L)^2} L^2 R^2 = \frac{L}{L_0} \left(\frac{1}{L_0} \frac{LR^2}{R^2 + (\omega L)^2} \right) = \frac{L}{L_0} \mu' \quad (4.144)$$

or

$$\left(\mu' - \frac{1}{2} \frac{L}{L_0} \right)^2 + \mu''^2 = \left(\frac{1}{2} \frac{L}{L_0} \right)^2 \quad (4.145)$$

This is the equation of a circle having radius equal to $(1/2)(L/L_0)$ and center at the point $(L/(2L_0), 0)$ on the μ'' versus μ' plot. As μ' and μ'' are positive quantities [see Eqs. (4.133) and (4.134)], this plot would be a semicircle passing through the origin, would have an intercept equal to L/L_0 at the μ' axis at the low-frequency side and traverse from right to left, in the first quadrant. Also, the maximum value of μ'' occurs at a frequency where $\omega L/R = 1$, i.e. at a frequency given by inverse of the time constant.

Normalized complex plane plots are shown in Figures 4.14(b–e).

4.15 A SERIES COMBINATION OF R AND L

A series combination of inductor L and resistance R is shown in Figure 4.15(a).

The expressions for various immittance functions are given as

$$Z = Z' - jZ'' = R + j\omega L \quad (4.146)$$



(a)

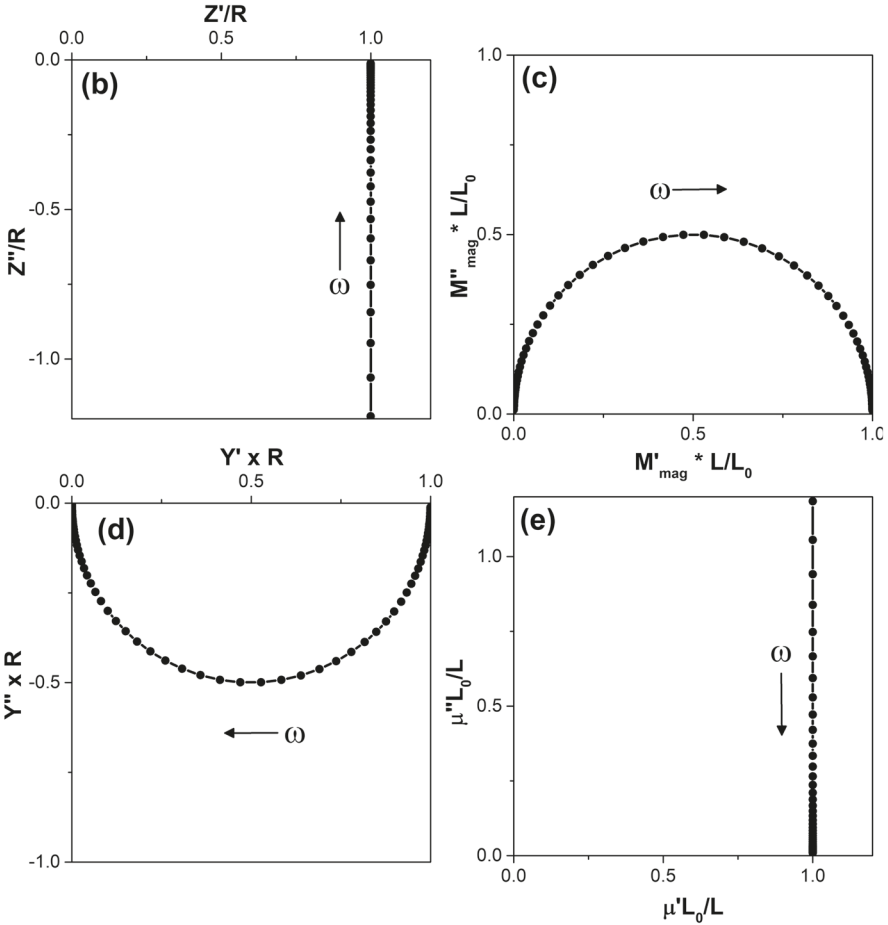


FIGURE 4.15 (a) A series combination of R and L. Plots of (b) Z''/R versus Z'/R , (c) $M''_{mag} * L/L_0$ versus $M'_{mag} * L/L_0$, (d) $Y'' * R$ versus $Y' * R$, (e) $\mu'' * L_0/L$ versus $\mu' * L_0/L$. (Reproduced with Permission from CSIR-NIScPR Delhi, Katere et al. 1999, Figure 2, A Novel Approach Based on Impedance Spectroscopy for Measurement of Magnetic Permeability of Ceramics, Indian Journal of Engineering and Materials Sciences, 6: 34–42.)

$$Z' = R, Z'' = -\omega L \quad (4.147)$$

$$Y' = \frac{R}{R^2 + (\omega L)^2}, Y'' = -\frac{\omega L}{R^2 + (\omega L)^2} \quad (4.148)$$

$$\mu' = -\frac{Z''}{\omega L_0} = \frac{L}{L_0}, \mu'' = \frac{Z'}{\omega L_0} = \frac{R}{\omega L_0} \quad (4.149)$$

$$\text{Magnetic modulus } M_{\text{mag}} = (\mu)^{-1} = \frac{1}{\mu} = \frac{1}{\frac{Z}{j\omega L_0}} = \frac{j\omega L_0}{Z} = j\omega L_0 Y \quad (4.150)$$

$$= j\omega L_0 (Y' + jY'') = M'_{\text{mag}} + jM''_{\text{mag}} \quad (4.151)$$

$$M'_{\text{mag}} = -\omega L_0 Y'' = L_0 \frac{\omega^2 L}{R^2 + (\omega L)^2},$$

$$M''_{\text{mag}} = \omega L_0 Y' = \omega L_0 \frac{R}{R^2 + (\omega L)^2} \quad (4.152)$$

The limiting values are given as

$$Z'|_{\omega \rightarrow 0} = R, Z'|_{\omega \rightarrow \infty} = R, Z''|_{\omega \rightarrow 0} = 0, Z''|_{\omega \rightarrow \infty} = -\infty \quad (4.153)$$

$$Y'|_{\omega \rightarrow 0} = \frac{1}{R}, Y'|_{\omega \rightarrow \infty} = 0, Y''|_{\omega \rightarrow 0} = 0, Y''|_{\omega \rightarrow \infty} = 0 \quad (4.154)$$

$$\mu'|_{\omega \rightarrow 0} = \frac{L}{L_0}, \mu'|_{\omega \rightarrow \infty} = \frac{L}{L_0}, \mu''|_{\omega \rightarrow 0} = \infty, \mu''|_{\omega \rightarrow \infty} = 0 \quad (4.155)$$

$$M'_{\text{mag}}|_{\omega \rightarrow 0} = 0, M'_{\text{mag}}|_{\omega \rightarrow \infty} = \frac{L_0}{L}, M''_{\text{mag}}|_{\omega \rightarrow 0} = 0, M''_{\text{mag}}|_{\omega \rightarrow \infty} = 0 \quad (4.156)$$

The simulated plots are shown in Figures 4.15(b–e).

4.16 A PARALLEL COMBINATION $R_1 L_1$ CONNECTED IN SERIES WITH R_2 AND L_2

Figure 4.16(a) shows a parallel combination $R_1 L_1$ connected in series with R_2 and L_2 .

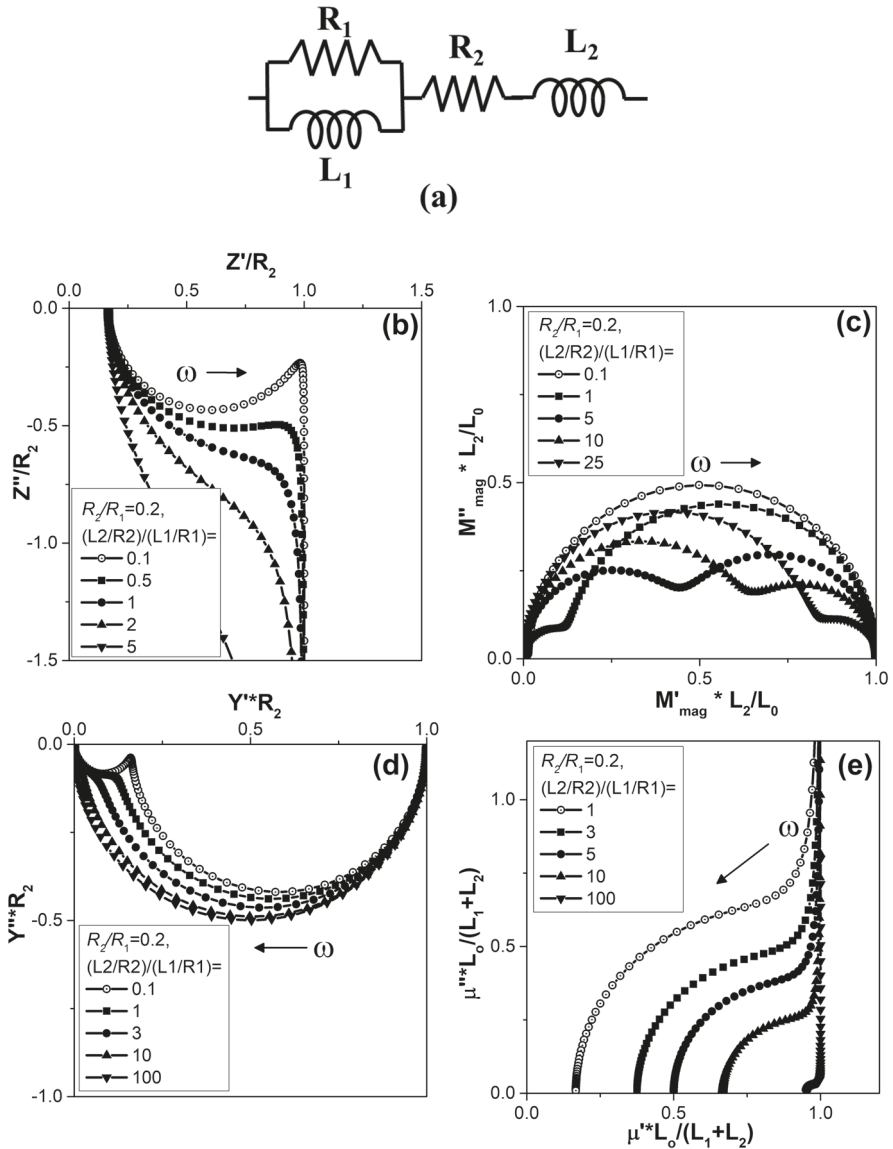


FIGURE 4.16 (a) A parallel R_1L_1 combination connected in series with resistance R_2 and inductor L_2 . Normalized plots of (b) Z''/R_2 versus Z'/R_2 (c) $M''L_2/L_0$ versus $M'L_2/L_0$ (d) $Y''R_2$ versus $Y'R_2$ and (e) $\mu''L_0/(L_1+L_2)$ versus $\mu'L_0/(L_1+L_2)$ for various values of resistances and time constants. (Reprinted with Permission from CSIR-NIScPr Delhi, Katare et al. 1999, Figure 4, A Novel Approach Based on Impedance Spectroscopy for Measurement of Magnetic Permeability of Ceramics, Indian Journal of Engineering and Materials Sciences, 6: 34–42.)

The impedance is given by

$$Z' = \frac{\left(\omega \frac{L_1}{R_1}\right)^2 R_1}{1 + \left(\omega \frac{L_1}{R_1}\right)^2} + R_2, Z'' = - \left\{ \frac{\left(\omega \frac{L_1}{R_1}\right)^2 R_1}{1 + \left(\omega \frac{L_1}{R_1}\right)^2} + \omega L_2 \right\} \quad (4.157)$$

The limiting values of the immittance functions are given below

$$Z'|_{\omega \rightarrow 0} = R_2, Z'|_{\omega \rightarrow \infty} = R_1 + R_2, Z''|_{\omega \rightarrow 0} = -0, Z''|_{\omega \rightarrow \infty} = -\infty \quad (4.158)$$

$$Y'|_{\omega \rightarrow 0} = \frac{1}{R_2}, Y'|_{\omega \rightarrow \infty} = 0, Y''|_{\omega \rightarrow 0} = 0, Y''|_{\omega \rightarrow \infty} = 0 \quad (4.159)$$

$$M'_{mag}|_{\omega \rightarrow 0} = 0, M'_{mag}|_{\omega \rightarrow \infty} = \frac{L_0}{L_2}, M''_{mag}|_{\omega \rightarrow 0} = 0, M''_{mag}|_{\omega \rightarrow \infty} = 0 \quad (4.160)$$

$$\mu'|_{\omega \rightarrow 0} = \frac{L_1 + L_2}{L_0}, \mu'|_{\omega \rightarrow \infty} = \frac{L_2}{L_0}, \mu''|_{\omega \rightarrow 0} = \infty, \mu''|_{\omega \rightarrow \infty} = 0 \quad (4.161)$$

Complex plane plots are shown in Figures 4.16(b–e).

4.17 SERIES R_1C_1 IN PARALLEL WITH SERIES R_2C_2 AND R_3

Figure 4.17(a) shows Series R_1C_1 in parallel with series R_2C_2 and R_3 .

Expression for $Y = Y' + jY''$ is given as

$$Y' = \frac{1}{R_3} + \frac{1}{R_1} \frac{(\omega C_1 R_1)^2}{1 + (\omega C_1 R_1)^2} + \frac{1}{R_2} \frac{(\omega C_2 R_2)^2}{1 + (\omega C_2 R_2)^2} \quad (4.162)$$

$$Y'' = \frac{1}{R_1} \frac{\omega C_1 R_1}{1 + (\omega C_1 R_1)^2} + \frac{1}{R_2} \frac{\omega C_2 R_2}{1 + (\omega C_2 R_2)^2} \quad (4.163)$$

The limiting values of the immittance functions are given below

$$Z'|_{\omega \rightarrow 0} = R_3, Z'|_{\omega \rightarrow \infty} = \frac{1}{1/R_3 + 1/R_1 + 1/R_2}, Z''|_{\omega \rightarrow 0} = 0, Z''|_{\omega \rightarrow \infty} = 0 \quad (4.164)$$

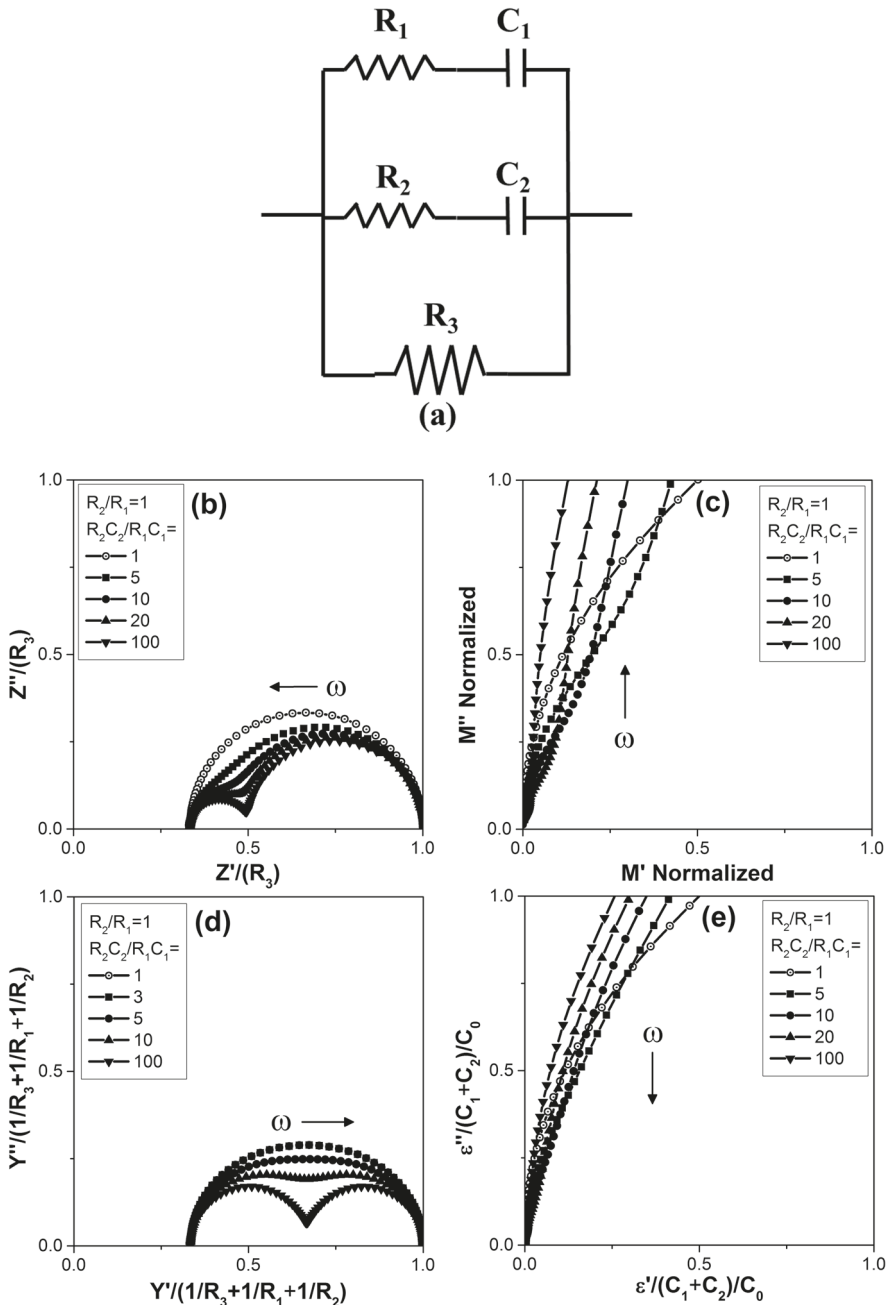


FIGURE 4.17 (a) Series R_1C_1 in parallel with series R_2C_2 and R_3 . Normalized plots of (b) Z''/R_3 versus Z'/R_3 (c) $M''_{\text{normalized}}$ versus $M'_{\text{normalized}}$ normalization done by using limiting value of M' as $\omega \rightarrow \infty$, (d) $Y''/(1/R_3+1/R_1+1/R_2)$ versus $Y'/(1/R_3+1/R_1+1/R_2)$ and (e) $\epsilon''/((C_1+C_2)/C_0)$ versus $\epsilon'/(C_1+C_2)/C_0$ for various values of resistances and time constants.

$$M'_{|\omega \rightarrow 0} = 0, M'_{|\omega \rightarrow \infty} = \frac{C_0}{C_1} \left(\frac{\frac{1}{R_1}}{\frac{1}{R_3} + \frac{1}{R_1} + \frac{1}{R_2}} \right)^2 + \frac{C_0}{C_2} \left(\frac{\frac{1}{R_2}}{\frac{1}{R_3} + \frac{1}{R_1} + \frac{1}{R_2}} \right)^2 \quad (4.165)$$

$$M''_{|\omega \rightarrow 0} = 0, M''_{|\omega \rightarrow \infty} = \infty \quad (4.166)$$

$$Y'_{|\omega \rightarrow 0} = \frac{1}{R_3}, Y'_{|\omega \rightarrow \infty} = \frac{1}{R_3} + \frac{1}{R_1} + \frac{1}{R_2}, \quad (4.167)$$

$$Y''_{|\omega \rightarrow 0} = 0, Y''_{|\omega \rightarrow \infty} = 0$$

$$\varepsilon'_{|\omega \rightarrow 0} = \frac{C_1 + C_2}{C_0}, \varepsilon'_{|\omega \rightarrow \infty} = 0, \varepsilon''_{|\omega \rightarrow 0} = \infty, \varepsilon''_{|\omega \rightarrow \infty} = 0 \quad (4.168)$$

The complex plots of the immittance functions are shown in Figures 4.17(b–e).

4.18 A SERIES COMBINATION R_1 - L_1 - C_1 CONNECTED IN PARALLEL WITH C_2

Figure 4.18(a) shows a series combination of resistance R_1 , inductor L_1 and capacitor C_1 connected in series with another capacitor C_2 .

For this circuit we get

$$\frac{1}{z} = Y = Y' + jY'' = \frac{1}{R_1 + j\omega L_1 + \frac{1}{j\omega C_1}} + \frac{1}{\frac{1}{j\omega C_2}} \quad (4.169)$$

which yields

$$Y' = \frac{R_1}{R_1^2 + \left(\omega L_1 - \frac{1}{\omega C_1} \right)^2}, Y'' = \frac{-\left(\omega L_1 - \frac{1}{\omega C_1} \right)}{R_1^2 + \left(\omega L_1 - \frac{1}{\omega C_1} \right)^2} + \omega C_2 \quad (4.170)$$

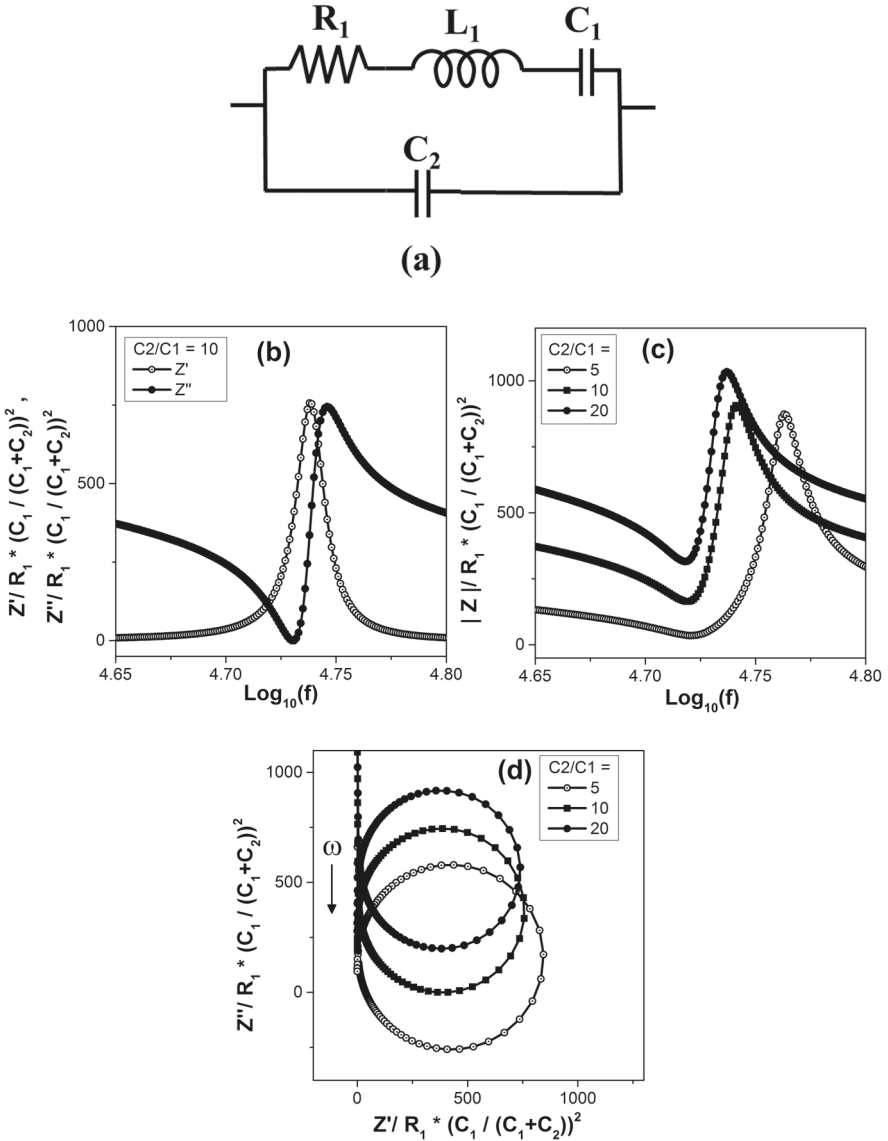


FIGURE 4.18 (a) A series combination of resistance R_1 , inductor L_1 and capacitor C_1 connected in parallel with another capacitor C_2 . Normalized plots of (b) $Z'/(R_1(C_1/(C_1+C_2))^2)$ and $Z''/(R_1(C_1/(C_1+C_2))^2)$ versus $\log_{10}(f)$. (c) $|Z|/(R_1(C_1/(C_1+C_2))^2)$ versus $\log_{10}(f)$ (d) $Z''/(R_1(C_1/(C_1+C_2))^2)$ versus $Z'/(R_1(C_1/(C_1+C_2))^2)$ (e) $M'/(C_0/C_2)$ and $M''/(C_0/C_2)$ versus $\log_{10}(f)$. (f) $|M|/(C_0/C_2)$ versus $\log_{10}(f)$. (g) $M'/(C_0/C_2)$ versus $M''/(C_0/C_2)$ (h) $Y'/(1/R_1)$ and $Y''/(1/R_1)$ versus $\log_{10}(f)$ (i) $|Y|/(1/R_1)$ versus $\log_{10}(f)$. (j) $Y''/(1/R_1)$ versus $Y'/(1/R_1)$. (k) $\epsilon'/((C_1+C_2)/C_0)$ and $\epsilon''/((C_1+C_2)/C_0)$ versus $\log_{10}(f)$. (l) $|\epsilon|/((C_1+C_2)/C_0)$ versus $\log_{10}(f)$. (m) $\epsilon''/((C_1+C_2)/C_0)$ versus $\epsilon'/((C_1+C_2)/C_0)$ for various values of C_2/C_1 .

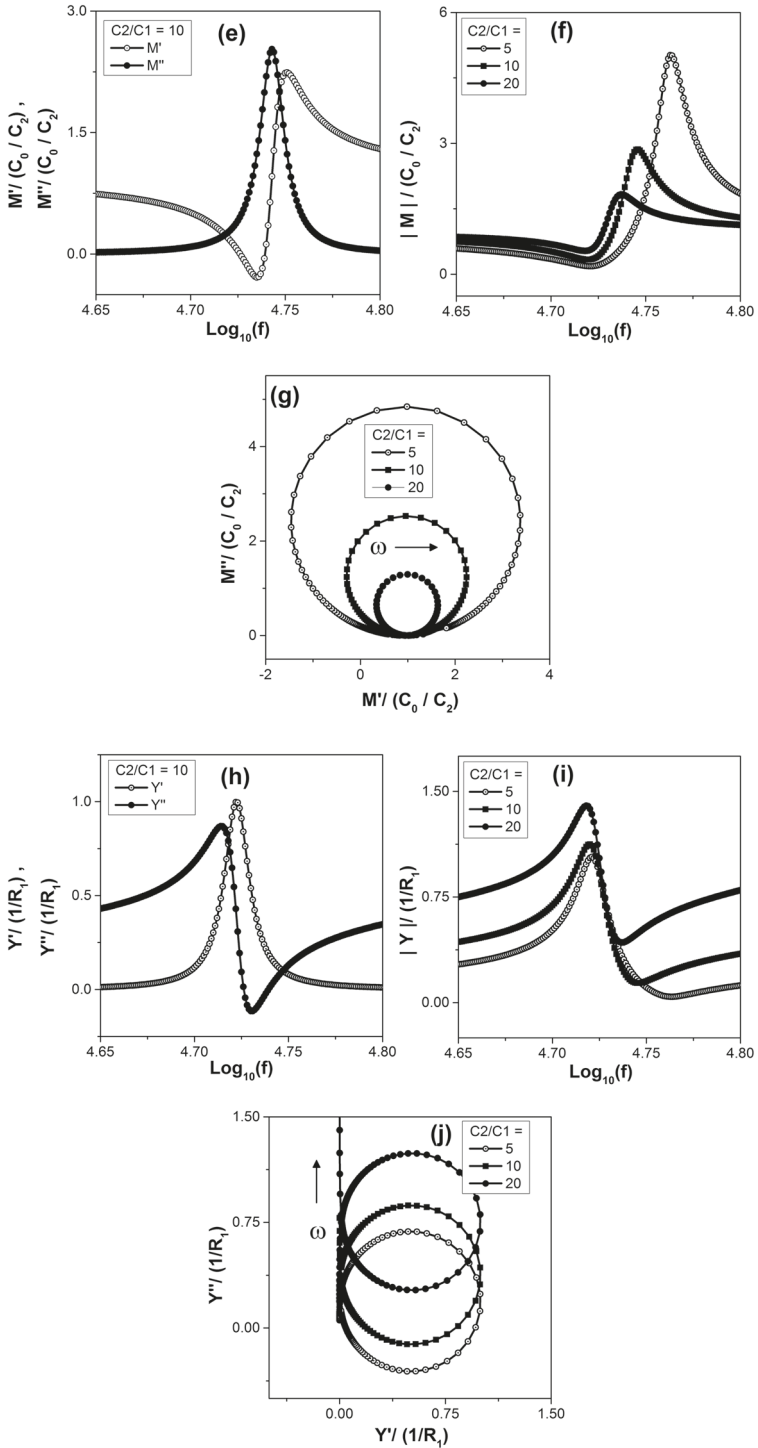


FIGURE 4.18 (Continued)

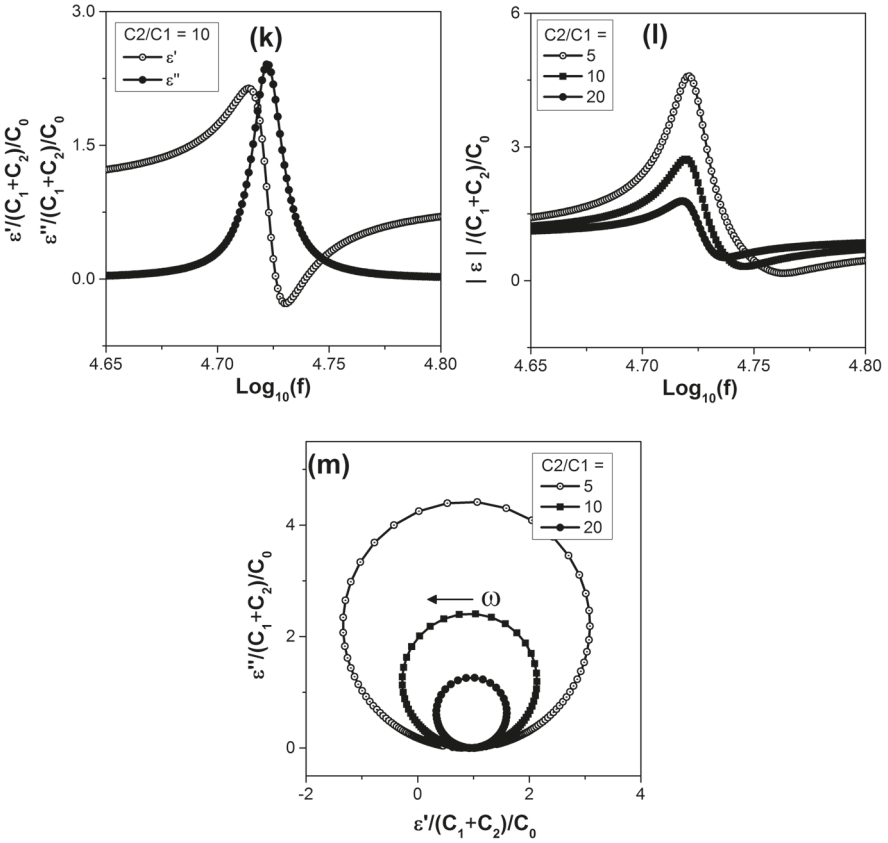


FIGURE 4.18 (Continued)

Real and imaginary parts of $Z = Z' - jZ''$ are given as

$$Z' = \frac{R_1}{\left[1 - \omega C_2 \left(\omega L_1 - \frac{1}{\omega C_1}\right)\right]^2 + [\omega C_2 R_1]^2} \tag{4.171}$$

$$Z'' = \frac{\omega C_2 \left(\omega L_1 - \frac{1}{\omega C_1}\right)^2 - \left(\omega L_1 - \frac{1}{\omega C_1}\right) + \omega C_2 R_1^2}{\left[1 - \omega C_2 \left(\omega L_1 - \frac{1}{\omega C_1}\right)\right]^2 + [\omega C_2 R_1]^2} \tag{4.172}$$

Other immittance functions are obtained by using $M = M' + jM''$ and $\varepsilon = \varepsilon' - j\varepsilon''$ as

$$M' = \omega C_0 Z'', M'' = \omega C_0 Z', \varepsilon' = Y''/(\omega C_0) \text{ and } \varepsilon'' = Y'/(\omega C_0) \text{ as usual.}$$

The values of the immittance functions as $\omega \rightarrow 0$ and $\omega \rightarrow \infty$ are given below

$$Z'|_{\omega \rightarrow 0} = R_1 \left(\frac{C_1}{C_1 + C_2} \right)^2, Z'|_{\omega \rightarrow \infty} = 0, Z''|_{\omega \rightarrow 0} = \infty, Z''|_{\omega \rightarrow \infty} = 0 \quad (4.173)$$

$$Y'|_{\omega \rightarrow 0} = 0, Y'|_{\omega \rightarrow \infty} = 0, Y''|_{\omega \rightarrow 0} = 0, Y''|_{\omega \rightarrow \infty} = \infty \quad (4.174)$$

$$M'|_{\omega \rightarrow 0} = \frac{C_0}{C_1 + C_2}, M'|_{\omega \rightarrow \infty} = \frac{C_0}{C_2}, M''|_{\omega \rightarrow 0} = 0, M''|_{\omega \rightarrow \infty} = 0 \quad (4.175)$$

$$\varepsilon'|_{\omega \rightarrow 0} = \frac{C_1 + C_2}{C_0}, \varepsilon'|_{\omega \rightarrow \infty} = \frac{C_2}{C_0}, \varepsilon''|_{\omega \rightarrow 0} = 0, \varepsilon''|_{\omega \rightarrow \infty} = 0 \quad (4.176)$$

It is to be mentioned that this the most accepted equivalent circuit model for piezoelectric materials (Cady 1946; Moulson and Herbert 2003; Chaitanya 2008, Chaitanya et al. 2011). A piezoelectric material, e.g. quartz, is one in which applied mechanical stress creates electric polarization, and conversely, applied electric field creates mechanical strain. This is exploited in variety of device applications such as gas igniters, high-frequency acoustic generators, filters, etc. The mechanical vibrations of the piezoelectric can be studied by representing it as a spring-mass system, i.e. as an object of mass m connected to a spring and placed in a damping medium. The motion of m is described by the equation

$$m \frac{d^2x}{dt^2} + r \frac{dx}{dt} + kx = F \quad (4.177)$$

where, r is a positive constant related to damping and loss and known as dissipation factor, k is the spring constant, with kx being the restoring force, and F is the applied force, which, for piezoelectrics, is equal to voltage multiplied by electromechanical coupling coefficient. This mechanical model can be represented by an electrical series LCR circuit as well. The flow of charge q in a series LCR (here it is L_1, C_1, R_1) circuit is described by

$$L_1 \left(\frac{d^2q}{dt^2} \right) + R_1 \left(\frac{dq}{dt} \right) + \frac{1}{C_1} q = V \quad (4.178)$$

Looking at the similarity of these equations, the behavior of a piezoelectric is represented by a series LCR circuit. L_1 , C_1 and R_1 are electrical equivalents of the mechanical properties of the piezoelectric crystal (The Radio Amateur Handbook 1968, p 51). The inductance L_1 corresponds to the inertial component related to displacement of mass m . The resistance R_1 corresponds to energy dissipation due to friction. The capacitance C_1 corresponds to the energy stored in the spring. In practice, the piezoelectric is placed between two electrodes giving a capacitance C_2 . Thus, equivalent circuit model of a piezoelectric becomes a series $L_1C_1R_1$ circuit connected in parallel to C_2 . The values of these parameters can be calculated by solving the wave equation and using the values of dielectric permittivity, density, dimensions of the piezoelectric crystal, etc. Also, by knowing the values of circuit components, the material parameters can be calculated (Buttry and Ward 1992; Moulson and Herbert 2003).

When the frequency is varied, the impedance shows a minimum at a certain frequency f_{\min} and a maximum at a frequency f_{\max} . Resonance occurs at two frequencies: one called the series resonance frequency f_r ($\omega_r = 2\pi f_r$), where $j\omega L_1 = 1/(j\omega C_1)$, and the other one called the parallel resonance frequency f_p ($\omega_p = 2\pi f_p$), where currents flowing in the two arms are antiphase, i.e. where $(j\omega L_1 + 1/j\omega C_1 = 1/j\omega C_2)$. Thus, we have $\omega_r^2 = 1/(L_1 C_1)$ and $\omega_p^2 = (1/C_1 + 1/C_2)/L_1$ for low R_1 . This may be viewed as L_1 resonating with C_1 in the first case and resonating with the series combination of C_1 and C_2 in the second case (Buttry and Ward 1992; Moulson and Herbert 2003).

The behavior of this equivalent circuit is displayed in detail near the resonance frequency. Let us analyze this near the series resonance frequency $\omega_r = 1/\sqrt{L_1 C_1}$. It can be shown that values of Z' and Z'' at frequencies close to ω_r are given by

$$Z' = \frac{R_1}{(1 - C_2 L_1 2\omega_r \delta\omega)^2 + (\omega C_2 R_1)^2} \quad (4.179)$$

$$Z'' = \frac{1}{\omega_r C_2} \frac{-1 + \omega_r C_2 L_1 2\delta\omega}{(1 - C_2 L_1 2\omega_r \delta\omega)^2 + (\omega_r C_2 R_1)^2} \quad (4.180)$$

where the approximation, $\omega + \omega_r \sim 2\omega_r$ and $\omega - \omega_r \sim \delta\omega$, has been used. It can be shown that Z' and Z'' satisfy the following relation (Chaitanya 2008; Chaitanya et al. 2014)

$$\left[Z' - \frac{1}{2} \left(\frac{1}{\omega_r C_2} \right)^2 \frac{1}{R_1} \right]^2 + \left[Z'' - \frac{1}{\omega_r C_2} \right]^2 = \left[\frac{1}{2} \left(\frac{1}{\omega_r C_2} \right)^2 \frac{1}{R_1} \right]^2 \quad (4.181)$$

Thus, Z'' versus Z' plot would be a circle with center at $((1/2) (1/\omega_r C_2)^2 (1/R_1), 1/(\omega_r C_2))$ and radius equal to $(1/2) (1/\omega_r C_2)^2 (1/R_1)$. Similarly, it is found that real and imaginary parts of Y , M and ϵ satisfy the following relations

$$\left(Y' - \frac{1}{2R_1}\right)^2 + (Y'' - \omega_r C_2)^2 = \left(\frac{1}{2R_1}\right)^2 \quad (4.182)$$

$$\left(M' - \frac{C_0}{C_2}\right)^2 + \left(M'' - \frac{1}{2} \frac{C_0}{C_2} \frac{1}{\omega_r C_2 R_1}\right)^2 = \left(\frac{1}{2} \frac{C_0}{C_2} \frac{1}{\omega_r C_2 R_1}\right)^2 \quad (4.183)$$

$$\left(\epsilon' - \frac{C_2}{C_0}\right)^2 + \left(\epsilon'' - \frac{1}{\omega_r C_2 R_1}\right)^2 = \left(\frac{1}{2} \frac{1}{\omega_r C_2 R_1}\right)^2 \quad (4.184)$$

Using the limiting values of ϵ' and ϵ'' or of M' and M'' and value of C_0 , values of C_1 and C_2 can be estimated. The value of R_1 can be estimated by noting the coordinates of the circle obtained from Y'' versus Y' plot or ϵ'' versus ϵ' plot and the resonance frequency. Simulated immittance patterns are shown in Figures 4.18(b–m). As this circuit is used to represent piezoelectrics as well, plots of modulus of immittance values as function of frequency are also given. When an alternating voltage is applied, a piezoelectric material behaves as a normal dielectric, but as the frequency of the voltage reaches the resonance frequency of the piezoelectric, the amplitude of the mechanical vibrations increases and the electrical impedance shows a specific behavior. As this circuit shows resonance, it is worth observing the variations in the immittance functions plots near the resonance frequency. It can be seen that knowledge of C_0 and limiting values of ϵ would yield estimates for C_1 and C_2 . Also complex plane plots of Y'' versus Y' at frequencies close to resonance would yield a circle with center as $(1/(2R_1), (\omega_r C_2))$ and radius at $1/(2R_1)$. Values of L_1 can be estimated from the resonance frequencies.

Inclusion of inductor in equivalent circuit models have been found to be useful in representing data where complex plane plots show loops (Guerrero et al. 2021; Chaitanya 2008)

It may be mentioned that this circuit model has been useful in developing single-coil nuclear magnetic resonance (NMR) sample probes where the NMR radiofrequency pulses are fed across C_2 and NMR signals are received by connecting the high gain receiver across C_2 . The routine 50- Ω transmitter–sample probe–signal receiver tuning in the NMR equipment is achieved by adjusting the values of C_1 and C_2 where C_2 is much higher than C_1 and the sample is housed in the coil L_1 (Fukushima and Roeder 1981). This circuit has also been used for detecting and studying piezoelectric ringing of samples during solid-state pulsed NMR investigations (Hughes and Pandey 1984; Pandey and Hughes 1984).

A computer program in GW BASIC is given in Appendix A1 for an easy visualization of the progress of Z'' versus Z' plots for a model in slow pace.

Problem 4.1 Consider a parallel $R_p C_p$ circuit. Obtain the values of resistance R_s and capacitance C_s for the corresponding equivalent series $R_s C_s$ circuit and vice versa.

Problem 4.2 Show that a parallel R-CPE equivalent circuit gives a depressed arc in the Z'' versus Z' plot.

Problem 4.3 Obtain the values of resonance frequencies for the equivalent circuit model 4.18.

SUMMARY

Various useful equivalent circuit models comprising R, C, CPE and L elements have been considered. Expressions for impedance and limiting values of all the four immittance functions for $\omega \rightarrow 0$ and $\omega \rightarrow \infty$ and their complex plane plots are given. Need for inclusion of CPE arises to model systems showing depressed arcs in the Nyquist plots. Inductive elements are included when systems under investigation are magnetic, piezoelectric, possess large contributions from current flows inside or from leads. A small computer program written in GW BASIC is given in Appendix A1 for creating the plots to help beginners observe the progress of plots at a slow pace as frequency ω is varied.

5 Analysis of Experimental Data

5.1 EQUIVALENT CIRCUIT MODELING AND DATA ANALYSIS

The purpose of analysis of the immittance data is to develop understanding about various charge transfer processes present in the system. This is facilitated by representing the system by an equivalent circuit model. A charge transfer process can be represented by a RC circuit, to begin with. The equivalent circuit model may comprise combinations of R, C, L and CPE elements. In this technique, depending on the possible charge transfer processes thought to be present in the material, suitable equivalent circuits are chosen to represent the electrical behavior by comparing the experimental plots with the simulated ones for various model circuits. Usually, combinations of resistances (R) and capacitances (C) suffice for dielectrics, combinations of R and inductance L suffice for magnetic systems and combinations of R, L and C suffice for ferro-/piezoelectrics (Macdonald 2005; Jonscher 1983; Sinclair and West 1994; Pandey et al. 1995; Katare et al. 1999; Katare 1997; Chaitanya 2009; Chaitanya et al. 2014; Chaitanya et al. 2015; Chaitanya et al. 2011; Pandey et al. 1997; Pandey et al. 1998; Maiti and Basu 1986; Kumar et al. 2005). Sometimes, it is found that the lumped-component type of models do not yield good fits and their simulated patterns do not show even qualitative resemblance with the experimental plots. The situation is then rescued by assuming presence of distributed components and/or resorting to constant phase angle elements (CPEs) connected in a suitable way in the model circuit (Macdonald 2005; Jonscher 1983).

A general practice is to choose one parallel RC circuit to represent one process and add further RCs in series to represent the other processes. Thus, a simple equivalent circuit model for representing grain-grain boundary-electrode system may comprise three parallel RCs connected in series. Choice of a suitable model is a difficult process, becoming more so since several models can be found that show the same behavior (Macdonald 2005; Pandey et al. 1995). However, attempts are made to choose a simple equivalent circuit model, to start with. This is greatly facilitated by comparing the experimental plots with simulated ones and keeping in mind the charge transfer/polarization processes thought to be possibly present in the system (Macdonald 2005; Jonscher 1983; Sinclair and West 1994; Pandey et al. 1995; Katare et al. 1999; Katare 1997; Chaitanya 2009; Chaitanya et al. 2014; Chaitanya et al. 2015; Chaitanya et al. 2011; Pandey 1998). In what follows, some extremely useful

hints for choosing a model to represent experimental results are summarized (Pandey et al. 2017, 2019a; Pandey 2018)

- i. Study of a system based on the information conveyed by only one of the four immittance functions might lead to erroneous conclusions and two or more functions, viz impedance (Z) and modulus (M) or admittance (Y) and permittivity (ϵ), should be looked at (Pandey et al. 1995; Chaitanya et al. 2015).
- ii. Appearance of clear semicircular arc in both Z and M complex plane plots indicates that the experimental data may be modeled by a single parallel RC circuit (Macdonald 2005; Pandey et al. 1995).
- iii. A semicircle in Z'' versus Z' plot and a little depressed looking arc in M'' versus M' plot or vice versa indicate that the model may comprise at least two parallel RC's (say R_1C_1 and R_2C_2) in series with ratios of time constants, R_2C_2/R_1C_1 , in the range of 1 to 5 (Pandey et al. 1995). Appearance of two clear semicircular arcs indicates presence of two processes.
- iv. A semicircular arc with a steeply rising branch (not a linear) at low-frequency side in Z'' versus Z' plot and a shifted arc in the corresponding M'' versus M' plot indicate that a series C should be included in the model (Pandey et al. 1998).
- v. A semicircular arc with a steeply rising branch (not a linear) at high-frequency side in M'' versus M' plot and a shifted arc in Z'' versus Z' plot indicate the presence of series R in the equivalent circuit (Pandey et al. 1995).
- vi. A semicircular arc with a changed sign of Z'' in the whole frequency range in Z'' versus Z' plot points toward the possible presence of parallel RL circuits (Katare et al. 1999).
- vii. From an experimental Z'' versus Z' plot showing a crossover from positive values of Z'' to negative values or vice versa within the overall frequency range covered in the experiment presence of all R, L and C is inferred. Z'' becomes zero at the crossover frequency indicating occurrence of resonance (Macdonald 2005; Chaitanya et al. 2014; Chaitanya et al. 2011).
- viii. A linear portion in the Z'' versus Z' or/and other immittance plots may indicate the presence of a series CPE in the model (Macdonald 2005, Katare et al. 2003). A depressed semicircular Z'' versus Z' plot may indicate the presence of parallel R-CPE, whereas depressed semicircular Y'' versus Y' plot indicates presence of series R-CPE in the model (Macdonald 2005; Casciola and Fabiani 1983).
- ix. A shift toward right in Z'' versus Z' plot indicates presence of series resistance in the model, whereas a right shift in Y'' versus Y' plot indicates presence of overall parallel resistance in the model.

A glance at all the immittance plots of the experimental data obtained for different variables, such as composition and temperature, collectively together, and keeping in mind the hints listed above is found to be of great help in choosing a model (Chaitanya et al. 2011). Once the model has been chosen, the values of the components are estimated by comparing the experimental plots with the simulated ones. The values

are determined more accurately by using these as initial guesses in a complex non-linear least square (CNLS) fitting procedure (Macdonald 2005; Pandey 1992). When the fittings are poor, the model is modified, keeping in mind the possibilities of processes present/dormant, emerging or dominating in the system under study as the variables are altered. In the situations where two or more models seem physically feasible, the model to be accepted is the one that gives the lowest value of the sum of squares of errors in the CNLS runs (Macdonald 2005).

For usual dielectric materials, models involving lumped resistive (R) and capacitive (C) components suffice, whereas for magnetic or piezoelectric materials, inductive (L) elements are also included (Macdonald 2005; Katare et al. 1999; Chaitanya et al. 2014; Chaitanya et al. 2011). For the cases where the experimental impedance data cannot be represented by equivalent circuit models based on lumped circuit elements (i.e. the CNLS does not show a good fit), presence of certain distributed elements or CPEs is invoked (Macdonald 2005). A CPE is a mathematical realization of a system in which the phase angle between applied ac voltage and resulting current remains independent of the frequency (Macdonald 2005).

There are various viewpoints for the possible sources of such a behavior. However, larger consensus leans toward the belief that the CPE behavior arises due to the presence of distribution in time constants in the material–electrode systems. This is one of the reasons for the widespread use of CPE in impedance spectroscopy (Macdonald 2005; Orazem et al. 2013; Boukamp et al. 2004; Dissado and Hill 1988; Hirschorn et al. 2010; Lario-Garcia and Pallas-Areny 2006). Therefore, when good fits are achieved by using models involving CPE, it is concluded that the system at hand possesses distribution in certain properties.

Development of equivalent circuit model is illustrated by taking Example 5.1. For getting an easy and quick hands on experience, only Z' and Z'' are considered.

Example 5.1

The values of Z' and Z'' observed in an impedance spectroscopic measurements on a system are given in Table 5.1. Develop an equivalent circuit model representing this behavior.

Solution:

The complex plane plot (Z'' vs Z') is shown in Figure 5.1(c).

It is seen that

1. The curve has two humps that look like depressed arcs. A depressed semi-circular arc in Z'' versus Z' plot may be, in general, represented by a parallel R-CPE combination. Thus two such combinations in series may be used. Let us denote these as R_1 -CPE₁ and R_2 -CPE₂.
2. Also, the curve does not pass through the origin and appears shifted toward right, indicating the presence of series resistance, say R_3 .

Therefore, an equivalent circuit shown schematically in Figure 5.1(a) may be used to represent the data.

TABLE 5.1
Values of real and imaginary parts Z' and Z'' ($Z = Z' - jZ''$) at various frequencies

Sr No	Frequency (in Hertz, Hz)	Z' (in Ohms)	Z'' (in Ohms)
1	100	14294.93	872.97
2	150	14063.08	1065.70
3	200	13858.25	1211.23
4	300	13605.77	1416.86
5	500	12953.98	1645.76
6	700	12534.82	1756.32
7	1000	12061.08	1824.12
8	1500	11515.91	1834.66
9	2000	11143.72	1804.62
10	3000	10661.16	1729.06
11	5000	10139.67	1627.68
12	7000	9844.49	1589.63
13	10,000	9558.23	1598.45
14	15,000	9236.44	1691.24
15	20,000	8985.365	1817.98
16	30,000	8551.81	2077.43
17	50,000	7781.05	2469.58
18	70,000	7106.59	2676.11
19	100,000	6285.71	2753.1
20	150,000	5346.46	2603.35
21	200,000	4761.21	2363.58
22	300,000	4120.34	1928.50
23	500,000	3609.77	1378.44
24	700,000	3407.79	1071.90
25	1000,000	3268.95	808.24

Now we proceed to get the values of the components of the model. This may be done by comparing the plot of Figure 5.1(c) with the simulated plots shown in Chapter 4. The impedance of a CPE is given by inverse of $A_0(j\omega)^n$. Thus, the parameters to be estimated are R_1, A_{01}, n_1 for R_1 -CPE₁ and R_2, A_{02}, n_2 for R_2 -CPE₂, and series resistance R_3 . From the shift in the plot, we get $R_3 \sim 3000 \Omega$. We draw two tentative semicircular arcs, one each for the humps, as shown Figure 5.1(c). Let us assume that R_1 -CPE₁ and R_2 -CPE₂ correspond to higher and lower frequencies, respectively. The intercept with the Z' axis at the lowest-frequency side at point B_3 gives the values of $R_3+R_1+R_2$. In the middle, at B_2 , the intercept gives the value of R_3+R_1 , and at high-frequency side, at B_1 , it gives the value of R_3 . A rough estimate of these can be obtained by looking at Table 5.1 as well as by observing the occurrence of maximum and minimum values of Z'' . As the frequency increases [we traverse from right to left in Figure 5.1(c)], value of Z'' starts increasing, showing a maximum around 1500 Hz, then starts decreasing showing a minimum around 7 kHz (which corresponds to $Z' = 9844 \Omega$) and again increases, showing maximum at 100

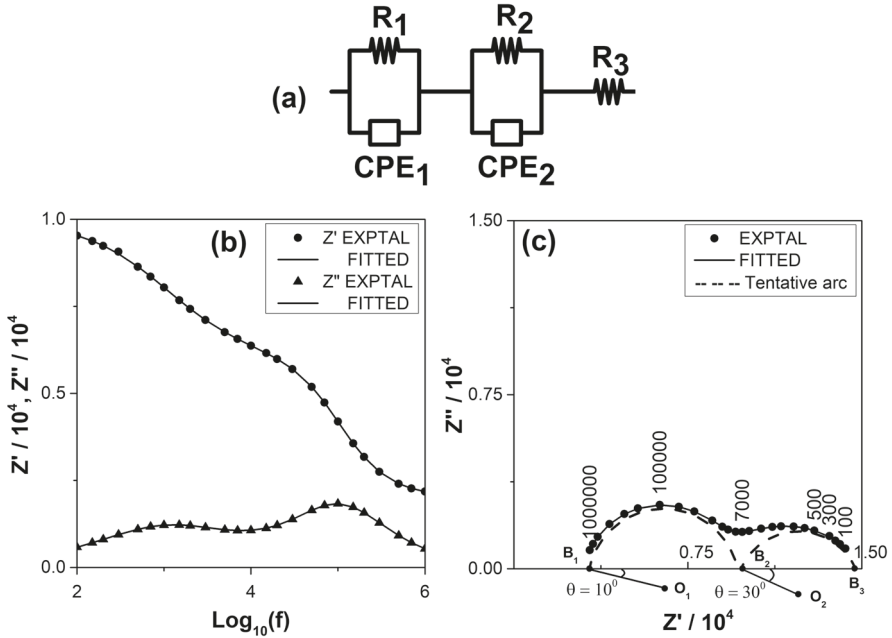


FIGURE 5.1 (a) Equivalent circuit model, (b) experimental and fitted values for Z' , Z'' versus $\log f$ and (c) experimental and fitted values for Z' versus Z'' , frequencies corresponding to certain points also shown. The dashed arcs are tentative depressed circular arcs used to obtain initial guesses of the parameters.

kHz. Thus, $R_3+R_1+R_2 \sim 15,000 \Omega$, $R_3+R_1 \sim 9000 \Omega$, i.e. $R_1 \sim 6000 \Omega$, $R_2 \sim 6000 \Omega$ and $R_3 \sim 3000 \Omega$. Had the arcs been not depressed, i.e. n_1 and n_2 were equal to one, the parallel combination R_1 -CPE₁ would behave like a parallel combination R_1C_1 , where C_1 is equal to A_{01} , and the parallel combination R_2 -CPE₂ would behave like a parallel combination R_2C_2 , where C_2 is equal to A_{02} . Now, at the peak of the hump at lower-frequency side, we will have $\omega_2R_2C_2 = 1$ which gives

$$C_2 = \frac{1}{\omega_2R_2} = \frac{1}{2\pi \times 1500 \times 6000} = 1.768 \times 10^{-8} \text{ F} \tag{5.1}$$

Similarly

$$C_1 = \frac{1}{\omega_1R_1} = \frac{1}{2\pi \times 100000 \times 6000} = 2.653 \times 10^{-10} \text{ F} \tag{5.2}$$

We may let $A_{01} \sim C_1$ and $A_{02} \sim C_2$ to begin with. The value of the angle θ_1 between Z' axis and the line B_1O_1 is nearly 10° , which gives $n_1 (= 1 - \theta_1/90)$. Similarly, the angle

θ_2 between Z' axis and the line B_2O_2 is nearly 30° , which gives $n_2 (= 1 - \theta_2/90)$, where O_1 and O_2 are the centers of the R_1 -CPE $_1$ and R_2 -CPE $_2$ arcs, respectively.

Thus, the estimated values of the parameters are

$$R_1 = 6000 \Omega, A_{01} = 2.65 \times 10^{-10} \text{ F}, \theta_1 = 10^\circ \quad (5.3)$$

$$R_2 = 6000 \Omega, A_{02} = 1.77 \times 10^{-8} \text{ F}, \theta_1 = 30^\circ \quad (5.4)$$

$$R_3 = 3000 \Omega, \quad (5.5)$$

The values of A_{01} and A_{02} can also be estimated by using the values of n_1 and n_2 and the relations $\omega_2 \tau_2 = 1$, $\omega_1 \tau_1 = 1$, $(\tau_1)^{n_1} = A_{01} R_1$ and $(\tau_2)^{n_2} = A_{02} R_2$. These are approximate values obtained graphically, which can be determined more accurately by using CNLS program. For running a CNLS program, the expressions for Z' and Z'' given in Section 4.10 may be used where a term R_3 is added to the expression for Z' . These expressions are reproduced in Eq. (5.6) and (5.7).

$$Z' = R_3 + \frac{R_1 \left(1 + A_{01} R_1 \omega^{n_1} \cos \left(\frac{n_1 \pi}{2} \right) \right)}{\left(1 + A_{01} R_1 \omega^{n_1} \cos \left(\frac{n_1 \pi}{2} \right) \right)^2 + \left(A_{01} R_1 \omega^{n_1} \sin \left(\frac{n_1 \pi}{2} \right) \right)^2} + \frac{R_2 \left(1 + A_{02} R_2 \omega^{n_2} \cos \left(\frac{n_2 \pi}{2} \right) \right)}{\left(1 + A_{02} R_2 \omega^{n_2} \cos \left(\frac{n_2 \pi}{2} \right) \right)^2 + \left(A_{02} R_2 \omega^{n_2} \sin \left(\frac{n_2 \pi}{2} \right) \right)^2} \quad (5.6)$$

$$Z'' = \frac{R_1 A_{01} R_1 \omega^{n_1} \sin \left(\frac{n_1 \pi}{2} \right)}{\left(1 + A_{01} R_1 \omega^{n_1} \cos \left(\frac{n_1 \pi}{2} \right) \right)^2 + \left(A_{01} R_1 \omega^{n_1} \sin \left(\frac{n_1 \pi}{2} \right) \right)^2} + \frac{R_2 A_{02} R_2 \omega^{n_2} \sin \left(\frac{n_2 \pi}{2} \right)}{\left(1 + A_{02} R_2 \omega^{n_2} \cos \left(\frac{n_2 \pi}{2} \right) \right)^2 + \left(A_{02} R_2 \omega^{n_2} \sin \left(\frac{n_2 \pi}{2} \right) \right)^2} \quad (5.7)$$

By using the software IMPSPEC.BAS developed in our laboratory (Pandey 1992), the correct values are obtained as

$$\begin{aligned}
 R_1 &= (6006.55 \pm 6.91) \text{ Ohms}, & A_{01} &= (2.50 \pm 0.008) \times 10^{-10} \text{ Farad}, \\
 & & \theta_1 &= (10.02 \pm 0.14)^0, & n_1 &= 0.889 \pm 0.001 \\
 R_2 &= (5996.03 \pm 11.37) \text{ Ohms}, & A_{02} &= (2.50 \pm 0.01) \times 10^{-8} \text{ Farad} \\
 & & \theta_2 &= (29.90 \pm 0.14)^0, & n_2 &= (0.668 \pm 0.001) \\
 R_3 &= (3000.60 \pm 5.21) \text{ Ohms},
 \end{aligned} \tag{5.8}$$

It may be mentioned that the example given earlier only illustrates how an equivalent circuit model may be proposed and the values of parameters determined. The improvements in the model and the interpretation of the parameters depends on what system is being studied and what might be various phases and interfaces. For further improvements in model, plots using other formalisms, such as M'' versus M' , may be looked at. The commercially available softwares use their built-in functions corresponding to the models chosen.

5.2 COMPLEX NONLINEAR LEAST SQUARES PROCEDURE

Sometimes, set of experimental data points (x_i, y_i) ($i = 1$ to N) can be represented by a functional relation of the form $y = mx + c$, where m and c are constants. In this relation, m and c appear in a linear way. Some dataset can be represented by some functional relation, say, $y = ax^b$, where a and b are constants. This relation can be written as $\ln(y) = \ln(a) + b \ln(x) = a_1 + b \ln(x)$, where $a_1 = \ln(a)$, in which constants a_1 and b appear in a linear way. These constants can be obtained by fitting the dataset to such relations by using method of least squares. As the parameters to be determined appear in a linear way, the least square procedure falls in the category of linear least squares. Some dataset may seem to be represented by a relation of the form (or predicted by some theoretical considerations), say, $y = a_0 + a_1 \exp(-a_2 t) + a_3 \exp(-a_4 t)$. Here, the parameters appear in a nonlinear way and the relation cannot be put in a form where the parameters appear in a linear way. The least squares procedure to obtain the values of these parameters is called nonlinear least squares. In the examples considered above, the dataset comprises values y_i measured at given inputs x_i , i.e. one type of dependent variable y and one independent variable x . In impedance spectroscopy we measure Z' and Z'' for various given frequencies ω . So we have two dependent variables and one independent variable. As Z' and Z'' are real and imaginary components of complex function Z measured under a sinusoidal excitation, the least square procedure is termed as CNLS. It is known that real and imaginary components are related through Kronig–Kramers relations, which tell that if values of one of the real or imaginary parts are known over all frequencies, the value of the other part can be obtained at any frequency. So, it may seem that fitting of only real or imaginary part should suffice. However, in Kronig–Kramers calculations

frequencies up to infinity are considered, and in actual experiments finite frequency regions are used and, therefore, both Z' and Z'' are simultaneously fitted (Macdonald 1987). The sum of squares of residuals (differences in calculated and experimental values) to be minimized is given by

$$\chi^2 = \sum_{i=1}^N \left\{ \begin{array}{l} \text{weight}'_i \left[Z'_i \text{ (calculated)} - Z'_i \text{ (experimental)} \right]^2 \\ + \text{weight}''_i \left[Z''_i \text{ (calculated)} - Z''_i \text{ (experimental)} \right]^2 \end{array} \right\} \quad (5.9)$$

where weight'_i and weight''_i are weights for the values of Z' and Z'' at i th frequency ω_i . The weights can be assigned to equal to $1/(\sigma'_i)^2$ and $1/(\sigma''_i)^2$, where σ'_i and σ''_i are the standard deviations in the i th value Z'_i and Z''_i , respectively. The sum χ^2 is our goodness of fit parameter. χ^2 is minimized with respect to all the parameters a_1, a_2, a_3, a_4 , etc. (i.e. R_1, C_1, R_2, C_2 , etc.) by following the procedure of nonlinear least squares and choosing initial guesses for R_1, C_1, R_2, C_2 , etc. from the experimental graphs, getting corrections to these initial values and repeating the process with the new corrected set of values of parameters till desired convergence is achieved. It is advisable that initial values of the parameters should be carefully estimated by looking at the experimental plots and limiting values of the immittance function corresponding to the chosen model, otherwise iterations fall around some local minima, delaying speedy and proper convergence. The linear least squares and nonlinear least squares procedures are briefly described in Appendix A2.

5.3 ELECTRODE EFFECTS

A sample holder design was described in Chapter 3. This is a two-probe setup and is generally used for dielectrics, electroceramics, etc. For samples having relatively higher conductivity three-probe or four-probe setups are useful. In the four-probe setup, the outer electrodes carry current, and voltage is measured across the middle electrodes. For impedance measurements on electrolytes, the sample holder (electrochemical cell) has electrodes named as working electrode, reference electrode and counter electrode. Working electrode is the designation for the electrode being studied. In corrosion experiments, this is usually the material that is corroding. Otherwise, this is made of some inert material such as gold, platinum or carbon. The counter electrode is usually made of platinum or carbon and forms the working electrode-counter electrode pair for completing the current path. Reference electrodes are electrodes that serve as experimental reference points for potential (sense) measurements and are usually made of a conducting material such as silver/silver chloride, mercury/mercury (mercurous) oxide, etc. For liquid electrolytes the electrodes are immersed in the electrolyte. For solids, there may be solid electrolyte or no electrolyte. In a four-probe arrangement, the cell would have working electrode-counter electrode pair that carries current and two electrodes, called working sense electrode and reference electrode, used for voltage measurement. This arrangement may be used to measure impedance across some solution-phase interface, such as a membrane, liquid-liquid

junction or surface of some material by placing the sense electrode on one side and the reference electrode on the other side of the interface.

By connecting the working electrode and working sense electrode together and the other two, namely, reference electrode and counter electrode together, a four-probe setup becomes a two-electrode setup. In a two-electrode experiment the voltage dropped by the current across the whole electrochemical cell is measured. This setup measures impedance between the working electrode and the counter electrode. Two-electrode setups have been found to be suitable when precise control of the potential across the electrochemical interface is not critical and has been used for electrochemical energy devices (e.g. batteries, fuel cells, supercapacitors, etc.), where investigation on electrolyte properties, such as conductivity, is important.

When the working electrode and working sense electrodes are the same (i.e. joined together) and the reference electrode is not connected to the counter electrode, but placed near the working electrode, it becomes a three-electrode setup. Since the absolute potential of a single electrode cannot be measured, all potential measurements, in electrochemical systems, are performed with respect to a reference electrode. The potential of the reference electrode should remain constant during the course of the measurement. The impedance is measured between the working electrode and the reference electrode. This arrangement is useful in studies related to changes occurring near the working electrode.

The impedance measurements may be carried out at a fixed dc potential (the so-called potentiostatic mode). For this, a small sinusoidal ac voltage signal superimposed on a dc potential is applied to the cell and measurements are done. Similarly, measurements may be carried out at fixed dc current (the so-called galvanostatic mode), where a small sinusoidal ac current superimposed on a dc current is used (www.gamry.com, www.ecochemie.nl)

Experimental limitations and instrumental artifacts due to electrodes in impedance spectroscopic measurements have been discussed in detail by Hsieh et al. (1996a, 1996b, 1997) and Hwang et al. (1997).

It was shown that three-point measurements are susceptible to voltage divider distortion artifacts if the reference electrode impedance approaches the analyzer input impedance. These effects can be removed by using reference electrode having low-input impedance or using an instrument with high-input impedance. The accuracy of three-point impedance measurements and electrode impedances depends on the geometry and placement of the reference electrode. Electrode impedances are accurately measured as long as electrode spacing is much larger than the diameter of the probe and the current is not disturbed by the presence of reference electrode. For electroceramic samples the impedance measurements may lead to erroneous conclusions if electrode–solid sample interface has spreading resistances and gap capacitance that arise due to improper contacts because of poor polishing. Due to this, distorted arcs may appear in the complex plane plots that might be erroneously considered as two arcs representing grain and grain boundary or some other contributions. This can be avoided by fine polishing and electroding the sample by using sputtering (Hwang et al. 1997).

In two-probe measurements voltage applied to the electrodes gives rise to a current that passes through the cables, electrodes, contacts and sample. The measured

impedance will then be that of all these combined. A method was proposed to remove the electrode and cable contributions (Pandey et al. 1996).

This method involves two steps: (a) impedance measurements are carried out over the desired frequency range, placing the solid pellet between the parallel plates as usual (see Figure 3.1); and (b) the experiment is repeated keeping the gap between the electrodes and other variables same as before in (a) but without the sample in place. Complex plane plots (Z'' vs Z') are obtained and an equivalent circuit model, and functional dependence representing the behavior, is developed. This function is then used to subtract the electrode and cable contributions from the measured impedance values in (a). This corrected data are then used for further analysis.

Electrodes made from different materials may affect the real sample behavior. This may be exploited for better applications also. The effects of different electrode materials like Ag, In, In-Ga and Ni on the positive temperature coefficient of resistance (PTCR) behavior of doped polycrystalline BaTiO_3 was systematically studied by using impedance spectroscopy. The contact resistance was exceptionally high for Ag and In, but negligible in case of either In-Ga or Ni (Basu and Maiti 1986).

An equivalent circuit model consisting of a resistance R_b (representing the bulk), a parallel combination $R_{gb}-C_{gb}$ (representing grain boundary) and another parallel combination R_E-C_E (representing electrode interface) connected in series was used for analyzing the data. It was found that the best PTC effect was observed in 0.3 atom% Sb-doped BaTiO_3 with Ni electrode.

The electrical behavior of strontium titanate borosilicate glass ceramics ($\text{SrO} \cdot \text{TiO}_2 \cdot 2\text{SiO}_2 \cdot \text{B}_2\text{O}_3$) with additives K_2O , La_2O_3 , CoO and Nb_2O_5 was studied by using impedance spectroscopy as a function of temperature and composition. An equivalent circuit model comprising three parallel RC combinations (R_1C_1 , R_2C_2 and R_3C_3) and a capacitor C_4 all connected in series represented the data well. A glass ceramic sample comprises crystalline regions, uncrystallized glassy matrix, interface regions between the crystallites and surrounding glass and can be modeled by three parallel RC circuits, R_1C_1 , R_2C_2 and R_3C_3 , connected in series. Thus, a glass ceramic-electrode system can then be modeled by four parallel RC circuits, R_1C_1 , R_2C_2 , R_3C_3 and R_4C_4 , connected in series, where R_4C_4 is representing the sample-electrode interface. As a capacitor connected in parallel to a resistor of large value is effectively a capacitor only, C_4 was assigned to represent the sample-electrode interface. The values of components of the model were obtained by using CNLS fitting of the immittance data. It was found that when the glass ceramic sample contained only SrTiO_3 crystalline phase and the remaining glassy matrix, the sample-electrode interface capacitance C_4 showed an Arrhenius type of nature with an activation energy (0.11 ± 0.04) eV (eV is short form of electron volts), and when the glass ceramic sample contained a number of crystalline phases, no clear trend appeared (Chaitanya et al. 2015).

Similar results were obtained with iron-doped BaTiO_3 samples also. The ceramic samples utilized were (i) $\text{BaFexTi}_{1-x}\text{O}_3$ ($x = 3\%$, containing predominant tetragonal phase and a small amount of hexagonal phase) and (ii) $\text{BaFexTi}_{1-x}\text{O}_3$, ($x = 5\%$, containing almost equal amounts of hexagonal and tetragonal phases). The impedance spectroscopic studies were carried in the frequency range of 20 Hz–1 MHz and in the temperature range of 450–650 K. The impedance data above the ferroelectric-paraelectric transition temperature (393 K) could be well represented by four parallel

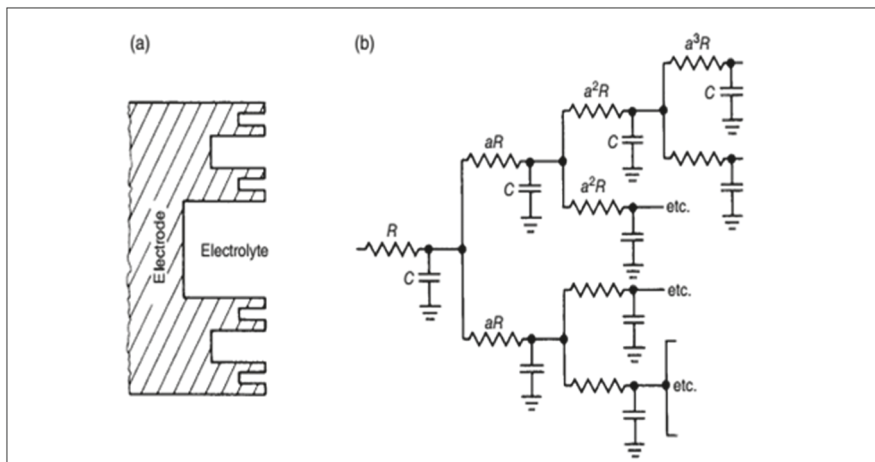


FIGURE 5.2 (a) Formal model for a fractal electrode-electrolyte interface and (b) an equivalent circuit that models the double-layer charging behavior. (Reprinted with Permission from John Wiley & sons, Barsoukov and Macdonald 2018, Figure 2.1.20, Impedance Spectroscopy: Theory, Experiment, and Applications, Third Edition).

RC combinations connected in series. The time constant (R_4C_4) corresponding to the sample-electrode interface showed Arrhenius behavior when the sample contained predominantly single phase. It was conjectured that sample-electrode behavior may be used to infer whether a given solid sample is a single phase or comprises more than one phases (Pandey et al. 2018a).

The impedance pattern of a system is influenced by the surface behavior of electrodes (Macdonald 2005). Rough and porous electrodes may be modeled by treating the pores as V-shaped grooves and applying transmission line analogies of distributed circuit components. A rough electrode surface may be modeled as a fractal entity as shown schematically in Figure 5.2(a). The equivalent circuit corresponding to such an interface is shown in Figure 5.2(b).

Role of electrodes are extremely important in performance of high-energy Li-ion batteries useful for electrical vehicles and other applications. This is governed by the reactions occurring at electrode-electrolyte interface. Understanding the effect of electrode-electrolyte interface on the kinetics of electrode reaction is critical to design high-energy batteries, and an intensive research activity is being witnessed at present (Tatara R. et al. 2019).

SUMMARY

Analysis of experimental data is carried out by proposing an equivalent circuit model for the system under investigation keeping in view various charge transfer processes possibly present. A charge transfer process may be represented by one parallel RC circuit, and further such circuits are connected for more processes. Thus, a single-phase ceramic sandwiched between two electrodes may be represented, to begin with, by

three parallel RC circuits connected in series corresponding to grain, grain boundary and sample–electrode contact. Choice of a suitable model is greatly facilitated by comparing the experimentally observed patterns with those simulated for different models. A right shift in Z'' versus Z' plot indicates that a series resistance should be included in the model. Similarly, a right shift in M'' versus M' plot indicates that a series capacitance should be inserted in the model. A little depressed semicircular Z'' versus Z' plot indicates that at least two series-connected parallel RC circuits having time constants close to each other within a factor 5 may be considered as a possible model. For a depressed Z'' versus Z' arc, a parallel R-CPE may be chosen, and so on. Values of the components of the model are estimated by comparing the experimental plots with simulated ones. Their values are determined more accurately by fitting the data to the chosen model by CNLS procedure, using the estimated values as initial guesses. These are further utilized to extract values of material properties such as conductivity, permittivity, etc., which are further plotted as function of variables like temperature, composition, etc., to study the behavior of material. Impedance spectroscopy is highly useful in the study of sample–electrode contact behavior and can be utilized to enhance certain properties. It was found that the best positive temperature coefficient of resistance was displayed by 0.3 atm% Sb-doped ferroelectric BaTiO_3 when Ni electrodes were used. It has been also demonstrated that study of sample–electrode contact behavior may be used to infer whether the sample is a single-phase or multiphase material.

6 Applications

Impedance spectroscopy is a nondestructive and easy-to-implement technique for study of materials. The technique essentially involves measurement of electrical impedance (Z) and the phase difference (θ) between the applied ac voltage and the resulting current in the system under investigation as a function of frequency. This is presented in an easy-to-handle way in the form of real part ($Z' = Z \cos \theta$) and imaginary part ($Z'' = Z \sin \theta$) of impedance ($Z = Z' - jZ''$). The analysis of the data is carried out by using suitable equivalent circuit models representing the observed impedance behavior. Due to ready availability of versatile impedance analyzers working over extended frequency regions, the technique has found increasing widespread applications encompassing ceramics, polymers, corrosion, agriculture, biosciences, medical diagnostics, dairy, petroleum, etc. A common thread in all the applications is the representation of the system by a suitable equivalent circuit model that would mimic the experimentally measured electrical impedance behavior over the given frequency range. Development of such a model is a difficult process and is greatly facilitated by comparing the experimental plots with those simulated for various model circuits and keeping in mind all possible charge transfer processes present in the system and hints given in Chapter 5. With a view to just give an exposure to the beginner, few simple applications of impedance spectroscopy in various fields are briefly described in this chapter with emphasis on equivalent circuit modeling. Before giving the impedance spectroscopic details, a short introduction to related systems is also presented. Keeping in view the highly diverse background of scholars keen to apply impedance spectroscopy to their work, the presentation has been kept as simple as possible, and preferably more qualitative. For detailed studies of various applications, the reader may look into the references cited there in and in books by Barsoukov and Macdonald (2005) and others.

6.1 CERAMICS AND GLASS CERAMICS

The word ceramic is derived from “keramos”, the Greek word for potter’s clay or ware made from clay and fired. The earlier notion of ceramics as being a material related to clay and pottery has undergone modifications, and ceramics, at present, are defined as inorganic nonmetallic materials that have acquired mechanical strength

through a firing process. These are generally polycrystalline oxides and nitrides. However, the term ceramic now encompasses all inorganic materials including single crystals as well. Thus, structural clay products, pottery, porcelain, cement, glasses, nonmetallic magnetic materials, etc. all are ceramics. Due to ease of preparation, processing, shaping and several technologically useful properties, today, ceramics are the most important beginning materials for device applications such as a capacitor, thermistor, fuel cell, battery, microwave filter, chemical sensor, actuator, etc. Depending on their applications various names have been given, viz ceramics whose thermal insulating properties are exploited are called refractories, ceramics whose electrical properties are used are called electroceramics, etc. (Kingery et al. 1976; Moulson and Herbert 2003).

The polycrystalline ceramics can be visualized as aggregate of small crystallites called grains joined in a random way. The joining regions, called the grain boundary, have strained bonds due to mismatch. The properties of grain boundaries are, therefore, different from those of the grains. The overall properties of a ceramic stem from contributions from grains and grain boundaries. In ceramics, the properties of grains may be altered by changing the ingredients, whereas those of grain boundary may be altered by changing the processing variables. By using suitable processing strategies, such as heating/cooling rates, presence/absence of oxygen during thermal treatment, etc., ceramics can be made to exhibit certain properties that are not possible in single crystal form. It is the interplay of grain and grain boundary contributions that bestows upon ceramics variety of technologically useful properties. How to control this interplay so that the ceramic may possess desired and reproducible properties is one of the most intense activities in current ceramics research.

When a solid is heated beyond its melting point, a liquid called melt is obtained. When this melt is rapidly cooled so that crystallization is suppressed, a material having viscosity approaching that of solids is obtained. This material is called glass and can be visualized as something like a snapshot of a liquid where the substance is a solid but the structure is like a liquid (no long-range order), i.e. a liquid where the kinetic movements have been suddenly frozen by rapid cooling without giving sufficient time for rearrangement of entities to yield a long-range order (crystalline). The glass is, thus, also equivalently called a supercooled liquid. A glass, therefore, is a material in metastable state. When suitable heat treatment is given, glass gets crystallized and gives rise to the so called glass ceramic. Glass ceramics are polycrystalline materials produced by the controlled crystallization (devitrification) of a glass. Glass ceramics are pore-free materials where grains are crystalline and the grain boundary would comprise uncrystallized glass and is a very important technological material.

The overall properties of ceramics are governed by contributions from grain and grain boundary behaviors. The development of ceramics having desired and reproducible properties is greatly facilitated by separating out the grain and grain boundary contributions. This may be achieved by using impedance spectroscopic studies. Vast literature is available on impedance spectroscopy of ceramics (Moulson and Herbert 2003; Barsoukouvand Macdonald 2005; Jonscher 1983). Impedance spectroscopy has been applied for the study of electroceramics by various groups such as of West (Irvine et al. 1990).

Impedance measurements are performed by placing the ceramic sample in contact with electrodes (usually sandwiching the solid pellet between two electrodes in the two-probe arrangement) [see Figure 2.5(a)], and impedance spectroscopic analysis is carried out by representing the material by an equivalent circuit representing the electrical behavior of grains, grain boundary and sample–electrode interface. It may be vaguely visualized that charge gets two paths to reach the other electrode: one is through the continuous grain boundary phase and the other via a path going through grain–grain boundary–grain chain. A simplified view of this is presented in the so-called brick wall model of ceramic microstructure where the grains are assumed to be cubes with their faces parallel to the electrode plates and separated from each other by the surrounding continuous grain boundary as shown schematically in Figure 2.5(b) (Waser and Hagenbeck 2000; Waser 1999; Barsoukov and Macdonald 2005; Wang 2001). Usually, the grain boundaries are less conductive and the continuous path provides a larger impedance and this model reduces to that shown in Figure 2.5(c). It has been found that this brick wall model works reasonably well for cases where grain boundary has uniform property throughout the sample and grains have uniform distribution. This model, shown in Figure 2.5(c) and reproduced here for quick reference as Figure 6.1, is now routinely used, to begin with, for representing grain–grain boundary–electrode system in a ceramic (Pandey 2018; Pandey et al. 2019b; Upadhyay 2013). Suitable modifications are made in this model to account for observed impedance behavior and to include other possible charge transfer routes in ceramic samples. For example, in the case of wet ceramic sample, a RC circuit representing the current flow through the surface water layer may be connected in parallel to the series combination of Figure 6.1 (Katare et al. 2005).

Impedance spectroscopy has emerged as a powerful nondestructive tool for the study of the electrical properties and microstructure of ionic-, electronic- or mixed-conductor ceramics and the detection of structural defects in ceramics, especially in zirconia-based materials and cementitious materials (Lanfredi and Rodrigues 1999; Kleitz et al. 1995; McCarter et al. 1988; Wang 2001).

Ease of measurement, low cost of equipment and portability, adaptation to online manufacturing environment without stopping/slowing down the process have made impedance spectroscopy very popular in the area of ceramics. As described earlier, impedance spectroscopy probes electrical impedance of the material. Therefore, conduction behavior of a ceramics, including contributions from different phases, can

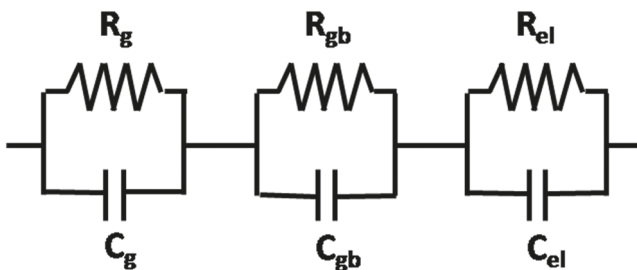


FIGURE 6.1 A general equivalent circuit model of a ceramic system.

be studied (Pandey et al. 2018b). For example, preparation of clay-based objects, such as porcelain, involves formation of liquid phase during heating which becomes glassy after cooling. The clay-based ceramic can be visualized as a composite having a glassy phase which shows alkali ion conductivity and insulating phase comprising pores, undissolved silica and other particles. Ceramics of our day-to-day use, such as floor and wall tile, artware, pottery, dinnerware, sanitary ware, food-service ware, etc., are clay based. Clay is the principal raw material for producing these conventional ceramics. The production involves a sintering process (firing process during which particles of the object join together) which is difficult to control by only temperature measurements due to the complicated reactions taking place in the clay. Certain components (such as glass) of the clay melt at the sintering temperatures giving rise to liquid phase which helps in the shrinkage (sintering). Liquid phase sintering is the dominant mechanism in the sintering of clay-based ceramics (Kingery et al. 1976). This liquid is an ionic conductor and acts as an electrolyte and its quantity and electrical conductivity vary with temperature. Porosity and electrical properties of different solid phases and of this liquid phase affect the electrical impedance. This is manifested as changes in equivalent circuit parameters. Impedance spectroscopy has been used in situ while a clay compact was being fired at different temperatures (Wang 2001). Wang and Xiao (2002) have reported that the complex plane impedance plots contain two arcs where the high-frequency arc may be associated with the bulk and the low-frequency arc with the electrodes. The variation of electrical conductance of bulk compact versus sintering time can be used to monitor the real time densification process of clay compact under firing.

Portland cement is one of the most-used materials in the world. Cement is a principal construction material which is subjected to water sprinkling for settling and hardening. It gets hardened and gains strength by hydration. Cement hydration determines the final microstructure and physical and mechanical properties of the hydrated cement paste. The full understanding of cement hydration is, therefore, of great importance (Gallardo and Provos 2021). Characterization of cementitious materials has been carried out by using some novel techniques, such as X-ray photoelectron spectroscopy (XPS), nuclear magnetic resonance spectroscopy (NMR), X-ray microtomography, atomic force microscopy and lateral force microscopy (AFM and LFM) (Khoshnazar and Shao 2018; Kupwade-Patil et al. 2018; Peled et al. 2013) together with the most commonly used techniques, such as X-ray diffraction (XRD), Fourier transform infrared spectroscopy (FT-IR) and scanning electron microscopy with energy-dispersive X-ray spectroscopy (SEM-EDS). Recently, impedance spectroscopy has been demonstrated to be a promising technique for tracing hydration feature of different cementitious systems (Madej 2020; Dong et al. 2016; McCarter 1996; Dotelli et al. 2001; Kim et al. 2003; Scuderi and Mason 1991; Husain et al. 2017; Kim and Kim 1995).

The cement paste comprises unreacted solid cement grains, pores containing fluids and air entrapped in empty or partially filled pores whose ratio changes as hardening proceeds. Thus, the mechanical properties and lifetime of concrete structures are defined by porosity and ionic conductivity (Andrade et al. 1999; McCarter et al. 1988), which may be monitored by impedance spectroscopy. The dielectric properties

of the hardened cement paste are governed by two contributions: the solid phase and the electrolyte inside pores.

Cement-based ceramics containing mainly strontium aluminate hydrates have been extensively studied owing to their possible applications as thermal insulating refractory materials and in developing radiation shielding concretes for providing protection against X-ray and gamma radiation. The hydration of strontium monoaluminate (SrAl_2O_4) cement was studied by using impedance spectroscopy (Madej 2020). A cement paste was prepared by using water to cement ratio of 0.5, and impedance measurements were carried out in the frequency range 0.1 Hz–1 MHz over a duration of several days. Impedance spectra taken after 4 days (early stage), 18 days (intermediate stage) and 102 days were analyzed and equivalent circuits were obtained that represented the data best. It was observed that the low-frequency intercept, which corresponds to the total resistance of the sample, increases as the hydration time increases. This would happen since the solid hydration products are formed as the hydrations proceeds.

It is well known that a gel layer forms on the surface of cement grains immediately after mixing cement. The viscous liquid transforms to solid state during the cement hydration. In the early stage of hydration, significant movement of ions occurs in the pore solution and the system can be treated as an electrochemical system, which may be represented by an equivalent circuit $R_1-(C\parallel(R_2-W))$, where series combination of R_2 and Warburg element W is connected in parallel to C with this whole circuit being connected in series with R_1 (a dash is used to indicate a series connection and “ \parallel ” for indicating a parallel connection). Here, solution resistance was represented by R_1 . Electrode/electrolyte interface double layer capacitance and the related charge transfer resistance are represented by C_2 and R_2 , respectively. The diffusional processes at the interfaces were represented by Warburg element W . At the mid of the hydration process, cement paste hardens and an arc appears at the high-frequency side in the impedance plot. This behavior was successfully represented by an equivalent circuit model $R_1-(C_1\parallel(R_2-W_1))-(C_2\parallel(R_3-W_2))$. During hydration, the system transforms from a viscous suspension through a rigid gel/solid into a fully hydrated solid. The diffusion processes at the electrode interface and in the paste proceed at different rates. The impedance behavior at early stage of hydration (4 days) could be well represented by a model $R_1-(C_1\parallel(R_2-W_1))-W_2$ where two Warburg elements were used to represent slow ionic diffusion effects at the electrode interface and ionic resistance in the strontium aluminate hydrates (SrAH) paste. The data for intermediate stage (taken after 18 days) could be well fitted by an equivalent circuit model $R_1-(C_1\parallel(R_2-W_1))-(C_2\parallel(R_3-W_2))-W_3$ (Figure 6.2), where slow ionic diffusion at the electrode interface and ionic resistance in the rigid gel SrAH cement paste were considered.

The impedance pattern after 102 days consisted of a linear, low-frequency branch and two high-frequency arcs. These were related to the appearance of C_3AH_6 and $\text{Al}(\text{OH})_3$ well-developed crystals after full hydration. By taking into consideration that SrAH cement paste–electrode interface gets transformed from liquid–solid interface to solid–solid interface, the low-frequency response was represented by the circuit $(C_3\parallel(R_4-W_3))-(C_4\parallel(R_5-W_4))$. The overall equivalent circuit model that represented the data best was obtained as $R_1-(CPE_1\parallel(R_2-W_1))-(C_2\parallel(R_3-W_2))-(C_3\parallel$

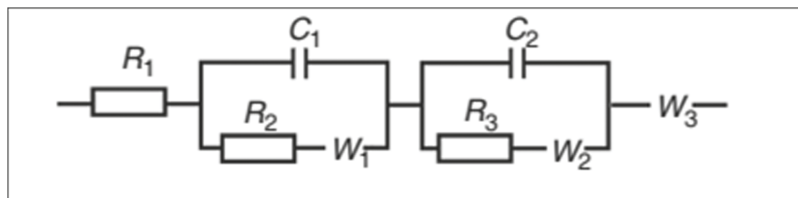


FIGURE 6.2 Equivalent circuit model $R_1-(C_1 \parallel (R_2-W_1))-(C_2 \parallel (R_3-W_2))-W_3$. (Reprinted with Permission from Madej D. 2020. Figure 5, Open Access, Springer, A New Implementation of Electrochemical Impedance Spectroscopy (EIS) and Other Methods to Monitor the Progress of Hydration of Strontium Monoaluminate (SrAl_2O_4) Cement. *Journal of Thermal Analysis and Calorimetry*. 139:17–28.)

$(R_4-W_3)-(C_4 \parallel (R_5-W_4))$ (Madej 2020). Understanding the complexity of the chemical and microstructural evolution of cement during hydration remains a controversial subject. Various factors, including electrodes, leads, etc., that contribute to the measured impedance values, need to be taken care of (Gallardo and Provis 2021).

Mortar is a workable paste, prepared by mixing cement, sand and water, which hardens to bind building blocks, such as bricks, stones and masonry concrete units, and plays a very important role in construction industry. The durability of concrete structures is highly influenced by the properties of mortar. One of the causes of the deterioration of the mortar is carbonation, which occurs due to reaction of alkaline components present in concrete with CO_2 dissolved in pore water. Impedance spectroscopy (frequency range 0.01 Hz–1 MHz) has been used as a nondestructive tool for describing the carbonation behavior of mortar. As the processes occurring in the mortar are predominantly diffusion based, an equivalent circuit model involving combinations of resistances, capacitances and Warburg elements were successfully used (Dong et al. 2014).

Estimation of durability of concrete structures is one of the major civil engineering problems. Concrete is a porous material having calcium silicate hydrate C-H-S ($\text{C} = \text{CaO}$, $\text{H} = \text{H}_2\text{O}$, $\text{S} = \text{SiO}_2$) gel pores, capillary pores, microcracks and micropores (Wu et al. 2016). Intrusion of hazardous substances into the pores highly affects the durability. Among many transport parameters, the chloride ion diffusion coefficient is the most important one regarding service life prediction. AC impedance spectroscopy was used for determining chloride ion diffusion coefficient (Wu et al. 2016). When a concrete sample is placed between two electrodes, basically, three conduction pathways were considered to exist for alternating current to flow. These are continuous conduction (arising due to connected capillary pores or connected microcracks), discontinuous conduction (arising due to the breaking of the pore connectivity by cementitious material or its hydration products and the insulating ac conduction due to remaining solid concrete block). However, the connected capillary pore path was considered to be relevant for diffusion processes. Samples of Portland cement concrete, cement + fly ash composite binder concrete, etc., were prepared, and impedance measurements were carried out in the frequency range 40 Hz–40 MHz by using stainless steel plate electrodes in two-probe configuration. As the experimental

Z'' versus Z' plots showed a single shifted arc, an equivalent circuit model comprising a parallel R_1C_1 circuit connected in series to a resistance R_0 , where R_1 and C_1 correspond to the interconnected pores, was chosen to represent the data. The values of R_0 and R_1 were obtained by using the high-frequency and low-frequency intercepts of the arc with the Z' axis. This value of R_1 was used to obtain the chloride ion diffusion coefficient D_{Cl^-} by using the relation

$$D_{Cl^-} = \frac{l}{A} \frac{RT}{1.6F^2 R_1 C_{Cl^-}} \quad (6.1)$$

where l and A are the thickness of the sample and the area of the contact electrode, respectively, R is the universal gas constant, T is the absolute temperature (K), F is Faraday constant and C_{Cl^-} is the chlorine ion concentration (Wu et al. 2016).

One of the ways to reduce CO_2 emissions and pollution is the use of by-products of traditional industries. One such product is fly ash, which is produced as a waste in the thermal powerhouses using coal as a fuel. This material can be used to fully/partially replace cement in certain constructions. The suitability of fly ash is governed by its particle size, which decides its reactivity, and the free carbon content, which is quantified by the loss-on-ignition in the powerhouse. Impedance spectroscopy has been used to characterize fly ash (Suryanto et al. 2017; Ortega et al. 2017).

Zirconia doped with low-valent cations (e.g. Y^{3+} or Ca^{2+}) exhibits an exceptionally high ionic conductivity, making them ideal candidates for various electrochemical applications, including solid oxide fuel cells (SOFCs) and oxygen sensors (Eder and Kramer 2006). It was reported that higher electrical conductivity arises at grain boundaries. To address the question of whether introduction of interfaces by nanocrystallization would further enhance the electrical conductivity and to get a detailed picture of the conduction behavior, impedance spectroscopy was applied to investigate the electric performance of pure monoclinic zirconia with different surface areas developed by nanocrystallization (Eder and Kramer 2006). It was observed that pure zirconia acts as an insulator at room temperature and exhibits a capacitive behavior in the frequency range 1 mHz–100 kHz (range of measurement). When temperature is raised, it starts showing semiconducting behavior, i.e. having capacitive conduction at higher frequencies and a parallel ohmic conduction at low frequencies. The low-frequency resistance decreases as the temperature is further raised. Impedance measurements were carried out on nanocrystalline zirconia samples treated in flowing dry oxygen and in ambient air. The Z'' versus Z' plots are shown in Figure 6.3 (Eder and Kramer 2006).

For the conduction mechanism a scheme involving two pathways for charge flow was proposed: (i) pathway A, providing electronic conduction and (ii) pathway B, providing ion movement. In path way A, electrons move through sample–electrode interfaces, grains and grain boundaries and may be represented by a series combination of parallel R_g-C_g (representing grains), $R_{gb}-C_{gb}$ (representing gb) and $R_{ct}-C_{ct}$ (representing contact electrode interfaces) circuits. In the pathway B, ions move and may be blocked at the grain boundaries and at electrodes. Also, it is seen from Figure

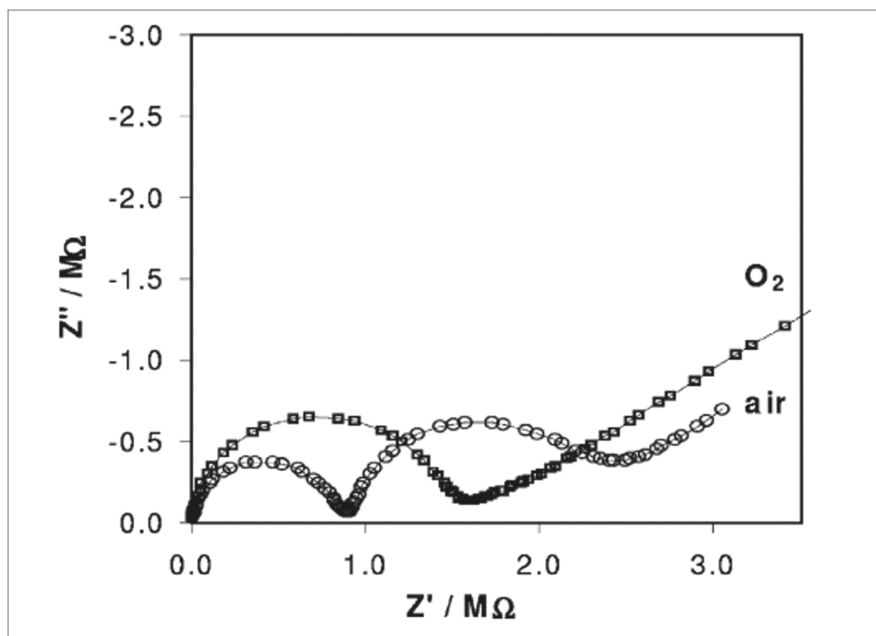


FIGURE 6.3 Nyquist plots for nanocrystalline ZrO_2 treated in dry oxygen (\square) and in ambient air (\circ) at 1073 K. (Reprinted with Permission from Owner Societies 2006, Eder and Kramer 2006, Figure 4, Impedance Spectroscopy of Reduced Monoclinic Zirconia, *Phys. Chem. Chem. Phys.*, 8: 4476–4483.)

6.3 that linear branch inclined at about 45° appears at low-frequency side. Thus, pathway B was represented by a series combination of resistance R_i (corresponding to ions), electrode capacitance C_e and a Warburg element W_i . The overall equivalent circuit is shown in Figure 6.4.

The values of the parameters were obtained by fitting the data to this model. This equivalent circuit model was used for analysis of the impedance data obtained for samples subjected to oxidation/desorption. It was found that hydrogen treatment below 873 K gives rise to oxygen vacancies at the grain surface, whereas with hydrogen treatment above this temperature, the vacancies diffused into the bulk. Electrons are released as a result of formation of these vacancies and are confined to the surface with their number being proportional to the surface area (Eder and Kramer 2006).

Impedance spectroscopy has been used to study glass ceramics. As described earlier, a glass subjected to suitable heat treatment gives rise to glass ceramics. A glass ceramic may be visualized as randomly oriented crystallites submerged in glassy matrix. If the crystallites have similar electrical behavior, then the system may be modeled by equivalent circuit containing four RCs connected in series, to begin with, representing crystalline phase, glassy phase, the glass–crystallite interface region and sample–electrode interface. The existence of a glass–crystallite interface region may be visualized in the following way. The glass has no long-range order

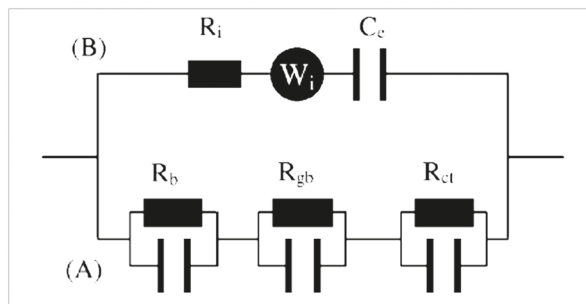


FIGURE 6.4 Circuit diagram equivalent to the conduction mechanism, subscripts of the RC combinations are as follows: b for bulk, gb for grain boundary, ct for charge transfer at the electrode, R_i and W_i denote the ionic resistance and Warburg impedance, respectively, and C_e denotes the ionic capacitance at the electrodes. (Reprinted with Permission from Owner Societies 2006, Eder and Kramer 2006, Figure 6, Impedance Spectroscopy of Reduced Monoclinic Zirconia, *Phys. Chem. Chem. Phys.*, 8: 4476–4483.)

whereas crystals have. The glass ceramics possess crystallites that have emerged from the glass itself by structural reorganization. However, there ought to be some region around the crystallites that have structural order in between that of crystal and glass. As the electrical properties of these would be generally different, their presence may be sensed in impedance spectroscopic measurements. Strontium titanate glass ceramics have a wide scope of applications, such as cryogenic capacitive temperature sensors (Thakur et al. 2004). The glass ceramics based on perovskite SrTiO_3 are technologically very useful due to the ambient temperature applications requiring temperature compensation of the dielectric constant. This is achieved by appropriate proportion in between the negative temperature coefficient of SrTiO_3 and positive temperature coefficient of the residual glassy matrix.

Crystallization of SrTiO_3 phase in $[\text{SrO}.\text{TiO}_2]\text{-}[\text{SiO}_2.\text{B}_2\text{O}_3]$ system was studied by Thakur et al. (2004) by using impedance spectroscopy where the M'' versus M' plots were used for data analysis. The plots exhibited a shift toward right (i.e. high-frequency side in the M plot), indicating the presence of series capacitance in the equivalent circuit. A typical plot is shown in Figure 6.5, where the equivalent circuit model is also shown in the inset. The circuit segments R_1C_1 , R_2C_2 and R_3C_3 represent the crystallites, crystal–glass interface region and glassy matrix, respectively, whereas C_4 represents the sample–electrode interface. To estimate the values of the components, three tentative arcs were drawn as shown by continuous line in Figure 6.5. By noting the values of intercepts, values of C_1 , C_2 , C_3 and C_4 were estimated as described in Chapter 5. The values of R_1 , R_2 and R_3 were obtained by noting the frequencies corresponding to the peaks of the arcs in the respective frequency regions and using the relation $\omega RC = 1$. These values were obtained more accurately by fitting the data to the equivalent circuit model shown in the inset of Figure 6.5. Variation in the values of the components as function of temperature was used to describe the temperature dependence of the overall dielectric permittivity of the glass ceramic.

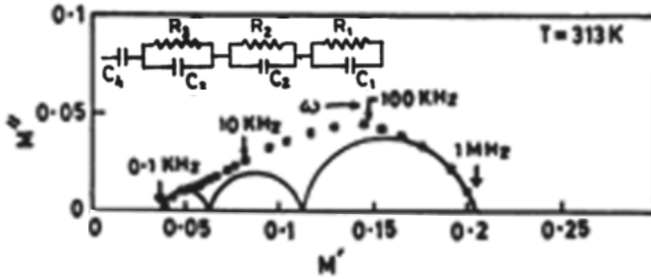


FIGURE 6.5 Complex plane electric modulus plot for glass ceramic sample at 313 K. (Reprinted with Permission from Thakur et al. 2004, Figure 5, Dielectric and Impedance Spectroscopic Behavior of Alkali Oxide Containing Glass Ceramics in the System [SrO.TiO₂]-[SiO₂.B₂O₃], Journal of Ceramic Processing Research, 5(2): 106–113.)

Hydroxyapatite (HA) is one of the most important orthopedic bioactive implant materials owing to its structural and compositional resemblance with the natural bone. However, as interfacial failures are possible due to presence of abrupt interfaces, functionally graded materials (FGMs) are more promising, since they provide a continuous change in mechanical, chemical and physical properties and thus reduce the stress between the implant and bone tissue. As the living bone possesses inherent polarization regulated functionality, composites with ferroelectric materials such as BaTiO₃ have been considered. The perovskites BaTiO₃ and CaTiO₃ were sandwiched between HA layers via buffer interlayers to provide the structural integrity to the FGMs. Impedance spectroscopic studies in the temperature range (35–500°C) and frequency (1 Hz–1 MHz) revealed almost two times increase in polarizability as compared to HA. An equivalent circuit comprising parallel combinations R-CPE connected in series represented the data best (Saxena et al. 2019b).

6.2 FERROELECTRICS AND PIEZOELECTRICS

Ferroelectrics are materials possessing spontaneous electric polarization which can be reoriented in at least two directions by applying external electric field (E). These materials may be polycrystalline or in the form a single crystal. However, due to ease of preparation, processing, casting in desired shapes and development of certain characteristics, usually not observed in single crystals, ferroelectrics in polycrystalline ceramic form are usually preferred for commercial device applications. Electric dipole moment per unit volume is called electric polarization (P). Ferroelectrics possess certain characteristic features, which are described below. The polarization (P) may stem from relative shift of the positive ions with respect to negative ions in the unit cell structure such that the center of positive charges and that of negative charges do not coincide giving rise to an electric dipole. These types of ferroelectrics, e.g. BaTiO₃, are known as displacive ferroelectrics. Ferroelectrics where polarization arises due to net ordering of number of fluctuating dipoles along one direction, such as NaNO₂, are called order–disorder type. However, mixed behavior is also observed.

As the temperature is raised, the ordering gets destroyed due to thermal motions, and polarization disappears at a certain temperature called the Curie temperature T_c , and the ferroelectric behaves as a paraelectric above T_c . The dielectric permittivity versus temperature curve shows a peak at T_c above which the material usually obeys Curie–Weiss law (Lines and Glass 1977; Kittel 2005; Dekker 1958; Jona and Shirane 1962; Moulson and Herbert 2003).

The ferroelectric shows a P-E hysteresis. Under an applied electric field the polarization first increases in a nonlinear way with increasing electric field E and reaches a saturation. When E is reversed, P decreases and attains a saturation value in the opposite direction. When the field is again increased in the positive direction, P increases but does not retrace its earlier path and shows hysteresis (Sawyer and Tower 1930; Kittel 2005). The P versus E curve is called ferroelectric hysteresis loop.

Ferroelectrics get strained also when subjected to electric field. Materials which develop electric polarization when stressed, or vice versa, are known as piezoelectrics (Moulson and Herbert 2003; Cady 1946; Nye 2006). All ferroelectrics are piezoelectrics, but not the other way round. The generally high value of dielectric permittivity, presence of ferroelectric transition, P-E hysteresis loop and piezoelectric behavior are the properties exploited in commercial devices, such as high-value miniaturized capacitors, infrared and strain and other sensors, nonvolatile computer memories, positive temperature coefficient of resistance (PTCR) thermistors, electrocaloric devices, piezoelectric transducers, etc. (Lines and Glass 1977; Moulson and Herbert 2003; Scott and Araujo 1989; Ishiwara et al. 2004; Bain and Chand 2017).

A polycrystalline ceramic, after synthesis, is usually in the form of powder, which is further processed and cast in desired shape and size, such as a pellet, tape, etc., to which mostly electrodes are attached for measurements or device applications. A sintered ceramic piece with attached electrodes may be visualized as grain, grain–boundary and grain–electrode system as described earlier in Section 6.1. Properties of ceramics can be altered by using additives/dopants, by controlling microstructure through processing variables, such as heating/cooling rates and atmosphere, presence of external electric/magnetic fields, etc. To develop ferroelectric/piezoelectric ceramics having desired and reproducible properties, the grain, grain boundary and sample–electrode interface behavior must be separated out. Impedance spectroscopy has emerged as an extremely useful tool for this (Hodge et al. 1976; Irvine et al. 1990; Barsoukov and Macdonald 2005) and knowledge gained about the grain, grain boundary and electrode contributions is further utilized to develop better ferroelectric/piezoelectric materials. Number of polymers possessing ferroelectric/piezoelectric properties have also been developed and are being extensively used in industry. However, only ceramic ferroelectrics are described in this presentation.

As described earlier, the impedance spectroscopic studies involve equivalent circuit models. These models usually comprise three parallel RCs connected in series (see Figure 6.1) and generally represent the data of electroceramics well. The procedure of impedance analysis is the same for ferroelectrics and non-ferroelectrics. However, as a ferroelectric shows a permittivity versus temperature peak, impedance studies as function of temperature reveal certain features typical of ferroelectrics. One such feature is the PTCR behavior found in donor-doped ferroelectrics such

as BaTiO_3 and is briefly described here. BaTiO_3 is an insulator which can be made semiconducting by doping (adding in small amounts) with trivalent ions such as La^{3+} , Sb^{3+} , Gd^{3+} , Y^{3+} on the Ba^{2+} site or with pentavalent ions such as Nb^{5+} and Ta^{5+} on Ti^{4+} sites in the structure (Basu and Maiti 1986). Barium titanate undergoes ferroelectric to paraelectric phase transition at 120°C (T_c). The resistivity decreases as the temperature is raised but shoots up by several orders of magnitude as the temperature approaches T_c and exhibits a very high positive value of temperature coefficient of resistivity. At temperatures above T_c , the resistance starts decreasing and the material acts as a normal insulator. This is the so-called PTCR behavior. Materials exhibiting such behavior are used as constant temperature heat sinks, rice cookers, hair driers, etc. (Basu and Maiti 1986). From the application point of view, the materials with lower room temperature resistivity and steeper resistivity rise are preferred because of their better power limiting capability [materials, such as semiconductors and insulators, whose resistivity decreases after heating are called negative temperature coefficient of resistance (NTCR)]. The PTCR effect is explained by using theories proposed by Heywang (Heywang 1961, 1971; Lines and Glass 1977; Daniels et al. 1978; Lewis et al. 1985; Jonker 1967), which assume that electron acceptor states in the grain boundary together with ionized nearby donor states in grains form an electrical double layer. This creates a potential barrier for the conduction electrons reaching up to the grain boundary. The height of this potential barrier depends inversely on the dielectric permittivity. As the temperature increases, the permittivity increases, causing the potential barrier to drop that leads to decrease in resistivity (below T_c , the slope of the resistivity vs temperature curve remaining negative). As the temperature approaches T_c , the permittivity drops and the potential barrier rises very fast, rendering the grain boundary highly resistive. The resistance versus temperature slope now becomes positive.

Basu and Maiti (1986) used impedance spectroscopy to study the PTCR behavior of semiconducting BaTiO_3 ceramics. They prepared doped BaTiO_3 samples possessing various dopants (La, Gd, Y, Nd, Sb, Y) with concentrations varying from 0.1 to 0.5 atom% in pellet form and carried out impedance measurements using different electrodes in a two-probe setup. By observing the variation of room temperature resistivity with concentration of different dopants, they found that the lowest resistivity was obtained with 0.3 atom% of almost all the dopants. They further measured the variation in resistivity of all the samples having 0.3 atom% of various dopants as function of temperature. The resistivity jump near Curie temperature was the highest in case of Sb doping, indicating that this dopant was the most suitable dopant from the application point of view. Study of temperature variation of resistivity of the 0.3 atom% Sb-doped BaTiO_3 specimen with different electrodes was also undertaken. It was found that resistivity jump by using In-Ga (indium-gallium) was the highest. A Z'' versus Z' plot for the 0.3 atom% Sb-doped BaTiO_3 specimen with indium electrode is shown in Figure 6.6.

Attempt was made to analyze the data with the help of equivalent circuit model. The complex plane plots (Z'' vs Z') showed shifts toward right indicating that series resistance should be included in the model. The high-frequency and low-frequency arcs appear little depressed by angles 3.4° and 7.4° which may be neglected. A model comprising a resistance (representing grains), and two parallel RCs connected in

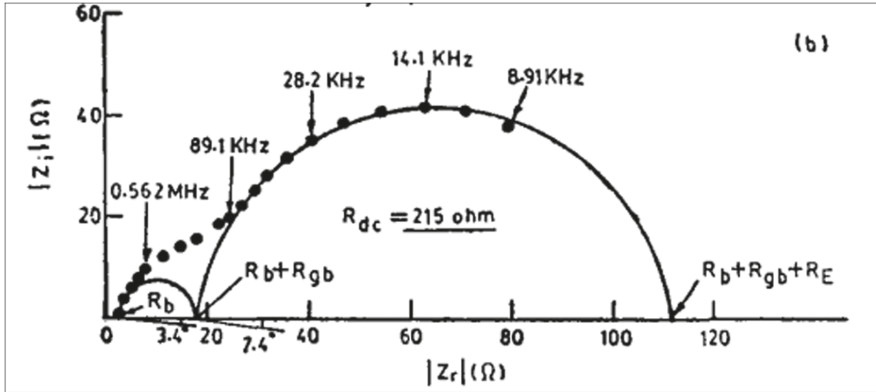


FIGURE 6.6 Complex plane impedance plot of 0.3 atom% Sb-doped BaTiO₃ specimen with indium electrode. (Reprinted with Permission from Taylor & Francis, Basu and Maiti 1986, Figure 5, PTC Behavior of Semiconducting BaTiO₃ Ceramics, Transactions of the Indian Ceramic Society, 45(6): 140–146.)

series (representing grain boundary and sample–electrode interface), represented the data well.

The grain, grain boundary and electrode contributions were successfully separated out (i.e. values of the Rs and Cs were obtained). They observed that the size of the low-frequency arc changed when the electrodes were changed. The impedance measurements were carried out as function of temperature using different electrodes and the plots of resistivity ρ versus temperature were obtained. They concluded that the best PTC effect was observed in 0.3 atom% Sb-doped BaTiO₃ (see Figure 6.7).

Impedance spectroscopic measurements as function of temperature were used by Irvine et al. (1990a) to separate contributions from ferroelectric and non-ferroelectric parts of donor-doped BaTiO₃ ceramic sample by analyzing the data using Z and M formalisms. The system comprises ferroelectric grains and non-ferroelectric grain boundary. So, they used two parallel RCs (R_1C_1 and R_2C_2) connected in series to represent grain and gb behavior and obtained the values of the components. They found that C_2 remained unchanged, whereas C_1 increased nonlinearly as temperature was raised toward T_c . Also, value of permittivity obtained from C_1 followed Curie–Weiss law, indicating that C_1 represents the bulk ferroelectric part (i.e. grains) and C_2 represents non-ferroelectric grain boundary.

They also demonstrated that impedance spectroscopy can be used for study of behavior of ferroelectrics in single crystal form as well. In single crystal form, there would be no grain boundaries and the whole sample would be a single crystal having ferroelectric domains. They carried out impedance measurements as function of temperature on a LiTaO₃ crystal, an important ferroelectric used for its nonlinear optical properties, by placing the crystal between electrodes such that (i) the external electric field E was parallel to the crystal polar c axis, i.e. polarization P is parallel to external E, and (ii) the external electric field E was perpendicular to the crystal polar axis.

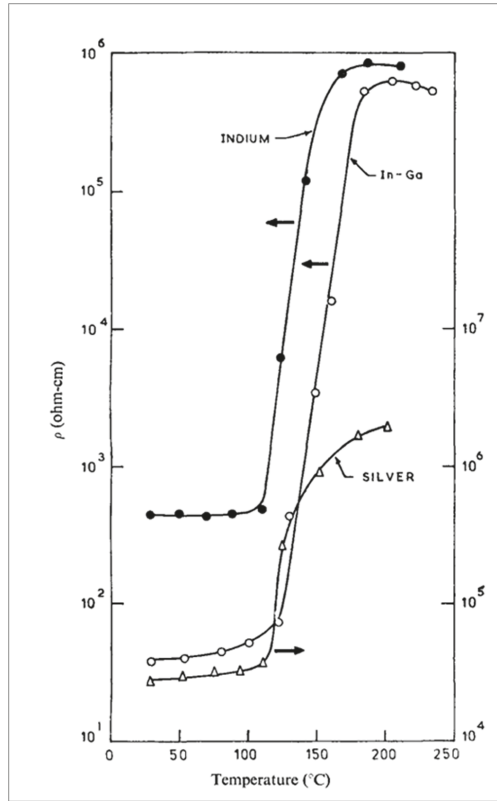


FIGURE 6.7 Temperature variation of resistivity of the 0.3 atom% Sb-doped specimen with different electrodes. (Reprinted with Permission from Taylor & Francis, Basu and Maiti 1986, Figure 4, PTC Behavior of Semiconducting BaTiO_3 Ceramics, Transactions of the Indian Ceramic Society, 45(6): 140–146.)

They found that for the case (ii), i.e. non-ferroelectric orientation, the impedance data could be represented well by a parallel RC circuit and the values of R showed an Arrhenius behavior (a linear $\log R$ vs $1000/T$ plot) indicating that the crystal behaves just like an usual semiconductor. In the case (i) (ferroelectric case), by looking at the indications from the AC response, they considered that there would be presence of capacitive charging when field is applied, reversal or switching of the ferroelectric domains, bulk polarization of the lattice, a leakage current due to migration of ions and possible blocking of the Li ions at the sample electrode interface. Therefore, a slightly complicated model, as shown in Figure 6.8, was proposed to represent the behavior. They used a series R_1C_1 circuit where capacitor C_1 represents the processes of overall charging of the sample and resistance R_1 represents losses due to reversal or switching of ferroelectric domains. A resistance R_2 was connected in parallel to R_1C_1 series combination to represent the leakage resistance of the migrating Li ions in this crystal orientation. Another large capacitance C_2 in parallel to R_1 was connected

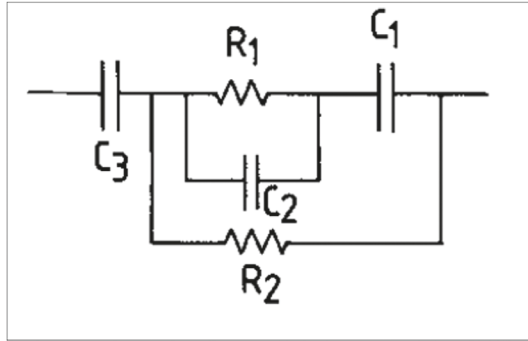


FIGURE 6.8 Equivalent circuit for voltage applied parallel to ferroelectric polar c axis of LiTaO_3 crystal. (Reprinted with Permission from VCH VerlagsgesellschaftmbH, D-6940 Weinheim 19190, Irvine et al. 1990a, Figure 6, *Electroceramics: Characterization by Impedance Spectroscopy*, Adv. Mater., 2: 132–138.)

to represent the bulk polarization of the lattice, independent of the domain structure. This whole circuit representing the processes within the crystal was further connected in series with a capacitor C_3 , which would represent the formation of charge double layer at the crystal–electrode interface. By studying the temperature dependence of the components, they demonstrated that impedance spectroscopy can be used for quantifying the difficulty in domain reorganization in terms of R_1 .

Sinclair and West (1989), yet in another work, have used both impedance and modulus formalisms to study PTCR in doped BaTiO_3 , where they proposed the existence of an outer layer on the grains. This layer and the bulk, both, show PTCR behavior. Very useful description is presented by West and Hirose (1995) regarding application of impedance spectroscopy in the study of ferroelectrics.

Another illustrative example is that of the valence-compensated ceramic system $\text{Ba}_{1-x}\text{La}_x\text{Ti}_{1-x}\text{Co}_x\text{O}_3$, which was studied using impedance spectroscopy with $x = 0.2, 0.1, 0.05, 0.01$ in the temperature range 300–500 K (Pandey et al. 1997) (La^{3+} ions occupy the Ba^{2+} sites whereas Co^{3+} go to Ti^{4+} sites in the structure yielding a valence-compensated material). The data was analyzed by using a model comprising three parallel RCs (R_1C_1 - R_2C_2 - R_3C_3) connected in series and values of Rs and Cs corresponding to grain, grain boundary and electrodes were obtained. A typical complex plane and spectroscopic plots for $x = 0.1$ are shown in Figures 6.9(a, b).

The parallel RC that corresponded to lowest value of the product RC was assigned to grains (labeled as R_1C_1) and that which gave largest value was assigned to electrodes (labeled as R_3C_3). The values of $\log R_1$ and $\log R_2$ were plotted as function of $1000/T$ to explore the possibility of presence of Arrhenius behavior [Figures 6.10(a, b)].

Similarly $\log R_1$, $\log R_2$, C_1 and C_2 were also plotted as function of T [Figures 6.11(a,b)].

It was found that for $x = 0.20, 0.10, 0.05$, the system behaves as a semiconductor in the whole temperature range (i.e. R_1 and R_2 exhibit a decreasing trend as T increases), whereas for $x = 0.01$, both R_1 and R_2 show a PTCR behavior [T rapidly increases by

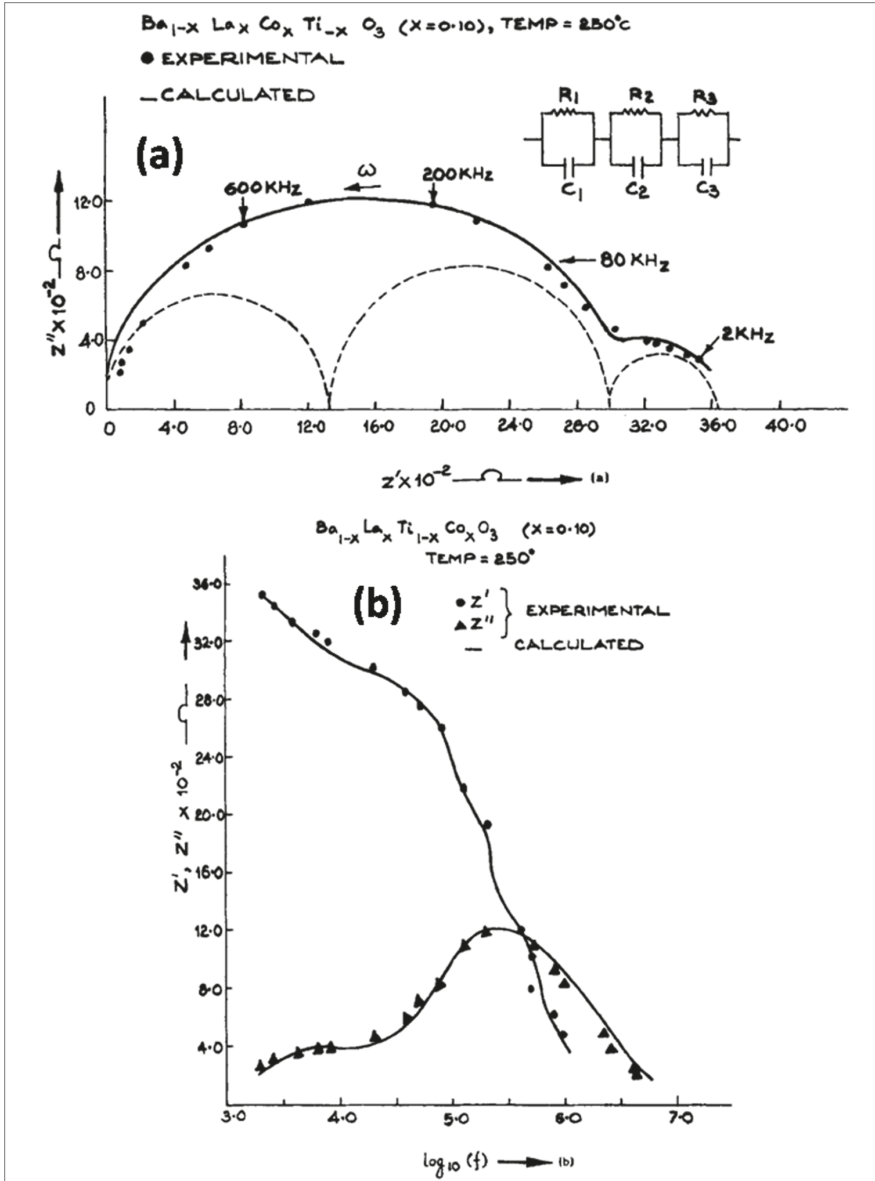


FIGURE 6.9 (a) Z'' versus Z' and (b) Z' and Z'' versus $\log_{10}(f)$ plots for the system $Ba_{1-x}La_xTi_{1-x}Co_xO_3$ ($x = 0.10$) at 250°C (●, ▲, experimental values, —, values calculated using CNLS fitting of the model shown in the corner, - - -, tentative arcs indicating the independent contributions of R_1C_1 , R_2C_2 and R_3C_3). (Reprinted with Permission from Springer, Pandey et al. 1997, Figure 3, Evidence of Two PTCR Components in Valence Compensated Ceramic System $Ba_{1-x}La_xTi_{1-x}Co_xO_3$, Bull. Mater. Sc., 20: 933–947.)

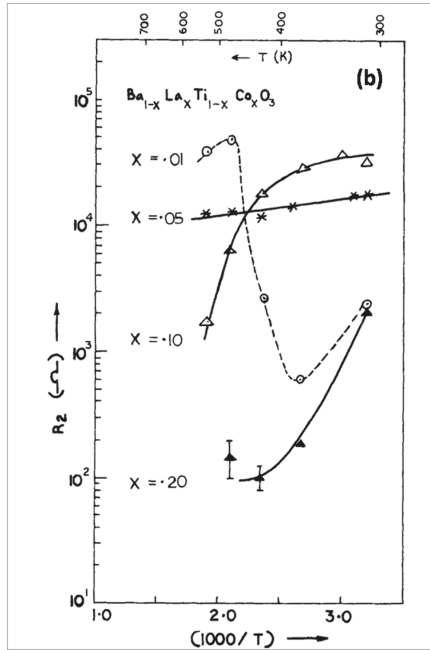
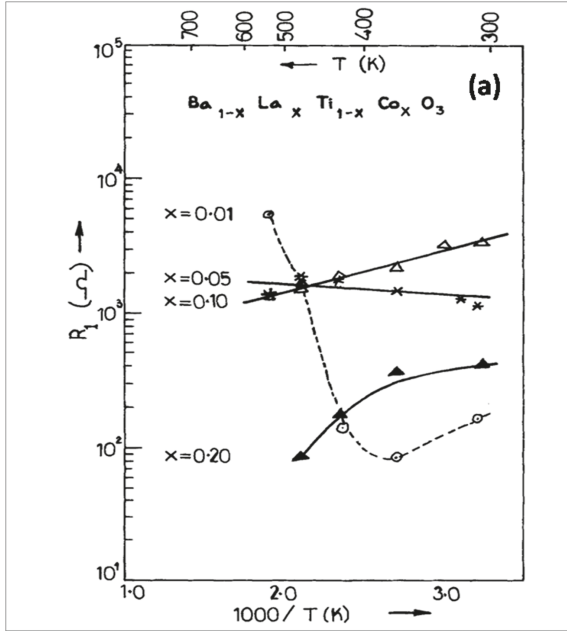


FIGURE 6.10 (a) R_1 versus $1000/T$ plots, (b) R_2 versus $1000/T$ plots for the ceramic $Ba_{1-x}La_xTi_{1-x}Co_xO_3$ ($x = 0.01, 0.05, 0.10$ and 0.20). (Reprinted with Permission from Springer, Pandey et al. 1997, Figures 5, 6, Evidence of Two PTCR Components in Valence Compensated Ceramic System $Ba_{1-x}La_xTi_{1-x}Co_xO_3$, Bull. Mater. Sc., 20: 933–947.)

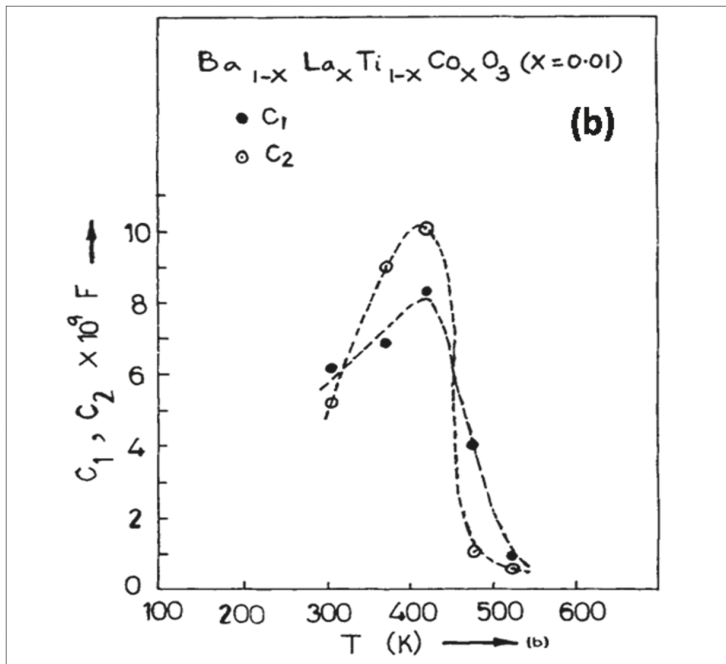
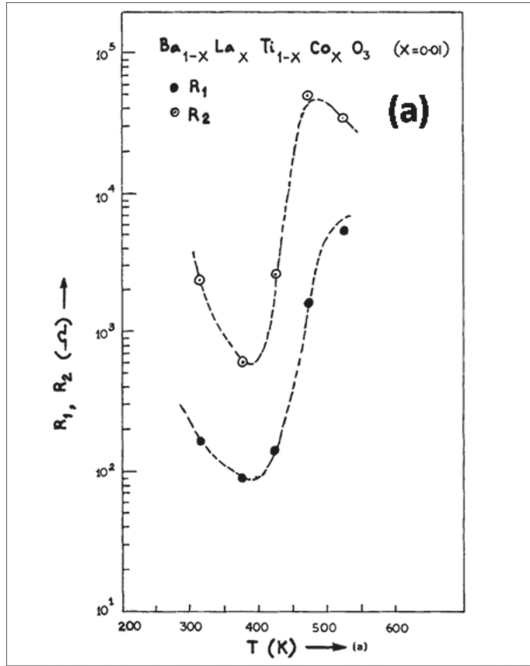


FIGURE 6.11 Plots of (a) R_1 and R_2 and (b) C_1 and C_2 versus T for $\text{Ba}_{1-x}\text{La}_x\text{Ti}_{1-x}\text{Co}_x\text{O}_3$ ($x = 0.01$). (Reprinted with Permission from Springer, Pandey et al. 1997, Figure 7, Evidence of Two PTCR Components in Valence Compensated Ceramic System $\text{Ba}_{1-x}\text{La}_x\text{Ti}_{1-x}\text{Co}_x\text{O}_3$, Bull. Mater. Sc., 20: 933–947.)

orders of magnitude near $T_c = 393$ K, Figure 6.11(a)]. This was also supported by the plots of C_1 and C_2 versus T where peaks were observed at T_c [Figure 6.11(b)]. It was concluded that both grain and grain boundary possess PTCR behavior. The data were qualitatively explained by invoking Heywang model assuming that there would be global charge compensation in the sample, but a local charge inhomogeneity may be present due to statistical nature of locations of dopant atoms situated in various unit cells (Pandey et al. 1997).

The piezoelectric ceramic system $\text{PbZr}_{0.6}\text{Ti}_{0.4}\text{O}_3$ (PZT) was studied as function of temperature (Chaitanya et al. 2011, Chaitanya 2008). Though all ferroelectrics are piezoelectric, the piezoelectric behavior would not become visible unless the piezoelectric coupling coefficient is large. Therefore, equivalent circuit models involving only resistive and capacitive components might work well in some cases. Piezoelectrics can be represented by a model comprising a series R, L, C_1 circuit further connected in parallel to another capacitor C_2 . It was found that in this PZT, the model R_1C_1 - R_2C_2 - R_3C_3 represented the impedance data well above the ferroelectric to paraelectric phase transition temperature T_c (at temperatures above T_c the system is not ferroelectric). At temperatures below T_c (when the system is ferroelectric, and hence piezoelectric), the sample–electrode system could be represented by a series R_1 - C_1 - L_1 circuit connected in series to a parallel R_3 - C_3 combination. The R_1 - C_1 - L_1 circuit represented the piezoelectric sample and R_3 - C_3 the sample–electrode interface. The values of the components were obtained by comparing the experimental plots with simulated ones and using complex nonlinear least square (CNLS) fitting. Development of equivalent circuit for piezoelectrics is useful for integration of the components to other parts of the electronic device.

Impedance spectroscopy was used to study defects in piezoelectric actuators (Bowen et al. 2000). The Z'' versus Z' plots for resonant piezoelectric specimen are full circles, where the intercept of the arc with the Z' axis corresponds to the resonance frequency, to the maximum value of the total impedance $|Z|$ and zero phase angle between applied voltage and resulting current. Multilayer actuators (piezoelectric devices) are used for applications which require large displacements at comparatively low-drive voltages (50–200 V) and low power consumption compared to monolithic materials. Performance of the multilayer actuators deteriorates due to delamination of the electrode layers during processing, binder burnout, inadequate adhesion of the electrode and piezoelectric layer, reactions of electrode metals with organic additives and sintering shrinkage mismatch, etc. The change in resonance behavior of typical multilayer actuators due to the presence of delaminations and/or cracks introduced into the device was studied by using impedance spectroscopy. It was observed that when defects, such as cracks, are present, Z'' versus Z' plots shrink (Bowen et al. 2000). This signature can be used for rapid detection of defects in actuators during large production processes (Bowen et al. 2000).

6.3 MAGNETIC SYSTEMS

It has been established that impedance spectroscopy can be used to study the ferroelectric domain reorganization in ferroelectrics (Irvine et al. 1990a). In continuation to and keeping an analogy with this it was further shown that impedance spectroscopy

can be used to study magnetic domain reorganization as well (Irvine 1990a, 1990b). For measurements on ferroelectrics, the sample is placed in an electric field, which is produced between the parallel plate electrodes of the sample holder, and the impedance of this capacitor is measured. The equivalent circuit usually involves combination of resistive (R) and capacitive (C) components. For studies on magnetic systems the sample has to be placed in a magnetic field, which can be produced inside a coil, and the impedance of this coil may be measured with the sample inside. The equivalent circuit would usually involve combinations of resistive (R) and inductive (L) components (see Chapter 4).

Impedance measurements as function of temperature were carried out by Irvine et al. (1990a, 1990b) on Ni-Zn ferrite samples placed in a low-capacitance copper coil in the frequency range 5 Hz–13 MHz as function of temperature at different values of the voltage across the coil (i.e. different magnetic fields). An equivalent circuit model was developed to represent the impedance behavior by looking at various plots. Three plateaux are observed in the logarithmic conductivity versus frequency plot; the lowest frequency one corresponds to the resistance of the coil, the other two correspond to resistances associated with the magnetization dynamics of the ferrite. Therefore, a model comprising two parallel RL circuits connected in series with another resistance (resistance of the coil) was initially considered for representing the behavior. Each RL element corresponds to a magnetic relaxation, L being the inductance, which is proportional to the permeability, and R being a measure of loss or of the difficulty of domain reorganization. Among the two magnetic relaxations, the one associated with higher time constant L/R (i.e. low frequency) was attributed to domain wall bulging. The other, associated with smaller time constant (i.e. higher frequency) was attributed to domain rotation. The complex plane plot at higher voltage across the coil possessed a linear 45° inclined part at low-frequency side. This was attributed to hysteresis effects and a magnetic Warburg impedance, $Z_{mw} = A\sqrt{\omega} + jA\sqrt{\omega}$ (where A is a function of voltage), in analogy with the Warburg impedance, was introduced to model the observed response. The Warburg element corresponds to diffusive processes in electrical impedance measurements (Macdonald 1987). Hysteresis also involves the domain wall motion in a series of jumps through the lattice. Domain walls normally pass through imperfections or defects in magnetic materials. Domain walls bulge in the direction of the magnetic field but remain pinned at the imperfections when small magnetic fields are applied. However, applying a larger magnetic field causes the domain wall to jump from being pinned at one set of imperfections to being pinned at another set. An equivalent circuit model as shown in Figure 6.12 was used which represented the data well (Irvine et al. 1990a, 1990b).

Impedance behavior of a coil with a magnetic sample within was studied by using impedance spectroscopy (Katare et al. 1999; Katare 1997). Impedance measurements were carried out for a YIG (yttrium iron garnet) sample in the frequency range 100 Hz–10 kHz at room temperature. A solenoidal coil of 32-mm length and 15-mm diameter and having 40 turns of 24 SWG copper wire was used as a sample holder. The impedance measurements were carried out for the empty sample holder first. The Z'' versus Z' plot was a vertical straight line as shown in Figure 6.13. It indicated that the empty coil may be represented by a series RL circuit, where the low-frequency intercept is equal to R. The values of R and L were estimated to be 0.17Ω and 5.8

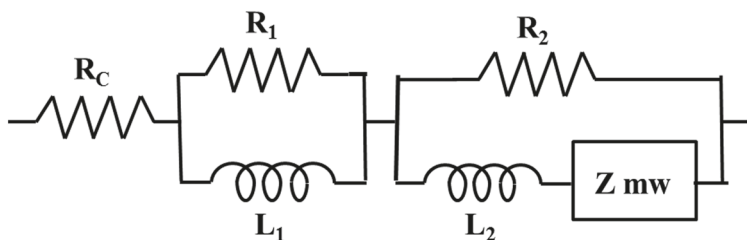


FIGURE 6.12 Equivalent circuit model for representing magnetic behavior of Ni-Zn ferrite $[(\text{Ni}_{0.36}\text{Zn}_{0.64})\text{Fe}_2\text{O}_4]$ sample. (Reprinted with Permissions from Elsevier, Irvine et al. 1990b, Figure 5, Characterization of Magnetic Materials by Impedance Spectroscopy, Solid State Ionics, 40/41: 220–223.)

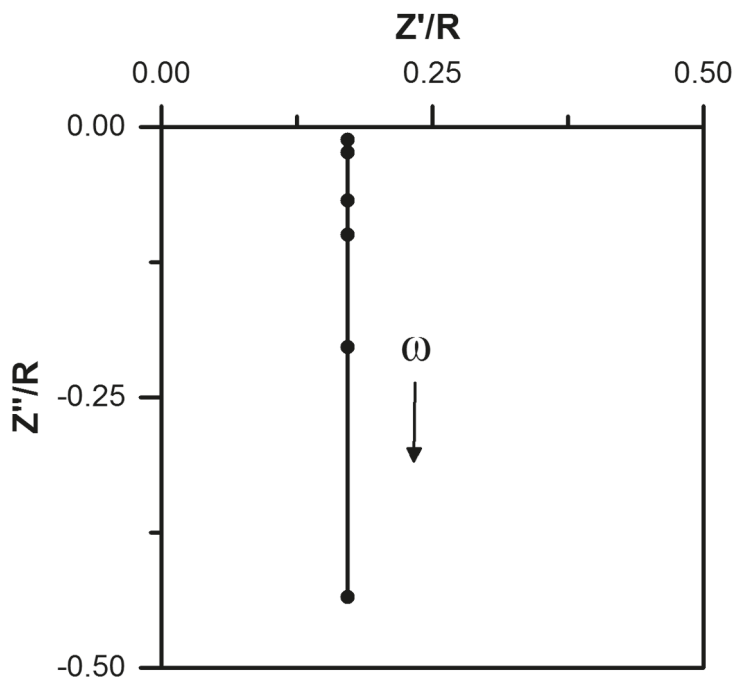


FIGURE 6.13 Z'' versus Z' plot for the empty coil [(●) experimental values, (—) vertical straight line through the experimental points] (Reprinted with Permission from CSIR-NIScPR Delhi, Katara et al. 1999, Figure 5, A Novel Approach Based on Impedance Spectroscopy for Measurement of Magnetic Permeability of Ceramics, Indian Journal of Engineering and Materials Sciences, 6: 34–42.)

$\times 10^{-6}$ H, respectively. The value of L was close to the value of inductance of the coil calculated by using the expression L (in microhenry) $= a^2n^2/(9a + 10b)$ where, a and b are the radius and length of the coil, respectively, in inches, and n is the number of turns in it (The Radio Amateur 1968).

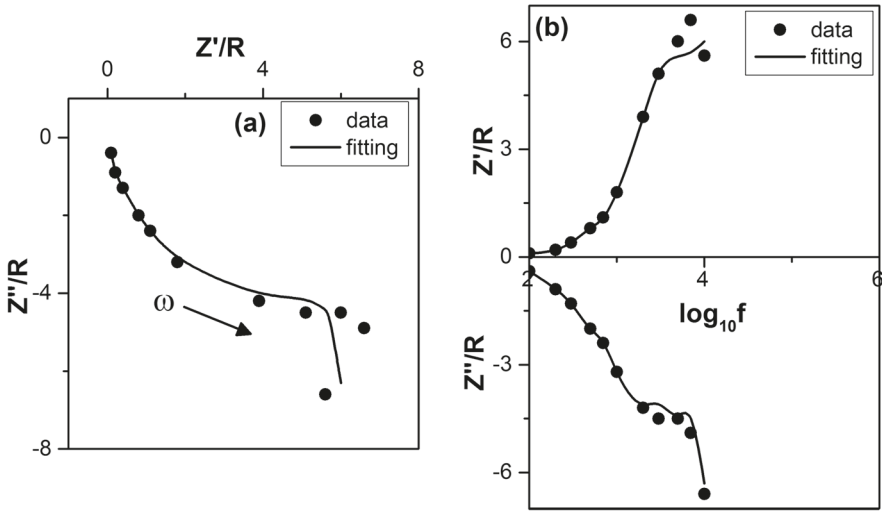


FIGURE 6.14 (a) Z'' versus Z' plot, (b) Z' versus $\log_{10} f$ and Z'' versus $\log_{10} f$ plots for the coil having YIG pellet inside it [(●) experimental values, (—) calculated values corresponding to the model shown in Figure 6.16 with $R_1 = 5.8 \Omega$, $L_1 = 5.9 \times 10^{-4}H$, $R_2 = 0.2 \Omega$ and $L_2 = 7.7 \times 10^{-5}H$ obtained from CNLS fitting]. (Reprinted with Permission from CSIR-NIScPR Delhi, Katare et al. 1999, Figure 6, A Novel Approach Based on Impedance Spectroscopy for Measurement of Magnetic Permeability of Ceramics, Indian Journal of Engineering and Materials Sciences, 6: 34–42.)

Impedance measurements were again carried out by inserting a 4-mm-thick YIG pellet of diameter about 15 mm coaxially into the coil. The Z'' versus Z' and corresponding spectroscopic plots for the coil with the sample inside are shown in Figures 6.14(a, b). Values of real and imaginary parts of magnetic permeability were obtained by using the relations $\mu' = -Z''/(\omega L_0)$ and $\mu'' = Z'/(\omega L_0)$, where L_0 is the inductance of empty coil, ω is the angular frequency, $Z = Z' - jZ''$ and $\mu = \mu' - j\mu''$. The $\mu''L_0 (= Z'/\omega)$ versus $\mu'L_0 (= -Z''/\omega)$ plot is shown in Figure 6.15.

An equivalent circuit model was developed to represent the data in the following way. The Z'' versus Z' plot in Figure 6.14(a) does not pass through the origin and is shifted toward the right by about 0.2Ω , indicating presence of a series resistance in the equivalent circuit. Also, there is a steeply increasing branch at high-frequency side. Comparison of the plot shown in Figure 6.14(a) with the simulated plots given in Chapter 4 indicate that the impedance behavior may be represented by a model comprising a parallel R_1 - L_1 circuit in series with resistance R_2 and inductance L_2 . This model is reproduced here for ready reference (Figure 6.16).

Also, the value of the series resistance R_2 , which is the low-frequency side intercept, may be taken as equal to 0.2Ω and L_2/L_1 equal to 0.1. The limiting value of Z' at high-frequency end is about 6Ω [Figure 6.14(a)] and that should be equal to $R_1 + R_2$ [see Eq. (4.158) in Chapter 4], which yields $R_1 = 5.8 \Omega$. For estimating values of L_1 and L_2 , μ'' versus μ' plot (Figure 6.15) was used. Comparing the $\mu''L_0$ versus

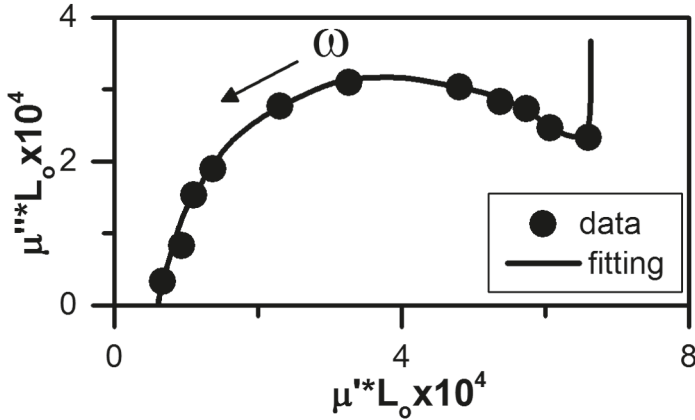


FIGURE 6.15 $\mu'' L_0 (= Z''/\omega)$ versus $\mu' L_0 (= -Z'/\omega)$ plot for the coil having YIG pellet inside [(●) experimental values, (—) calculated values corresponding to the model shown in Figure 6.16 with $R_1 = 5.8 \Omega$, $L_1 = 5.9 \times 10^{-4}H$, $R_2 = 0.2 \Omega$ and $L_2 = 7.7 \times 10^{-5}H$ obtained from CNLS fitting]. (Reprinted with Permission from CSIR-NIScPR Delhi, Katare et al. 1999, Figure 7, A Novel Approach Based on Impedance Spectroscopy for Measurement of Magnetic Permeability of Ceramics, Indian Journal of Engineering and Materials Sciences, 6: 34–42.)

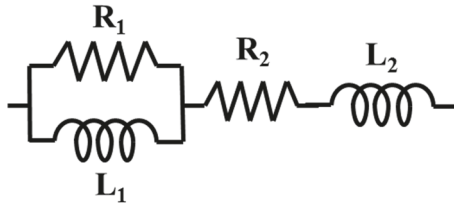


FIGURE 6.16 A parallel R_1 - L_1 combination connected in series with resistance R_2 and inductor L_2 . (Reprinted with Permission from CSIR-NIScPR Delhi, Katare et al. 1999, Figure 4a, A Novel Approach Based on Impedance Spectroscopy for Measurement of Magnetic Permeability of Ceramics, Indian Journal of Engineering and Materials Sciences, 6: 34–42.)

$\mu' L_0$ plot with simulated plots (Section 4.16) indicates that the limiting values of μ' at low-frequency and high-frequency sides are given by $\mu' L_0 \times 10^4 \sim 7$ and ~ 0.7 , respectively, i.e. $\mu' \sim 7 \times 10^{-4}/L_0$ at low-frequency side and $\mu' \sim 0.7 \times 10^{-4}/L_0$ at the high-frequency side. These values should be equal to $(L_1+L_2)/L_0$ and L_2/L_0 , respectively [see Eq. (4.161) Section 4.16]. From this we get $L_2 \sim 7 \times 10^{-5} H$ and $L_1 \sim 6.3 \times 10^{-4} H$. The values of the components were obtained more accurately by CNLS fitting utilizing these values as initial guesses. These accurate values are $R_1=5.8 \Omega$, $L_1 = 5.9 \times 10^{-4} H$, $R_2 = 0.2 \Omega$ and $L_2 = 7.7 \times 10^{-5} H$, subject to 20% error. The continuous lines in Figures 6.14(a, b) and Figure 6.15 correspond to the fitted values.

The analysis presented above indicates that the coil without the magnetic sample behaves like a series RL circuit, but when YIG sample is inserted, it behaves like a

series R_2L_2 circuit, further connected in series to a parallel R_1L_1 circuit. This may be explained as follows. The portion of the coil covering the pellet may be represented by an inductor L_1 and the remaining portion by a series-connected inductor L_2 . Since L_1 contains the sample, its value will be equal to the inductance of that portion of the empty coil multiplied by the relative permeability of the sample. The thickness of the sample is such that it covers about 5 turns of the coil. The inductance of an empty coil of length “ $b=4\text{mm}$ ” and radius “ $a=7.5\text{mm}$ ” having 5 turns, would be 0.6×10^{-6} H. The value of L_1 divided by this is 963, subject to 20% error, and should be the value of the permeability of the sample. The values of R_1 , L_1 , R_2 and L_2 obtained by impedance spectroscopy are frequency independent. Therefore, the value of permeability may be taken to be the low-frequency value. It agrees with the fact that measurements were carried out below 10 kHz. The value of permeability obtained above is close to the value 1000, reported by using other methods. It may be noted that the value $R_2 = 0.2 \Omega$ is close to the series resistance of the empty coil and may be taken to be coil resistance. However, R_1 is about 30 times larger than R_2 . This may be attributed to the domain reorientation in YIG sample.

6.4 CORROSION AND ELECTROCHEMISTRY

Corrosion is the process of deterioration of metals and related materials due to the destructive attack by its reaction with the environment. It is electrochemical and ordinarily begins at the surface. It destroys the metals by converting them to oxides or other corrosion products (Van Vlack 1989; McCafferty 2010; Callister 2001). Erosion–corrosion arises from the combined action of chemical attack and mechanical abrasion or wear as a consequence of fluid motion. Other materials such as plastics, concrete, wood, ceramics, and composite materials also undergo deterioration when placed in some environment. Ceramic materials are relatively resistant to deterioration and undergo corrosion at elevated temperatures and in extreme environments. During exposure to a solvent, polymers may absorb the solvent and swell or get dissolved. Also, their structure may change and bonds may be broken when exposed to heat and radiation. The general term “degradation” is used in the case of polymers. The word “rusting” applies to the corrosion of iron and plain carbon steel.

Various types of corrosion and their mechanisms are described in great detail in text books (Barsoukov and Macdonald 2005; Van Vlack 1989; McCafferty 2010). To fix the ideas of application of impedance spectroscopy to the study of corrosion, we will consider metal corrosion only. For describing metal corrosion, consider a metal piece exposed to an electrolyte. A metal atom M^0 near a low-oxygen-concentration area at the surface loses electrons and becomes a positive ion M^{m+} (the superscript represents the charge on the ion), and this process is expressed by the equation



If these electrons are accepted by a nonmetallic element N^0 or by another metallic ion, then the metal ions which lost their electrons would either dissolve in the surrounding

electrolyte, such as water, or combine with nonmetallic ions to form a surface deposit. This is corrosion reaction. This process is described as (Van Vlack 1989)



Or



Electron loss is called oxidation and electron gain is called reduction. The location where electron loss (oxidation) occurs is called anode and where the electron gain (reduction) occurs is called cathode. Examples of anodic and cathodic reactions are schematically shown in Figures 6.17 and 6.18 (McCafferty 2010).

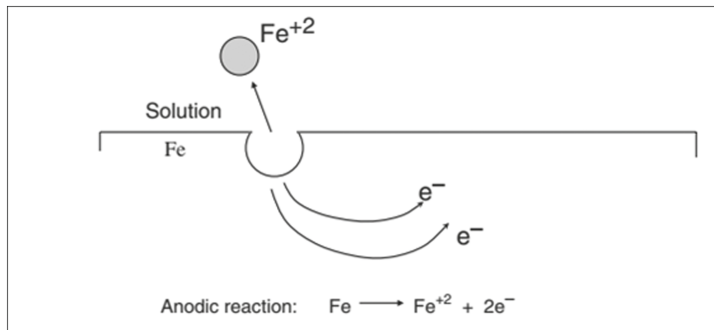


FIGURE 6.17 Example of an anodic reaction. (Reprinted with Permission from Springer, McCafferty 2010, Figure 2.2, Introduction to Corrosion Science, Springer, New York.)

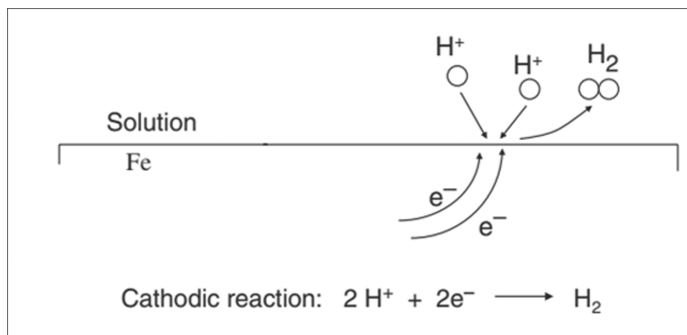
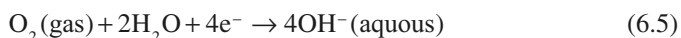


FIGURE 6.18 Example of a cathodic reaction – hydrogen evolution on iron immersed in an acid solution. (Reprinted with Permission from Springer, McCafferty 2010, Figure 2.3, Introduction to Corrosion Science, Springer, New York.)

Another common cathodic reaction that takes place with neutral or basic solutions involves reduction of dissolved oxygen to yield hydroxyl ions.



On a corroding metal surface, anodic and cathodic reactions occur in a coupled manner. For example, for iron plate immersed in acid solution, these reactions would occur at different places on the metal surface. At a certain place on the surface, iron atom moves to the solution as Fe^{2+} and the two electrons are liberated here, which are consumed at some other place by joining with two H^+ ions from the acid solution to yield H_2 gases. This process is schematically illustrated in Figure 6.19.

The anode and cathode locations may be situated either close to each other or far away from each other. It means that the oxidation and reductions reactions can take place physically side by side or may be physically separated, provided there exists an electrical connection for charge transfer. For the corrosion to proceed the electron loss (oxidation) and electron gain (reduction) processes must occur simultaneously, and the required conditions for this to happen are presence of an anodic reaction, a cathodic reaction, a metallic path of contact between anodic and cathodic sites and an electrolyte in contact. An electrolyte is a material possessing ions capable of conducting a current. The metal atom moves away at the anode site only. Therefore, all corrosion takes place at anode, as there is no metal loss at the cathode. Corrosion will stop when the electrical connection is interrupted, so that charge transfer does not take place, reactants receiving electrons are depleted or anode products are saturated (i.e. electrons and metal ions produced at the anode are not getting removed). The

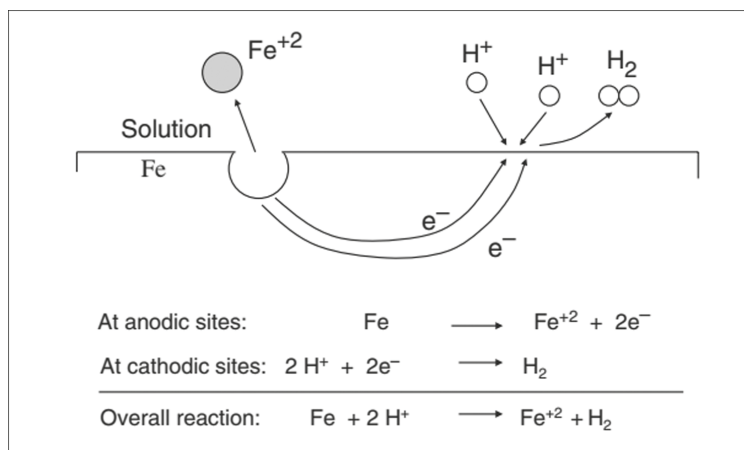


FIGURE 6.19 Coupled electrochemical reaction occurring at different sites on the same metal surface for iron in an acid solution. The electrons lost by the oxidation of Fe atoms are consumed in the reduction of two H^+ ions to form H_2 gas. (Reprinted with Permission from Springer, McCafferty 2010, Figure 2.4, Introduction to Corrosion Science, Springer, New York.)

procedures facilitating these are called corrosion control (Van Vlack 1989; McKafferty 2010). When electrons produced at the anode are not removed, reverse reaction would establish an equilibrium.

Two major forms of corrosion are uniform corrosion, where the whole metal surface is attacked, and localized corrosion, where corrosion occurs at some high-energy sites on the surface. The high-energy sites emerge due to presence of crystal imperfections, kinks, stress points, etc. In the case of uniform corrosion the anode and cathode sites keep on changing their locations on the metal surface, whereas in localized corrosion their locations remain fixed. In the uniform corrosion the metal sheet would get thinner and thinner and finally get completely dissolved, whereas in localized corrosion the anode site may develop a pit which may propagate. When two metals are in mechanical or electrical contact in a corrosive environment, one metal may act as anode and get corroded while the other acts as cathode. Such a corrosion is called galvanic corrosion.

An electrolyte is a solution that contains dissolved ions. The interior of an electrolyte may consist of a variety of charged and uncharged species such as Na^+ , Cl^- ions, H_2O molecules and other materials. Owing to the fact that oxygen atom is more electronegative as compared to hydrogen atom, there is partial negative charge at the oxygen end of the H_2O molecule. Thus, the water molecule has an electric dipole moment directed from oxygen toward middle of hydrogen atoms. Because these H_2O dipoles are randomly oriented and other positive and negative ions are equal in number, there is no electric field in the electrolyte and no net charge within a volume element in the electrolyte. However, due to electrostatic forces, the positive or negative ions reorient the water dipoles lying in their vicinity. As a result, a positive ion gets surrounded by water dipoles (molecules) with their negative ends oriented toward it, and a negative ion gets surrounded by water dipoles (molecules) with their positive ends oriented toward it. Such water molecules are called water of hydration (McKafferty 2010). In the absence of external electric field the dipoles are randomly oriented. When an external dc field is applied, they reorient themselves along the field direction. This process is like charging/discharging of a capacitor and is characterized by a time constant τ . The same dipole in different materials will have different time constants. In an alternating field these dipoles would tend to follow the direction of varying field by turning back and forth. However, the dipoles cannot exactly follow the field. The delayed response to the applied field is called relaxation. When an ac field is applied to an electrochemical system, the system would attain steady state with the time constant τ , which is also called relaxation time.

The common boundary separating two phases is called an interface. We can supply electrons to the metal side of the metal/solution interface, or we can extract electrons from the metal side of the interface by connecting the metal to an external device. The metal side may thus be made to be negatively charged or positively charged, respectively. The formation of electrical double layer is described by taking an example. When a positively charged metal sheet is in contact with an electrolyte, the metal side of the interface may be thought of having an array of positive lattice ions since electrons are delocalized and are moving freely inside the metal. As a result, negative ions or negative ends of dipoles present in the electrolyte get attracted and accumulated on the electrolyte side of the interface. But these ions are in constant thermal motion.

Therefore, the electrolyte side of the interface has a diffuse region having relatively higher number of negative ions, so as to balance the positive charge on the metal side. This is an electrical double layer. This view of the electrical double layer is called the Gouy–Chapman model. There are several other views of the electrical double layer (McCafferty 2010) and are not given here. Due to the electrical double layer, there exists a potential difference across the interface, and this potential difference gives rise to electrode potential. The potential V_A at a point is defined as the work that would be required to be done for bringing a unit positive charge from infinity to that point. The quantity $V_B - V_A$ is the potential difference between points B and A or the potential of point B with respect to A. This potential difference across the metal/solution interface is commonly referred to as an electrode potential. Practically, a point at a location away from the metal–solution interface may be chosen as a reference point, and an electrode called as standard reference electrode may be installed there with respect to which V_B and V_A can be measured. The hydrogen electrode is universally accepted as a standard reference electrode. However, another commonly used reference electrode is silver–silver chloride reference electrode, which consists of a silver wire coated with AgCl immersed in a solution of KCl plus saturated AgCl. Several other reference electrodes have been developed to suite specific systems (McCafferty 2010), e.g. copper–copper sulphate reference electrode is used for measurements with buried structures, such as pipe lines. Electrode potentials are measured by using electrometer which is a high-impedance device, so that negligible current flows through the meter. This would not interfere with the electrode reactions at the interface and the electrode potential would not be altered during measurement. When two half cells are coupled, the so-called electrochemical cell is formed.

During corrosion, anodic and cathodic reactions occur, which are charge transfer processes that take place at the metal–electrolyte interfaces. Therefore, study of corrosion (i.e. determination of the corrosion rate and identifying the degradation mechanisms) is essentially the study of these charge transfer processes at the interface where the ions have to pass through the double layer during corrosion. The emergence of electrical double layer is like charging of a capacitor. The passage of ions across the interface (double layer) has to face a potential difference and hence some energy loss, i.e. ions would face some resistance. Thus the metal–solution interface may be represented by an equivalent circuit shown in Figure 6.20 (McCafferty 2010). In Figure 6.20, C_{dl} is the capacitance of the double layer, R_p is the polarization resistance (charge transfer resistance) and R_s is the solution resistance (i.e. resistance between double layer and tip of the reference electrode). It has been shown that the steady-state corrosion current is inversely related to the dc resistance, R_p , across the interface (Stern and Geary 1957; Barsoukov and Macdonald 2005). Thus, study of R_p can be used to study the corrosion rate.

The Z'' versus Z' plot for this circuit (Figure 6.20) is a semicircular arc having high-frequency intercept with the Z' axis at $Z' = R_s$ and low-frequency intercept at $Z' = R_s + R_p$. The arc peaks at the frequency given by $\omega R_p C_{dl} = 1$, where $R_p C_{dl}$ is the time constant. The values of the equivalent circuit parameters can be obtained in this way. These values may also be estimated by looking at Z'' versus frequency and Z' versus frequency plots. When the arc appearing in the Z'' versus Z' plot is not clearly semicircular, presence of more than one time constants, i.e. relaxation

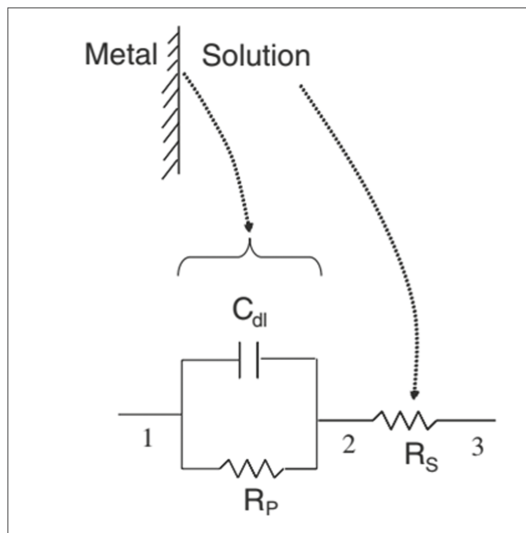


FIGURE 6.20 Equivalent circuit for an electrical double layer (edl). C_{dl} is the capacitance of the edl, R_p is the polarization resistance and R_s is the solution resistance. (Reprinted with permission from Springer, McCafferty 2010, Figure 14.4, Introduction to Corrosion Science, Springer, New York.)

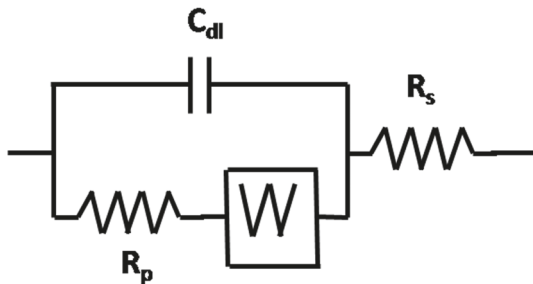


FIGURE 6.21 Equivalent circuit model for an electrochemical interface having a diffusion component represented by Warburg impedance W .

processes, is implied. If there appear two clear arcs, then two processes are implied (see Chapter 4). Appearance of a linear portion inclined at 45° to the Z'' in the Z'' versus Z' plot indicates the presence of diffusion-controlled process and can be modeled by including the so-called Warburg impedance W as shown in Figure 6.21.

Warburg impedance is given by

$$Z_w = Z'_w - jZ''_w = \frac{\sigma}{\omega^{1/2}}(1 - j) \quad (6.6)$$

where σ is the conductivity and $j = \sqrt{-1}$.

Corrosion inhibition of iron in acid solutions was studied by McCafferty and McArdle (1995). It was found that the low-frequency intercept increases for the treated iron, i.e. the value of R_p is increased. The increased value of R_p indicates that corrosion rate has decreased.

One of the most successful applications of impedance spectroscopy has been in the evolution of the impedance properties of polymer-coated metals and their changes during exposure to corrosive environment (Mansfield 1995). Polymer coating is used for corrosion protection. The model shown in Figure 6.20 is suitably modified to represent possible charge transfer processes that might contribute to the impedance of the corroding system. For example, equivalent circuit model generally used to represent a polymer-coated metal placed in aqueous media is shown in Figure 6.22.

Here, C_c is the coating capacitance that appears between solution and metal, R_s is the solution resistance, R_{cp} is the pore resistance of the coating, resulting from the formation of ionically conducting paths across the coating, R_p is the polarization resistance of the area at the metal/coating interface where corrosion occurs and C_{dl} is

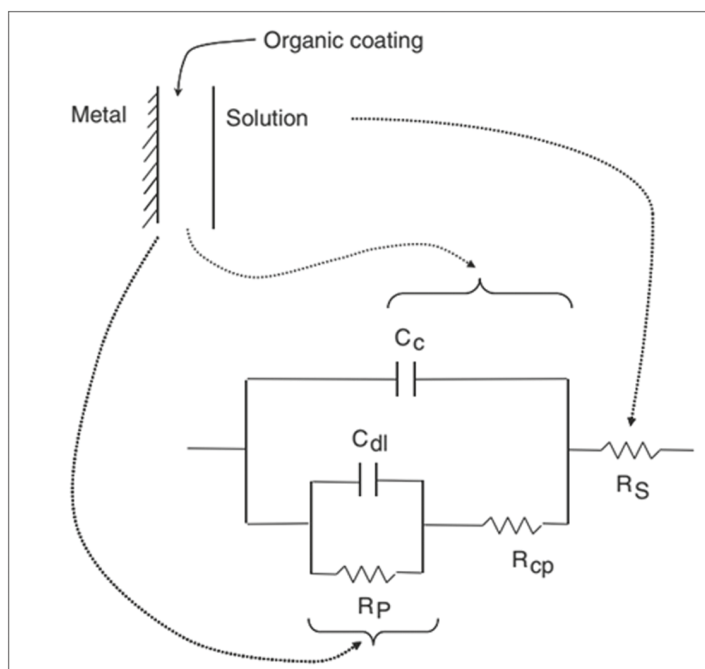


FIGURE 6.22 Equivalent circuit for an organic coating on a metal substrate. C_c is the coating capacitance, R_s is the solution resistance, R_p is the polarization resistance at the metal/solution interface, C_{dl} is the corresponding double-layer capacitance and R_{cp} is the pore resistance of the coating. (Reprinted with Permission from Springer, McCafferty 2010, Figure 14.18, Introduction to Corrosion Science, Springer, New York and from Springer, Mansfield 1995, Figure 1, Use of Electrochemical Impedance Spectroscopy for the study of corrosion Protection by Polymer Coatings. *J. Appl. Electrochemistry*, 25: 187–202.)

the corresponding double layer capacitance. The metal comes in direct contact with the solution through the pores in the coating.

The value of C_c is given by $C_c = \epsilon \epsilon_0 A/d$, where ϵ is the relative permittivity of the polymer used for coating, A is the area of electrode exposed to the solution and d is the thickness of coating. The increase in C_c with exposure time can be used to determine the water uptake of the coating. The parameters R_{CP} , R_p and C_{dl} are related to the total area, A_d (called the delaminated area, disbonded or wetted area), of the metal electrode coming in contact to the solution through the pores. The effect of change in A_d can be vaguely seen by visualizing the pore as a small cylinder of area of cross section A_d and length d filled with a liquid of resistivity ρ . If the value of ρ is not changed, then increase in A_d will create an increase in C_{dl} and decrease in R_{CP} and R_p . Also, R_{CP} would decrease if the resistivity of the coating polymer decreases. Changes in these parameters can be monitored by using impedance spectroscopy and value of delaminated area, A_d , can be estimated, which, in turn, may be used to obtain the fraction of the total electrode area delaminated (wetted) by the solution.

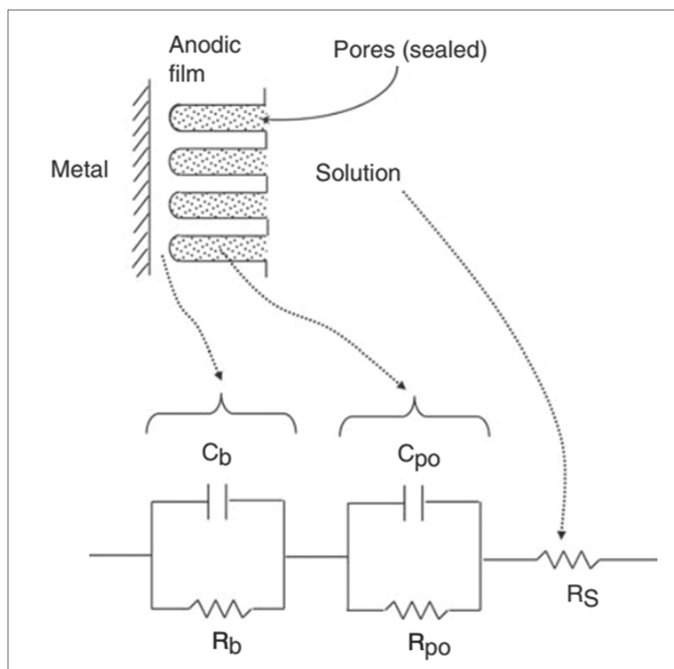


FIGURE 6.23 Schematic diagram and the corresponding equivalent circuit of an anodized coating. R_b - C_b combination represents the barrier layer of the oxide, R_{po} - C_{po} represents the porous oxide layer. (Reprinted with Permission from Springer, McCafferty 2010, Figure 14.21, Introduction to Corrosion Science, Springer, New York and from Pergamon, Mansfield 1993, Figure 5, Models for the Impedance Behavior of Protective Coatings and Cases of Localized Corrosion, *Electrochimica Acta*, 38: 1891–1897.)

There are different methods of corrosion control, such as cathodic protection, corrosion protection by organic coatings and the use of corrosion inhibitors. One of the corrosion protection methods is the use of metals or alloys which have inherently low corrosion rates in a solution due to the existence of a passive oxide film. Passivity is defined as the reduction in chemical or electrochemical activity of a metal due to the action of the metal with its environment so as to form a protective film on the metal surface. An electrolytic passivation process used to increase the thickness of the natural oxide layer on the surface of metal parts is termed as anodizing. The part to be treated forms the anode electrode of an electrolytic cell. Anodizing increases resistance to corrosion and wear and provides better adhesion for paint primers and glues than bare metal does.

An equivalent circuit frequently used to represent anodized metal surfaces in contact with a solution is shown in Figure 6.23, where the barrier layer is represented by a parallel R_b - C_b combination, and the porous layer by R_{po} - C_{po} circuit. R_s is the solution resistance as usual. During anodization of aluminum alloys by sulfuric acid, oxide films are formed having barrier layer close to the metal surface and an outer porous layer in which the pores can be sealed in aqueous solutions.

6.5 POLYMERS AND COMPOSITES

Polymers, e.g. plastics, are a commodity of modern life. Their use is ubiquitous from low-tech, high-volume consumer products, such as packaging materials, tubing or furniture, to high-tech specialized products, such as medical implants or technical garments (Ates 2011).

The word polymer is derived from two Greek words “poly”, which means many, and “mer”, which means unit or part. Polymer is a material consisting of very large molecules (macromolecules) composed of many repeating subunits (called monomers) and have a chain of covalently bonded atoms that forms a backbone structure (Van Vlack 1989). The number of monomers contained in a macromolecule is called degree of polymerization. Few popular polymers are polythene (a thermoplastic polymer which softens on heating and hardens on cooling), Teflon (obtained by heating tetrafluoroethene with a free radical or persulfate catalyst at high pressure and is chemically inert and resistant to attack by corrosive reagents and is used in making oil seals and gaskets and also used for nonstick surface-coated utensils), nylons 6, 6 (prepared by the condensation polymerization of hexamethylenediamine with adipic acid under high pressure and at high temperature and used to make high-strength fibers, sheets, bristles for brushes and in textile industry), Nylon 6 (obtained by heating caprolactum with water at a high temperature and used for making tyre cords, fabrics and ropes), Dacron or terylene (the best-known polyester produced by heating ethylene glycol with terephthalic acid in the presence of zinc acetate–antimony trioxide catalyst, is crease resistant and is used in blending with cotton and wool fibers and also as glass-reinforcing materials in safety helmets, etc.), melamine–formaldehyde polymer (formed by the condensation polymerization of melamine and formaldehyde, used to make unbreakable crockery) etc. (NCERT Chemistry Part II 2021).

Polymers, in general, are considered as insulators. A typical polymer such as polyethylene (PE) has a conductivity of 10^{-16} S/m, which is much smaller than that of copper ($\sim 5.8 \times 10^7$ S/m). However, they become conducting when suitably doped. It was observed that polyacetylene (CH_x) which is an insulator having a conductivity of about 10^{-6} S/m, shows high conductivities (up to 10^7 S/m) (Ito et al. 1974; Shirakawa et al. 1977) when doped with doping elements such as Br_2 , I_2 , AsF_5 , and could be n or p doped. This discovery led to the development of novel class of organic materials, called synthetic metals (Ates 2011). A polymer that can transport charges, independently of their intrinsic conductivities (conductor or semiconductor) and charge transport characteristics, is termed as conducting polymer. These are π -conjugated polymers, i.e. polymers having backbone with alternating single and double (or triple) covalent bonds. The conducting polymers are also sometimes called conductive polymers or organic polymeric conductors or conjugated conductive polymers (Guo and Facchetti 2020; Chandrasekhar 2018; Namsheer and Rout 2021). A conjugated carbon chain consists of alternating single and double bonds, where the highly delocalized, polarized and electron-dense p bonds are responsible for its electrical and optical behavior. Typical conducting polymers include polyacetylene (PA), polyaniline (PANI), polypyrrole (PPY), polythiophene (PTH), poly(para-phenylene) (PPP), poly(-phenylenevinylene) (PPV), and polyfuran (PF). As-synthesized conductive polymers exhibit very low conductivities. When an electron is removed from the valence band (p-doping) or added to the conduction band (n-doping, which is far less common), a conducting polymer becomes highly conductive. Positive and negative charge carriers generated by doping move to opposite electrodes when electric field is applied enhancing the conductivity.

Areas of recent applications of conducting polymers include Li-ion battery cell, organic solar cells (OSCs) for photovoltaic modules, organic thin-film transistors (OTFTs) for displays and circuits and organic light-emitting diodes (OLEDs) for display and lighting (Guo and Facchetti 2020). Applications for development of supercapacitors are also being explored (Wang et al. 2016; Namsheer and Rout 2021). Conducting polymers are deposited on carbon electrodes for achieving improved performance. Carbon-based materials are popular for the electrochemical applications, as an electrode material due to good polarization of the electrode, high surface area, processability, low cost, accessibility and thermal and chemical stability. These electrodes modified by deposition of conducting polymers are used in various applications, such as batteries, capacitors, electrochromic displays, light-emitting diodes (LEDs), photovoltaic cells and microfabricated biosensing devices. The conjugated double bonds in the polymer backbone allow free movement of electrons within the conjugating length, which makes them electrically conductive. The conductivity of conducting polymers results from the formation of charge carriers upon oxidizing (p-doping) or reducing (n-doping) their conjugated backbone. It is believed that conductivity is caused by polarons, which are formed due to localized electronic states created during oxidation. Impedance spectroscopic studies on polypyrrole, polycarbazole, polyaniline and polythiophene have been reviewed by Ates (2011).

By combining materials (polymeric, ceramic, metals, etc.) in certain ways it is often possible to develop a newer material, called composites, to achieve a property

which the individual materials did not possess (Ruoff 1973). A composite material is composed of at least two materials, which combine to give properties superior to those of the individual constituents. Many composite materials are composed of just two phases: one is termed the matrix, which is continuous and surrounds the other phase, often called the dispersed phase (Callister 2007). In general, most of the composites possess discontinuous phases in the form of particles or fibers dispersed in a matrix that is usually a polymer but may be a metal or a ceramic. Composites may be classified as particle-reinforced, fiber-reinforced and structural. Thus we have carbon fiber-reinforced polymer (CFRP) composites, metal-matrix composites (in which the matrix is a ductile metal), ceramic-matrix composites, carbon-carbon composites (which is carbon fiber-reinforced carbon-matrix composite), hybrid composites (which is obtained by using two or more different kinds of fibers in a single matrix). A structural composite is normally composed of both homogeneous and composite materials. Carbon is a high-performance fiber material that is the most commonly used reinforcement in advanced (i.e. nonfiber glass) polymer-matrix composites.

Some examples of composites are reinforced concrete (composite of steel rods in a concrete matrix), fiber-reinforced plastics (glass fibers in polymeric matrix), concrete (composite of coarse rock aggregate, fine sand aggregate and hydrated Portland cement (Van Vlack 1989; Ruoff 1973; Callister 2007).

Now, we describe few very simple examples of use of impedance spectroscopy in the study of polymers and composites. Impedance spectroscopy was used for studying the electrical transport properties of bulk heterojunction solar cells utilizing conducting polymers (Knipper et al. 2007). In polymer photovoltaics, the material combination most frequently investigated has been the p-type conjugated polymer poly [3-hexylthiopoly [3-hexylthiophene-2, 5-diy]] (P3HT) blended with the electron acceptor [6, 6]-phenyl-C61 butyric acid methyl ester (PCBM). Impedance spectroscopy was used for study of the electrical transport properties of bulk heterojunction solar cells comprising composites of P3HT and PCBM, sandwiched between a transparent ITO (indium tin oxide) front electrode and an aluminum back electrode, as well as a polymer buffer layer (Knipper et al. 2007). The samples were prepared by spin coating poly(3, 4-ethylenedioxythiophene) polystyrene sulfonate (PEDOT:PSS) film onto a cleaned ITO substrate followed by polymer and polymer-fullerene blend spin coating. Then metal (Al or Au) electrode was fixed (by using evaporation). The measurements were carried out in the frequency range 0.05 Hz–5 MHz. By varying the PEDOT:PSS and the active layer thickness, an equivalent circuit model shown in Figure 6.24 was developed that represented the experimental results best.

The equivalent circuit of Figure 6.24 can be described by visualizing the traversal of current (charge) entering at the Al electrode and returning to the impedance meter from ITO side. The inductance (L_1) is related to the connecting wires and its contribution becomes significant only at frequencies above 1 MHz. The Al electrode to P3HT blend contact is represented by R_1C_1 combination. The R_3C_3 and R_2C_2 combinations were attributed to the semiconductor P3HT layer and to the PEDOT:PSS layer, respectively. The resistances due to feed line and ITO contact are represented by the resistance R_0 . The assignments of these components to various layers were

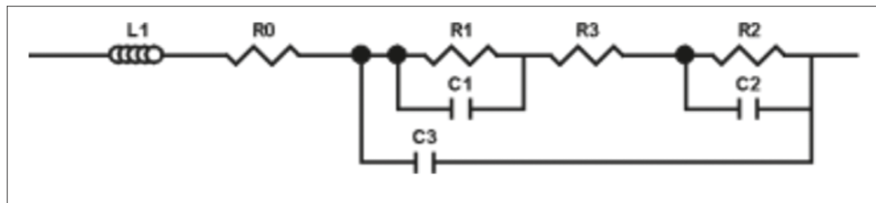


FIGURE 6.24 Equivalent circuit for polymer-fullerene solar cell. R_2 and C_2 correspond to PEDOT:PSS, R_3 and C_3 to P3HT, R_1 and C_1 are assigned to the P3HT/AI interface, R_0 represents the ITO contact resistance and inductance L_1 refers to lead contributions. (Reprinted with Permission from Knipper et al. 2007, Figure 1, Impedance Spectroscopy on Polymer-Fullerene Solar Cells. *Zeitschrift für Naturforschung A*, 62: 490–494. Open Access.)

achieved by performing measurements by varying the PEDOT:PSS and the active layer thicknesses and repeating the measurements on (ITO/P3HT/AI) system and on (ITO/PEDOT:PSS/P3HT/AI) system. The simpler equivalent circuits having two or three parallel RC circuits in series could not give a good fit to the thickness dependence of the data. A typical fitted dataset is shown in Figure 6.25.

A method utilizing impedance spectroscopy has been described (Arof et al. 2014) for determining the values of the diffusion constant (D), mobility (m) and charge carrier concentration (n) in polymer electrolytes and ionic conductors. A polymer electrolyte is a polymer matrix capable of ion conduction. Coordination of an inorganic or organic salt to a polymer matrix gives rise to a solid-state polymer electrolyte. Ion exchange takes place through coordination when potential is applied. The polymer electrolytes have advantages over liquid electrolytes in terms of leakproof, size and shape flexibility. Polymer electrolytes are substituted for the liquid electrolyte in new-generation electrochemical devices such as batteries, supercapacitors, solar cells and electrochromic windows, etc. (Winie et al. 2020). The fundamental property of a polymer electrolyte is conductivity (s). Conductivity in principle is the product of the number density (n), the mobility (m) of charge carriers and the elementary charge (e) (Arof et al. 2014; Bandara and Mellander 2011, Bandara et al. 2011). Impedance measurements were carried out by sandwiching a polymer electrolyte between two blocking electrodes. The system was represented by an equivalent circuit model comprising a parallel RC circuit (representing the electrolyte) and a capacitor C_e (representing the blocking electrode). When the Nyquist plot showed a depressed arc, C was replaced by a CPE. The frequencies where the arc has a maximum Z'' value (at the higher-frequency side) and a minimum Z'' value (at lower-frequency sides) were used for the calculations.

Impedance spectroscopy was used to study the effect of grains and grain boundaries in the electrical response and transport properties of flexible bismuth ferrite and polyvinylidene fluoride (BFO-PVDF) nanocomposites (Singh and Sharma 2020). The high dielectric constant polymer-based nanocomposite materials are extensively used for their possible applications in electronic devices like dynamic random access memory, actuators, transducers and energy storage devices. The polymer polyvinylidene fluoride (PVDF) is a popular polymeric material having different

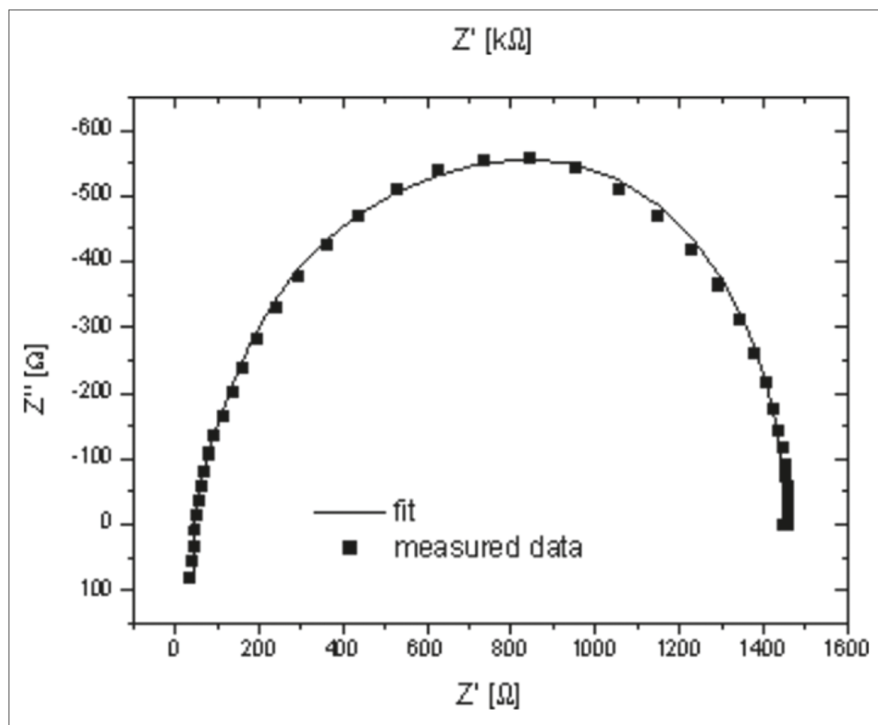


FIGURE 6.25 Figure 4 Z'' versus Z' plot of the impedance data of the heterostructure ITO/PEDOT:PSS (75 nm)/P3HT:PCBM (120 nm)/Au (100 nm) in the frequency range $0.05\text{--}5 \times 10^6$ Hz. The active area of this sample is 5.3 mm^2 . Fit results: $L_1 = 3.5 \mu\text{H}$; $R_0 = 40 \Omega$; $R_1 = 485 \Omega$; $R_2 = 553 \Omega$; $R_3 = 373 \Omega$; $C_1 = 1.8 \text{ nF}$; $C_2 = 9.7 \text{ nF}$; $C_3 = 1.3 \text{ nF}$. (Reprinted with Permission from Knipper et al. 2007, Figure 4., Impedance Spectroscopy on Polymer-Fullerene Solar Cells. *Zeitschrift für Naturforschung A*, 62: 490–494. Open Access.)

phases and is widely used to develop devices like capacitors, piezoelectric sensors, energy-harvesting microwave absorber, pyroelectric detectors, etc., owing to its excellent dielectric, pyroelectric, ferroelectric and piezoelectric properties. Bismuth ferrite (BFO) nanopowder was prepared by the sol-gel autocombustion method. Flexible BFO-PVDF nanocomposite films with different compositions were prepared by pouring the solution of PVDF and dimethylformamide (DMF) containing BFO on a glass plate followed by solvent evaporation by keeping in an oven. The impedance measurements were carried out in the frequency range of 100 Hz–1 MHz at different temperatures.

A typical Z'' versus Z' plot for the composite having 10% at. wt. of PVDF is shown in Figure 6.26. The Z'' versus Z' plots have a depressed arc and M'' versus M' plots (not shown here) also have depressed arcs. An equivalent circuit model comprising a parallel combination of resistance R_g , capacitance C_g and a CPE representing the grain behavior, further connected in series to a parallel combination of a resistance R_{gb} and capacitance C_{gb} representing the grain boundary behavior, was used

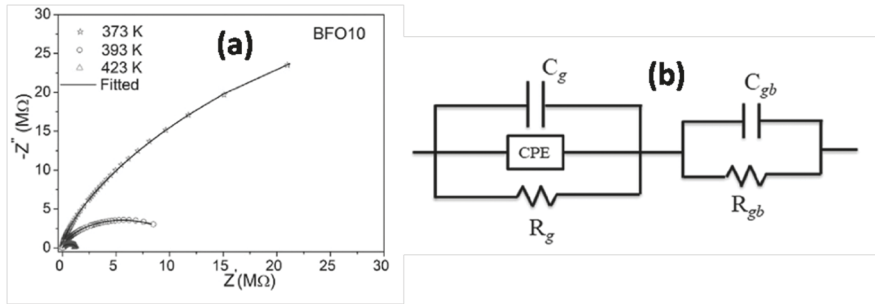


FIGURE 6.26 (a) Nyquist plots (Z'' vs Z') of BFO-PVDF (10% at. wt. of PVDF) (nanocomposites at different temperatures) and (b) equivalent electrical circuit. (Reprinted with Permission from Elsevier, Singh and Sharma 2020, Figure 9, Impedance Spectroscopy and Transport Properties of Polymer-Based Flexible Nanocomposites, Solid State Communications, 319: 114012–114025.)

to represent the impedance behavior. The parameters of the equivalent circuit were determined and the relaxation time was calculated by using the peak values of M'' in the M'' versus M' plots (plots not shown here). As is seen in Figure 6.26, the low-frequency intercept on the Z' axis, i.e. resistivity of the sample, decreases as temperature is raised, indicating the NTCR behavior of the system. Value of ac conductivity (σ_{ac}) was calculated by using the relation $\sigma_{ac} = \omega \epsilon \epsilon_0 \tan \delta$, where ϵ_0 is the permittivity of free space, ϵ is the dielectric constant, ω is the angular frequency and $\tan \delta$ is the loss tangent. The frequency dependence of σ_{ac} was analyzed by using the relation $\sigma_{ac} = \sigma_{dc} + A\omega^s$, where A is temperature-dependent constant and s is the frequency exponent. The value of the parameter s was obtained by plotting $\log(\sigma_{ac} - \sigma_{dc})$ versus $\log(\omega)$. The value of s was found to decrease with temperature indicating that the most dominating conduction mechanism is possibly the correlated barrier hopping.

Impedance spectroscopy has been applied to study the effect of compression on electrical behavior of multiwalled carbon nanotubes (MWCNTs)–polydimethylsiloxane (PDMS) composites (Helseth 2018). Composites made of elastomers and carbon nanotubes are promising materials for soft electronics applications due to their enhanced permittivity, conductivity and piezoresistive characteristics. It is known that electrical conductivity of rubbers increases when it is loaded with carbon black. The conductivity shows a steep rise when the volume fraction of carbon particles approaches a critical value called the percolation threshold, where the carbon particles are closely spaced and electron tunneling occurs resulting in enhanced conductivity. As carbon nanotubes (CNT) have higher aspect ratio and polarizability, lower threshold values are observed for CNT-polymer composites. Also, the value of this threshold is greatly influenced by polymer matrix and method of preparation, allowing to get tunable electrical properties. MWCNTs have a tendency to form aggregates because of van der Waals interactions, which deteriorates the electrical properties. Natural rubbers or synthetic elastomers are useful for obtaining stretchable, bendable and squeezable composites. Elastomers loaded with carbon nanotubes hold considerable

promise as multifunctional materials. For example, PDMS loaded with MWCNTs has been shown as a promising multifunctional material for developing sensors for small forces and metamaterials in electromagnetics. For further applications, it is useful to understand the electrical behavior of MWCNT-PDMS composites when subjected to pressure.

Impedance spectroscopy was applied to study the effect of compression on electrical behavior of MWCNT-PDMS composites near percolation threshold (Helseth 2018). Impedance measurements were carried out by using two-probe method up to 1 MHz under various values of applied force. Conductive elastomer samples of dimensions 20 x 15 x 1 mm were prepared by mixing MWCNTs having length of 5–9 μm and diameters of 110–170 nm with PDMS in various compositions (mass fractions MWCNT of 1.1, 4.5, 5.5, 10.0, 16.7 and 23.4 wt%) and curing at 110°C for 30 minutes. Impedance measurements at frequencies up to 1 MHz were done by mounting the samples between two copper electrodes, one of which was fixed and the other was moved with a linear stage that had a Vernier force sensor with range 0–50 N having resolution 0.05 N attached to it. Measurements were carried out for forces 2, 5, 10, 15, 20 and 30 N.

The Z'' versus Z' typical plots for the composition 5.5 wt% for these applied forces are shown in Figure 6.27. The plots are semicircular arcs. These plots for other compositions except 1.1 wt% were similar to this. The experimental data were fitted to an equivalent circuit model comprising a parallel $R_p C_p$ combination in series with a resistance R_s , and their values were calculated. Corresponding fits are shown as solid lines in the figure. The values of R_s are much smaller as compared to R_p , and, therefore,

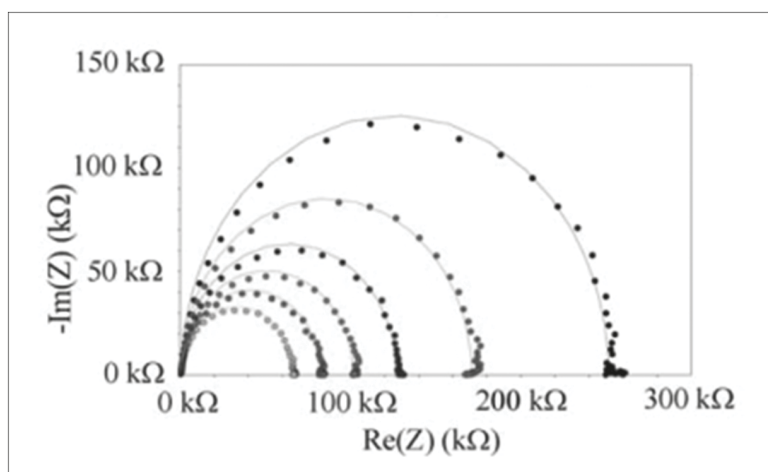


FIGURE 6.27 Z'' ($-\text{Im}(Z)$) vs Z' ($\text{Re}(Z)$) plots for forces 2- (outermost arc), 5-, 10-, 15, 20 and 30 N (innermost arc). The solid lines show the fitted values using the equivalent circuit model comprising a parallel $R_p C_p$ in series with R_s . (Reprinted with Permission from IOP Publishing, Helseth 2018, Figure 3(b), Electrical Impedance Spectroscopy of Multiwall Carbon Nanotube–PDMS Composites under Compression, Mater. Res. Express. 5: 105002–105011.)

the expected shift in the Z'' versus Z' plots is not visible. It was found that R_s and R_p both decrease, while C_p increases, with applied force. R_s was attributed to the contact between sample and electrodes and the decrease in R_s was considered to be due to the increased contact between carbon nanotubes and the external copper electrodes when pressure is applied. The decrease in R_p and increase in C_p was explained by keeping in mind that in polymer solutions, MWCNTs have a tendency to form clusters due to van der Waals interactions and there may be electron tunneling between arms of the neighboring clusters. Under applied force the MWCNT clusters (relatively more conducting regions of the composites) would move closure which would raise the capacitance C_p due to decreased distance between conducting clusters, and lower the resistance R_p due to increased intercluster tunneling. Effort was made to establish a functional relationship of resistances and capacitance with the applied forces and with volume fraction of MWCNTs in the composite.

Impedance spectroscopy was used to monitor the process of dedoping in a planar junction between an electrolyte and a conducting polymer by performing the impedance measurements during a moving front on a planar electrolyte/PEDOT:PSS junction. An equivalent circuit model comprising a time-varying resistor in parallel with a capacitor represented the data well, where the resistance corresponds to ion transport in the dedoped region of the film and the capacitor corresponds to the doping/dedoping processes at the moving front. The resistor was found to be in good agreement with values of ion density, and drift mobility obtained from the moving front measurements. This work offers a physical description of the impedance of conducting polymer/electrolyte interfaces based on materials parameters and helps demystify the interface behavior by using parameters such as ion density and drift mobility (Stavrinidou et al. 2014).

Impedance spectroscopy has been used to study $Ba_{0.5}Sr_{0.5}TiO_3-Ca_{10}(PO_4)_6(OH)_2$ ceramic biocomposites with a view to develop suitable compositions for designing bioelectrets and bone scaffolds (Das and Dobbidi 2021). It is known that electric fields can induce biological reactions on the interfaces producing cell proliferation and directional migrations (known as electrotaxis), leading to faster healing of damaged bones (Tofail and Bauer 2016a, 2016b; Lang et al. 2011; Willner and Willner 2001). Properties such as piezoelectricity and pyroelectricity have shown to modulate the bone remodeling process and accordingly, electrically active ceramic materials have been considered for application as scaffolds, bone grafts, and so forth. This has led to heavy research activities toward the study of electrical response of bioceramic composites in recent years. The study of electrical behavior of biomaterials, such as electrets, which are capable of maintaining electrical polarization (and hence electric field), has become utmost important for the development of materials suitable for external insertion to help in healing ailments. Bioceramics, including hydroxyapatite ($Ca_{10}(PO_4)_6(OH)_2$)(HAP), $SrTiO_3$ (ST), $BaTiO_3$ (BT), $CaTiO_3$ (CT), and so forth, are among the widely used electroactive components for developing scaffolds and bone grafts and composite materials, such as HAP-BT and HAP-CT, have been successfully developed for this application.

For impedance studies, series of ceramic composite were developed out of HAP and $Ba_{0.5}Sr_{0.5}TiO_3$ (BST), by mixing them in different ratios. These dielectric materials are highly applicable for designing biomedical electrets. Pellets of diameter

~10 mm and thickness ~1 mm were made whose parallel faces were coated by Ag paste for contacts. The dielectric measurements were carried out in the frequency range 1–500 MHz at different temperatures. The impedance data were fitted to equivalent circuit model comprising a series combination of two parallel R-C/CPE circuits (representing grain and grain boundary contributions) and the values of the components were obtained. From the impedance data, values of components of relative permittivity (ϵ' , ϵ'') were calculated. It was observed that ϵ' was in the range 1–30, which are close to the values for natural bones. It was further found that the composition 20H–80B (20 atom% HAP–80 atom% BST) has the highest value of grain capacitance, which indicates that this composition is most capable of storing externally applied field. This is favorable for designing bioelectrets and scaffolds, which would be able to retain the electrical stimulation (as polarizing fields) and, in turn, would lead to faster bone regeneration.

Impedance spectroscopy was used for study of influence of short fibers on electrical behavior of fiber-reinforced composites (Mason et al. 2002; Woo et al. 2005). It is known that the mechanical properties of cement-based composites can be significantly improved by fiber reinforcement and are greatly influenced by fiber dispersion and their orientation in the cement matrix. In the case of oriented fibers, improvements in performance vary in different directions. Crack growth is easier in a matrix having nonuniform distribution compared to one with uniform distribution of randomly oriented fibers. Appearance of cracks begins with development of fine microcracks in fiber-free areas of matrix which coalesce to form bigger cracks causing material failure. The fibers play the main role in bridging and inhibiting the growth of these microcracks. Therefore, controlling and characterizing the fiber dispersion is vital for development of fiber-reinforced cement composites (FRCs).

There is strong influence of inclusions (particles, fibers) on dc electrical properties and ac impedance response of composites, including ceramic-matrix (Wang et al. 2000; Gerhardt and Ruh 2001; Gerhardt et al. 2001), cement-matrix composites (Gu et al. 1993; Ford et al. 1998; Torrents et al. 2000; Torrents et al. 2001; Mason et al. 2002), and polymer-matrix systems (Kaushik et al. 1991). The dc electrical properties of fiber-reinforced composites are sensitive to strain-induced changes in microstructure, and the fact that the dc conductivity of unidirectional composites is maximum in the fiber direction has been used to assess fiber content and damage produced by static and dynamic loading of composites (Mason et al. 2002; Muto et al. 1993; Wang et al. 1997; Chung 1998). The strain-induced changes in dc resistance are observed in polymer-matrix, ceramic-matrix and concrete-matrix composites containing short conductive fibers even when the fiber content is below the threshold value, i.e. there is no continuous conduction path (Chung 1998; Wang et al. 1998; Chen et al. 1995; Chen et al. 1996).

In ac impedance measurements, a single arc was observed in the Nyquist plot for cement-matrix composites with insulating wollastonite microfibers (Guo et al. 1993) and two arcs for mullite-matrix composites with 10% SiC whiskers (Gerhardt 1994), where the relative sizes of the arcs varied with the direction of the applied field. Similar result was observed with silicon nitride-matrix composites with 20% SiC whiskers, where the low-frequency arc disappeared when the field was in a direction perpendicular to the fibers (Wang et al. 2000). It was found that cement composites without

fibers showed a single arc (Ford et al. 1998; Mason et al. 2002), whereas composites having 1% steel fibers show two arcs in addition to the electrode-related arc. The dual-arc impedance response of steel fiber–reinforced cement paste was explained by developing the so-called “fiber-switchable coating model”. This model is based on the consideration that a passive oxide coating film is formed on the steel fibers in the cement. Dual-arc behavior was also observed when carbon fibers were used in the place of steel fibers where the presence of polarization layer/double layer on carbon was considered, which would play the same role as the coating. At low frequency, the impedance of this film is very high and the overall impedance, for low-fiber content, is governed by the matrix only, resulting in a single arc. At higher frequencies, the capacitive impedance of the coating decreases (impedance $\sim 1/\omega C$), which results in the creation of conducting paths between fibers as well. However, the fibers create short circuits for the matrix region in the vicinity along their length. Further, while entering the fiber at one end (tip), the current flows from the matrix (different conductivity medium) into the tip, and while leaving the fiber at the other end (tip), the current flows from a fine fiber tip to the matrix (different conductivity medium), a contribution from spreading resistance also arises (Newman 1966; Woo et al. 2005). Thus, the current flow from one electrode to the other through the composite (sample) may be visualized to have two paths: one through the bulk region away from the fibers and the other through the region involving material between the fiber tips, the coating and the fibers. An equivalent circuit model based on above considerations was proposed to explain the experimental results and is shown in Figure 6.28 (Mason et al. 2002). In the work done by Mason et al. (2002) fiber-reinforced composites with 1 wt% of short (1–2 mm) steel or carbon fibers prepared from ordinary Portland cement (OPC) with a water-to-cement ratio of 0.4 by weight were used. Impedance measurements were carried out by using stainless steel electrodes in the frequency range few Hz to 10 MHz. The Nyquist plots of impedance data are shown in Figure 6.29, which exhibits

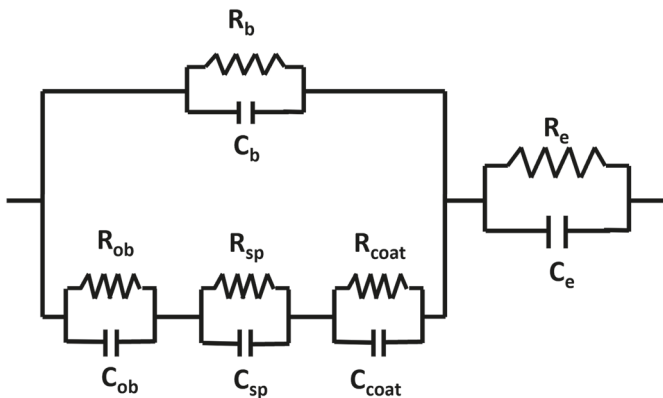


FIGURE 6.28 Equivalent circuit for the frequency-switchable fiber coating model. Subscript code: b = bulk, ob = outer bulk, sp = spreading, coat = coating. (Reprinted with Permission from Elsevier, Mason et al. 2002, Figure 3, Impedance Spectroscopy of Fiber-Reinforced Cement Composites, Cement & Concrete Composites, 24: 457–465.)

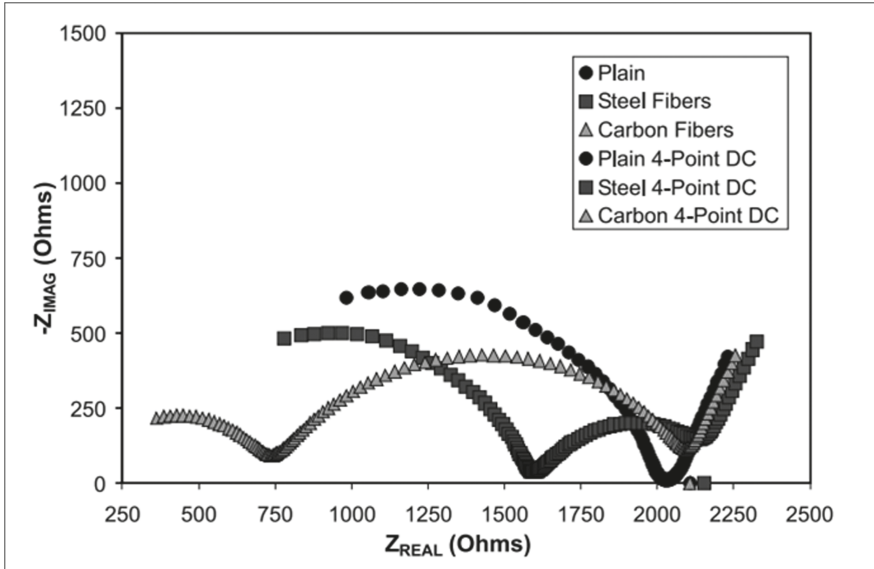


FIGURE 6.29 Nyquist plots for water/cement ratio = 0.4 for ordinary Portland cement (OPC) matrices without and with 1 wt% addition of either steel or carbon fibers. Four-point dc resistances are shown for comparison. (Reprinted with Permission from Elsevier, Mason et al. 2002, Figure 1, , *Impedance Spectroscopy of Fiber-Reinforced Cement Composites, Cement & Concrete Composites*, 24: 457–465.)

two arcs in addition to low-frequency electrode tail. The dc resistance of the sample was obtained by noting the low-frequency intercept of the Z'' versus Z' arc with the Z' axis without the electrode part. To further verify these values, the dc resistance of the composite specimens were also obtained by using four-point measurements which agree with the values obtained from Nyquist plots as shown in Figure 6.29.

Several factors govern the impedance response such as fiber length and aspect ratio (aspect ratio is defined as the length-to-diameter ratio of the fibers employed), fiber volume fraction, fiber orientation and fiber shape. It was proposed that impedance spectroscopy may be useful for characterizing oriented composites (full or partial alignment) and also those involving fibers with unusual shapes. Impedance spectroscopy has been used to investigate fiber properties such as fiber loading and aspect ratio (length divided by diameter) in non-percolating systems (Woo et al. 2003), effect of fiber dispersion, including their orientation, formation of small, uniformly distributed fiber agglomerates and global segregation due to gravity (Woo et al. 2005).

6.6 BIOLOGICAL SYSTEMS AND MEDICAL DIAGNOSTICS

Application of impedance spectroscopy in the study of biological systems is based on the frequency-dependent electrical properties of body tissues. Tissues have cells, cells

have smaller components in them, and so on. Depending on the functions performed, tissues have been given different names. An animal body may be visualized as an object, covered by the skin (epithelial tissues) and containing large number of different types of tissues inside. A tissue can be visualized as a cluster of cells and intercellular matter (another type of tissue). Living organisms are well-organized structures. This organized, ordered nature of living structures is very likely to keep breaking down over time due to various environmental effects. A living creature would die once this order breaks. So, living organisms have to keep repairing and maintaining their structures all the time. These would involve continuous movements of molecules and the associated charge transfers processes taking place at various levels. Every tissue has different electrical impedance determined by its molecular composition. This impedance varies with frequency of the applied electric voltage and thus, a tissue may be regarded as a conductor (of electrical conductivity, σ) or a dielectric (relative dielectric permittivity, ϵ). Therefore, the possible charge transfer processes occurring at various segments would have different characteristic times (time constants) and would show their maximum response at different frequencies (NCERT IX Science Ch 5 2020).

Any changes occurring in values of impedance/time constant/response frequency, keeping other external environment same, would indicate some growth/decay activity in the related tissue/organ. This is the basis of application of ac electrical impedance measurements in the study of biological systems. Due to ease of measurement, ready availability of versatile impedance meters and simplicity of visualization of possible biochemical processes and their equivalent circuit representations, impedance spectroscopy has emerged as a nondestructive, nonoptical and no – hazard promising tool in biological and medical applications, such as biosensing technologies and diagnosis of diseases, including cancer and virus detection. The dielectric properties of tissues and biological materials and basics of their electrical behavior are described in detail by Grimnes and Martinsen (2015), Foster and Schwan (1989) and Gabriel et al. (1996a, 1996b, 1996c). In general, impedance would be the resultant of conductivity, permittivity and magnetic permeability. However, in impedance spectroscopy work, magnetic part is usually ignored (Riu 2004). The values of conductivity of various tissues of human body are summarized in Table 6.1 (Grimnes and Martinsen 2015).

Similarly, the relative permittivity of different human body tissues are shown in Figure 6.30.

Bioimpedance measurements at a single frequency are used in many applications. In strict sense, this does not fall under impedance spectroscopy. However, such measurements are helpful in biological studies and in choosing the range of frequencies in related impedance spectroscopic multifrequency measurements. Thus, single-frequency studies are also widely considered. The single-frequency or multifrequency impedance measurements may be carried out easily by adopting two- or four-probe configurations. These electrodes are attached to points at the body between which impedance studies are to be carried out. For example, for body water estimation, two probes are connected to wrist and the other two of the four probes are connected to the foot on the same side in a four-probe arrangement. AC current is fed in the outer probes and voltage appearing across the inner probes is measured (Foster and

TABLE 6.1
Tissue conductivity: low frequency and 1 MHz

Tissue	σ [S/m] 1–10 Hz	σ [S/m] ~1 MHz	Φ_{\max} < 10 MHz	Anisotropy
Human skin, dry	10^{-7}	10^{-4}	80°	?
Human skin, wet	10^{-5}	10^{-4}	30°	?
Bone	0.005–0.06		20°	Strong
Fat	0.02–0.05	0.02–0.05	3°	Small
Lung	0.05–0.4	0.1–0.6	15°	Local
Brain (gray matter)	0.03–0.4	0.15	15°	Small
Brain (white matter)	0.03–0.3			Strong
Liver	0.2	0.3	5°	?
Muscle	0.05–0.4	0.6	30°	Strong
Whole blood	0.7	0.7	20°	Flow dependent
Urine	0.5–2.6	0.5–2.6	0°	0
Cerebrospinal fluid (CSF)	1.6	1.6	0°	0
Saline, 0.9% 20°C	1.3	1.3	0°	0
Saline, 0.9% 37°C	2	2	0°	0
Seawater	5	5	0°	0

Source: Data from Grimnes Sverre and Ørjan G Martinsen, 2015. Table 4.2, Bioimpedance and Bioelectricity Basics. Third Edition. Academic Press, Elsevier, New York.

Lukaski 1996; Grossi and Bruno 2017) to get the value of impedance. Commonly, metallic electrodes are used, which are attached to the skin by applying an electrolytic gel. The most common type of electrode is the silver/silver chloride (Ag/AgCl) hydrogel electrode, with an electrolyte based on Cl^- . Other electrodes have also been proposed. Also, to avoid some irritation produced by the metal electrodes and gel, recently, textile electrodes have become popular as they provide greater comfort to users (Naranjo-Hernández et al. 2019; Kusche et al. 2018). An equivalent circuit model that accurately represents impedance characteristics of the human body and a measurement method for low-impedance tissues by using armpit electrodes have been proposed by Chinen et al. (2015).

Impedance studies have been used for various purposes such as for detecting cardiomyocyte beating (Peters et al. 2015), for breast tissue classification (Estrela da Silva et al. 2000), for quantitative imaging inside the body, particularly in the diagnosis of breast cancer, by using the observation that the admittivity spectra of malignant and benign tumors differ significantly (McGivney et al. 2012). This technique has also been proposed for possible use in neurological intensive care unit (NICU) settings based on the principle that acute hemorrhagic stroke may produce detectable changes in the impedance spectrum measured on the subject's scalp due to parenchymal local increases of blood volume (Bonmassar et al. 2009).

Bioimpedance analysis is a broadly applied method for body compartments estimation in nutrition studies, sport medicine and evaluation of hydration rate, fat mass and

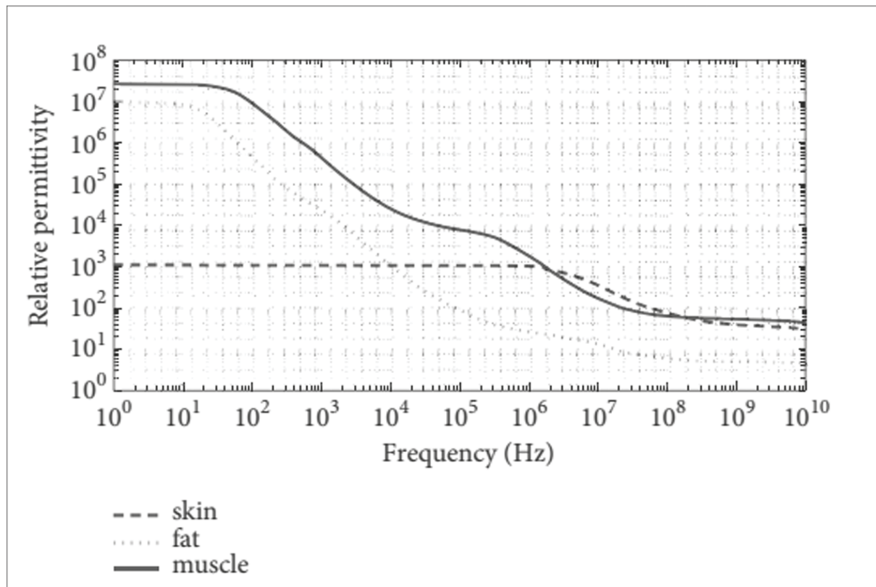


FIGURE 6.30 Relative permittivity of skin, fat and muscle. (Reprinted with Permission from Naranjo-Hernández et al. 2019, Figure 1, Recent Advances, and Future Challenges in Bioimpedance Devices for Healthcare Applications, Hindawi, Journal of Sensors Volume., Article ID 9210258, 42 pages, <https://doi.org/10.1155/2019/9210258>, open access and from IOP publishing, Gabriel et al. (1996c), Figure 1, The Dielectric Properties of Biological Tissues: III. Parametric Models for the Dielectric Spectrum of Tissues, Physics in Medicine and Biology, 41(11): 2271–2293, 1996; and Gabriel C., S. Gabriel and E. Corthout, 1996a, Figure 1, The Dielectric Properties of Biological Tissues: I, Literature Survey, Phys. Med. Biol., 41:2231–2249.)

fat-free mass in healthy and diseased populations. Fat mass, fat-free mass, including skeletal muscle mass, bone minerals and total body water, which is composed of intercellular fluid and extracellular fluid, are compartments that can be predicted and analyzed (Khalil et al. 2014).

Bioimpedance spectroscopy is applied to measure the composition of the body, in particular body fat and muscle mass, or the hydration level for certain body areas such as chest or abdomen and is widely used by dieticians, cardiologists and neurologists. The overall impedance would be the result of impedances offered by different types of tissues. Tissues that contain large amounts of fluid and electrolytes, such as blood, would have high conductivity and low impedance, whereas fat and bone would have high impedance. Most body water is stored in muscle. A more muscular person would have more body water, leading to lower impedance. By measuring the impedance, body water and fat are estimated. This information is used to assess the state of health, evaluation of nutritional status and estimating potential health risks (Szuster et al. 2017; Aandstad et al. 2014; Sergi et al. 2016; Khalil et al. 2014; Muller et al. 2021). A new smart bioimpedance spectroscopy device has been investigated, developed

and validated for its application to the estimation of body composition. The device uses specially developed software and hardware for measurement of real and imaginary parts of impedance and identification of Cole model parameters which are used in estimation of body composition (Naranjo-Hernández et al. 2020). The same measurements may be applied for management of heart problems. Decompensated heart failure generally leads to fluid volume overload, which leads to low-impedance values in the thorax. Impedance measurements can be used to recognize and quantify fluid retention, which is critical for the treatment of heart failure and lung function (Brown 2001; Muders et al. 2010; Zink et al. 2020; Zink et al. 2015; Bera 2014). Methods for bioimpedance are described by Schreiner et al. (2016).

It has been shown that impedance spectroscopy can be applied for detection and differentiation of bacteria (Gnaim et al. 2020). The electrical impedance of a biological sample reflects the electronic and physical properties of its cellular membranes, as well as the molecular shape, structure and composition, the concentration and the interaction of molecules in a solution that undergo a water dipole effect (Gabriel et al. 1996). Most of the methodologies that can distinguish between gram-negative and gram-positive bacteria take advantage of the differences in the bacterial cell walls. Gram-positive bacteria has a much thicker peptidoglycan layer as compared to gram-negative bacteria. The gram-negative bacteria have a thin peptidoglycan layer as well as cell wall/membrane composed of lipid bilayer. Because each bacterium has a distinct shape, size and composition, impedance spectroscopy can be used as a marker of bacterial types, properties or even species by establishing clusters (Gnaim et al. 2020). Gram staining is still the most common method for detecting bacteria and distinguishing between gram-negative and gram-positive species. However, this is time consuming (~ few days) whereas impedance spectroscopic method is very fast. Impedance spectroscopy has been used to develop a point-of-use disposable paper-based impedimetric sensor for generic differentiation of bacteria and virus based on their interaction with chitosan stabilized silver nanoparticles (ChAgNPs) (Sadani et al. 2020). A characteristic decrease in the electrochemical impedance spectrum at low frequencies was observed for bacteria while an increase in the response was noted for viruses. Decrease in low-frequency impedance response (10 Hz–1 kHz) for the case of bacteria occurs due to partial release of its intracellular fluid, on polyaniline nanofibers, created by perforation of bacterial cell membrane by the silver nanoparticles, whereas ChAgNPs-induced viral aggregation was a possible cause of increase in impedance spectra.

Electrical impedance tomography (EIT) is an exciting application of impedance spectroscopy (Bayford 2006). This is a noninvasive medical imaging technique in which an image of the conductivity or permittivity of part of the body is inferred from surface electrode measurements. The fact that electrical conductivity depends on free ion content and differs considerably between various biological tissues or different functional states of one and the same tissue or organ (Brown 2003) is exploited in EIT. A number of hardware and software components have been developed for its ready use (Kerner et al. 2002). One of the most important benefits of EIT is that the patient need not be taken to the imaging lab [such as in the case of computed tomography (CT) scan, magnetic resonance imaging (MRI)], but the EIT setup can be taken to the patient's bed providing a portable bedside compact facility (Brown 2001;

Harikumar et al. 2013; Bayford 2006; Muders 2010). Magnetic resonance electrical impedance tomography (MREIT) is a new and promising noninvasive method for finding conductivity data in vivo (Oh et al. 2005).

Impedance spectroscopy can be used to detect the presence of cancer in tissues at an early stage. When cancer develops in the tissue, e.g. breast, extracellular space and nucleus growth decrease due to change in chromatin structure and expansion in cell volume. Also, various differentiations, such as abnormal plasma membrane transitions, decreased cell connection and new antigen formations, occur in the membrane and its contents. The sodium, potassium and calcium ion ratios inside the cell change and can lead to a loss of shape, movement and intercellular communication disorders. These changes that occur during progression of cancer influence the cell physiology, which is manifested as change in the electrical behavior of the tissue. It has been shown that it is possible to use electrical bioimpedance to assess skin cancer lesions. It was demonstrated that impedance measured noninvasively can be used to separate nonmelanoma skin cancers from harmless benign nevi with a high accuracy. Also, malignant melanoma (MM) can be sorted out from benign nevi with clinically adequate accuracy. It was shown that use of surface electrodes having extremely small spikes that penetrate through the stratum corneum would be more efficient for detecting subtle skin alterations that manifest beneath the stratum corneum, such as MM (Aberg et al. 2005).

In order to differentiate malignant anomalies from nonmalignant anomalies using impedance spectroscopy and to aid early detection of cancerous tissue, an electrical impedance-based tool was designed and developed by Moqadam et al. (2018). Cases of skin cancer were studied. It was observed that the admittance values for cancerous tissues were higher than those for healthy tissues. This difference was clearly revealed by the admittance complex plane plots (Y'' vs Y' plots) for cancerous portion and that for healthy portion of the skin.

The impedance measurements can be used for generating an image of the suspected region with cancer. For tomography, an array of electrodes is used around the region to be imaged. For example, a circular array of electrodes that may be used for breast impedance measurements is shown in Figure 6.31. The fields between adjacent electrodes will measure properties near the tissue surface, whereas more diametrically opposed electrodes will measure the composite properties across the tissue region. Such a sequence of measurements is carried out to include all electrode pairs surrounding the region, i.e. between electrode pairs starting from electrode number 1, then starting from electrode number 2, and so on. The whole region is mapped based on the differing electrical properties within the region, as the malignant breast tissue (cancerous) has a much lower electrical impedance than normal tissue and benign (noncancerous) tumors. These measured impedances are used to obtain image of the breast clearly showing the cancerous parts (Joins et al. 2006; Kerner et al. 2002).

To distinguish low metastatic human breast cells from normal human breast cells, the fiber optic bioimpedance spectroscopy (FOBIS) system has been recently developed utilizing both fiber optics and bioimpedance spectroscopy (Denkçeken and Cort 2020). A number of hardware and image reconstruction softwares have been put forward for its ready use in general (Frerichs et al. 2017).

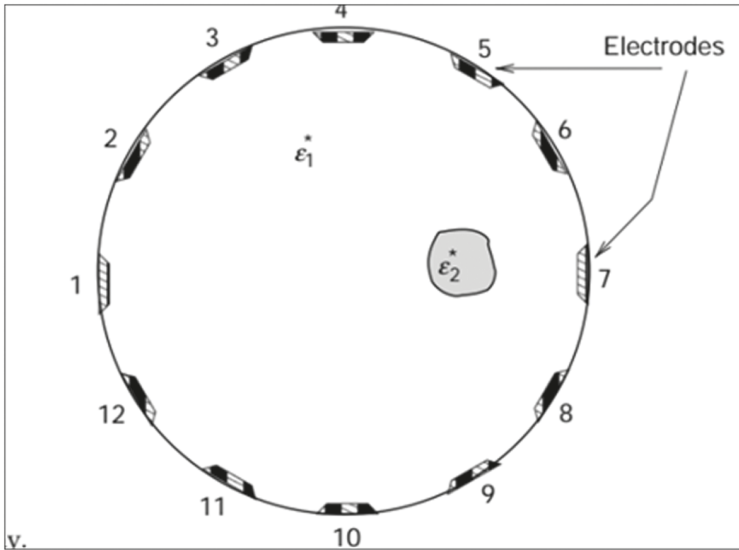


FIGURE 6.31 Configuration of electrical impedance tomography. (Reprinted from CRC Press, Taylor & Francis Group, Joins et al. 2006, Figure 12.5, *Electromagnetic Imaging of Biological Systems*, In: *Bioengineering and Biophysical Aspects of Electromagnetic Fields, Handbook of Biological Effects of Electromagnetic Fields*, Third Edition, ed Frank S. Barnes and Ben Greenebaum, CRC Press, Taylor & Francis Group, 6000 Broken Sound Parkway NW, Suite 300, Boca Raton, FL 33487-2742.)

In recent years, impedance spectroscopy has been used for various applications, including tissue engineering, characterization of biological cells and cell culture monitoring. Tissue engineering is the science of generating tissues for replacing the malfunctioning tissues or organs in the body. Advances in biotechnology and material science have led to rapid developments in the field of tissue engineering. Due to the potential of generating differentiated cells, the tissue engineered constructs are commonly, first cultured *in vitro* before their *in vivo* transplantation and need to be evaluated regarding their morphological and functional behavior in a real-time. Current monitoring techniques are mainly histological staining and involve destructive tests to characterize cell cultures. Impedance spectroscopy has emerged as a promising technique for this. As the characteristics of the cell membrane and intra- and extracellular spaces influence the impedance spectrum, measuring electrical impedance of a volume of a biological tissue over a frequency spectrum provides information with regard to the quantitative changes of cells, such as cell population. Impedance spectroscopy has been used for monitoring the growth and differentiation of stem cells in different tissue engineering applications, quantification of cell size and number and classification of cell type and shape. This technique is useful in extracting information regarding cell toxicity, cell invasion or inflammation, real-time monitoring of cell attachment and spreading on substrates, real-time and *in vivo* monitoring of the healing of bone critical size defects (CSD), as well as effectiveness

of biomaterials and bone tissue engineering for the treatment of CSD (Kozhevnikov et al. 2016; Amini et al. 2018).

One of the most popular biological applications of impedance spectroscopy is in the research on living cells. Impedance measurements were carried out and a quantity known as cell index given by $(Z(t) - Z(0))/Z(0)$, where $Z(t)$ and $Z(0)$ are values of impedance at time t and at $t = 0$ (i.e. beginning of the measurement), was calculated. Cells were grown on the planar electrodes located on the bottom of the Petri dish. A plot of cell index as function of time of the HeLa cells is shown in Figure 6.32. It is seen that the cell index of the empty electrode is stable, whereas that for electrode covered with cells rises, exhibiting a logistic growth (Stupin et al. 2021).

Similarly, another important application is the identification of the cell state (living or dead). For HeLa cancer cells, the impedance measurements were carried out for metal/electrolyte/cell interface before and after the addition of the toxin Triton x 100 (Union Carbide, USA) to cell medium. The results of impedance measurements carried out over a wide frequency range are shown in Figure 6.33. It is seen that higher-frequency impedances of electrode covered by cells before and after the addition of toxin are distinct, and the impedance values corresponding to the situation where toxin has been added are lower, indicating that the toxin has affected the cells (Stupin et al. 2020).

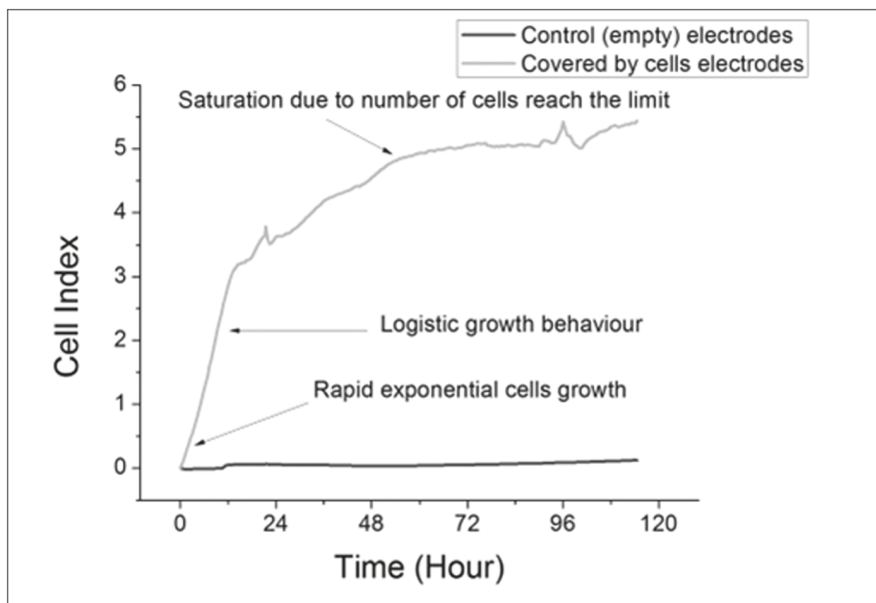


FIGURE 6.32 The impedance evolution of a cell-covered electrode (green) and an empty electrode (red). During fission and growth of cells the impedance of the cell-covered electrode demonstrates a logistic growth. In contrast, the impedance of the empty electrode is stable in time. (Reprinted with Permission from ACS Publications, Stupin et al. 2020, Figure 10, *Bioimpedance Spectroscopy: Basics and Applications*, ACS Biomater. Sci. Eng., 7: 1962–1986.)

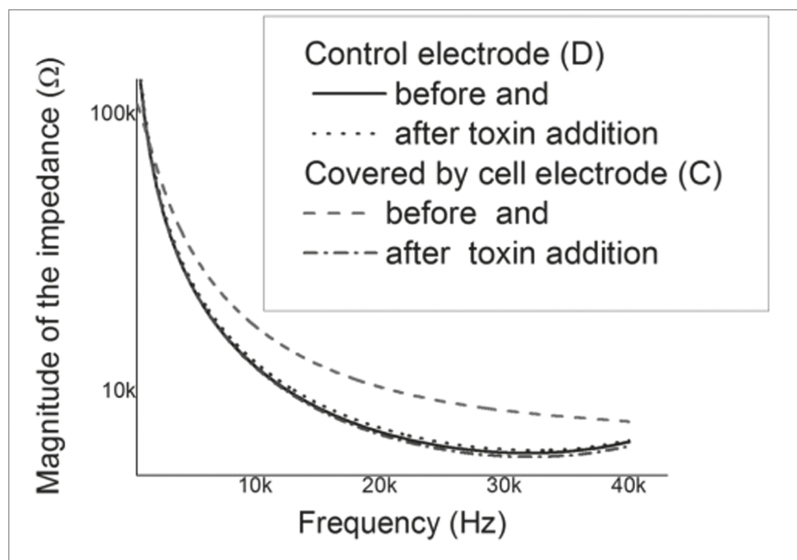


FIGURE 6.33 The effect of a toxin addition on the metal/electrolyte/cell interface measured in broad-frequency range. One can see that after the addition of a toxin, the high-frequency part of the impedance of the cell-covered electrode decreases to the level of the empty control electrode. (Reprinted with Permission from ACS Publications, Stupin et al. 2020, Figure 12, *Bioimpedance Spectroscopy: Basics and Applications*, ACS Biomater. Sci. Eng., 7: 1962–1986.)

Impedance spectroscopy can be used to study the relaxation processes in tissues. The electric and dielectric properties of living cells provide information about kinetic processes in the cell membrane and the dynamics of ions and water molecules inside the cells. A cell consists of a nucleus immersed in a fluid called cytoplasm contained by the so-called cell (or plasma) membrane. The cell membrane is permeable and permits entry and exit of materials selectively (NCERT Science IX Ch 5 2020). A steady-state potential difference exists across the membrane. In plants, the cell membrane has another cover called as cell wall, which is made up of cellulose. Only the living cells are capable of absorbing water, not the dead cells. The nucleus has a double-layered covering called nuclear membrane, which has pores that allow transfer of material from interior of the nucleus to outside the cytoplasm. The nucleus contains chromosomes. Chromosomes are composed of deoxyribonucleic acid (DNA) and protein molecules. Functional segments of DNA are called genes. The nucleus plays a central role in the process of cell division (cellular reproduction). Living tissues show high electrical resistivity. Thus, at low frequencies and dc, the cell membrane behaves as a capacitor and offers high impedance. As a result, very small fraction of current flows through the cells and the low-frequency ac currents tend to bypass the cells (Amini et al. 2018; Moqadam et al. 2018; NCERT Science IX 2020–2021). The flow of current and a simple equivalent circuit model are schematically shown in Figure 6.34.

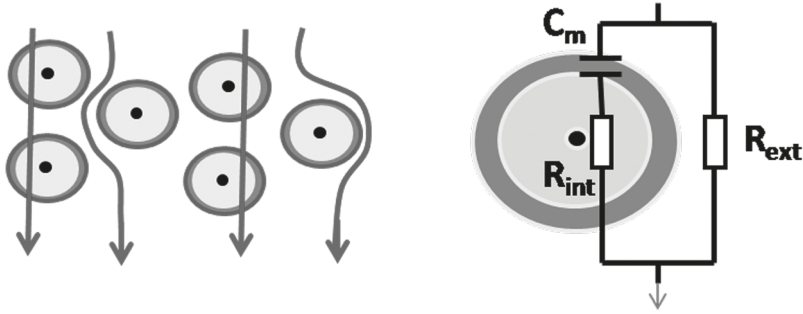


FIGURE 6.34 Paths of high- and low-frequency current in a biological tissue and electrical equivalent circuit model.

Values of membrane capacitance have been estimated for human erythrocytes over wide frequency and temperature ranges (Bao et al. 1992). At higher frequencies, the impedance of the cell membrane ($\sim 1/\omega C$) decreases and the current would flow through the cell as well as through the intercellular material. Thus, variation in high-frequency impedance as compared to healthy tissues indicates deterioration in the cell state. Under an applied electric field polarization is developed in different segments by specific modes responding at various time scales. As the frequency of applied ac voltage increases, certain polarizations cease to follow the field causing a lowering of the overall polarization. Such lowered values are maintained till certain other polarization modes cease to respond. This is reflected in appearance of lowering of relative dielectric permittivity in steps as frequency rises. These dispersions indicate the dielectric relaxations, which arise from the polarization mechanisms that occur in complex biological environments, and has been described as α -, β -, δ - and γ -dispersions (Figure 6.35) (Nasir and Ahmad 2020).

The cell membrane acts as a capacitor and offers high impedance ($\sim 1/\omega C$) at low frequencies, causing most of the current to flow outside the cell, i.e. tangentially to the cell surface. This so-termed α -dispersion occurs in a low-frequency range, i.e. 10 Hz (or below) to 10 kHz (relaxation times ~ 6 ms) and arises from the ions flow touching the surface of the cell and may carry information about surface shape, structure etc. α -dispersion is more sensitive to age and environmental factors than β -dispersion and disappears when tissue dies. Blood has no α -dispersion. As the frequency increases, the cell membrane impedance decreases letting flow of current crossing the membrane and via intracellular cytoplasm. This current creates charging of the membrane interface as the current flows through the intercellular medium and intracellular cytoplasm, which have different permittivities and impedances. This accumulation of the charges at the cell membranes, because of the Maxwell–Wagner interfacial polarization, gives rise to the so called β -dispersion and occurs in the frequency range of 10 kHz–10 MHz with a relaxation time approximately 300 ns. δ -dispersion occurs in the frequency range of 0.1–5 GHz and is believed to arise from the dipolar movements of large molecules and relaxation of the dipolar moments of proteins, other large molecules such as biopolymers, cellular organelles and protein-bound

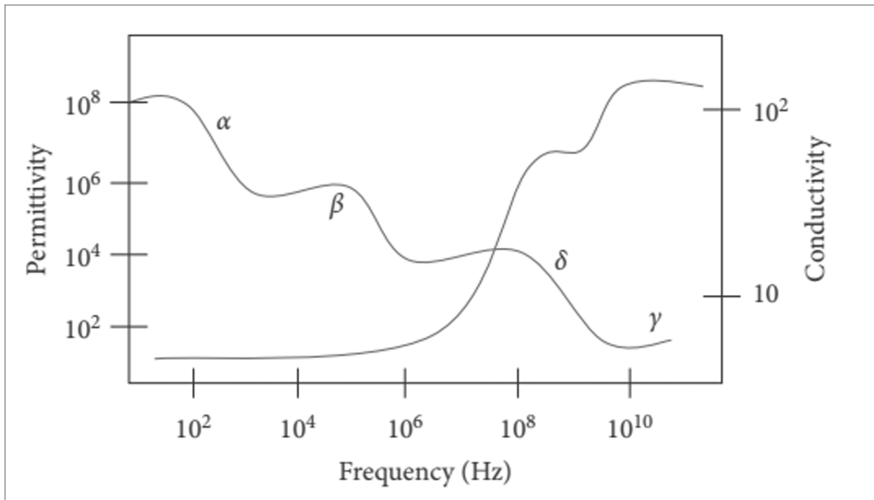


FIGURE 6.35 Permittivity and conductivity over the frequency spectrum, depicting the α -, β -, δ - and γ -dispersions. (Reprinted from Hindawi, Open Access, Nasir and Ahmad 2020, Figure 2, Cells Electrical Characterization: Dielectric Properties, Mixture, and Modeling Theories, Hindawi Journal of Engineering, 2020, Article ID 9475490, 17 pages, <https://doi.org/10.1155/2020/9475490>, Open access.)

water. The movement of tissue-bound water is rotationally hindered as compared to free water. γ -dispersion, occurring at frequencies above 0.1 GHz, is related to dipolar rotation of intercellular and cellular free water and other smaller molecules. Thus, in a nutshell, ions' tangential flow across the cell surfaces gives α -dispersion, the accumulation of the charges at the cell membranes because of interfacial polarization gives β -dispersion, dipolar movements of large molecules and relaxation of the bound water gives δ -dispersion, and the dipolar rotation of smaller molecules, mainly water, gives γ -dispersion (Markx and Davey 1999; Amini et al. 2018; Schwan 1957). So, impedance measurements as function of frequency may be used to get information about interior/exterior parts of cells.

As an example, α -dispersion in live human tissue, in vivo in situ, is illustrated in Figure 6.36 (Grimnes and Martinse 2010). Impedance measurements were made using a four-probe method by attaching AgCl solid gel electrodes of radius 1.25 cm, each placed with center-to-center distance of 3.3 cm and rim-to-rim distance of 0.8 cm on a straight line on the normal skin of the forearm. Electrodes had a more than 15-minute contact period before measurements started. Complex plane admittance plot for the tissues related to forearms for the short distance to small muscle masses are shown in Figure 6.36, where the four electrodes were placed in line at the ventral side of the forearm. The plot clearly indicates the dispersions.

An attempt can be made for obtaining an equivalent circuit model to represent the behavior shown in Figure 6.36. It is seen that at high-frequency side there is a change in sign of Y'' , indicating that some inductive behavior dominates in this frequency

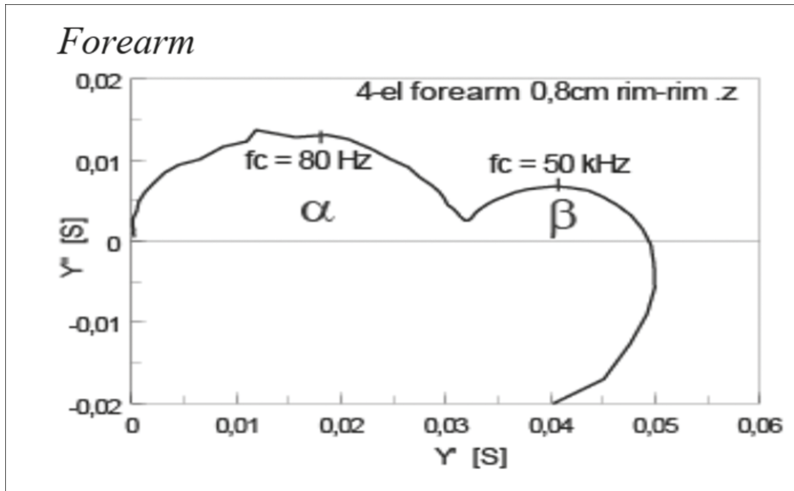


FIGURE 6.36 Y'' versus Y' plot for forearm. The four electrodes of radius 1.25 cm each are placed in line at the ventral side of the forearm with center-to-center distance of 3.3 cm and rim-to-rim distance of 0.8 cm. (Reprinted with permission from IOP Publishing, Grimnes Sverre, Ørjan G Martinsen 2010, Figure 1, Alpha-Dispersion in Human Tissue, Journal of Physics: Conference Series, 224: 012073.)

region presumably arising due to leads, connections, dominating conductivity of liquids, etc. So, for qualitative analysis, we may confine to the data up to a frequency where Y'' becomes zero at the high-frequency side. In Figure 6.36, the arc passes through the origin and has two separate semicircular-looking arcs. By comparing this with the simulated patterns given in Chapter 4, it can be seen that an equivalent circuit model comprising two series RC circuits connected in parallel may be chosen to start with. The values of the circuit components can be obtained by using CNLS fitting and can be further used for cell studies. Equivalent circuit models for human body have been developed by Chinen et al. (2015).

6.7 AGRICULTURE, FOOD QUALITY AND DAIRY

Impedance spectroscopy is a powerful nondestructive technique useful in plant, crop and food sciences and dairy. In the field of agriculture, this technique is used to assess the health of the seeds and plants *in vivo* and *in vitro*, without damaging (cutting, crushing or excising) the sample (leaf, seed, roots, etc.). This technique has been used to study plant health, mineral deficiency, the presence of viruses, fruit damages, structural cell changes during fruit ripening, freezing or chilling damage, growth of roots, etc. Being noninvasive, this technique can be used repeatedly *in situ* (Jocsak et al. 2019; Azzarello et al. 2006; Yang Liu et al. 2021).

All physiological or pathological phenomena are intrinsically bioelectrical and are manifested as changes in the electrical properties of tissues or organs. Thus, the measurements of electrical parameters, such as impedance, are useful for the study of

conditions in human, animal and plant tissues (Azzarello 2006; Ackmann and Seitz 1984; Jocsak et al. 2019). A tissue can be visualized as a cluster of cells and intercellular matter having continuous movement of molecules which, in turn, would involve the associated charge transfer processes taking place at various levels. Different tissues would have different values of electrical impedance and the possible charge transfer processes occurring at various segments would have different characteristic times (time constants) exhibiting their maximum response at different frequencies. Any changes occurring in values of impedance/time constant/response frequency would indicate some growth/decay activity in the related tissue. In this way, electrical impedance spectroscopy is fairly widely applied in plant, crop and food sciences, besides biomedical diagnostics (Jocsak et al. 2019).

A cell consists of a nucleus immersed in a fluid called cytoplasm, contained by the so-called cell (or plasma) membrane. The cell membrane is permeable and permits entry and exit of materials selectively (NCERT IX Science Ch 5 2020, NCERT X Science Ch 6 2020). In plants, the cell membrane has another cover called as cell wall, which is made up of cellulose. Cell wall is a specialized form of extracellular matrix that surrounds every cell of the plant. The cell wall is responsible for many of the characteristics that distinguish plant cells from animal cells. Cell wall is a porous medium providing a mechanical protection and facilitating distribution of water, minerals and other nutrients to the cell. It also provides rigid building blocks from which stable structures of higher order, such as leaves and stems, can be produced, and provides a storage site of regulatory molecules that sense the presence of pathogenic microbes and control the development of tissues (Staehelin 2019).

The plant tissue impedance basically depends on three factors: intracellular (symplastic) resistance, intercellular (apoplastic or extracellular) resistance and impedance of the cell membrane. The cell membrane separates the intracellular and extracellular regions, and electric current may flow through the membrane entering the cell interior as well as traveling outside. From a biological point of view, the cell membrane is a selectively permeable barrier that divides the intracellular and extracellular compartments. It protects the interior of the cell, allowing the passage of some materials to which it is permeable (Azzarello et al. 2006). From an electrical point of view, the cell membrane behaves as a capacitor which offers a high impedance at low frequencies (impedance $\sim 1/\omega C$). The impedance decreases as frequency of applied voltage increases. Therefore, when ac voltage is applied, most of the current flows via the intercellular region at low frequencies. At high frequencies, the cell membrane has low impedance and the current flows through both the intracellular (symplastic) and intercellular (apoplastic) regions.

The impedance spectra of plant tissues have been characterized by different equivalent circuit models (Jocsak et al. 2019; Voza'ry et al. 1999). The core part of the models is the equivalent circuit of a tissue proposed by Hayden et al. (1969), Azzarello (2006) and Jocsak et al. (2019) as shown in Figure 6.37. Here flow of current via two parallel paths is considered: one via the extracellular region (represented by resistance R_1) and the other via the intracellular region crossing the cell membrane (represented by parallel R_3 -C circuit) and the intracellular fluid (cytoplasm) (represented by resistance R_2).

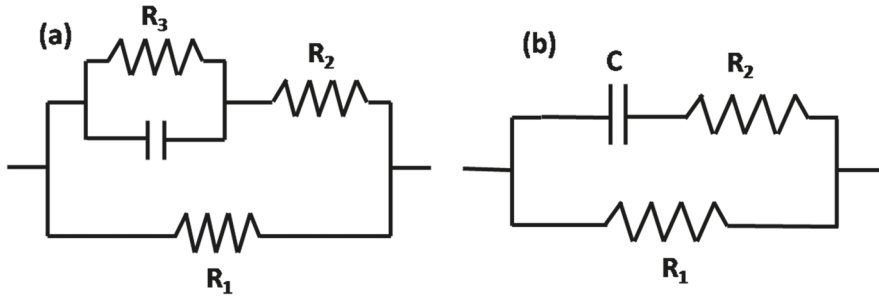


FIGURE 6.37 (a) The Hayden model: R_1 is the resistance of the extracellular (apoplasmic) region, R_3 and C are the resistance and capacitance of cell membrane, respectively, and R_2 is the resistance of the intracellular region (cytoplasm) (b) Simplifying Hayden model [(a) Reprinted with Permission from Oxford University Press, Hayden et al. 1968, Figure 3, *Electrical Impedance Studies on Potato and Alfalfa Tissue*, *Journal of Experimental Botany*, 20(63): 177–200. (b) Reprinted with Permission from Global Science Books, UK, Elisa Azzarello, Sergio Mugnai, Camilla Pandolfi, Elisa Masi, Stefano Mancuso, 2006, Figure 2, *Stress Assessment in Plants by Impedance Spectroscopy*, In *Floriculture, Ornamental and Plant Biotechnology Volume III* (pp 140–148).]

A huge literature is available regarding the use of impedance measurements where values of the circuit components were monitored to study plant health. Electrical impedance of plant tissues can be measured by using Ag/AgCl electrodes placed on the stem or leaves with a conducting paste (Azzarello et al. 2006).

Typically, the experimental complex plane impedance plots of plant tissues comprise one or two arcs which are correlated to the physiological properties by representing the tissue behavior by equivalent circuit models. Model shown in Figure 6.37 can be used to begin with. The cell membrane offers high impedance to the current flow and therefore, most of the low-frequency current flows through R_1 (apoplasmic region). At higher frequencies, the impedance of the cell membrane ($1/j\omega C$) decreases and the current flows through the parallel combination of R_1 and R_2 . Thus, the values of these components can be obtained by noting the limiting values of the impedance at low- and high frequencies. These values are then used to assess the health of the tissue/plant. For homogeneous tissues, such as potato tuber and apple fruit, simple model works. For heterogeneous highly differentiated tissues having number of cells with different sizes and morphology, such as stems and needles of Scot pine seedlings, equivalent circuit models involving distributed elements (CPE) are found to be appropriate. In general, when complex plane immittance plots show depressed humps, distributed components may be used by incorporating constant phase angle elements (CPE) (Azzarello et al. 2006; Repo et al. 2002). By monitoring the changes occurring in the components of the models' sensitivity to salinity and measurement of tree root growth, presence of viruses and fruit damages, structural cellular changes during fruit ripening, damages due to freezing (chill or frost), nutrient status and mineral deficiency, seed growth, etc. have been studied (Azzarello et al. 2006).

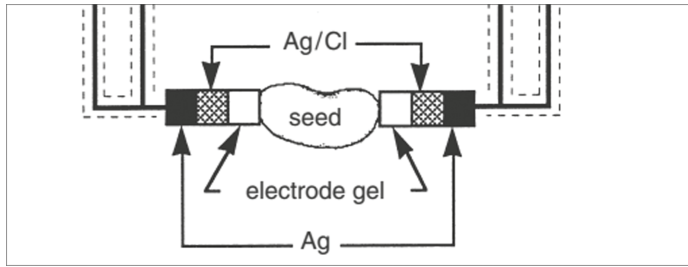


FIGURE 6.38 Custom-designed apparatus to take the impedance spectra of bean seeds using four probes where the current is flown through the outer wires and the voltage is measured between the inner pair of leads. (Reprinted with Permission from Cambridge University Press, Repo et al. 2002, Figure 2, *Electrical Impedance Spectroscopy in Relation to Seed Viability and Moisture Content in Snap Bean (*Phaseolus vulgaris* L.)*, *Seed Science Research*, 12: 17–29.)

As an example, studies on snap bean seed (Repo et al. 2002; Paine et al. 2001) is now briefly presented. High-quality seeds are essential for successful germination and seedling growth in agriculture and forestry. Deterioration in seed quality takes place due to ageing during storage as is indicated by reduced germination. This demands a need for testing for viability of the stored seeds. Standard germination test methods are time consuming and also destructive to the seed sample. Impedance spectroscopy has been shown to be a quick method for viability tests. Impedance spectroscopy was used to obtain the optimal range of moisture content for separation of viable and nonviable snap bean seeds by observing effect of water content on the impedance. Snap bean nonviable seed samples were prepared by subjecting the seeds to suitable treatment and ageing in controlled conditions at 40°C for a duration sufficient to give 0% germination. Impedance measurements were carried out between 60 Hz and 8 MHz on both nonviable and viable seed samples possessing varying amount of known moisture levels by using Ag/AgCl electrodes placed on the stem with a conducting paste. A seed sample placed between the electrodes, which are connected to the impedance meter, is schematically shown in Figure 6.38 (Repo et al. 2002; Paine et al. 2001).

Complex plane plots obtained by Repo et al. (2002) for viable and nonviable seeds possessing different quantities of moisture content are shown in Figure 6.39.

It was observed that both the real and imaginary parts of the impedance decreased and the difference in their values for viable and nonviable seeds became more prominent as the moisture content increased. The plot contains a single arc at low value of moisture content splitting into two depressed arcs at higher moisture levels. The data for low values of moisture were represented by a parallel R_1 - CPE_1 circuit whereas the data for higher moisture contents were represented by a series combination of R_1 - CPE_1 and R_2 - CPE_2 circuits. The values of the parameters were obtained by using CNLS fitting (Repo et al. 2002). Increased water content in the seeds reduces the impedance due to increased ion movements and greatly affects the equivalent circuit model parameters. Changes in the spectrum with increase in moisture content during rehydration may occur due to different types of water bonding. The

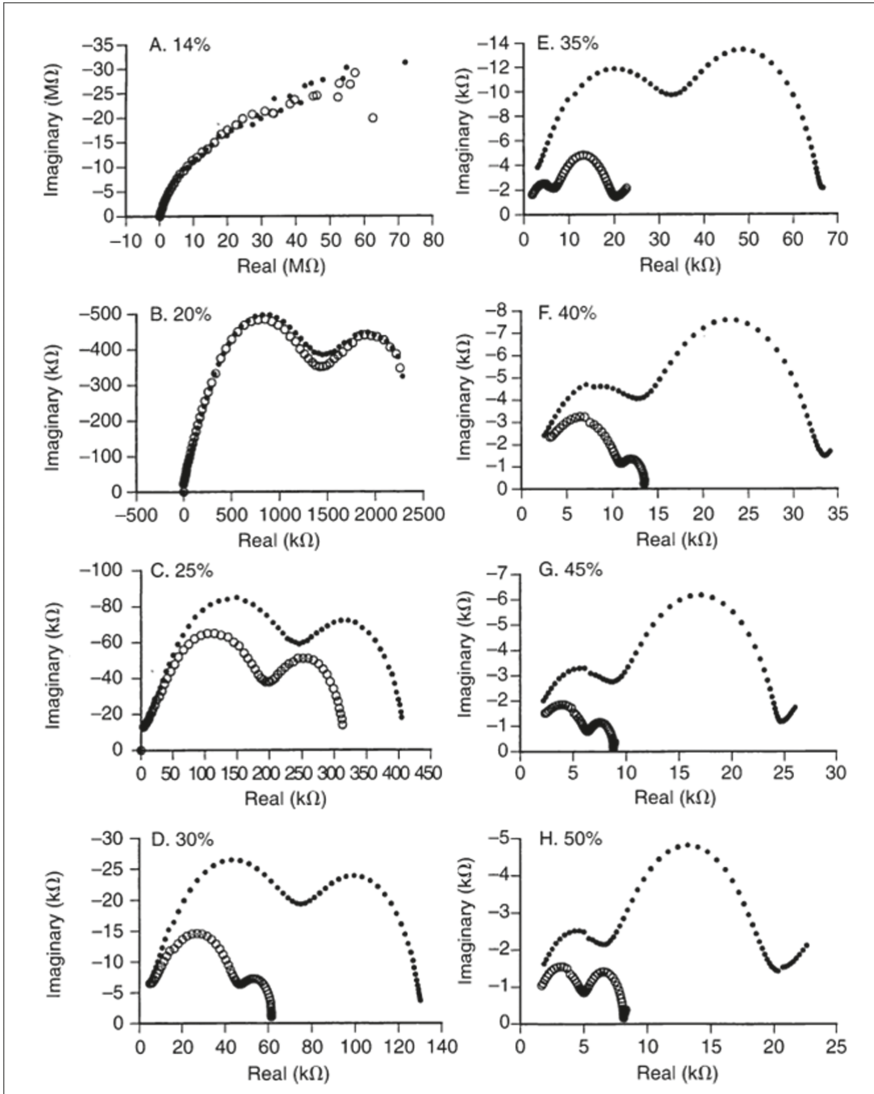


FIGURE 6.39 Mean electrical impedance spectra of viable and nonviable bean seeds at different moisture content levels (MC): 14% MC (A), 20% MC (B), 25% MC (C), 30% MC (D), 35% MC (E), 40% MC (F), 45% MC (G) and 50% MC (H). Closed symbols refer to viable seeds and open symbols to nonviable seeds. Frequency increases from right (60 Hz) to left (8 MHz). (Reprinted with Permission from Cambridge University Press, Repo et al. 2002, Figure 3, *Electrical Impedance Spectroscopy in Relation to Seed Viability and Moisture Content in Snap Bean (*Phaseolus vulgaris* L.)*, *Seed Science Research*, 12: 17–29.)

impedance spectroscopic parameters were found to be quite different for viable and nonviable seeds, and moisture content has strong effect on impedance spectroscopic characteristics for both. Strongest effects were observed for moisture content in the range 35–40% (Repo et al. 2002).

Impedance spectroscopy has been widely used for detection of fruit ripening and control and in postharvest quality measurements of different fruit and vegetable (Jocsak et al. 2019). A few examples are now briefly mentioned. Electrical impedance of peaches was found to increase until the fruit reach the ripe stage after which it declines. Harker and Maindonald (1994) used impedance spectroscopy for characterizing the intracellular and the extracellular resistances and cell membrane changes during ripening of nectarine. It was found that during ripening, the high-frequency measurements (yielding the intracellular behavior) and cell membrane capacitance did not show pronounced changes, whereas the low-frequency resistance (extracellular resistance) showed a marked decrease. Decrease in cell wall resistance was found to be closely related to the changes in the fruit texture. It was concluded that increased concentration of mobile ions in the cell wall and increased cross section of cell walls due to cell wall dissolution and ion leakage on ripening are responsible for this decrease in resistance (Harker and Maindonald 1994; Jocsak et al. 2019). Decrease in extracellular resistance was also observed in melon (Sugiyama et al. 1989) and in apple during ripening with no changes in intracellular resistance (Voza'ry and Horva'th 1998; Voza'ry et al. 1997).

It is known that CaCl_2 infiltration slows the ripening of apple fruit and this is reflected in increased resistance. The resistance would increase as calcium is known to maintain membrane structure and function and cellular integrity (Lougheed et al. 1981; Jocsak et al. 2019). The physiological state of plants may get severely affected by environmental conditions and these effects are reflected as changes in electrical properties of tissues. For example, decrease in low-frequency impedance of plants was observed after watering (Hayden et al. 1969), the symplasmic to apoplasmic resistance ratio changed during dehydration of potato and carrot pieces (Toyoda 1994), the ratio of impedance values at 50- and 5 kHz for potato tuber whose sprouting was inhibited by gamma radiation were found to strongly depend on the radiation dose (Felfoldi et al. 1993). It has been shown that impedance spectroscopy can be used to distinguish between bruised and non-bruised apples. Impedance measurements in the frequency range of 1 kHz–1 MHz were carried on Jonathan apples exposed to different pressing forces. The data were analyzed by using modified Hayden model comprising a series combination of symplasmic resistance R_s and plasma membrane impedance Z_m having CPE with this R_s - Z_m series circuit being further connected in parallel to apoplasmic resistance R_a . The values of R_a , R_s and the ratio R_a/R_s were obtained as function of force and deformation. No changes were observed in the value of R_a/R_s below the bioyield deformation, whereas this value decreased markedly above this. The ratio R_a/R_s decreased due to decreased value of apoplasmic resistance R_a which occurred because of increased ion concentration in the apoplasmic part and reduced cell membrane resistance produced by cell membrane rupture as a result of bruise. During loading and transport, apple can get bruised without visible signs. It was concluded that impedance spectroscopy can be used to get information about the invisible bruise (Voza'ry et al. 1999). A correlation was established between

proper harvest date of different peach varieties with impedance (Weaver et al. 1966). Similarly, impedance spectroscopy was used for monitoring sequential changes in potato tissue during heating (Fuentes et al. 2014; Jocsak 2019). Changes occurring in the equivalent circuit parameters for fruits, leaves and vegetables subjected to low-temperature freezing and frosting have been used for harvest quality measurements.

The development in food industry rely basically on the concepts of food quality and food safety. Food quality can be understood as a set of factors which are able to differentiate food products according to their organoleptic characteristics, composition and functional properties. Food quality assessment involves scientific evaluation of the food freshness and food safety. The food containing harmful substances which are not intentionally added is said to be contaminated. Such substances may enter the food during cultivation, preparation or through natural degradation of the components, etc. Presence of antimicrobial drug resistance and harmful aggregates, such as pesticides, animal drug residues and pathogen microorganisms, are the main concerns for food safety. Traditional methods such as high-performance liquid chromatography (HPLC), gas chromatography (GC), etc., widely used for the identification and quantification of nutrients (fats, carbohydrates, proteins, water, mineral elements and vitamins), additives or contaminants (aflatoxin, pesticides, pathogens, antimicrobial agents, growth promoters, additives, etc.), are time consuming and expensive. Electroanalytical techniques involving electroanalysis, sensors and biosensors (electronic tongue) are low cost, rapid and sensitive for such applications. Impedance spectroscopy is another fast tool that has been used to study food quality, to detect the freshness or ripeness of some agricultural products and foods and to monitor the dairy product processing such as fermentation, coagulation, dewatering, freezing and emulsification (Escarpa et al. 2015).

Impedance spectroscopy has been used to study yogurt processing (Escarpa et al. 2015; Kitamura et al. 2000). Market milk as substrate and yogurt as starter were used to process yogurt experimentally. The sample containing substrate milk and starter yogurt was stirred and put in a glass container which was then put in a water bath for temperature control. The impedance measurements were carried out in every 10 minutes by using two platinum electrodes in the range of 0.05–100 kHz. The quantity given by the Z value taken at 100 kHz divided by Z value taken at 0.1 kHz was used for analysis. Time course curves for both pH and acidity had only gentle slopes showing the progress of lactic fermentation. However, the time course for hardness had bending point indicating the start of coagulation. This bending point coincided with the bending point observed in the time course curve for the quantity $Z(100 \text{ kHz})/Z(0.1 \text{ kHz})$. It was concluded that impedance spectroscopy is applicable for online monitoring of yogurt processing and is more sanitary than the conventional methods.

Impedance spectroscopy has been found to be very useful in the field of metal packaging, using steel and aluminum as base materials. The packaging should be such that the corrosion stability is enhanced and metal migration into food is minimized. When a biological fluid is heated, deposition on the walls of the container takes place. For example β -lactoglobulin, which is the main constituent of milk deposits, gets deposited on the austenitic stainless steel heat exchanger walls. The effect of this deposit on the corrosion of the austenitic stainless steel heat exchanger

walls was studied by using impedance spectroscopy. When a stainless steel electrode is immersed in an electrolyte, Cr/Fe-rich oxide film gets formed on the surface. This passivating film prevents further dissolution of alloy atoms, and this process is represented by the charge transfer resistance in the equivalent circuit models used in impedance spectroscopy. When β -lactoglobulin was added to the solution, a decrease in charge transfer resistance was observed, indicating enhanced dissolution rate of the passive film, i.e. corrosion rate (Escarpa et al. 2015, p 387).

Similarly, impedance spectroscopy was used to examine the quality of coatings packages, such as lacquered tinplated cans, which are one of the most common packaging materials (Escarpa et al. 2015, p 389) used for canned foodstuffs. Due to the insulating properties of the lacquer, a perfectly protected (lacquered) tin plate with undamaged coating will have a high impedance and would behave like a capacitor which will give a straight line inclined at 90° in the Bode plot. In the case of a damaged coating, water would penetrate into the coating and form a new liquid/metal interface under the damaged area giving rise to corrosion. As a result, the interface would not be purely capacitive and the impedance spectroscopic plots would be different. In this way, impedance spectroscopy was successfully used to identify insufficient protection provided by the lacquer at stressed areas of samples which could not be detected by visual and microscopic examinations (Escarpa et al. 2015; Pournaras et al. 2008).

Impedance spectroscopy has been used to differentiate between different types of unifloral honeys, thus making it possible to find the floral origin of different honeys. By using this technique, the total soluble solid (TSS) content may be obtained that can be used for estimating the amount of adulteration in fruit juices based on conductivity (Jocsak et al. 2019; Scandurra et al. 2013; Zywica et al. 2015).

Various types of impedance spectroscopy-based sensors have been developed for detection of microbes and other systems by analyzing the interfacial resistance and capacitance changes occurring at the biomaterial functionalized electrodes due to biocatalytic transformations at the electrode surface in the presence of biomaterials (Escarpa et al. 2015, p 306). Formation of nucleic acid/DNA complex at an electrode surface gives rise to negatively charged interface which repels the negatively charged redox indicator $\text{Fe}(\text{CN})_6$ that leads to an enhanced charge transfer resistance. Increased charge transfer resistance indicates increased hybridized DNA. This technique has been widely used in recent years for detection of variety of foodborne pathogens. Detection of DNA by impedance spectroscopy using nanomaterials such as graphene have been reported (Giovanni et al. 2012; Bonanni and Valle 2010; Bonanni et al. 2010). Similarly, conductometric biosensing systems have been developed where specific biological interaction occurs on a supporting surface may vary the resistance or conductance of the substrate.

6.8 FUEL CELLS, SOLAR CELLS AND MISCELLANEOUS SYSTEMS

6.8.1 FUEL CELLS

A fuel cell is an environment-friendly device that directly converts chemical energy into electrical energy through electrochemistry. The basics of fuel cells are very nicely elaborated by O'hayre et al. (2016). A fuel cell essentially consists of two

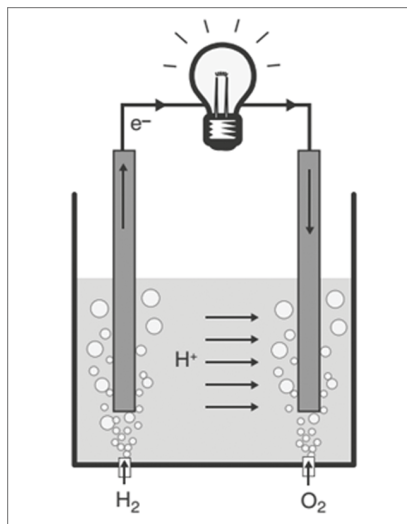
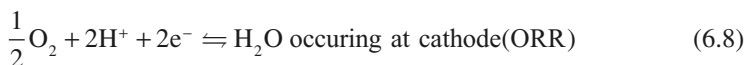
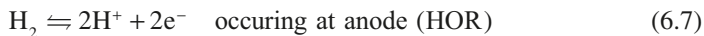


FIGURE 6.40 A simple fuel cell. (Reprinted with Permission from John Wiley & Sons, O'Hayre et al. 2016, Figure 1.4, Fuel Cell Fundamentals, Third Edition.)

electrodes (a cathode and an anode) separated by an electrolyte and a provision for supply of fuel on the anode side and oxygen or air on the cathode side. The system sustains on two coupled half-reactions: an oxidation reaction, liberating electrons at the so-called anode and a reduction reaction, consuming electrons, at the cathode. In $\text{H}_2\text{-O}_2$ fuel cell, where H_2 is the fuel, these are called hydrogen oxidation reaction (HOR) and the oxygen reduction reaction (ORR). A $\text{H}_2\text{-O}_2$ fuel cell is schematically shown in Figure 6.40.

The hydrogen combustion reaction is split in two electrochemical half-reactions



The electrons transferred from the fuel at the anode are made to move through an external circuit by spatially separating these reactions. The spatial separation is provided by using a suitable material (called electrolyte) between the electrodes which allows ions to pass through, but not the electrons. For example, as shown in Figure 6.40, two platinum electrodes dipped in sulfuric acid (H_2SO_4 working as electrolyte having large number of H^+ ions) are used and hydrogen gas is bubbled at the left electrode. Hydrogen is split into H^+ ions and electrons following Eq. (6.7). The H^+ ions can flow through the electrolyte and move toward the cathode, whereas the electrons cannot enter the electrolyte and move to the cathode through a wire connected externally between the anode and cathode. At the cathode, where oxygen

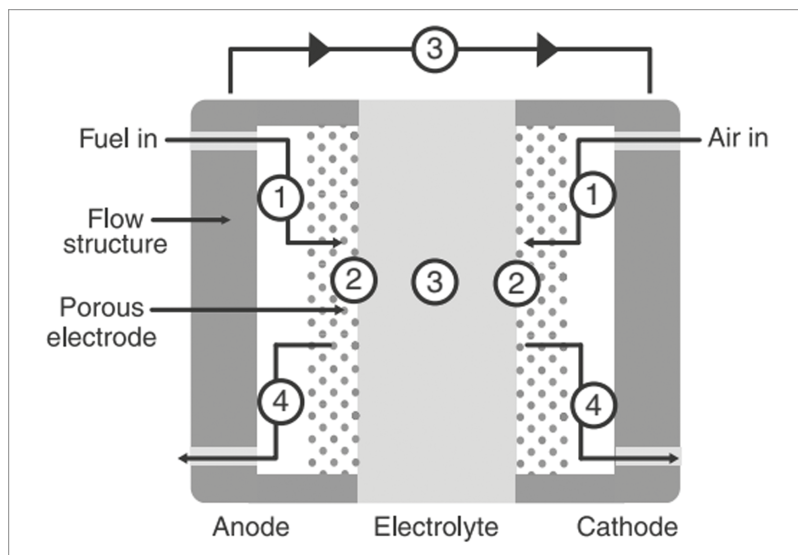


FIGURE 6.41 Cross section of fuel cell illustrating major steps in electrochemical generation of electricity: (1) reactant transport, (2) electrochemical reaction, (3) ionic and electronic conduction and (4) product removal. (Reprinted with Permission from John Wiley & Sons, O’Hayre et al. 2016, Figure 1.10, *Fuel Cell Fundamentals*, Third Edition.)

is being bubbled, these electrons combine with the H^+ ions and oxygen yielding H_2O following Eq. (6.8). The current flowing through the wire may be used to run a load (e.g. a bulb in Figure 6.40). The anode and cathode are separated by the electrolyte, so that the reduction and oxidation reactions occur in isolation from each other. The generation of electricity involves several steps, namely, reactant delivery to the cell, electrochemical reaction (at the electrode–electrolyte interface), conduction of electrons (ions) and product (unused gases, H_2O) removal from the cathode side. A fuel cell cannot get depleted as long as the fuel is supplied. The fuel used is hydrogen or a hydrocarbon such as methane. A fuel cell depicting these steps is schematically shown in Figure 6.41 (O’hayre et al. 2016).

In hydrogen–oxygen polymer electrolyte membrane fuel cell, electrons and H^+ ions accumulate at the anode and are consumed at the cathode. Accumulation of electrons at the anode and their depletion at the cathode creates a voltage gradient that gives rise to flow of electrons from anode to cathode through the external circuit. Similarly, accumulation of H^+ ions at the anode side of the electrolyte and their depletions at the cathode side of the electrolyte creates both voltage and a concentration gradient, which forces ions to move from the anode to the cathode through the electrolyte. Depending on the electrolytes used, fuel cells are divided into five major types (O’hayre et al. 2016).

1. Polymer electrolyte membrane fuel cell (PEMFC). Here, a thin polymer membrane (commonly made of material called Nafon) works as electrolyte,

- H_2 or methanol is the fuel and charge carrier is H^+ . The cell components are carbon based and the cell operates at 80°C .
2. Phosphoric acid fuel cell (PAFC). Here, the electrolyte is liquid H_3PO_4 , fuel is H_2 and charge carrier is H^+ . The components are carbon based and the cell operates at 200°C .
 3. Alkaline fuel cell (AFC), where liquid KOH is the electrolyte, fuel is H_2 and charge carrier is OH^- . The components are carbon based and the cell operates at $60\text{--}200^\circ\text{C}$.
 4. Molten carbonate fuel cell (MCFC). Here, molten carbonate is the electrolyte, H_2 or CH_4 is the fuel and charge carrier is CO_3^- . The components are stainless steel based and the cell operates at 650°C .
 5. Solid oxide fuel cell (SOFC). Here, a ceramic is the electrolyte [the most common SOFC electrolyte is yttria-stabilized zirconia (YSZ)]. H_2 , CH_4 or CO is the fuel and charge carriers are O_2^- ions. The components are ceramic based and the cell operates at $600\text{--}1000^\circ\text{C}$. In a PEMFC, reactions proceed by the movement of H^+ ions and water is produced at the cathode, whereas in a SOFC, the reactions proceed by the motion of oxygen ions (O_2^-), and water is produced at the anode. Various potential materials for SOFC are reviewed in Vostakola and Horri (2021).

For the development of efficient fuel cells, various characterizations such as measurements related to overall performance (current density–voltage curves, power density), mass transport, electrode structure, heating, ohmic properties (overall resistance, electrolyte conductivity, contact resistance, interconnect resistance), etc. are to be performed. The cell which provides larger reaction area (interfacial area where the reactants, the electrode and the electrolyte meet) produces more current. The reaction area is increased by making the electrodes highly porous, which, in turn, gives more access to gases. Fuel cells typically operate at much higher current densities than solar cells or batteries. This necessitates use of low-resistance materials in order to reduce ohmic losses. Thus, measurement of the cell resistance is of utmost importance in the development of a fuel cell.

One of the greatest sources of resistance in a fuel cell is the electrolyte. Electrolyte resistivity depends on operating conditions which demand that the resistance should be determined while the cell is operating. The electrode–electrolyte interface behaves as a capacitor due to formation of charge double layer. Therefore, cell resistance can be obtained by using alternating current–based techniques. Here, the technique of impedance spectroscopy has been found to be extremely useful. It is a powerful technique that can be used in situ to characterize the impedances in a fuel cell. AC impedance measurements can be helpful in identifying the kinetic, ohmic, electrolytic and diffusion layer resistances, as well as the transport limitations in the system by analyzing the impedance data utilizing suitable equivalent circuit model incorporating the possible charge transfer processes. Impedance spectroscopy is useful both in modeling fuel cell with electrical circuits and detecting malfunctions and low performances. Impedance spectroscopy is the most widely used technique for distinguishing different losses.

During an electrochemical reaction, charge separation occurs at the electrode–electrolyte interface, with electrons accumulating in the electrode side and the

ions accumulating at the electrolyte side of the interface. This causes the interface to behave like a capacitor, C_{dl} , due to the charge double-layer formation. Thus, the electrode–electrolyte interface can be modeled by a parallel R_f - C_{dl} combination, where the resistance R_f represents the kinetic resistance of the electrochemical reaction process. Mass transport, being of diffusive nature, can be modeled by Warburg circuit element (Z_W). Thus, a tentative simple equivalent circuit model for a fuel cell may be given as shown in Figure 6.42, where a simulated complex plane plot for some selected values of the parameters is shown.

In Figure 6.42, the resistance R_Ω represents ohmic losses present in the cell. The combination $R_{f,A}$ - $C_{dl,A}$ represents the anode-electrolyte interface and the combination $R_{f,C}$ - $C_{dl,C}$ represents the cathode-electrolyte interface, where $R_{f,C}$ has been replaced by a series combination $R_{f,C}$ - Z_W . In the Z'' versus Z' plot, it has been assumed that the anode kinetics are faster compared to the cathode activation kinetics, i.e. the anode contributions appear at the high-frequency side in Figure 6.42. The complex plane plot corresponds to $R_\Omega = 10\text{ m}\Omega$, $R_{f,A}$ (anode Faradic resistance) = $5\text{ m}\Omega$, $C_{dl,A}$ (anode double-layer capacitance) = 3 mF , $R_{f,C}$ (cathode Faradic resistance) = $100\text{ m}\Omega$, $C_{dl,C}$ (cathode double-layer capacitance) = 30 mF , cathode Warburg coefficient $\sigma = 15\text{ m}\Omega\text{s}^{1/2}$ (O’hayre et al. 2016). σ is the Warburg coefficient and characterizes the effectiveness of transporting species to or away from a reaction interface. The Warburg

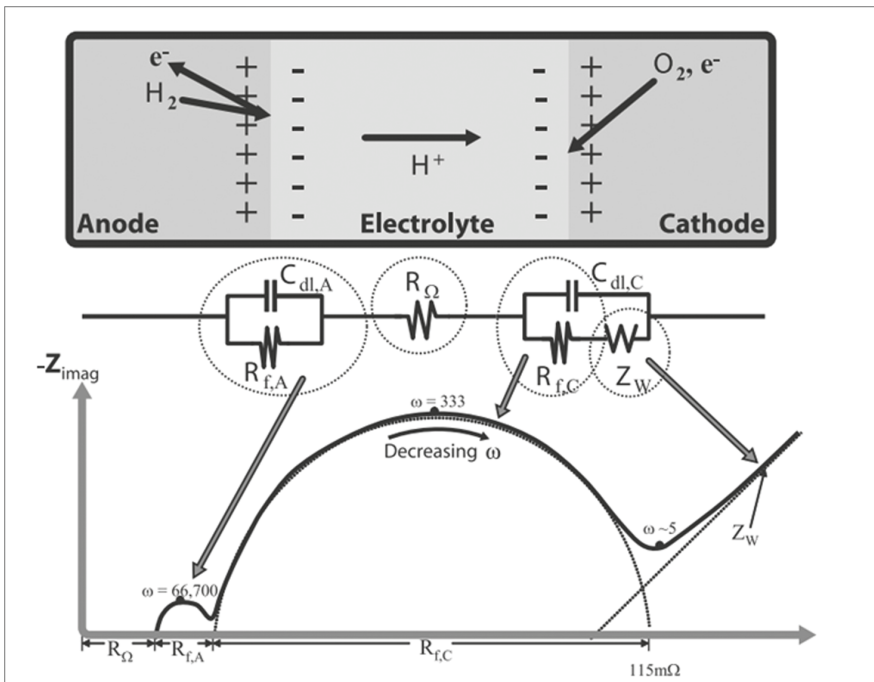


FIGURE 6.42 Physical picture, equivalent circuit diagram and complex plane plot for a simple fuel cell. (Reprinted with Permission from John Wiley & Sons, O’Hayre et al. 2016, Figure 7.12, Fuel Cell Fundamentals, Third Edition.)

impedance is given by $Z = \sigma (1 - j)/\omega^{1/2}$, where ω is the angular frequency. For anode, the value of time constant $R_{f,A} C_{dl,A}$ is 15 μ s, whereas it is about 3000 μ s for cathode. Therefore, the left arc appearing at higher-frequency side would correspond to the anode process and its peak value would occur at angular frequency ω equal to $1/(15 \times 10^{-6})$, i.e. 66,700 rad/s'. The arc that appears at the right low-frequency side would correspond to the cathode process.

The electrical behavior of solid electrolytes may be represented by equivalent circuit models involving R-C or R-CPE combinations. For example, an equivalent circuit model comprising two parallel R-CPE circuits, representing the grain and grain boundary behavior, connected in series, was used to represent the data for co-doped ceria samples of $Ce_{0.95-x}Ca_{0.05}Sr_xO_{1.95-x}$ where ($x = 0.00, 0.01, 0.02$ and 0.03), studied using impedance spectroscopy in the temperature and frequency range 200–600°C and 1 Hz–1 MHz, respectively, for its use in SOFC. The Z'' versus Z' plots typically possessed two depressed arcs and an emerging low-frequency straight tail. The low-frequency tail was attributed to the sample electrode interface. It was found that $Ce_{0.93}Ca_{0.05}Sr_{0.02}O_{2-\delta}$ exhibits maximum conductivity (i.e. minimum resistance) among all the compositions and may be a potential candidate as a solid electrolyte for intermediate temperature SOFCs (IT-SOFCs) (Jaiswal et al. 2013). Such studies on ceria having various dopings are reviewed by Jaiswal et al. (2019). When cell stacks are used, leads start becoming important which reflects in Nyquist plot as a tail extending below the Z' axis. This may be represented by including inductor (to represent leads) in the model.

SOFCs with liquified natural gas (LNG) as fuel, when incorporated in power supplies having conventional diesel engine, are expected to lower the fuel consumption and reduce the toxic air pollutant [NO_x , SO_x , particulate matter (PM), CO_2] emissions. SOFC-diesel hybrid motive power are promising power sources for applications, such as in marine, where the SOFC power units operate as auxiliary power unit (APU) for the steady power demand and the diesel engine responds to the load change. The working of SOFC and degradation must be regularly monitored in real time to improve the reliability and durability in order to ensure long-term safety, stable operation and prevention of accidents due to breakdown of the cell. Impedance spectroscopy has been proposed for this purpose by prior abnormality detection of the SOFC through an elucidation of the degradation factor accompanying the marine operation. Behavior of an operating anode-supported microtubular SOFC was investigated by using impedance spectroscopy. Anode substrate tube was made of $NiO/(ZrO_2)_{0.9}(Y_2O_3)_{0.1}(NiO/YSZ)$, which was coated with anode interlayer of $NiO/(Ce_{0.9}Gd_{0.1})O_{1.95}$ (NiO/GDC10) for low-temperature operation. Electrolyte used was $La_{0.8}Sr_{0.2}Ga_{0.8}Mg_{0.2}O_{2.8}$ (LSGM). To prevent undesirable nickel diffusion during cell preparation at high temperature, a layer of $(Ce_{0.6}La_{0.4})O_{1.8}$ (LDC40) was inserted between the anode interlayer and electrolyte. Cathode was made of $(La_{0.6}Sr_{0.4})(Co_{0.2}Fe_{0.8})O_3$ (LSCF) and was coated on the electrolyte. Anode gas line was supplied with mixtures of H_2/N_2 or the simulated syngas and the cathode gas line was supplied with dry air. An equivalent circuit model consisting of two parallel RCs representing the anode and cathode processes and a resistor representing the cell resistance, all connected in series, was used. The values of the circuit parameters were obtained. It was concluded that changes observed in the circuit parameters by internal reforming

and anode degradation can be used for the real-time diagnosis of operating SOFCs (Nakajima et al. 2016).

Rapid fault diagnosis of PEM fuel cells by using impedance spectroscopy tests have been recently reported (Najafi et al. 2020). For controlling pollution and global warming, intensive efforts are being made toward development of renewable and environment-friendly systems to replace fossil fuel-based power generation. Production of battery-driven electric vehicles are being encouraged. However, the batteries take much longer time to get fully charged as compared to the current refueling time of a gasoline-based vehicle, and this has compelled for consideration of other alternatives such as PEMFC, where hydrogen is the fuel. However, in addition to cost, its operation is strongly dependent on the operating conditions. For stable power generation, the unit needs to be operated within the optimal ranges otherwise various issues emerge, such as problems related to water content of the membrane, which should remain well-hydrated during the operation. Nonoptimal water content results in conditions of dehydration or flooding faults within the cell. This necessitates a regular checkup and diagnosis of PEMFCs. Impedance spectroscopy has been found to be a promising diagnostic tool for recognizing faults and in particular water management-related ones (Najafi et al. 2020). In the state of dehydration, the ionic conductivity of the membrane is reduced, i.e. the resistance is increased and as a result, the Nyquist plot shifts toward the right (higher real values). Presence of too much water in the cell increases the conductivity of the membrane (i.e. reduces its resistance) but at the same time blocks the cathode diffusion layer pores, which, in turn, hinders mass transport and reduces the active sites in cathode catalyst layer. This results in a wider Nyquist plot having low real part (Najafi et al. 2020). These observations may be used to raise safety alarms.

6.8.2 SOLAR CELL

Solar cell is a device that directly converts the energy of light into electrical energy through photovoltaic effect. Due to depleting fossil fuels and environmental concerns, solar cells are getting increasing attention worldwide. It is basically a pn junction which generates electromotive force (emf) when solar radiation falls on it. A typical photovoltaic solar cell is schematically shown in Figure 6.43.

The n-region is heavily doped and is thin so that the light can penetrate easily. The p-region is lightly doped and most of the depletion region lies in the p-region. When the energy of the incident light photon matches with the band gap of the electrons, photons are absorbed in the depletion region (W) within the neutral p-side (l_p) and electron-hole pair is produced. Due to the inbuilt potential difference present across the depletion region giving rise to an electric field (E_0) directed from n-region to p-region, the electrons move to the n-region and the holes toward the p-region. When the electron reaches the n-region, the region gains a charge $-e$. Similarly, the neutral p-side becomes positive when a drifting hole reaches there. Thus, an open circuit voltage (V_{oc}) is developed across the electrodes connected to n- and p-regions with the p-side being positive with respect to n-inside. These excess electrons on n-side can travel through an externally connected load to recombine with the excess holes on the p-side.

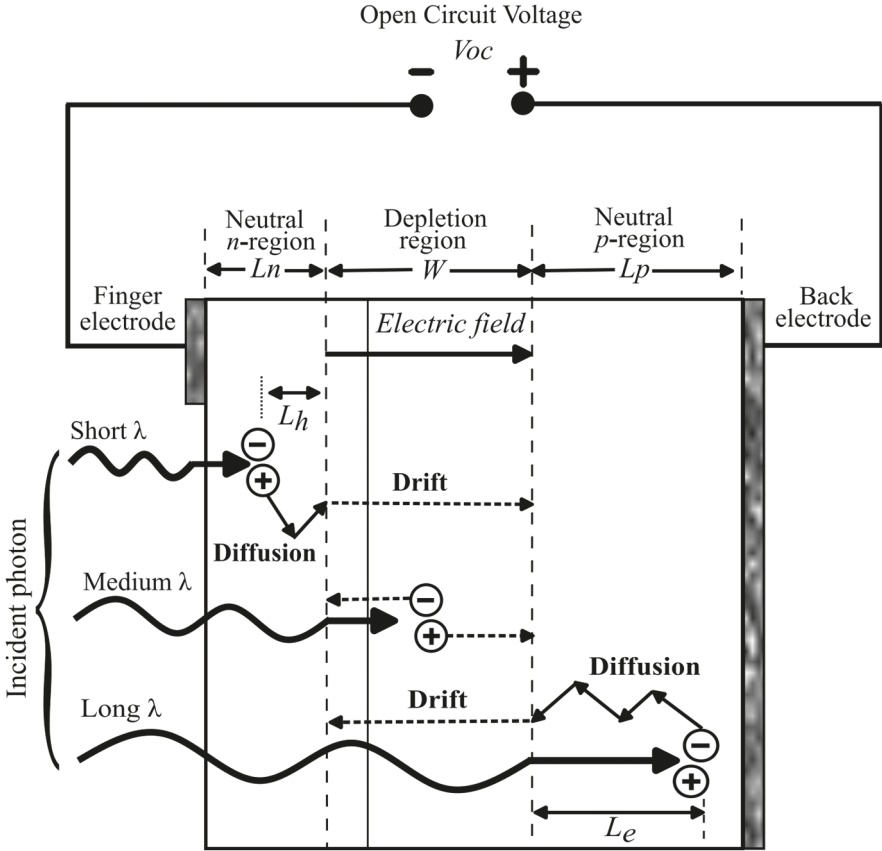


FIGURE 6.43 Working of a solar cell. Solar radiation of wave length λ falls on the n region giving rise to a voltage V_{oc} across the electrodes.

Further, it is seen that the shorter wavelengths have higher absorption coefficient and are absorbed in the n-region creating electron–hole pairs. The longer wavelengths get absorbed in the p-region that too create electron–hole pairs. As there is no electric field in the neutral n-region or neutral p-region, the photogenerated electron and holes diffuse around. For example, if electron recombination time is τ_e and D_e is the diffusion coefficient in the p-side, the electron would diffuse by a distance $L_e = \sqrt{2D_e \tau_e}$ in time τ_e due to its random motion before it recombines. It means that electrons present in the p-region within the distance L_e away from the depletion region would be able to reach the depletion region where they will be drifted to the n-side by the field E_0 and contribute a negative charge to the n-region. The corresponding hole left behind would contribute a positive charge to the p-region. Thus, electrons present in the p-side within a distance L_e away from the depletion region and the holes present in the n-side within a distance L_h away from the depletion region would be able to diffuse to the depletion region, where they would be swept by the field E_0 to the n-side and p-side, respectively, and would contribute a negative charge to n-region

and a positive charge to p-region. Carriers produced in this way as well as those generated in the depletion region contribute to the current. The current produced by the photogenerated carriers is called photocurrent and the electron–hole pairs contributing to this cover the region $L_h + W + L_e$. The pairs produced at sites farther than L_h or L_e from the depletion region are lost by recombination and do not contribute to current.

The flow of current is facilitated by fixing electrodes at the n-side and p-side surfaces. Finger electrodes are used on the top n-side (shown at the left side in Figure 6.43) so that maximum light penetrates through. For Si solar cell, the band gap is 1.1 eV. The photons with wavelengths above 1.1 μm are not absorbed as their energy is lower than the band gap. Photons with wavelengths much shorter than 1.1 μm have high absorption coefficient and get quickly absorbed at the entry. Near the surface the electrons and holes may get trapped in the surface states and would not contribute to the current. Thus, there is an optimum range of wavelengths for proper working of a solar cell. For improving the efficiency, cells made of materials that provide different band gaps may be suitably connected so that various wavelengths are maximally absorbed (Kasap 2006).

Various types of solar cells have been developed with a view to have enhanced efficiency. New cells having increasing efficiencies are developed by utilizing improved fabrication techniques and better materials. However, due to their reduced cost and mature fabrication process, silicon solar cells and panels are still most widely used for the installation of photovoltaic power plants. For achieving improved optimization of the solar cells, determination of the characteristics of their performance is essential (Brana et al. 2015; Hauff 2019).

Solar cells tend to degrade over time due to many factors such as microcracks, potential-induced degradation (PID), disconnection of ribbons, etc. caused by thermal cycling, damp heat, UV exposure, mechanical stress, etc. (Sharma et al. 2020). Among several available diagnostic tools, study of the I-V characteristics is simple and, therefore, is frequently used in solar power plants to check the performance under various operating conditions. Impedance spectroscopy is a promising technique for solar cell degradation characterization as significant changes in equivalent circuit parameters are noticed after degradation tests. For example, impedance spectroscopy has been used for studying the performance of commercial silicon polycrystalline solar cell degraded by creating a hotspot, mechanical stress and disconnection of interconnection ribbon (Sharma et al. 2020). Impedance measurements were carried out in the frequency range of 0.1 Hz–1 kHz. The Z'' versus Z' plot had a single semicircular arc. Randles equivalent circuit model (a parallel $R_p C_p$ combination connected in series to another resistance R_s) was used to represent the data. In what follows, results of effects of mechanical stress are briefly presented. Mechanical stress up to 0.62 N/mm² was applied on solar cells at three different locations: right side, middle and left side. The area of applied stress accounted for 2.53% of the total area of the solar cell. It was observed that the value of R_s did not change much and remains below 0.7 Ω after mechanical stress. However, decrease in the value of R_p and shrinkage in the Nyquist plot was seen. The decrease in R_p was attributed to development of invisible minor cracks due to stress. This causes leakage current to increase through the pn

junction which reflects as reduction in the value of parallel resistance R_p (Sharma et al. 2020). Impedance spectroscopy has been recognized as a suitable technique for in-depth studies of thin-film polycrystalline solar cells (Proskuryakov et al. 2009, 2007) as it enables the separation of contributions from different layers or regions of the solar cell structure.

Perovskite solar cells (PSCs) are one of the fast-evolving next-generation photovoltaic devices (Chi et al. 2014; Hailegnaw et al. 2020; Bou et al. 2020; Khan et al. 2020; Yoo et al. 2019). The power conversion efficiency has been greatly improved over the years and exceeds 25%, which is comparable with crystalline silicon, cadmium telluride and other high-performance solar cells (Hailegnaw et al. 2020). The PSCs involve a perovskite absorber layer. A perovskite is a material having molecular formula ABO_3 , where A is a divalent and B is a trivalent ion. The mineral $CaTiO_3$ bears the name perovskite and materials having this structure are collectively termed as perovskites. The unit cell comprises a Ti ion sitting on the octahedral site at the center of a cube and surrounded by six oxygen atoms occupying face center positions. The corners have Ca atoms.

Improvements in the active layer, contacts and the interfaces have made perovskite solar cells a real candidate for commercialization (Bou et al. 2020). However, long-term stability needs to be addressed for a successful commercialization. The long-term stability is greatly influenced by degradation of material and the electrodes due to exposure to UV, moisture, etc. Compositional, structural and interface modifications have been applied for improving the stability. However, for improvement in stability, a detailed study is required to understand the charge transfer processes taking place in the bulk and interfaces and the changes occurring in the system under practical conditions. Impedance spectroscopy has been applied extensively in PSC research (Bou et al. 2020). In order to get an idea of how this technique is applied to PSCs, the work done by Hailegnaw et al. (2020) is now briefly described. A PSC is schematically shown in Figure 6.44 (Hailegnaw 2020).

Here patterned indium tin oxide (ITO)-coated glass substrate has been used. On the top of ITO, PEDOT:PSS layer was spin coated. After suitable heat treatment, a layer of perovskite $MAPbI_{3-x}Cl_x$ solution was spin coated on this. Then, [6, 6]-phenyl-C61-butyric acid methyl ester (PCBM) was spin coated followed by TiO_x spin coating on top of PCBM. Al back electrode was fixed by thermal evaporation. PCBM is an acceptor material working as electron transporting agent and PEDOT:PSS is a donor material. Solar light enters the cell through the glass shown at the bottom in Figure 6.44.

Impedance spectroscopy was applied to study the charge transfer processes in the PSC in the photoactive bulk as well as at the contact-absorber interfaces before and after continuous operation under simulated solar radiation, with a view to identify the processes and mechanisms responsible for the deterioration of device performance over time. The Z'' versus Z' plots showed two semicircles in two distinct frequency regions indicating presence of different processes in the device as is generally observed in PSCs.

The high-frequency arc is related to bulk recombination and geometrical capacitance. The low-frequency arc is related to interfacial phenomenon. The large

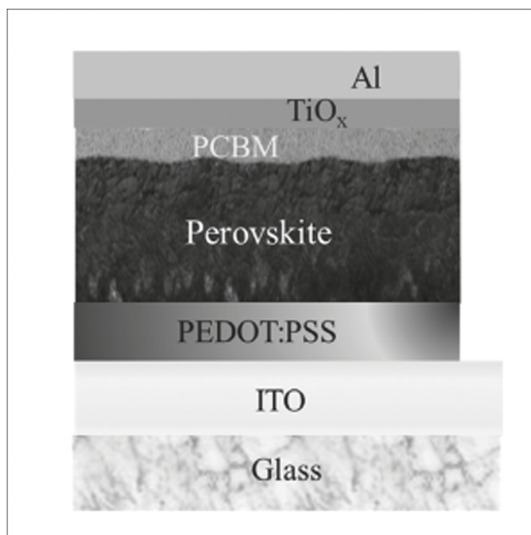


FIGURE 6.44 Schematic diagram of perovskite solar cell. (Reprinted from Hailegnaw Bekele, Niyazi Serdar Sariciftci, and Markus Clark Scharber, 2020, Figure 1, Impedance Spectroscopy of Perovskite Solar Cells: Studying the Dynamics of Charge Carriers before and after Continuous Operation, *Phys. Status Solidi A*, 217: 2000291–2000298. DOI: 10.1002/pssa.202000291, Open Access.)

capacitances associated with the low-frequency response have been interpreted to be arising from accumulation of ionic and electronic charges at interfaces. An equivalent circuit model used to analyze the impedance data is shown in Figure 6.45 (Hailegnaw et al. 2020).

Here, the series resistance R_1 is used to represent resistances including contact resistance, wire resistance and sheet resistance of the electrode, CPE_1 represents the dielectric response of the perovskite layer at high frequencies and R_2 is the corresponding charge transport resistance. The combination R_3 - CPE_2 represents the low-frequency response related to surface charge accumulation at the interfaces. Usual practice has been to use capacitors in the place of CPEs in this equivalent circuit model which may be further improved by including inductors to represent loops observed in complex plane impedance plots (Bou et al. 2020). Changes in the values of the components of the model shown in Figure 6.45 were observed before and after 48 hours of continuous illumination and were correlated with bulk and interface behaviors. It was found that both the device charge transport resistance and interface capacitance associated with charge accumulation at the interfaces increase upon continuous operation. It was inferred that ion migration from the photoactive perovskite layer to the charge transport layer interfaces was taking place leaving defects in the bulk. It was concluded that the deterioration in the cell performance on continuous operation was mainly due to changes in the bulk of the perovskite layer and accumulation of charges at the interfaces.

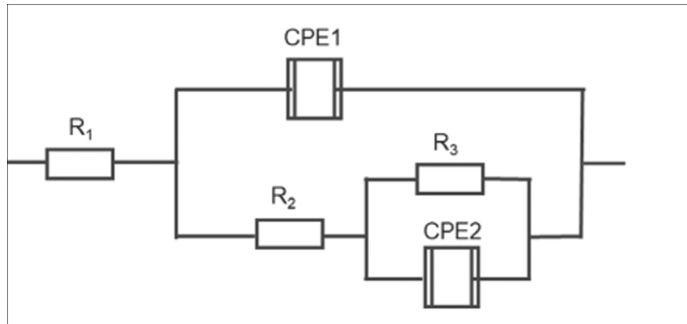


FIGURE 6.45 Equivalent circuit model for the perovskite solar cell. (Reprinted from Hailegnaw Bekele, Niyazi Serdar Sariciftci, and Markus Clark Scharber, 2020, Figure 2(c), Impedance Spectroscopy of Perovskite Solar Cells: Studying the Dynamics of Charge Carriers before and after Continuous Operation, *Phys. Status Solidi A*, 217: 2000291–2000298. DOI: 10.1002/pssa.202000291, Open Access.)

Graphene, being a transparent, conducting and low-cost item, is a promising material for solar cell development. When graphene is deposited on crystalline silicon, Schottky junction is formed with grapheme acting as the metal of a metal–semiconductor (MS) junction, which can be used for development of cost-effective solar cell (Matacena et al. 2020; Li et al. 2010). The overall performance of the cell is strongly influenced by the behavior of interfaces, such as electrode–graphene contact, grapheme–silicon interface, etc. In order to develop the device having optimum efficiency, the contribution of these interfaces must be separated out and impedance spectroscopy may be successfully used for this purpose. As an example of such a study work by Matacena et al. (2020) is now briefly described. All the finer details have been ignored, with focus being on the equivalent circuits. In their work, they applied impedance spectroscopy to decide whether a gold electrode gives a better performance or a graphite glue. The solar cell was fabricated by using commercial n-type Si wafers upon which graphene films were transferred. The back contact was realized by evaporating Al on the back side of the wafer. Two types of top contacts were made, one by depositing gold and the other by applying colloidal graphitic glue. The Z'' versus Z' complex plane plots for solar cell with gold contact (Au/G/Si/Al) and also for the solar cell with the graphitic glue contact (graphite/G/Si/Al) were obtained. The Z'' versus Z' plots for (Au/G/Si/Al) solar cell possessed distorted semicircular arcs and the data could be represented well by an equivalent circuit model having three parallel RC circuits and a resistance, all connected in series. These three parallel RCs were recognized to represent graphene–silicon interface, gold–graphene interface and the aluminum–silicon interface for (Au/G/Si/Al) solar cell. The Z'' versus Z' plots for the graphite/G/Si/Al solar cell were almost semicircular arcs and the data could be represented well by an equivalent circuit model having two parallel RC circuits and a resistance, all connected in series, indicating that less active interfaces are not playing an important role in this device. It was concluded that contact technology based on the graphitic glue gives better performance as compared to standard gold contact technology.

6.8.3 MISCELLANEOUS SYSTEMS

6.8.3.1 Gas Sensors

Impedance spectroscopy-based gas sensing has been considered as an ultrasensitive technique to identify and measure different toxic gases, and its performance is found to be superior to other conventional techniques (Balasubamani et al. 2019, 2020). Toxic gases commonly present in the environment include NH_3 , CO, methanol, NO, NO_2 , H_2S , SO_2 , etc., which are regularly emitted by industrial establishments, power plants, transportation, etc. and are hazardous to health if exposed beyond certain limits of duration and quantity. Various types of gas sensors have been developed. Optical gas sensors are based on the changes in optical properties like fluorescence, scattering, absorbance, refractive index, reflectivity and optical path length to detect target gases. Quartz crystal microbalance (QCM)-based gas sensors utilize the piezoelectric properties of quartz and the shift in the resonance frequency when there is mass change on the surface of the crystal. Field-effect transistors (FETs)-based gas sensor is a small device having low power consumption, low cost and ease of fabrication. The sensing semiconducting material such as graphene is placed between the source electrode and drain electrode. The change of the drain-source current of the semi-conductive sensing unit caused by the adsorbed target gas molecules on the semiconductor surface is used for detection. Chemiresistor-based gas sensors are based on the changes in resistance of a sensing layer produced by adsorbed gases. Impedance spectroscopy-based gas sensors utilize the changes in electrical impedance of the sensing material-electrode system caused due to exposure to gases. The technique not only detects the gases but also provides working details and information about the impedance changes occurring at grains, grain boundaries and material-electrode interfaces due to gas penetration, which, in turn, helps develop better sensor materials by elaborating the mechanisms involved. This is achieved by fitting the impedance data to suitable equivalent circuit model and observing the changes occurring in the circuit parameters in the presence of specific gases. For example, Balasubramani et al. (2019) have developed a H_2S gas sensor by fabricating a reduced graphene oxide (rGO) incorporated into ZnO (rGO/ZnO) composite with alumina substrate as electrode.

A typical Nyquist (Z'' vs Z') plots of ZnO/rGO composites that were exposed to air containing 2–100 ppm of H_2S gas are shown in Figure 6.46, where the equivalent circuit used is shown in inset. It is seen that the low-frequency intercept goes on decreasing as the H_2S concentration increases.

6.8.3.2 Petroleum

Impedance spectroscopy was used for in situ characterization of contents of petroleum- and water-in-oil emulsion (Perini et al. 2012; Qing et al. 2018) at different stages of the petroleum refining production process. Petroleum is a complex mixture of hydrocarbons (such as paraffins, naphthenes, aromatics, unsaturated hydrocarbons, sulfur compounds and large varieties of other compounds, such as thiols, sulfides, cyclic sulfides, disulfides, thiophenes, benzothiophenes, dibenzothiophene and naphthobenzothiophenes), oxygen-containing compounds (such as alcohols, phenols, ethers, carboxylic acids, esters, ketones and furans) and nitrogen-containing compounds (such as pyrrole, indole, carbazona, benzocarbazona, pyridine, quinoline, indoline and benzoquinolines), including their metallic constituents. Due to

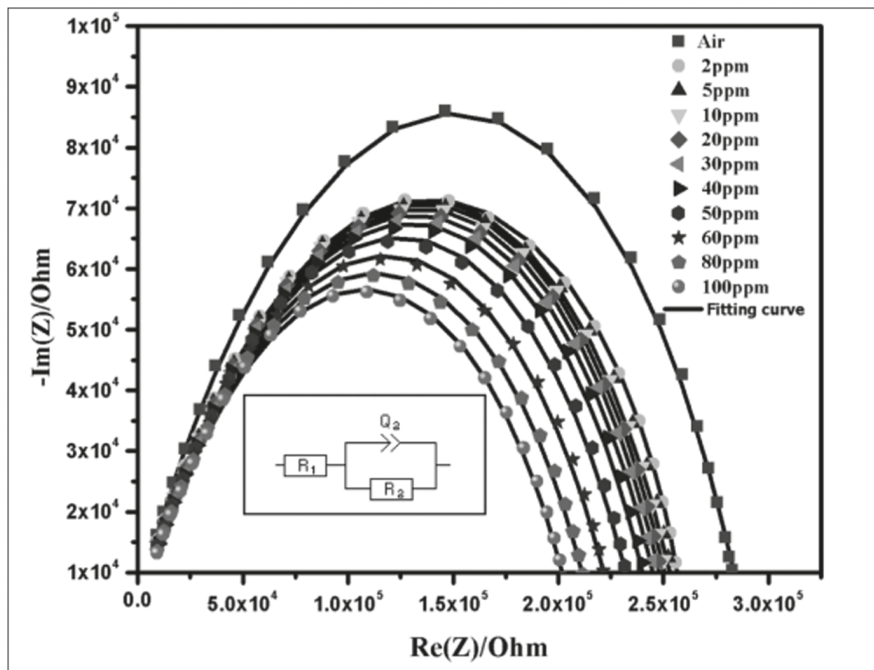


FIGURE 6.46 Nyquist impedance plot of ZnO/rGO nanocomposites exposed to air with various concentrations of H_2S gas (2–100 ppm) at 90°C . (Reprinted with Permission from ACS Publications, Balasubramani V., S. Sureshkumar, T. Subba Rao, and T.M. Sridhar, 2019, Figure 4, Impedance Spectroscopy-Based Reduced Graphene Oxide Incorporated ZnO Composite Sensor for H_2S Investigations, ACS Omega, 4: 9976–9982, doi:10.1021/acsomega.9b00754.)

difficulty in determining the composition, usually the physicochemical properties of oil are measured which are used for petroleum classification that is helpful in deciding refining strategies and other commercial planning. In the current oil fields, secondary exploitation strategies that rely on increasing the reservoir pressure by injecting water into the reservoir are used. Oil is extracted with a high concentration of water during the process of offshore production and therefore, in an offshore production, the extracted petroleum contains high concentration of water and the free water is removed using gravity. During the transportation, water-in-oil emulsion gets formed which can be removed by using various techniques. Perini et al. (2012) applied impedance spectroscopy for in situ characterization of contents of petroleum and water-in-oil emulsion. They analyzed their impedance data by using two parallel R-CPE combinations connected in series representing oil and water-in-oil emulsion. The resistances of oil and the emulsion were found to increase with water content. The increase in resistance shows that the emulsions become more stable with the addition of water. They also found that impedance behavior of samples containing water-in-oil emulsion is quite different from that of dehydrated samples. The complex plane

impedance plots for dehydrated samples exhibited a single semicircular arc only and could be well represented by a parallel RC circuit (Quing et al. 2018).

6.8.3.3 Battery

Impedance spectroscopy is a highly suitable method for battery diagnosis. A battery is a device that stores electrical energy and can then deliver that energy through an easily controlled electrochemical reaction. A battery is usually composed of a series of cells that produce electricity. A cell consists of two electrodes (the anode and the cathode) and an electrolyte which separates them. The battery's characteristics, including its capacity (total amount of energy it can deliver) and its voltage, are governed by the materials used for the electrodes and for the electrolyte. The anode and cathode materials are chosen so that the anode donates electrons, and the cathode accepts them. The tendency to donate or accept electrons is expressed as material's standard electrode potential, and the difference between the anode and cathode electrode potentials determines the cell voltage. When the electrodes are connected together by a conductor, the anode undergoes a chemical reaction (called oxidation) with the electrolyte in which it loses electrons, creating positive ions (cations). Flow of electrons occurs from anode to the cathode through the external conductor while the positive ions move toward the cathode through the electrolyte. The electrons meet these cations at the cathode. Release of electrons is called oxidation and acceptance of electrons is called reduction. The functioning of the cell is based on these so-called redox (reduction oxidation) reactions. The reaction would continue for some time until the anode gets completely depleted and then the cell stops working. In order to prevent this from happening, rechargeable batteries have been developed where this reaction is reversed by applying external voltage so that the battery gets charged. Due to their ability to supply high surge currents, which are required for starter motors in vehicles and low-cost lead-acid batteries are popular. However, other alternatives are looked for to avoid the use of toxic lead.

Lithium-ion batteries (LIBs) have been extensively used as rechargeable power sources for mobile and automotive products. Owing to their low cost, higher energy density, superior power capability and long cycle life, there is a rising demand of LIBs for being used as secondary battery in electric vehicles and large-scale renewable energy storage systems (Abe et al. 2019). A LIB may consist of graphite anode, lithium transition metal oxide (LiFePO₄ LFP) cathode, porous separator and nonaqueous electrolyte. Lithium (Li) is easily ionized to form Li⁺ and one electron. The electrolyte is typically a combination of lithium salts. The lithium ion is the cation that travels from anode to cathode through the electrolyte. LIBs can be recharged by running the anode and cathode reactions in reverse. Generally, battery systems with higher gravimetric energy densities (important for range and vehicle weight) and improved safety are desired. LIBs having solid electrolytes are found to be promising with respect to these requirements of high-energy density and safety (Vadhva et al. 2021; Ezpeleta et al. 2022).

The performance of batteries gets deteriorated over time and the performance degradation is generally accelerated by high rate and temperature (Abe et al. 2019). Therefore, usability of a battery for an application needs to be regularly checked

and indicated. This is facilitated by giving information about “state-of-health (SOH)” and “state of charge (SOC)” of the battery. SOC of a battery is the fraction usually expressed as percentage of the full capacity of the battery that is still available for further discharge. The SOC is reflected by the electrical response associated with the battery’s impedance where the application of a load causes the battery voltage to drop instantaneously. This phenomenon can be used to estimate the resistance of the battery. SOH refers to a measurement that reflects the state-of-health of a battery, taking into account its charge acceptance, internal resistance, voltage and self-discharge. It has been mostly associated to capacity fade (i.e. decrease in charge storage ability) or power fade (i.e. extractable power limitation due to increased cell impedance) or both. Aged batteries have larger resistances that may create heating and explosions. Therefore, SOH and SOC need to be continuously monitored.

A key criterion with respect to rechargeable batteries is cycle life, i.e. how many cycles a battery can undergo before significant loss of performance (Middlemiss et al. 2020) occurs. The performance of batteries decreases with cycling due to degradations associated with the components and interfaces. Drop in capacity occurs due to loss of alkali metal components or of the active anode/cathode material. Rise in internal cell impedance indicates deterioration of ionic transport in the electrolyte and is an important factor in assessing the SOH of a battery. The overall battery performance is determined by the bulk and interfacial transport processes. These processes have different time constants and therefore take place over many length- and timescales and display their maximum response at different frequencies. Impedance spectroscopy is a nondestructive technique which spans a large frequency domain (mHz to MHz) and is widely used to obtain the sample and interfacial contributions to the impedance. These contributions can be separated and tracked with respect to temperature, applied pressure, SOC, cycling and ageing. By using impedance spectroscopy, the SOH can be checked in situ for a battery on board (Middlemiss et al. 2020; Kallel et al. 2022; Vadhva et al. 2021).

The analysis of impedance data is carried out as usual by choosing a suitable equivalent circuit model and estimating the model parameters by using least squares fitting. Various models developed for batteries have been described by Westerhoff et al. (2016). As a small illustration, some of the results of the impedance spectroscopic studies on rechargeable LIBs performed by Wang et al. (2012) is now briefly described. For determining the cyclic performance of the battery and further improvement, knowledge about the kinetics of lithium ion transport in the oxide host and the stability of the host during charge/discharge process is useful. In their work, impedance spectroscopy was used to study the kinetics of promising electrode materials. The impedance measurements were carried out by using $\text{LiNi}_{1/3}\text{Co}_{1/3}\text{Mn}_{1/3}\text{O}_2$ as cathode, metallic lithium foil as counter electrode and LiPF_6 as electrolyte in a two-probe arrangement from 100 kHz to 5 mHz and the Nyquist plots at initial state, 40% SOC, 80% SOC and 100% SOC at first, second and tenth charge/discharge cycle, were investigated. These Nyquist plots are shown in Figure 6.47.

It is seen that, at the initial state, i.e. 0% SOC [Figure 6.47(a)], the plot consists of a depressed arc looking like a half ellipse covering the high- and intermediate-frequency ranges and a straight line inclined at a constant angle to the real axis

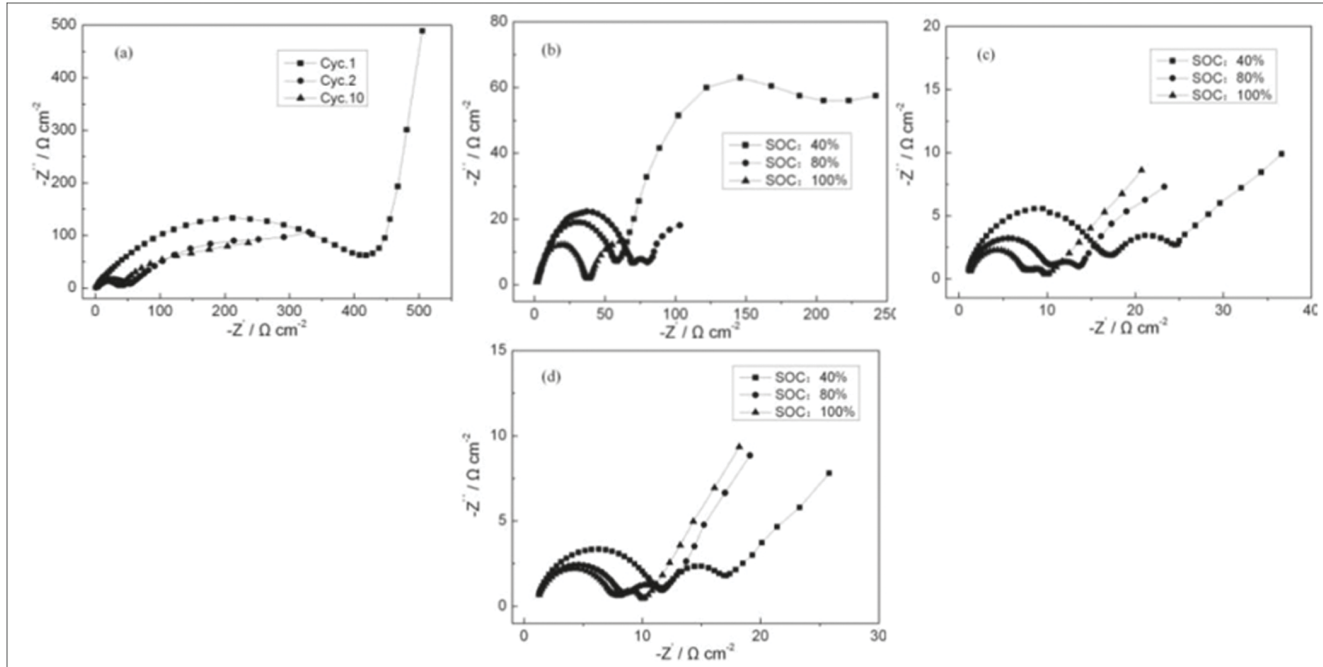


FIGURE 6.47 Nyquist plots of $\text{LiNi}_{1/3}\text{Co}_{1/3}\text{Mn}_{1/3}\text{O}_2$ cathode. (a) The plots at the initial state (0% SOC) of first, second and tenth cycle; (b) the plots at 40% SOC, 80% SOC and 100% SOC of the first cycle; (c) the plots at 40% SOC, 80% SOC and 100% SOC of the second cycle; (d) the plots at 40% SOC, 80% SOC and 100% SOC of the tenth cycle. (Reprinted with Permission from Li Wang, Jishi Zhao, Xiangming He, Jian Gao, Jianjun Li, Chunrong Wan, and Changyin Jiang, 2012, Figure 1, *Electrochemical Impedance Spectroscopy (EIS) Study of $\text{LiNi}_{1/3}\text{Co}_{1/3}\text{Mn}_{1/3}\text{O}_2$ for Li-ion Batteries*, *Int. J. Electrochem. Sci.*, 7: 345–353, Open Access.)

in the lower-frequency range. The plots for second and tenth cycles are similar to each other but are quite different from the plot at first cycle. The difference is in the low-frequency side and the arcs are smaller.

When the $\text{LiNi}_{1/3}\text{Co}_{1/3}\text{Mn}_{1/3}\text{O}_2$ electrode is charged to 40% SOC, the shape of the Z'' versus Z' plot changes totally and two semicircles are observed. Similar features were observed for 80% SOC and 100% SOC as well. Also, it is seen that when SOC increases from 80 to 100%, there are not much changes in the size of the semicircles in the high-frequency side, indicating that the passivating film has become stable. Moreover, the difference in radius between the first cycle and the second cycle is larger than that between the second cycle and the tenth cycle, revealing that the passivating film forms mostly during the first charge/discharge process and is stable during the latter charge/discharge cycles.

Equivalent circuit models involving resistances, capacitances (CPE) and Warburg elements were used to represent the data. Values of charge transfer resistance, electrode resistance, etc. were obtained and interpreted.

Very-low-frequency measurements are time consuming and drifts are observed in the impedance values for the same battery measured at different times. In order to facilitate impedance measurements at extra low frequencies (~microhertz), programmable two-quadrant power supplies to deliver multiple small-signal measurement tones in the presence of large-signal working currents have been recently reported. This enables impedance measurements with good precision and in reasonable time (Dunn and Scott 2022).

6.8.3.4 COVID-19

A virus is an infectious microbe of simple structure consisting of a segment of nucleic acid [either DNA or ribonucleic acid (RNA)] surrounded by a protein coat. The name is derived from a Latin word meaning “slimy liquid” or “poison”. All true viruses contain nucleic acid, either DNA or RNA, and protein. The true infectious part of any virus is its nucleic acid. They are not free-living, i.e. they cannot reproduce and carry on metabolic processes without a host cell. They consist of a genetic material, contained within a protein shell called a capsid. The infective, extracellular (outside the cell) form of a virus is called the virion. The virion capsid protects the viral nucleic acid from digestion by certain enzymes (nucleases). It provides sites on its surface that recognize and attach (adsorb) the virion to receptors present on the host cell surface. Further, it provides proteins enabling the virion to penetrate through the host cell surface membrane. In some cases, the protein shell is enclosed in a membrane called an envelope. The virus infects its host by attaching to the host cell (adsorption), penetrating the cell wall or membrane, and forcing it to replicate the viral genome and produce viral proteins to make new capsids. These, in turn, burst out of the host cell during a process called lysis, which kills the host cell. Thus, viral replication in the host organisms goes on and living organisms get infected. They can infect a variety of living organisms, including bacteria, plants and animals. Viruses that infect animals can jump from one species to another, causing a new, usually severe disease in the new host. The viruses that infect humans are only a small fraction of the viruses that are found in the world (genetics-glossary 2022, www.britannica.com/science/virus).

Viral genomes are very diverse, since they can be DNA or RNA, single- or double stranded, linear or circular and vary in length and in the number of DNA or RNA molecules (www.nature.com 2022). The size of most viruses lies in the range of about 20 nm to few hundred of nanometers and can be observed under an electron microscope. Viruses having “crownlike” fringe of projections, seen on their surface when viewed under the electron microscope, have been called as “corona viruses”. The name coronavirus derives from the Latin word “corona”, meaning crown or halo. Until 2002, coronaviruses were perceived primarily as causes of the “common cold” and were not generally a subject of major public health or research interest (Richman et al. 2017, p 1243; Saxena et al. 2021). In the winter of 2002–2003, an unusual and often lethal form of pneumonia appeared. This was named as severe acute respiratory syndrome (SARS) and the corresponding virus as SARS-CoV. In 2012, corona virus infections spread in middle east countries and the related virus was named as Middle East respiratory syndrome coronavirus (MERS-CoV). In December 2019, a novel corona virus having symptoms similar to that of SARS-CoV and MERS-CoV emerged and was called as SARS-CoV-2. The disease was named as novel corona virus disease-2019 or COVID-19 and, due to very fast rate of its spreading, was declared as pandemic (Saxena et al. 2021). SARS-CoV-2 is an enveloped, nonsegmented, positive-sense RNA virus having diameter of about 65–125 nm, containing single strands of RNA and has crownlike spikes on the outer surface. The spike or S glycoprotein forms homotrimers protruding in the viral surface and facilitates binding of envelope viruses to host cells by attraction with angiotensin-converting enzyme 2 (ACE2) expressed in lower respiratory tract cells. This virus can enter the human body through its receptors, ACE2, which are found in various organs such as heart, lungs, kidneys and gastrointestinal tract, thus facilitating viral entry into target cells. The process of CoV entering into the host cell begins through the attachment of the S glycoprotein to the receptor ACE2 in the host cells. The entry and binding processes are then followed by fusion of the viral membrane and host cell (Astuti and Ysrafil 2020).

Several techniques have been put forward for virus detection (Saxena et al. 2021). Tests based on gene amplification by polymerase chain reaction (PCR) like quantitative reverse transcriptase PCR (qRT-PCR) and RT-PCR have been widely recognized as standard confirmatory tests for coronavirus detection (Augustine et al. 2020; Carter et al. 2020). The testing involves chemically treating the sample by lysing the virus membranes. The released nucleic acids (RNAs) are transcribed to form stable complementary DNA (cDNA) by applying RT enzymes. These are then processed to amplify the target sequences which are detected by current/fluorescent probes. Another diagnostic tool, named as loop-mediated isothermal amplification (LAMP) has been reported, which is similar to PCR. This is cheaper as the use of thermal cyclers is avoided since the amplification of the target DNA is carried out at the same temperature. A rapid testing as compared to qRT-PCR can be achieved by LAMP along with RT enzyme assays (RT-LAMP) (Augustine et al. 2020; Thompson et al. 2020). An estimate of the extent of COVID-19 lung infection can be obtained by observing the X-Ray CT scan of the lung. The CT scan provides three-dimensional image where the infected areas appear as shadowy regions. Other imaging tools such as MRI, single-photon emission computerized tomography and positron emission tomography are

capable of providing high precision images. However, these techniques require access to infrastructural instrumentation facility and trained medical professionals and are time consuming (Saxena et al. 2021).

COVID-19 has killed millions of people (World Health Organization, 2022) and continues to threaten healthcare systems worldwide. The widespread use of currently available diagnostics for mass testing has been hampered in many countries by their high production cost, lack of scalability, need for trained medical professionals and relatively slow detection times. Therefore, easy-to-use, low-cost and rapid diagnostic tests are urgently needed (Torres et al. 2021, 2022). Intensive efforts are being made worldwide for alternatives in this direction and biosensors have emerged as very promising.

A biosensor is a compact analytical device that detects and quantifies a target analyte. It involves a biological receptor (DNA, antibodies, enzymes, cells) which specifically detects the target molecule, a transducer to translate the detection (recognition) event into a signal and a signal processing display. Biosensors for medical application are designed to detect and quantify biomedical analytes, such as pathogens, found in different biofluids like saliva, urine and blood. When antibodies are used as bioreceptors, they are called immunosensors. Electrochemical immunosensors are most useful. These consist of a solid matrix whose properties, such as impedance, change when it adsorbs the antigens/antibodies and these changes are observed by using suitable transduction. Electrochemical transduction is mostly adopted due to its rapid response time, user-friendly application, low-cost production and the possibility of miniaturizing the system. The working of an electrochemical immunosensor involves the observation of changes occurring at the electrode surface by monitoring the parameters such as electrolyte resistance, charge transfer at the electrode, etc., and this can be achieved by impedance spectroscopic measurements. The modified surface of the Faradic biosensor electrode is immersed in a solution containing an electron mediator. The commonly used redox pairs include $[\text{Fe}(\text{CN})_6]^{3-/4-}$ (ferricyanide/ferrocyanide), $[\text{Ru}(\text{NH}_3)_6]^{3+/2+}$ hexaammineruthenium (II/III) and ferrocene (Fc^+/Fc) (Leva-Bueno et al. 2020).

For analysis of the impedance data, an equivalent circuit is needed. The system may be visualized as a combination of resistive and capacitive elements as usual (Ramanavicius et al. 2010). At high frequencies, all the capacitors would get short circuited and an effective resistance would prevail. This resistance would be the solution resistance, R_s . At mid frequencies, the charge double layer would show its response that can be represented by a parallel combination of double-layer capacitance C_{dl} and the associated charge transfer resistance, R_{CT} . At very low frequencies, the diffusional processes may dominate and may be represented by a Warburg element W appearing in series with charge transfer resistance. The equivalent circuit is schematically shown in Figure 6.48 (Leva-Bueno et al. 2020). The corresponding Nyquist plot would be a semicircular arc with a high-frequency intercept of R_s and a linear tail at the low-frequency side. R_{CT} would be given by the diameter of the semicircular arc. When binding and accumulation of a target analyte occurs at the sensor surface, electron transfer is impeded and this is reflected as increased value of R_{CT} , i.e. a bigger semicircle in the Nyquist plot.

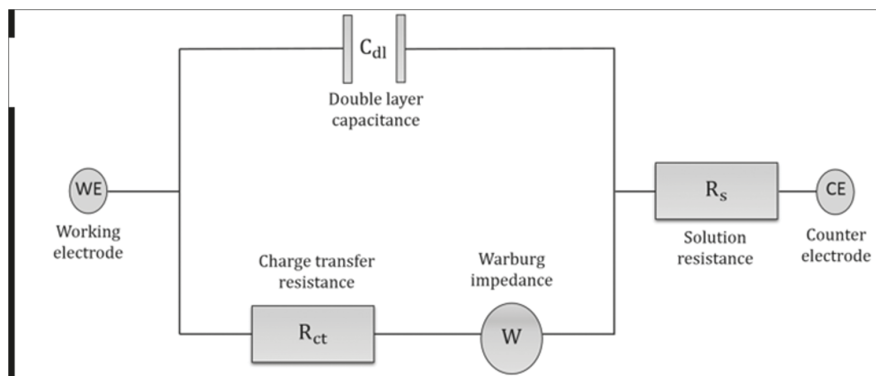


FIGURE 6.48 Equivalent circuit of electrochemical immunosensor. (Reprinted with Permission from Springer, Leva-Bueno J., Sally A. Peyman, P.A. Millner, 2020, Figure 3. A Review on Impedimetric Immunosensors for Pathogen and Biomarker Detection, *Medical Microbiology and Immunology*, 209: 343–362, Open Access.)

SARS-CoV-2 aptasensors utilizing low-cost gold electrodes and impedance spectroscopy have been reported to work with nasopharyngeal swab samples. This technique could be combined with low-cost electrodes, such as those produced for the blood glucose industry, to lower the cost (Lassere et al. 2022). Rapid detection of SARS-CoV-2 antibodies using electrochemical impedance-based sensor has been reported by Rashed et al. (2021). A real-time accurate portable impedimetric detection prototype (RAPID 1.0) based on impedance spectroscopy has been reported by Torres et al. (2022) for simple, inexpensive and rapid diagnosis of SARS-CoV-2 clinical samples. RAPID is an electrochemical biosensor that measures changes in the charge transfer resistance (R_{CT}) of the redox probe $[Fe(CN)_6]^{3-/4-}$, which is induced when the SARS-CoV-2 spike protein binds to an electrode previously functionalized with human ACE2 (Torres et al. 2021). Impedance measurements were carried out in the frequency range 10^5 – 10^{-1} Hz at room temperature. The Nyquist Z'' versus Z' plots exhibiting semicircular arcs were fitted to an equivalent circuit as shown in Figure 6.48. Selective binding between ACE2, which was immobilized on the electrode surface, and SARS-CoV-2 spike leads to lower interfacial electron transfer rates between the redox probe, ferricyanide/ferrocyanide and the electrode surfaces, which is reflected as increase in the charge transfer resistance, R_{CT} , in the model (i.e. increased semicircle diameter in the Nyquist plot). The working is schematically shown in Figure 6.49. The detection time of the RAPID assay (4 minutes) is substantially faster than conventional techniques (e.g. RT-PCR ~45 minutes) and highly sensitive. It is around 7–10 times cheaper than RT-PCR and at least two times cheaper than RT-LAMP. RAPID is proposed as an inexpensive and portable alternative to existing COVID-19 tests, allowing for decentralized diagnosis at the point of care (Torres et al. 2021, 2022).

Microfluidic paper-based analytical devices (μ PADs) have also emerged as promising diagnostic point-of-care tools for virus detection. An experimental approach

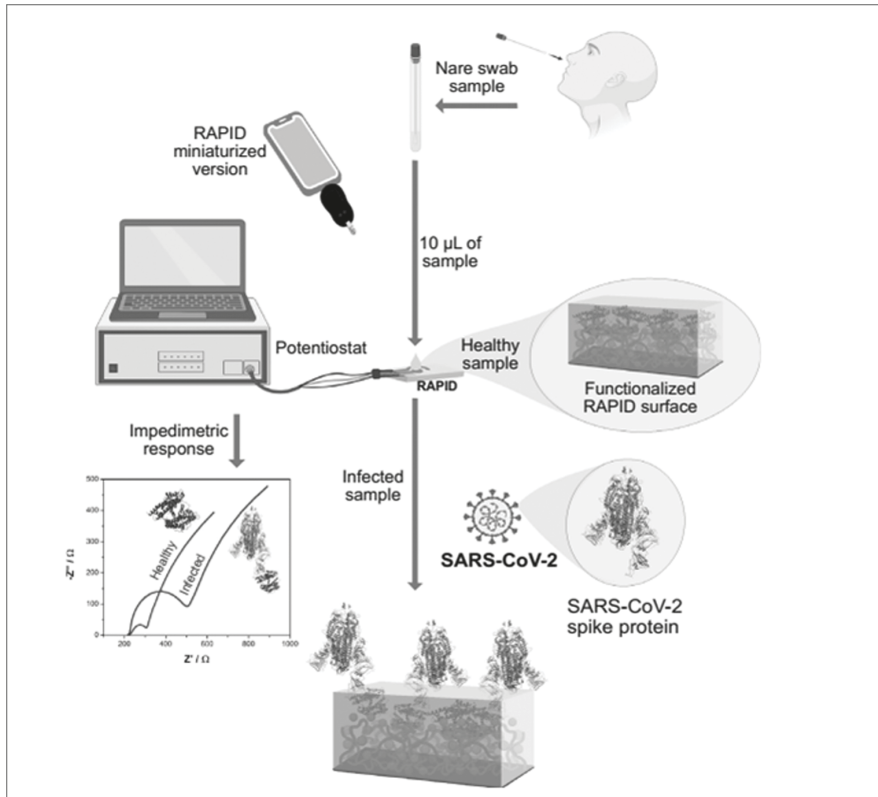


FIGURE 6.49 Detection of SARS-CoV-2 using RAPID in a prospective cohort study RAPID diagnoses COVID-19 in nare swab samples infected with SARS-CoV-2. (Reprinted with Permission from Torres Marcelo D.T., Lucas F. de Lima, Andre´ L. Ferreira, William R. de Araujo, Paul Callahan, Antonio Da´ vila, Jr., Benjamin S. Abella, and Cesar de la Fuente-Nunez, 2022, Figure 1, Detection of SARS-CoV-2 with RAPID: A Prospective Cohort Study, *iScience*, 25: 104055, <https://doi.org/10.1016/j.isci.>)

to enhancing the performance of paper-based impedance spectroscopic biosensors involving zinc oxide nanowires directly grown on working electrodes have been reported (Li et al. 2021). Detection of spike protein of SARS-CoV-2 by using impedance spectroscopy has been reported, which involves an immunosensor that contains a monolayer film of carboxymethyl chitosan as matrix, coated with an active layer of antibodies specific to the spike protein. A low limit of detection of 0.179 fg/mL within an almost linear behavior from 10 to 20 g/mL to 10 to 14 g/mL has been achieved (Soares et al. 2022).

Impedance spectroscopy has been shown to be a cost-effective tool for screening of drugs to be used against COVID-19 infection. For curbing the COVID-19 pandemic, efforts were made to repurpose the available drugs against the infection and several potential therapeutic leads, including remdesivir, lopinavir-ritonavir

combinations, chloroquine and hydroxychloroquine, were enrolled in the WHO's Solidarity Therapeutics Trial (Singh et al. 2020). Some success was reported initially. However, later on, it was reported by WHO that remdesivir, hydroxychloroquine, lopinavir/ritonavir and interferon regimens have little or no effect on a 28-day mortality or the in-hospital course of COVID-19 among hospitalized patients (Pan et al. 2020; Kiew et al. 2021). The drug repurposing efforts face problems due to the high technical complexity and cost involved in their conventional computational and biological experimental approaches. Impedance spectroscopy has been demonstrated to be a simple cost-effective tool for drug screening (Kiew et al. 2021).

During COVID-19 infection, the SARS-CoV-2 virus enters the cells through the binding of its spike protein (S-protein) to the cell surface-expressing ACE2. Therefore, spreading of the COVID-19 may be controlled by stopping the entry of the virus into the cells which may be achieved by inhibiting the S-protein-ACE2 binding. For screening of potential inhibitors against S-protein-ACE2 binding, an impedance spectroscopy-based biosensing platform was developed by using recombinant ACE2-coated palladium nano thin-film (NTF) electrode as the core sensing element.

A palladium NTF (Pd-NTF) electrode was fabricated through the epitaxial sputtering of Pd nanoparticles onto a polyethylene terephthalate (PET) substrate. A thin layer of indium tin oxide (ITO) was used to cover the surface to provide protection from environment. The ITO was later on removed and the electrode was exposed to the recombinant ACE2 protein (0.8 mg/mL) to allow its rapid immobilization (within 20 minutes) on the electrode surface to form the ACE2-coated Pd-NTF (ACE2-Pd-NTF) electrode. The electrode was further treated with known concentrations of the inhibitors. This was then exposed to solutions having varying concentrations of S-protein and impedance measurements were carried out. Changes in the electrical impedance at the interface of the solution and S-protein/virus-ACE2-Pd-NTF electrode were monitored that were further used to detect the binding of the virus to the immobilized ACE2 and the interfering effects of pharmacological inhibitors. The equivalent circuit used for analysis of the impedance spectra is shown Figure 6.48, where the charge transfer resistance (R_{CT}) represented the impedance from the ACE2-spike binding. The value of R_{CT} obtained for treated ACE2-Pd-NTF electrode without exposure to S-protein was taken as baseline for observing the changes. By using impedance spectroscopy, a few potential pharmacological leads, such as ramipril and perindopril, and their active metabolites ramiprilat and perindoprilat, that suppress SARS-CoV-2-ACE2 binding, were successfully identified (Kiew et al. 2021).

SUMMARY

Impedance spectroscopy is carried out by developing equivalent circuit models suitable for representing various charge transfer processes that would contribute to the electrical impedance of the system near frequencies governed by their time constants. As the impedance measurements are straightforward and involve low-cost and easy-to-transport equipment, this technique is finding an ever-increasing trend for its applications in wide variety of fields of science and technology, including medical diagnostics, agriculture, food processing dairy, etc. In this chapter, application

of impedance spectroscopy in the areas related to ceramics and glass ceramics; ferroelectrics and piezoelectrics; magnetic systems; corrosion and electrochemistry; polymers and composites; biological systems and medical diagnostics; agriculture, food quality and dairy; fuel cells, solar cells, gas sensors, petroleum, battery and COVID-19 are briefly described with a view to give the beginners a qualitative exposure. Due to the easy handling and portability of the impedance meters, impedance spectroscopy has been shown to be of great potential in online in situ testing of power sources, petroleum transport, seed germination and growth, curd forming, cement hydration and settling, etc. and differentiating between bacteria and virus and cancer detection at the point of care.

Problem 6.1

What is a Warburg impedance?



Taylor & Francis

Taylor & Francis Group

<http://taylorandfrancis.com>

Answers to Problems

Problem 1.1: Calculate the power dissipated in a resistor R when a dc voltage V is applied.

Solution 1.1: The potential difference between the two ends of the resistor is V volts. In transporting a charge q from low potential end to the high side, some work is done which is equal to qV . The energy lost per unit time is IV , as I is equal to charge per unit time. Power dissipated in a resistor R is given by

$$P = VI = IR^2 = I^2R = \frac{V^2}{R} \quad \text{volt - ampere (called watts)} \quad (\text{P1})$$

Problem 1.2: Consider a series RC circuit being connected to an ac voltage source $v(t) = V_0 \cos \omega t$. Solve the related equations to find the current in the circuit [solve Eq. (1.54)].

Solution 1.2: The relation between the applied voltage and current i in the circuit can, by using Kirchoff's law, be written as

$$Ri + \frac{1}{C} \int i dt = V_0 \cos \omega t \quad (\text{P2})$$

Differentiating we get

$$R \frac{di}{dt} + \frac{1}{C} i = -\omega V_0 \sin \omega t \quad (\text{P3})$$

or

$$\frac{di}{dt} + \frac{1}{RC} i = -\frac{\omega V_0}{R} \sin \omega t \quad (\text{P4})$$

The solution is

$$ie^{t/RC} = \int \left(-\frac{\omega V_0}{R} \sin \omega t \right) e^{t/RC} dt + c' \quad (\text{P5})$$

where c' is an integration constant. Now, integration by parts and rearranging the terms we get

$$i = c'e^{-t/RC} + \frac{\omega V_0}{R} \left[\frac{RC}{1 + (\omega CR)^2} \right] [\omega CR \cos \omega t - \sin \omega t] \quad (\text{P6})$$

or

$$i = c'e^{-t/RC} + \frac{\omega V_0}{R} \frac{RC}{\sqrt{1 + (\omega CR)^2}} \left[\frac{\omega RC}{\sqrt{1 + (\omega CR)^2}} \cos \omega t - \frac{1}{\sqrt{1 + (\omega CR)^2}} \sin \omega t \right] \quad (\text{P7})$$

We define an angle θ given by

$$\tan \theta = \frac{1}{\omega CR} = \frac{1/\omega C}{R} \quad (\text{P8})$$

So that

$$\sin \theta = \frac{1}{\sqrt{1 + (\omega CR)^2}} = \frac{1/\omega C}{\sqrt{\left(\frac{1}{\omega C}\right)^2 + R^2}},$$

$$\text{and } \cos \theta = \frac{R}{\sqrt{\left(\frac{1}{\omega C}\right)^2 + R^2}} \quad (\text{P9})$$

Equation (P7) can then be written as

$$i = c'e^{-t/RC} + \frac{V_0}{\sqrt{\left(\frac{1}{\omega C}\right)^2 + R^2}} \cos(\omega t + \theta) \quad (\text{P10})$$

At $t = 0$, the initial current is given as $i = i_0 = V_0/R$. This gives

$$C' = \frac{V_0}{R} - \frac{V_0}{\sqrt{\left(\frac{1}{\omega C}\right)^2 + R^2}} \cos \zeta \quad (\text{P11})$$

Substituting in Eq. (P10) we get

$$i = e^{-t/RC} \left[\frac{V_0}{R} - \frac{V_0}{\sqrt{\left(\frac{1}{\omega C}\right)^2 + R^2}} \cos \theta \right] + \frac{V_0}{\sqrt{\left(\frac{1}{\omega C}\right)^2 + R^2}} \cos(\omega t + \theta) \quad (\text{P12})$$

Problem 1.3: Obtain the units of the product RC .

Solution 1.3: The product RC appears in the equation of charging of a capacitor as

$$v(t) = V_0(1 - e^{-t/RC}) \quad (\text{P13})$$

where $v(t)$ is the voltage across the capacitor at time t , after the switch connecting the series RC circuit to the voltage source having voltage V_0 is put on. As an exponential of a quantity is always dimensionless, the quantity $t/(RC)$ has to be dimensionless. Therefore, dimensions of RC should be the same as that of t (seconds).

The units of RC may be obtained in an alternative way also. When a voltage source is connected to a capacitor C , charge q gets accumulated and is given by $q = \int i dt$, where i is the charging current (amperes). Thus, units q become ampere \times seconds. Then we have

$$C = q/V = (\text{ampere} \times \text{seconds})/\text{volts} \quad (\text{P14})$$

By Ohm's law $V = iR$, we have $i = V/R$ or amperes = volts/ohms. Thus, units of C become (volts/ohms) \times seconds/volts = second/ohms. Therefore, units of RC become ohms \times seconds/ohms, i.e. seconds.

Problem 1.4: Obtain the units of L/R .

Solution 1.4: This can be solved in the same way as was done for Problem 1.3. The current in an inductor L connected to source of V volts through a resistor R is given by $i(t) = (V/R)(1 - e^{-t/(L/R)})$, which tells that L/R has dimensions of t . Also, by using $v(t) = L di/dt$, we see that unit of L is volts \times seconds/amperes. Thus, unit of L/R is (volts \times seconds/amperes)/ohms. By using volts = ampere \times ohms, we see that unit of L/R is seconds.

Problem 1.5: Find the magnitude of Z' and Z'' for a series RL circuit when the applied frequency is such that $\omega L/R = 1$.

Solution 1.5: We have $Z = Z' - jZ'' = R + j\omega L$. Thus, magnitude of $Z' = R$ and magnitude of $Z'' = \omega L = R$. It means that at $\omega\tau = 1$, magnitudes of Z' and Z'' are R .

Problem 1.6: Obtain the units of ωRC .

Solution 1.6: Unit of RC is second and that of ω is 1/second. Therefore, the quantity ωRC is dimensionless.

Problem 4.1: Consider a parallel $R_p C_p$ circuit. Obtain the values of resistance R_s and capacitance C_s for the corresponding equivalent series $R_s C_s$ circuit and vice versa.

Solution 4.1: Consider series $R_s C_s$ and parallel $R_p C_p$ circuits. The two circuits will be equivalent if, for an applied voltage, the same current I flows from the source, i.e. the magnitude, and phase of the currents are equal. This would hold if the impedances of both are equal and phase angle of the currents are the same or, alternatively, if the real part of their impedances are equal and their imaginary parts are also equal.

For series circuit, we have

$$Z_s = R_s + \frac{1}{j\omega C_s} = R_s - j\frac{1}{\omega C_s} \quad (\text{P15})$$

Current is given as

$$I_s = \frac{v}{Z_s} = \frac{v}{R_s^2 + \left(\frac{1}{\omega C_s}\right)^2} \left(R_s + j\frac{1}{\omega C_s} \right) \quad (\text{P16})$$

Phase angle of current with respect to voltage is given by

$$\tan \theta_s = \frac{1}{\omega C_s R_s} \quad (\text{P17})$$

It may be noted that deviation δ from ideality for a capacitor is expressed as $\tan \delta$, and quality factor is written as $Q = 1/\tan \delta$, which gives

$$\tan \delta_s = \tan(90 - \theta_s) = \frac{1}{\tan \theta_s} = \omega C_s R_s; Q_s = \frac{1}{\omega C_s R_s} \quad (\text{P18})$$

For parallel circuit, we have

$$Z_p = \frac{R_p}{1 + j\omega C_p R_p} = \frac{R_p}{1 + (\omega C_p R_p)^2} - j \frac{R_p \omega C_p R_p}{1 + (\omega C_p R_p)^2}, \quad (\text{P19})$$

Phase angle is given by

$$\tan \theta_p = \omega C_p R_p \quad (\text{P20})$$

and

$$Q_p = \omega C_p R_p \quad (\text{P21})$$

Comparing real and imaginary parts and the phase angles we get

$$R_s = \frac{R_p}{1 + (\omega C_p R_p)^2}, \quad \frac{1}{\omega C_s} = \frac{R_p \omega C_p R_p}{1 + (\omega C_p R_p)^2} \quad (\text{P22})$$

or

$$R_s = \frac{R_p}{1 + (\omega C_p R_p)^2}, \quad C_s = \frac{1 + (\omega C_p R_p)^2}{\omega R_p \omega C_p R_p} \quad (\text{P23})$$

or

$$R_s = \frac{R_p}{1 + (Q_p)^2}, \quad C_s = C_p \frac{1 + (Q_p)^2}{(Q_p)^2} \quad (\text{P24})$$

Thus, we have values of series components R_s and C_s in terms of parallel components R_p and C_p .

Similarly, we have

$$\frac{1}{z_p} = \frac{1}{R_p} + j\omega C_p \quad (\text{P25})$$

and

$$\frac{1}{Z_s} = \frac{1}{R_s + \frac{1}{j\omega C_s}} = \frac{R_s + j\frac{1}{\omega C_s}}{R_s^2 + \left(\frac{1}{\omega C_s}\right)^2} \quad (\text{P26})$$

From Eqs. (P25) and (P26) we get, by equating real and imaginary parts

$$\frac{1}{R_p} = \frac{R_s}{R_s^2 + \left(\frac{1}{\omega C_s}\right)^2} = \frac{1}{R_s} \frac{(\omega C_s)^2}{1 + \left(\frac{1}{\omega C_s R_s}\right)^2} \quad (\text{P27})$$

$$R_p = \frac{1 + (\omega C_s R_s)^2}{R_s (\omega C_s)^2} = R_s \frac{1 + (\omega C_s R_s)^2}{(\omega C_s R_s)^2} = R_s \left(1 + (Q_s)^2\right) \quad (\text{P28})$$

and

$$\omega C_p = \frac{\frac{1}{\omega C_s}}{R_s^2 + \left(\frac{1}{\omega C_s}\right)^2} = \frac{\omega C_s}{(\omega C_s R_s)^2 + 1} \quad (\text{P29})$$

$$C_p = C_s \frac{1}{\left(\frac{1}{Q_s}\right)^2 + 1} = C_s \frac{Q_s^2}{1 + Q_s^2} \quad (\text{P30})$$

Thus, we have parallel components R_p and C_p in terms of series components R_s and C_s . It may be mentioned that as $\tan \theta_p$ is equal to $\tan \theta_s$, $Q_p = Q_s$.

Problem 4.2: Show that a parallel R-CPE equivalent circuit gives a depressed arc in the Z'' versus Z' plot.

Solution:

Z' and Z'' are given by Eqs. (4.67) and (4.68) as

$$Z' = R \frac{\left(1 + RA_0 \omega^n \cos \frac{n\pi}{2}\right)}{\left(1 + RA_0 \omega^n \cos \frac{n\pi}{2}\right)^2 + \left(RA_0 \omega^n \sin \frac{n\pi}{2}\right)^2} \quad (\text{P31})$$

$$Z'' = R \frac{\left(RA_0 \omega^n \sin \frac{n\pi}{2}\right)}{\left(1 + RA_0 \omega^n \cos \frac{n\pi}{2}\right)^2 + \left(RA_0 \omega^n \sin \frac{n\pi}{2}\right)^2} \quad (\text{P32})$$

Now we will describe how this model gives rise to a depressed Z'' versus Z' semicircular arc. Let

$$a = RA_0 \omega^n \quad (\text{P33})$$

Then, we can write the expressions for Z' and Z'' [Eqs. (P31) and (P32)] as

$$Z' = R \frac{\left(1 + a \cos \frac{n\pi}{2}\right)}{\left(1 + a \cos \frac{n\pi}{2}\right)^2 + \left(a \sin \frac{n\pi}{2}\right)^2} \quad (\text{P34})$$

$$Z'' = R \frac{\left(a \sin \frac{n\pi}{2}\right)}{\left(1 + a \cos \frac{n\pi}{2}\right)^2 + \left(a \sin \frac{n\pi}{2}\right)^2} \quad (\text{P35})$$

From this we see that

$$Z'^2 + Z''^2 = R^2 \frac{\left[\left(1 + a \cos \frac{n\pi}{2}\right)^2 + \left(a \sin \frac{n\pi}{2}\right)^2\right]}{\left[\left(1 + a \cos \frac{n\pi}{2}\right)^2 + \left(a \sin \frac{n\pi}{2}\right)^2\right]^2} \quad (\text{P36})$$

$$= R \frac{R}{\left[\left(1 + a \cos \frac{n\pi}{2} \right)^2 + \left(a \sin \frac{n\pi}{2} \right)^2 \right]} \quad (\text{P37})$$

$$= R \frac{R \left(1 + a \cos \frac{n\pi}{2} \right) - R \left(a \cos \frac{n\pi}{2} \right)}{\left[\left(1 + a \cos \frac{n\pi}{2} \right)^2 + \left(a \sin \frac{n\pi}{2} \right)^2 \right]} \quad (\text{P38})$$

$$= R \frac{R \left(1 + a \cos \frac{n\pi}{2} \right)}{\left[\left(1 + a \cos \frac{n\pi}{2} \right)^2 + \left(a \sin \frac{n\pi}{2} \right)^2 \right]} - R \frac{R \left(a \cos \frac{n\pi}{2} \right)}{\left[\left(1 + a \cos \frac{n\pi}{2} \right)^2 + \left(a \sin \frac{n\pi}{2} \right)^2 \right]} \quad (\text{P39})$$

$$= R \frac{R \left(1 + a \cos \frac{n\pi}{2} \right)}{\left[\left(1 + a \cos \frac{n\pi}{2} \right)^2 + \left(a \sin \frac{n\pi}{2} \right)^2 \right]} - R \frac{R \left(a \sin \frac{n\pi}{2} \right)}{\left[\left(1 + a \cos \frac{n\pi}{2} \right)^2 + \left(a \sin \frac{n\pi}{2} \right)^2 \right]} \frac{\left(\cos \frac{n\pi}{2} \right)}{\left(\sin \frac{n\pi}{2} \right)} \quad (\text{P40})$$

$$= RZ' - RZ'' \frac{\left(\cos \frac{n\pi}{2} \right)}{\left(\sin \frac{n\pi}{2} \right)} \quad (\text{P41})$$

or

$$Z'^2 + Z''^2 = RZ' - RZ'' \cot \frac{n\pi}{2} \quad (\text{P42})$$

$$Z'^2 - RZ' + Z''^2 + RZ'' \cot \frac{n\pi}{2} = 0 \tag{P43}$$

or

$$\begin{aligned} Z'^2 - RZ' + \left(\frac{R}{2}\right)^2 + Z''^2 + RZ'' \cot \frac{n\pi}{2} + \left(\frac{R}{2} \cot \frac{n\pi}{2}\right)^2 \\ = \left(\frac{R}{2}\right)^2 + \left(\frac{R}{2} \cot \frac{n\pi}{2}\right)^2 \end{aligned} \tag{P44}$$

or

$$\left(Z' - \frac{R}{2}\right)^2 + \left(Z'' + \frac{R}{2} \cot \frac{n\pi}{2}\right)^2 = \left(\frac{R}{2}\right)^2 \left[1 + \left(\cot \frac{n\pi}{2}\right)^2\right] \tag{P45}$$

Define

$$n = 1 - \alpha = 1 - \frac{\theta}{\pi/2}, \theta = \frac{\alpha\pi}{2}, (0 < n < 1, 0 < \alpha < 1), \tag{P46}$$

Therefore

$$n \frac{\pi}{2} = \frac{\pi}{2} - \theta \text{ and } \cot \frac{n\pi}{2} = \cot \left(\frac{\pi}{2} - \theta\right) = \tan \theta \tag{P47}$$

and Eq. (P45) becomes

$$\left(Z' - \frac{R}{2}\right)^2 + \left(Z'' + \frac{R}{2} \tan \theta\right)^2 = \left(\frac{R}{2}\right)^2 [1 + (\tan \theta)^2] \tag{P48}$$

This is equation of a circle on Z'' versus Z' plot having center at the point with coordinates $(R/2, -R \tan \theta/2)$ and radius equal to $(R/2) \sqrt{1 + \tan^2 \theta}$. From Eq. (P48) it is seen that when $Z'' = 0$, the values of Z' are 0 or R , i.e. the circle would pass through the origin and the point $(R, 0)$. As the ordinate of the center is negative, the center of the circle lies below the Z' axis, which is shown in Figure P1.

Problem 4.3: Obtain expressions for resonance frequencies of the circuit shown in Figure 4.18.

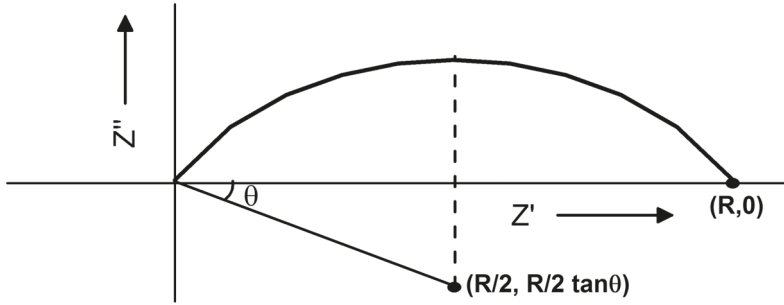


FIGURE P1 Z'' versus Z' plot for a parallel R-CPE equivalent circuit. The center of the depressed arc is at $(R/2, -(R/2)\tan\theta)$.

Solution 4.3: At resonance, the current is in phase with applied voltage. The phase difference between the current and the voltage is given by $\tan^{-1}(Z''/Z')$. Therefore, at resonance we have (see Eq. 4.172)

$$\omega C_2 \left(\omega L_1 - \frac{1}{\omega C_1} \right)^2 - \left(\omega L_1 - \frac{1}{\omega C_1} \right) + \omega C_2 R_1^2 = 0 \quad (\text{P49})$$

which gives for low loss

$$\left(\omega L_1 - \frac{1}{\omega C_1} \right) \left(\omega L_1 - \frac{1}{\omega C_1} + \frac{1}{\omega C_2} \right) = 0 \quad (\text{P50})$$

Thus

$$\omega_r = \sqrt{\frac{1}{L_1 C_1}}, \sqrt{\frac{1}{L_1 C_1 C_2 / (C_2 + C_2)}} \quad (\text{P51})$$

Problem 6.1: What is a Warburg impedance?

Solution 6.1: The process of diffusion is usually described by phenomenological equations known as Fick's laws, and the concentration of diffusing species at various distances is obtained by solving these differential equations for given boundary conditions. Solution of diffusion equation under small ac perturbation gives diffusional contribution W to the impedance as (Macdonald 1987, p 23)

$$W = \sigma \omega^{-\frac{1}{2}} (1 - j) \quad (\text{P52})$$

This impedance W is known as Warburg impedance. Here, ω is the angular frequency and σ is a function of temperature, diffusivity and concentration of ions, Faraday constant, number of electrons transferred, rate constant for the electrochemical charge transfer reaction. This solution corresponds to infinite thickness boundary condition and its form gets changed for finite thickness such as that for interfaces. The complex plane plot of this impedance gives a straight line inclined at an angle of 45° to the real axis. Presence of such straight line behavior in Nyquist plots at low frequencies is modeled by including a Warburg element in the equivalent circuit.



Taylor & Francis

Taylor & Francis Group

<http://taylorandfrancis.com>

Appendix A1: GW BASIC Program

GW BASIC Program for creating Z'' versus Z' plot for a model having parallel R_1C_1 in series with parallel R_2C_2

```
10 REM FILE NAME "RCRC3.BAS" PARALLEL R1C1 IN SERIES WITH
PARALLEL R2C2
20 PROGRAM$="RCRC2.BAS": THIS PROGRAM CALCULATES ZP AND ZDP
30 DIM F(1000),W(1000)
40 CLS
50 DEFDBL A-H,O-Z
60 DEFINT I-N
70 KEY OFF
80 SCREEN 2
90 REM WINDOW
100 LINE (0,0)-(639,0): LINE (639,0)-(639,190)
110 LINE (639,190)-(0,190):LINE (0,190)-(0,0)
120 LINE (319,0)-(319,190): LINE (0,100)-(639,100)
130 REM
140 PI=3.14159
150 R1=10^4:C1=2E-11
160 C0=1.6E-12
170 PRINT " PARALLEL R1,C1 IN SERIES WITH PARALLEL R2,C2"
180 REM
190 INPUT " R2/R1: ";R2BR1
200 R2=R1*R2BR1: FEED THE Z EXPRESSION FOR THE CHOSEN MODEL
AT SUB 540
210 INPUT "GIVE FILE NAME TO WRITE: ";XYZ$
220 OPEN "O",#1,XYZ$
230 INPUT " R2C2/R1C1: ";R2C2BR1C1
240 INPUT "GIVE FILE NAME TO WRITE: ";XYZ$
250 C2=R2C2BR1C1*C1/R2BR1
260 OPEN "O",#1,XYZ$
270 WRITE #1, "FILE NAME IS ",XYZ$,"R1C1 IN SERIES WITH R2C2"
280 WRITE #1, " DAT FILE CREATED BY BASIC PROGRAM", PROGRAM$
```

```

290 WRITE #1, "R1=";R1;" C1=";C1;" R2/R1 = ";R2BR1;"R2C2/R1C1 = ";
R2C2BR1C1
300 WRITE #1,"I; K; F(I); ZPN; ZDPN"
310 'OPEN "ZPZDP.TXT" FOR OUTPUT AS #1
320 'OPEN "ZDP4.TXT" FOR OUTPUT AS #2
330 I=0:FOR K=.5 TO 7.5 STEP .05: I=I+1
340 F(I)=10^K:W(I)=2*PI*F(I):WI=W(I)
350 GOSUB 540 'FOR CALCULATING ZP AND ZDP,ZPN AND ZDPN
360 'PRINT I;K;ZPN;ZDPN:INPUT JAB
370 REM
380 X=ZPN:Y=ZDPN:RAT=99/245:RAT1 =200
390 'PRINT #1,I;K;F(I);X;Y:'PRINT #2,Y
400 WRITE #1,I;K;F(I);ZPN;ZDPN
410 PSET(X*RAT1+319,-Y*RAT1*RAT+100)
420 FOR DELAY=1 TO 200!
430 REM
440 NEXT DELAY
450 NEXT K
460 IF R2C2BR1C1 >=100 THEN 500
470 WRITE #1,"-----"
480 WRITE #1,"-----"
490 GOTO 230
500 REM
510 CLOSE #1
520 END
530 STOP
540 REM SUBROUTINE,GIVE EXPRESSIONS FOR ZP AND ZDP
550 WC1R1=WI*C1*R1:DEN1=1+WC1R1*WC1R1:ZP1=R1/DEN1:ZDP1=
WC1R1*ZP1
560 WC2R2=WI*C2*R2:DEN2=1+WC2R2*WC2R2:ZP2=R2/DEN2:ZDP2=
WC2R2*ZP2
570 ZP=ZP1+ZP2:ZDP=ZDP1+ZDP2
580 ZPN=ZP/(R1+R2):ZDPN=ZDP/(R1+R2)
590 RETURN:'RETURN TO 270

```

Note: This program calculates the values of Z' (ZP) and Z'' (ZDP) for a model. Expressions for Z' and Z'' are given at the statement number 550–570. Normalized values, ZPN and ZDPN, are obtained by dividing Z' (ZP) and Z'' (ZDP) by a chosen normalization constant, such as limiting values of Z' at $\omega \rightarrow 0$; it is equal to $R_1 + R_2$ for the model having parallel R_1C_1 in series with parallel R_2C_2 considered in this program. The normalized Z'' versus Z' plot is created in the right top of the screen. The traversal of plot may be suitably slowed down by increasing the value of DELAY in statement number 420, so that the plotting of the Z'' versus Z' curve from right to left is clearly seen (by feeding expressions for M'' and M' , the M'' vs M' plot would traverse from left to right). The plots for various values of R_2C_2/R_1C_1 are shown on the same graph. The calculated values are written on the file whose name, e.g. RCRCZ.DAT, is fed as INPUT prompted at the statement 210. This .DAT file may be accessed by Notepad and used.

Appendix A2: Linear and Nonlinear Least Squares

The complex nonlinear least squares (CNLS) has been described in detail by Macdonald (Macdonald 2005). In order to get familiarity with CNLS, it is worth having a look at the ordinary least squares procedure. In what follows, basics of method of least squares are described (Scarborough 1966; Squires 1976) followed by nonlinear least squares and CNLS.

Let us consider an experiment in which some variable y , say voltage across a sample, is measured at different input currents, x . Let us assume that N values of x ($x_1, x_2, x_3, \dots, x_i, \dots, x_N$) are given and the corresponding observed values for y are $y_1, y_2, y_3, \dots, y_i, \dots, y_N$. The variable x is called independent variable and y is called dependent variable. Our aim is to establish some functional dependence of y on x by using these values, i.e. we want to find out a relation that, for a given value of x , would yield a value y which would be equal to the experimentally observed value corresponding to that of x , and this relation should hold for all the values of x from x_1 to x_N . This can be done if some relation is known a priori, such as Ohm's law, that is to be obeyed for the given sample. In that case, the parameters appearing in the relation are to be determined. Otherwise, a nuts-and-bolts approach would be to plot a graph of y_i versus x_i , placing y_i along the Y-axis and x_i along the X-axis on a linear graph sheet. Thus, we have a set of N data points (x_i, y_i). Suppose, this graph looks, more or less, like a straight line as shown in Figure A2.1.

Then, a relation showing the dependence of y on x may be written as

$$y = mx + c \quad (\text{A.1})$$

where m is the slope and c is the intercept on Y-axis. This line obviously would not pass through all the points and the observed values of y_i would deviate by a value e_i , called residual, from the calculated values $y_{i\text{calculated}} (= mx_i + c)$ for a given x_i . It means that had the Eq. (5.1) been correct, the value of y corresponding to x_i should have come out to be equal to $mx_i + c$, but when experimentally measured, it came out as y_i . Thus we will have

$$e_i = y_{i\text{experimental}} - y_{i\text{calculated}} = y_i - (mx_i + c) \quad (\text{A.2})$$

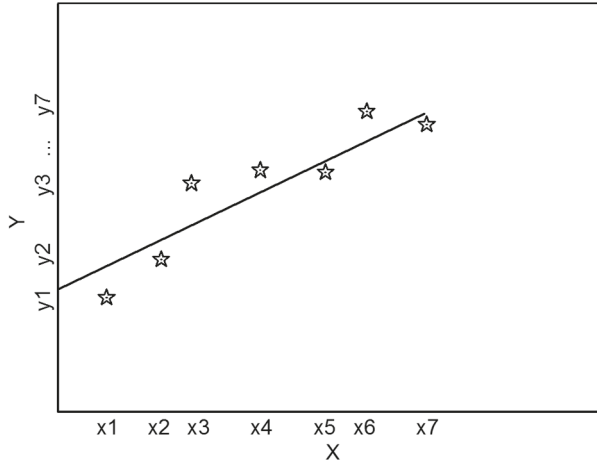


FIGURE A2.1 Plot of N data points (x_i, y_i) $i = 1-7$. Points are marked as stars.

$$e_2 = y_{2 \text{ experimental}} - y_{2 \text{ calculated}} = y_2 - (m x_2 + c) \quad (\text{A.3})$$

$$e_3 = y_{3 \text{ experimental}} - y_{3 \text{ calculated}} = y_3 - (m x_3 + c) \quad (\text{A.4})$$

$$e_t = y_{t \text{ experimental}} - y_{t \text{ calculated}} = y_t - (m x_t + c) \quad (\text{A.5})$$

$$e_N = y_{N \text{ experimental}} - y_{N \text{ calculated}} = y_N - (m x_N + c) \quad (\text{A.6})$$

Suppose the actual relationship is given by

$$y(x) = a + bx \quad (\text{A.7})$$

So, for $x = x_i$, the actual value would be $y(x_i)$, the observed value being y_i . It is generally assumed here that if large number of measurements are carried out for $x = x_i$, the observed values of y would follow Gaussian distribution having mean $y(x_i)$ ($= a + bx_i$) and standard deviation σ_i and the value $y_i(x_i)$ observed in a particular measurement falls within this distribution. Under this assumption, the probability P_i of getting the value y_i in a measurement for $x = x_i$ would be given as

$$P_i = \frac{1}{\sigma_i \sqrt{2\pi}} \exp \left(-\frac{1}{2} \left[\frac{y_i - y(x_i)}{\sigma_i} \right]^2 \right) \quad (\text{A.8})$$

The probability P of getting the set of values $y_1, y_2, y_3, \dots, y_N$ for $x = x_1, x_2, x_3, \dots, x_N$ will be the product of all the probabilities $P_1, P_2, P_3, \dots, P_N$ and is given by

$$P = \Pi \left(\frac{1}{\sigma_i \sqrt{2\pi}} \right) \exp \left(-\frac{1}{2} \sum_{i=1}^N \left[\frac{y_i - y_i(x_i)}{\sigma_i} \right]^2 \right) \quad (\text{A.9})$$

where the symbol Π represents the product. A quantity $\exp(-k)$ will attain maximum value when k becomes minimum. Thus, for the probability P to be maximum, the factor under summation should be minimum, i.e. sum of the squares of the weighted deviations should be minimum. This is the basis of method of least squares and this sum is defined as goodness-of-fit parameter, χ^2

$$\chi^2 = \sum_{i=1}^N \left[\frac{y_i - y(x_i)}{\sigma_i} \right]^2 \quad (\text{A.10})$$

In all, the sum and products given above the quantities $1/\sigma_i^2$ act as weighting factors. A proper way to assign these weights would be to carry out measurements number of times at each given value $x = x_i$ and find out the standard deviation σ_i . When all the experimentally observed values of y_i have same standard deviation, i.e. $\sigma_1, \sigma_2, \sigma_3, \dots$ etc. are all equal, then it is as good as putting these equal to unity. The method of least squares then says that the best representative curve is that for which the sum of the squares of the residuals is a minimum, i.e. $\sum (e_i)^2$ is a minimum. This sum is defined to be our goodness-of-fit parameter, χ^2 . While drawing a line, $y = mx + c$, passing as closely as possible to the points (x_i, y_i) by hand, what we actually do is rotate the line clockwise or counterclockwise (i.e. vary the slope m) and shift up and down (i.e. vary c). So the minimum value of the sum of squares of the residuals are to be found with respect to m and c . This gives

$$\frac{\partial}{\partial m} \chi^2 = \frac{\partial}{\partial m} \sum_{i=1}^N [y_i - (mx_i + c)]^2 = -2 \sum_{i=1}^N [y_i - (mx_i + c)] x_i = 0 \quad (\text{A.11})$$

and

$$\frac{\partial}{\partial m} \chi^2 = \frac{\partial}{\partial m} \sum_{i=1}^N [y_i - (mx_i + c)]^2 = -2 \sum_{i=1}^N [y_i - (mx_i + c)] x_i = 0 \quad (\text{A.12})$$

or

$$m \sum_{i=1}^N x_i + cN = \sum_{i=1}^N y_i \quad (\text{A.13})$$

$$m \sum_{i=1}^N x_i^2 + c \sum_{i=1}^N x_i = \sum_{i=1}^N x_i y_i \quad (\text{A.14})$$

These are solved to get

$$m = \frac{1}{\Delta} \left(N \sum_{i=1}^N (x_i y_i) - \sum_{i=1}^N x_i \sum_{i=1}^N y_i \right) \quad (\text{A.15})$$

$$c = \frac{1}{\Delta} \left(\sum_{i=1}^N x_i^2 \sum_{i=1}^N y_i - \sum_{i=1}^N x_i \sum_{i=1}^N (x_i y_i) \right) \quad (\text{A.16})$$

$$\Delta = N \sum_{i=1}^N x_i^2 - \left(\sum_{i=1}^N x_i \right)^2 \quad (\text{A.17})$$

When the individual values of y_i have different errors (standard deviations σ_i), then each value needs to be assigned certain weights and the values multiplied by the weights, w_i . For standard deviations σ_i , the weights may be taken equal to $1/\sigma_i^2$. Then, χ^2 becomes

$$\chi^2 = \sum_{i=1}^N \left(\frac{[y_i - (mx_i + c)]}{\sigma_i} \right)^2 \quad (\text{A.18})$$

and values of m and c become

$$m = \frac{1}{\Delta_1} \left(\sum_{i=1}^N \frac{1}{\sigma_i^2} \sum_{i=1}^N \left(\frac{x_i y_i}{\sigma_i^2} \right) - \sum_{i=1}^N \frac{x_i}{\sigma_i^2} \sum_{i=1}^N \frac{y_i}{\sigma_i^2} \right) \quad (\text{A.19})$$

$$c = \frac{1}{\Delta_1} \left(\sum_{i=1}^N \frac{x_i^2}{\sigma_i^2} \sum_{i=1}^N \left(\frac{y_i}{\sigma_i^2} \right) - \sum_{i=1}^N \frac{x_i}{\sigma_i^2} \sum_{i=1}^N \frac{x_i y_i}{\sigma_i^2} \right) \quad (\text{A.20})$$

Where,

$$\Delta_1 = \sum_{i=1}^N \frac{1}{\sigma_i^2} \sum_{i=1}^N \frac{x_i^2}{\sigma_i^2} - \left(\sum_{i=1}^N \frac{x_i}{\sigma_i^2} \right)^2 \quad (\text{A.21})$$

The errors σ_m and σ_c in m and c , respectively, are given by

$$\sigma_m^2 = \frac{1}{\Delta_1} \sum_{i=1}^N \frac{1}{\sigma_i^2} \quad (\text{A.22})$$

$$\sigma_c^2 = \frac{1}{\Delta_1} \sum_{i=1}^N \frac{x_i^2}{\sigma_i^2} \quad (\text{A.23})$$

when $\sigma_i = \sigma$ and is the same for all the data points, these become

$$\sigma_m^2 = \frac{\sigma^2}{\Delta} N, \sigma_c^2 = \frac{\sigma^2}{\Delta} \sum_{i=1}^N x_i^2 \quad (\text{A.24})$$

The value of σ can be estimated as

$$\sigma^2 \approx \frac{1}{N-2} \sum_{i=1}^N (y_i - (mx_i + c))^2 \quad (\text{A.25})$$

Thus, the straight line best fit to the data points (x_i, y_i) shown in Figure is $y = mx + c$, where m and c are given by Eqs. (A.19), (A.20) and (A.21) with standard deviations given by Eqs. (A.22) and (A.23).

The procedure described above can be applied as well to the case where a function of the form $y = a_0 + a_1x + a_2x^2$ has to be fitted to the data points (x_i, y_i) . In that case, the partial differentials $\partial\chi/\partial a_0$, $\partial\chi/\partial a_1$ and $\partial\chi/\partial a_2$ should be equated to zero and the resulting three simultaneous equations are solved to get the values of the three parameters a_0 , a_1 and a_2 . This may be generalized for cases having higher powers of x (a polynomial). It may be noted that in the cases discussed above the parameters to be determined occur in a linear way, i.e. the fitting function can be expressed as sum of separate terms, each multiplied by a single coefficient, and therefore, it is called linear least squares fitting. Thus, fitting of a function $y = a_0 + a_1x + a_2x^2 + a_3x^3 + a_4x^4$ to the set of data points (x_i, y_i) falls under linear least squares fitting (Squires 1976; Scarborough 1966; Bevington and Robinson 1992). One may come across functions of the type $y = ae^{-bx}$, which may be written as $\ln(y) = \ln(a) - bx$. Denoting $\ln(a)$ by a_1 we get $\ln(y) = a_1 - bx$. In these transformed relation, the parameters to be determined appear linearly and the procedure of linear least squares may be applied for the data set $(\ln(y_i), x_i)$. Similarly, the function of the type $y = ax^b$, which is not linear in the parameters, may be written as $\ln(y) = \ln(a) + b \ln(x)$. Denoting $\ln(a)$ by a_1 , this become $\ln(y) = a_1 + b \ln(x)$, which is linear in the parameters and procedure of linear least squares may be applied.

The case where the function to be fitted to a set of experimental points is nonlinear in the parameters, i.e. contains parameters that appear in a nonlinear way, such as $y = a_0 + a_1e^{-a_2t} + a_3e^{-a_4t}$, which cannot be transformed to make it linear in parameters, would fall under the category of nonlinear least squares. Various methods involving approximations are available for treating such cases. A simple and easy-to-follow method is that of linearization of the fitting function. This procedure of nonlinear least squares is elaborated by considering the following example (Scarborough 1966). Suppose an experiment yielded a set of values (x_i, y_i) , $i = 1$ to N , and x is the independent variable. Assume that all the values have equal weight of unity. Further, suppose that a function $y = f(x, a_1, a_2, a_3)$, which is nonlinear in a_1 , a_2 and a_3 , is to be fitted. The aim is to obtain the values of the parameters, a_1 , a_2 and a_3 by using method of least squares. Let the approximate values of a_1 , a_2 and a_3 obtained graphically or by some other method be a_{10} , a_{20} and a_{30} (called initial guesses), and let α_1 , α_2 and α_3 be

the corrections that should be applied to these to get the correct values of a_1 , a_2 and a_3 . Thus we have

$$a_1 = a_{10} + \alpha_1 \quad (\text{A.26})$$

$$a_2 = a_{20} + \alpha_2 \quad (\text{A.27})$$

$$a_3 = a_{30} + \alpha_3 \quad (\text{A.27})$$

The residuals will be written as

$$e_1 = f(x_1, a_1, a_2, a_3) - y_1 = f(x_1, a_{10} + \alpha_1, a_{20} + \alpha_2, a_{30} + \alpha_3) - y_1 \quad (\text{A.28})$$

$$e_2 = f(x_2, a_1, a_2, a_3) - y_2 = f(x_2, a_{10} + \alpha_1, a_{20} + \alpha_2, a_{30} + \alpha_3) - y_2 \quad (\text{A.29})$$

$$e_N = f(x_N, a_1, a_2, a_3) - y_N = f(x_N, a_{10} + \alpha_1, a_{20} + \alpha_2, a_{30} + \alpha_3) - y_N \quad (\text{A.30})$$

Since squares of residuals are to be used, these may be defined as $y_i - f(x_i, a_1, a_2, a_3)$ or as

$$f(x_i, a_1, a_2, a_3) - y_i.$$

The function f can be expanded about the values a_{10} , a_{20} and a_{30} by using the Taylor series expansion

$$f(x+h) = f(x) + hf'(x) + \frac{h^2}{2} f''(x) + \dots \quad (\text{A.31})$$

where prime and double prime denote first and second differentials, respectively.

By omitting higher-order terms, we get

$$e_1 = f(x_1, a_{10}, a_{20}, a_{30}) + \alpha_1 \left(\frac{\partial f_1}{\partial a_1} \right)_0 + \alpha_2 \left(\frac{\partial f_1}{\partial a_2} \right)_0 + \alpha_3 \left(\frac{\partial f_1}{\partial a_3} \right)_0 - y_1 \quad (\text{A.32})$$

where

$$\left(\frac{\partial f_1}{\partial a_1} \right)_0 \text{ is the value of } \frac{\partial f}{\partial a_1} \text{ at } x = x_1, a_1 = a_{10}, a_2 = a_{20}, a_3 = a_{30} \quad (\text{A.33})$$

$$\left(\frac{\partial f_1}{\partial a_2}\right)_0 \text{ is the value of } \frac{\partial f}{\partial a_2} \text{ at } x = x_1, a_1 = a_{10}, a_2 = a_{20}, a_3 = a_{30} \quad (\text{A.34})$$

$$\left(\frac{\partial f_1}{\partial a_3}\right)_0 \text{ is the value of } \frac{\partial f}{\partial a_3} \text{ at } x = x_1, a_1 = a_{10}, a_2 = a_{20}, a_3 = a_{30} \quad (\text{A.35})$$

$$\begin{aligned} f(x_1, a_{10}, a_{20}, a_{30}) \text{ is the value of } f(x, a_1, a_2, a_3) \text{ at } x = x_1, \\ a_1 = a_{10}, a_2 = a_{20}, a_3 = a_{30} \end{aligned} \quad (\text{A.36})$$

or

$$e_1 = \alpha_1 \left(\frac{\partial f_1}{\partial a_1}\right)_0 + \alpha_2 \left(\frac{\partial f_1}{\partial a_2}\right)_0 + \alpha_3 \left(\frac{\partial f_1}{\partial a_3}\right)_0 + [f(x_1, a_{10}, a_{20}, a_{30}) - y_1] \quad (\text{A.37})$$

Similarly,

$$e_2 = \alpha_1 \left(\frac{\partial f_2}{\partial a_1}\right)_0 + \alpha_2 \left(\frac{\partial f_2}{\partial a_2}\right)_0 + \alpha_3 \left(\frac{\partial f_2}{\partial a_3}\right)_0 + [f(x_2, a_{10}, a_{20}, a_{30}) - y_2] \quad (\text{A.38})$$

$$e_N = \alpha_1 \left(\frac{\partial f_N}{\partial a_1}\right)_0 + \alpha_2 \left(\frac{\partial f_N}{\partial a_2}\right)_0 + \alpha_3 \left(\frac{\partial f_N}{\partial a_3}\right)_0 + [f(x_N, a_{10}, a_{20}, a_{30}) - y_N] \quad (\text{A.39})$$

These equations are linear in the corrections α_1 , α_2 and α_3 . Thus, from now onward, we can apply the procedure of linear least squares described earlier. It means that best values of α_1 , α_2 and α_3 are those for which $\Sigma (e_i)^2$ is a minimum, which requires that

$$\frac{\partial}{\partial \alpha_1} \sum_{i=1}^N e_i^2 = 0 \quad (\text{A.40})$$

$$\frac{\partial}{\partial \alpha_2} \sum_{i=1}^N e_i^2 = 0 \quad (\text{A.41})$$

$$\frac{\partial}{\partial \alpha_3} \sum_{i=1}^N e_i^2 = 0 \quad (\text{A.42})$$

The values of α_1 , α_2 and α_3 are obtained by solving these simultaneous equations. With these values, the improved values of a_1 , a_2 and a_3 become $a_{10} + \alpha_1$, $a_{20} + \alpha_2$ and $a_{30} + \alpha_3$ respectively. The initial guess values a_{10} , a_{20} and a_{30} are now replaced by corrected values $a_{10} + \alpha_1$, $a_{20} + \alpha_2$ and $a_{30} + \alpha_3$, and the process is repeated till the corrections α_1 , α_2 and α_3 converge to the desired accuracy. This is ordinary nonlinear least squares method and can be extended to the case where we have several parameters. It may be noted that in writing the Eq. (A.32), higher-order terms, i.e. terms containing squares, cubes, etc., of the corrections α_1 , α_2 and α_3 were neglected. This may be a good approximation only if these corrections are small, i.e. the initial guesses in Eqs. (A.26), (A.27) and (A.28) are close to the correct values. One of the major problems is to select the initial values of the parameters. If these are not suitably chosen, the solution may converge to a local minima rather than absolute minima. A very useful method to arrive at the minima is that given by Marquardt (Bevington and Robinson 1992) and is widely used for developing nonlinear least squares programs.

It may be noted that in the above description we had one independent variable x and one dependent variable y , i.e. one variable y_i is measured for a given x_i . In the case of impedance spectroscopy, we have one independent variable, ω ($= x$), and two dependent variables, Z' and Z'' (real and imaginary parts of the complex function Z), i.e. two variables Z' and Z'' are measured for a frequency ω ($= 2\pi f$). Both Z' and Z'' are functions of ω , R_1 , C_1 , R_2 , C_2 , etc. These R_1 , C_1 , R_2 , C_2 , etc. are equivalent to a_1 , a_2 , a_3 , a_4 , etc. in the above treatment. The sum of squares of residuals to be minimized would be given by

$$\chi^2 = \sum_{i=1}^N \left\{ \text{weight } t'_i \left[Z'_i \text{ (calculated)} - Z'_i \text{ (experimental)} \right]^2 + \text{weight } t''_i \left[Z''_i \text{ (experimental)} \right]^2 \right\} \quad (\text{A.43})$$

where weight'_i and weight''_i are weights for the values of Z' and Z'' at i th frequency ω_i . The weights can be assigned to equal to $1/(\sigma'_i)^2$ and $1/(\sigma''_i)^2$, where σ'_i and σ''_i are the standard deviations in the i th value Z'_i and Z''_i , respectively. The sum χ^2 is our goodness-of-fit parameter. χ^2 is minimized with respect to all the parameters a_1 , a_2 , a_3 , a_4 , etc. (i.e. R_1 , C_1 , R_2 , C_2 , etc.) by following the procedure of nonlinear least squares, as described earlier, by choosing initial guesses for R_1 , C_1 , R_2 , C_2 , etc., getting corrections to these initial values and repeating the process till desired convergence is achieved. For faster convergence Marquardt algorithm may be adopted (Bevington and Robinson 1992). The initial guesses are obtained from the experimental plots and the models chosen. For example, for a model comprising parallel combinations R_1C_1 and R_2C_2 connected in series, Z' and Z'' would be written as

$$Z'_i = \frac{R_{11}}{1 + (\omega_i C_{11} R_{11})^2} + \frac{R_{12}}{1 + (\omega_i C_{12} R_{12})^2} \quad (\text{A.44})$$

$$Z_i'' = \frac{\omega_i C_1 R_1^2}{1 + (\omega_i C_1 R_1)^2} + \frac{\omega_i C_2 R_2^2}{1 + (\omega_i C_2 R_2)^2} \quad (\text{A.45})$$

and the parameters would be determined.

The least squares procedures are discussed in detail in literature (Bevington and Robinson 1992; Scarborough 1966; Macdonald 2005). Computer softwares are commercially available with graphical interfaces for CNLS fittings. A CNLS program IMPSPEC.BAS written in GW BASIC was developed using the procedure described above including Marquardt algorithm and has been successfully used in the authors' laboratory (Pandey 1992). This program provides the flexibility of feeding the expressions for Z' and Z'' for the model of user's choice and can handle 50 data points. Also, other immittance functions (M , Y , ε) can be fitted.



Taylor & Francis

Taylor & Francis Group

<http://taylorandfrancis.com>

References

- Aandstad A., K. Holtberget, R. Hageberg, I. Holme, and S.A. Anderssen. 2014. Validity and Reliability of Bioelectrical Impedance Analysis and Skinfold Thickness in Predicting Body Fat in Military Personnel, *Military Medicine*, 179: 208–217.
- Abe Y., N. Hori, and S. Kumagai. 2019. Electrochemical Impedance Spectroscopy on the Performance Degradation of LiFePO₄/Graphite Lithium-Ion Battery due to Charge-Discharge Cycling under Different C-Rates, *Energies*, 12: 4507–4521. doi:10.3390/en12234507.
- Aberg P., P. Geladi, I. Nicander, J. Hansson, and U.H.S. Ollmar. 2005. Non-invasive and Microinvasive Electrical Impedance Spectra of Skin Cancer – A Comparison between Two Techniques, *Skin Research and Technology*, 11: 281–286.
- Ackmann J.J. and M.A. Seitz. 1984. Methods of Complex Impedance Measurements in Biological Tissue, *Crit Rev Biomed Engg*, 11: 281–311.
- Amini M., J. Hisdal, and H. Kalvøy. 2018. Applications of Bioimpedance Measurement Techniques in Tissue Engineering, *J Electr Bioimp*, 9: 142–158.
- Andrade C., V.M. Blanco, A. Collazo, M. Keddam, X.R. Novoa, and H. Takenouti. 1999. Cement Paste Hardening Process Studied by Impedance Spectroscopy, *Electrochimica Acta*, 44: 4313–4318.
- Arfken G. 1985. *Mathematical Methods for Physicists*, Academic Press, London.
- Arof A.K., S. Amirudin, S.Z. Yusof, and I.M. Noor. 2014. A Method Based on Impedance Spectroscopy to Determine Transport Properties of Polymer Electrolytes, *Phys Chem Chem. Phys*, 16: 1856–1867.
- Astuti I. and Ysrafil. 2020. Severe Acute Respiratory Syndrome Coronavirus 2 (SARS-CoV-2): An Overview of Viral Structure and Host Response. *Diabetes Metab Syndr Clin Res Rev*, 14: 407–412.
- Ates M. 2011. Review Study of Electrochemical Impedance Spectroscopy and Equivalent Electrical Circuits of Conducting Polymers on Carbon Surfaces, *Progress in Organic Coatings*, 71: 1–10.
- Augustine R., A. Hasan, S. Das, R. Ahmed, Y. Mori, T. Notomi, B.D. Kevadiya, and A.S. Thakor. 2020. Loop-Mediated Isothermal Amplification (LAMP): A Rapid, Sensitive, Specific, and Cost-Effective Point-of-Care Test for Coronaviruses in the Context of COVID-19 Pandemic, *Biology*, 9: 182–199.
- Azzarello E., S. Mugnai, C. Pandolfi, E. Masi, and S. Mancuso. 2006. Stress Assessment in Plants by Impedance Spectroscopy, In: *Floriculture, Ornamental and Plant Biotechnology Volume III: Advances and Topical Issues*, Jaime A. Teixeira da Silva (ed), Global Science Books, London, pp 140–148.
- Bain A.K. and P. Chand. 2017. *Ferroelectrics, Principles and Applications*, Wiley-VCH Verlag GmbH & Co., Weinheim, Germany.
- Balasubramani V., S. Chandraleka, T. Subba Rao, R. Sasikumar, M.R. Kuppusamy, and T.M. Sridhar. 2020. Recent Advances in Electrochemical Impedance Spectroscopy Based Toxic Gas Sensors Using Semiconducting Metal Oxides, *Journal of The Electrochemical Society*, 167: 037572–17.
- Balasubramani V., S. Sureshkumar, T. Subba Rao, and T.M. Sridhar. 2019. Impedance Spectroscopy-Based Reduced Graphene Oxide Incorporated ZnO Composite Sensor for H₂S Investigations, *ACS Omega*, 4: 9976–9982. doi:10.1021/acsomega.9b00754.

- Bandara T.M.W.J., M.A.K.L. Dissanayake, I. Albinsson, and B.-E. Mellander. 2011. Mobile Charge Carrier Concentration and Mobility of a Polymer Electrolyte Containing EO and $\text{Pr}_4\text{N}^+\text{I}^-$ Using Electrical and Dielectric Measurements, *Solid State Ionics*, 189: 63–68.
- Bandara T.M.W.J. and B.-E. Mellander. 2011. Evaluation of Mobility, Diffusion Coefficient and Density of Charge Carriers in Ionic Liquids and Novel Electrolytes Based on a New Model for Dielectric Response, In: *Ionic Liquids: Theory, Properties, New Approaches*, A. Kokorin (ed), InTech, Croatia, pp 383–406.
- Bao J.Z., C.C. Davis, and R.E. Schmukler. 1992. Frequency Domain Impedance Measurements of Erythrocytes. Constant Phase Angle Impedance Characteristics and a Phase Transition, *Biophysical Journal*, 61(5): 1427–1434.
- Barsoukov E. and J.R. Macdonald. 2005. *Impedance Spectroscopy: Theory, Experiment, and Applications*, Second Edition, John Wiley & Sons, Hoboken.
- Barsoukov E. and J. Ross Macdonald (eds). 2005, 2018. *Impedance Spectroscopy Theory, Experiment, and Applications*, Third Edition, John Wiley & Sons, Hoboken.
- The Basics of Electrochemical Impedance Spectroscopy, www.gamry.com/application-notes/EIS/basics-of-electrochemical-impedance-spectroscopy/. Accessed 12 September 2022.
- Basu R.N. and H.S. Maiti. 1986. PTC Behaviour of Semiconducting BaTiO_3 Ceramics, *Transactions of the Indian Ceramic Society*, 45: 140–146.
- Bayford R.H. 2006. Bioimpedance Tomography (Electrical Impedance Tomography), *Annu Rev Biomed Eng*, 8: 63–91.
- Bera T.K. 2014. Bioelectrical Impedance Methods for Noninvasive Health Monitoring: A Review, *Journal of Medical Engineering*, 28 pages. <http://dx.doi.org/10.1155/2014/381251>.
- Bevington P.R. and D.K. Robinson. 1992. *Data Reduction and Error Analysis for the Physical Sciences*, McGraw Hill, New York.
- Bonanni A. and M. Del Valle. 2010. Use of Nanomaterials for Impedimetric DNA Sensors: A Review, *Anal Chim Acta*, 678: 7–17.
- Bonanni A., M.J. Esplandiú, and M. Del Valle. 2010. Impedimetric Geno Sensing of DNA Polymorphism Correlated to Cystic Fibrosis: A Comparison among Different Protocols and Electrode Surfaces, *Biosens Bioelectron*, 26: 1245–1251.
- Bonmassar G., S. Iwaki, G. Goldmakher, L.M. Angelone, J.W. Belliveau, and M.H. Lev. 2009. On the Measurement of Electrical Impedance Spectroscopy (EIS) of the Human Head, *International Journal of Bioelectromagnetism*, 12: 32–46.
- Bou A., A. Pockett, D. Raptis, T. Watson, M.J. Carnie, and J. Bisquert. 2020. Beyond Impedance Spectroscopy of Perovskite Solar Cells: Insights from the Spectral Correlation of the Electrooptical Frequency Techniques, *J Phys Chem Lett*, 11: 8654–8659. <https://dx.doi.org/10.1021/acs.jpcclett.0c02459>.
- Boukamp B.A., M.T.N. Pham, D.H.A. Blank, H.J.M. Bouwmeester. 2004. Ionic and Electronic Conductivity in Lead-Zirconate-Titanate (PZT), *Solid State Ionics*, 170: 239–254.
- Bowen C.R., M. Lopez-Prieto, S. Mahon, and F. Lowrie. 2000. Impedance Spectroscopy of Piezoelectric Actuators, *Scripta Mater*, 42 : 813–818.
- Brana A.F., E. Fornies, N. Lopez, and B.J. García. 2015. High Efficiency Si Solar Cells Characterization Using Impedance Spectroscopy Analysis, *Journal of Physics: Conference Series*, 647: 012069. doi:10.1088/1742-6596/647/1/012069-4.
- Brock J. (ed). 2017. *Electrochemical Impedance Spectroscopy Methods, Analysis and Research*, Nova Science Publishers, New York.
- Brown B.H. 2001. Medical Impedance Tomography and Process Impedance Tomography: A Brief Review, *Meas Sci Technol*, 12: 991–996.
- Brown B.H. 2003. Electrical Impedance Tomography (EIT): A Review, *Journal of Medical Engineering & Technology*, 27: 97–108.

- Buttry D.A. and Ward M.D. 1992. Measurement of Interfacial processes at Electrode Surfaces with the Electrochemical Quartz Crystal Microbalance, *Chemical Review*, 92: 1355–1379.
- Cady W.G. 1946. *Piezoelectricity*, McGraw Hill Book Co, New York.
- Callister, W.D. Jr. 2001. *Fundamentals of Materials Science and Engineering*, Fifth Edition, John Wiley & Sons, New York.
- Callister W.D. Jr. 2007. *Materials Science and Engineering: An Introduction*, Seventh Edition, John Wiley & Sons, New York. Carter Linda J., L.V. Garner, J.W. Smoot, Y. Li, Q. Zhou, C.J. Saveson, J.M. Sasso, A.C. Gregg, D.J. Soares, T.R. Beskid, S.R. Jervey, and C. Liu. 2020. Assay Techniques and Test Development for COVID-19 Diagnosis, *ACS Cent Sci*, 6: 591–605. <https://dx.doi.org/10.1021/acscentsci.0c00501>.
- Casciola M. and D. Fabiani. 1983. Ionic Conduction and Dielectric Properties of Anhydrous Alkali Metal Salt Forms of α -Zirconium Phosphate, *Solid State Ionics*, 11: 31–38.
- Chaitanya P. 2008. *Impedance Spectroscopy and RF Pulse Response of Piezoelectric Materials*, Ph.D. Thesis, Rani Durgavati University, Jabalpur.
- Chaitanya P., R. Mishra, P.K. Ahirwal, A. Shukla, O.P. Thakur, L. Pandey, O. Parkash, and D. Kumar. 2015. Study of Temperature Dependence of Electrode–Glass Ceramic Interface Using Impedance Spectroscopy, *Integrated Ferroelectrics*, 159(1): 121–126.
- Chaitanya P., A. Shukla, and L. Pandey. 2014. Determination of Equivalent Circuit Model Components of Piezoelectric Materials by Using Impedance Spectroscopy, *Integrated Ferroelectrics*, 150: 88–95.
- Chaitanya P., O.P. Thakur, V.A. Shukla, and L. Pandey. 2011. Equivalent Circuit Model of a $\text{PbZr}_{0.6}\text{Ti}_{0.4}\text{O}_3$ Ceramic Using Impedance Spectroscopy, *Journal of Ceramic Processing Research*, 12: 247–258.
- Chakrabarti A. 2008. *An Introduction to Network Filters and Transmission Lines*, Dhanpat Rai & Co, Delhi.
- Chakrabarti A. 2019. *Circuit Theory: Analysis and Synthesis*, Dhanpat Rai & Co, Delhi.
- Chandrasekhar P. 2018. *Conducting Polymers, Fundamentals and Applications Including Carbon Nanotubes and Graphene*, Second Edition, Springer International Publishing AG, Switzerland.
- Chen P-W and D.D.L. Chung. 1995. Carbon-Fiber-Reinforced Concrete as an Intrinsically Smart Concrete for Damage Assessment during Dynamic Loading, *J Am Ceram Soc*, 78: 816–818.
- Chen P-W and D.D.L. Chung. 1996. Carbon Fiber Reinforced Concrete as an Intrinsically Smart Concrete for Damage Assessment during Static and Dynamic Loading, *ACI Mater J*, 93: 341–350.
- Chi D., S. Qu, Z. Wang, and J. Wang. 2014. High Efficiency P3HT:PCBM Solar Cells with an Inserted PCBM Layer, *J Mater Chem C*, 2: 4383–4387.
- Chinen K, I. Kinjo, A. Zamami, K. Irei, and K. Nagayama. 2015. New Equivalent-Electrical Circuit Model and a Practical Measurement Method for Human Body Impedance, *Bio-Medical Materials and Engineering*, 26: S779–S786.
- Chung D.D.L. 1998. Self-Monitoring Structural Materials, *Mater Sci Eng R*, 22: 57–78.
- Cole K.S. and Cole R.H. 1941. Dispersion and Absorption in Dielectrics I. Alternating Current Characteristics, *J Chem Phys*, 9(4): 341–351.
- Condera J., C. Villevieillea, S. Trabesingera, P. Nováka, L. Gublera, and R. Bouchetb. 2017. Electrochemical Impedance Spectroscopy of a Li–S Battery: Part 2. Influence of Separator Chemistry on the Lithium Electrode/Electrolyte Interface, *Electrochimica Acta*, 255: 379–390.
- Daniels J., K.H. Härdtl, and R. Wernicke. 1978. The PTC Effect of Barium Titanate, *Philips Technical Review*, 38: 73–82.

- Das A. and P. Dobbidi. 2021. Impedance Spectroscopy and ac Conductivity in $\text{Ba}_{0.5}\text{Sr}_{0.5}\text{TiO}_3 - \text{Ca}_{10}(\text{PO}_4)_6(\text{OH})_2$ Ceramic Composites: An Electrical Approach to Unveil Biocomposites, *ACS Biomater Sci Eng*, 7: 2296–2308.
- Dekker A.J. 1958. *Solid State Physics*, Prentice Hall, Englewood Cliffs, p 184.
- Denkçeken Tuba and Ayşegül Çört. 2020. Determination of Cancer Progression in Breast Cells by Fiber Optic Bioimpedance Spectroscopy System, *J Surg Med*, 4: 84–88.
- Dissado L.A. and R.M. Hill. 1988. Constant-Phase-Angle and Power-Law Regimes in the Frequency Response of a General Determinate Fractal Circuit, *Physical Review B*, 37: 3434–3439.
- Dong B., Q. Qiu, J. Xiang, C. Huang, F. Xing, and N. Han. 2014. Study on the Carbonation Behavior of Cement Mortar by Electrochemical Impedance Spectroscopy, *Materials*, 7: 218–231.
- Dong B., J. Zhang, Y. Liu, G. Fang, Z. Ding, and F. Xing. 2016. Tracing Hydration Feature of Aluminophosphate Cementitious Materials by Means of Electrochemical Impedance Method, *Constr Build Mater*, 113: 997–1006.
- Dotelli G., and C.M. Mari. 2001. The Evolution of Cement Paste Hydration Process by Impedance Spectroscopy, *Mater Sci Eng A*, 303: 54–59.
- Dubey A.K., S.D. Gupta, R. Kumar, A. Tewari, and B. Basu. 2009. Time Constant Determination for Electrical Equivalent of Biological Cells, *Journal of Applied Physics*, 105: 084705–084708.
- Dunn C. and J. Scott. 2022. Achieving Reliable and Repeatable Electrochemical Impedance Spectroscopy of Rechargeable Batteries at Extra-Low Frequencies, *IEEE Transactions on Instrumentation and Measurement*, 71: 1–8. doi:10.1109/TIM.2022.3180429.
- Eder D. and R. Kramer. 2006. Impedance Spectroscopy of Reduced Monoclinic Zirconia, *Phys Chem. Chem. Phys*, 8: 4476–4483.
- Escarpa A., M.C. González, and M.Á. Lopez (eds). 2015. *Agricultural and Food Electroanalysis*, John Wiley & Sons, Chichester, West Sussex, UK.
- Estrela da Silva J., J.P. Marques de Sa, and J. Jossinet. 2000. Classification of Breast Tissue by Electrical Impedance Spectroscopy, *Med Biol Eng Comput*, 38: 26–30.
- Ezpeleta I., L. Freire, C. Mateo-Mateo, X. Ramón Nóvoa, A. Pintos, and S. Valverde-Pérez. 2022. Characterisation of Commercial Li-Ion Batteries Using Electrochemical Impedance Spectroscopy, *Chemistry Select*, 7: e202104464 (1 of 6). doi.org/10.1002/slct.202104464.
- Felföldi, J., P. Laszlo, S. Barabassy, and J. Farkas. 1993. Dielectric Method for Detection of Irradiation Treatment of Potatoes, *Radiat Phys Chem*, 41: 471–480.
- Ford S.J., J.D. Shane and T.O. Mason. 1998. Assignment of Features in Impedance Spectra of the Cement-Paste/Steel System, *Cem Concr Res*, 28: 1737–1751.
- Foster, K.R. and H.C. Lukaski. 1996. Whole-Body Impedance--What Does It Measure? *The American Journal of Clinical Nutrition*, 64: 388S–396S.
- Foster K.R. and H.P. Schwan. 1989. Dielectric Properties of Tissues and Biological Materials: A Critical Review, *Critical Reviews in Biomedical Engineering*, 17: 25–104.
- Frank S.B., B. Greenebaum (ed). 2007. *Handbook of Biological Effects of Electromagnetic Fields*, Third Edition, CRC Press, Boca Raton, FL, pp 52–81.
- Frerichs I., M.B.P. Amato, A.H. van Kaam et al. 2017. Chest Electrical Impedance Tomography Examination, Data Analysis, Terminology, Clinical Use and Recommendations: Consensus Statement of the TRanslational EIT developmeNt stuDy TREND study group, *Thorax*, 72: 83–93. doi:10.1136/thoraxjnl-2016-208357.
- Fricke H. 1932. The Theory of Electrolytic Polarization, *Philos Mag*, 14(90): 310–318.
- Fuentes A., Va'zquez-Gutiérrez J.L., Pérez-Gago M.B., Vonasek E., Nitin N., and Barrett D.M. 2014. Application of Nondestructive Impedance Spectroscopy to Determination of

- the Effect of Temperature on Potato Microstructure and Texture, *J Food Eng*, 133: 16–22. <https://doi.org/10.1016/j.jfoodeng.2014.02.016>.
- Fukushima E. and S.B.W. Roeder. 1981. *Experimental Pulse NMR: A Nuts and Bolts Approach*, Addition-Wesley Publishing Company, Massachusetts.
- Gabriel C., S. Gabriel, E. Corthout. 1996a. The Dielectric Properties of Biological Tissues: I. Literature Survey, *Phys Med Biol*, 41: 2231–2249.
- Gabriel S., R.W. Lau, and C. Gabriel. 1996b. The Dielectric Properties of Biological Tissues: II., Measurements in the Frequency Range 10 Hz to 20 GHz, *Phys Med Biol*, 41 : 2251–2269.
- Gabriel S., R.W. Lau, and C. Gabriel. 1996c. The Dielectric Properties of Biological Tissues: III., Parametric Models for the Dielectric Spectrum of Tissues, *Phys Med Biol*, 41: 2271–2293.
- Gallardo A.F.S. and J.L. Provis. 2021. Electrochemical Cell Design and Impedance Spectroscopy of Cement Hydration, *J Mater Sci*, 56: 1203–1220.
- Gerhardt R. 1994. Microstructural Characterization of Composites via Electrical Measurements. *Proc Ceram Eng Sci*, 15(5): 1174–1181.
- Gerhardt R. and R. Ruh. 2001. Volume Fraction and Whisker Orientation Dependence of the Electrical Properties of SiC-Whisker-Reinforced Mullite Composites, *J Amer Ceram Soc*, 84 : 2328–2334.
- Gerhardt R., J. Runyan, C. Sana, D.S. Mclachlan, and R. Ruh. 2001. Electrical Properties of Boron Nitride Matrix Composites: III, Observation near the Percolation Threshold in BN-B4C Composites, *J Amer Ceram Soc* 84: 2335–2342. Giovanni M., A. Bonanni, and M. Pumera. 2012. Detection of DNA Hybridization on Chemically Modified Graphene Platforms, *Analyst*, 137: 580–583.
- Gnaim R., A. Golberg, J. Sheviryov, B. Rubinsky, and C.A. Gonzalez. 2020. Detection and Differentiation of Bacteria by Electrical Bioimpedance Spectroscopy, *BioTechniques* 69: 27–36.
- Grimmes S. and Ø.G. Martinse. 2010. Alpha-Dispersion in Human Tissue, *AIP Journal of Physics: Conference Series*, 224: 012073–012074.
- Grimmes S. and Ø.G. Martinsen. 2015. *Bioimpedance and Bioelectricity Basics*. Third Edition. Academic Press, Elsevier, New York.
- Grossi M. and Bruno R. 2017. Electrical Impedance Spectroscopy (EIS) for Biological Analysis and Food Characterization: A Review, *J Sens Sens Syst*, 6: 303–325. <https://doi.org/10.5194/jsss-6-303-2017>.
- Gu P, Z. Xu, P. Xie, and J.J. Beaudoin. 1993. An ac Impedance Spectroscopy Study of Micro-Cracking in Cement-Based Composites during Compressive Loading, *Cem Concr Res*, 23: 675–682.
- Guerrero A., J. Bisquert, and G. Garcia-Belmonte. 2021. Impedance Spectroscopy of Metal Halide Perovskite Solar Cells from the Perspective of Equivalent Circuits, *Chem Rev*, 121(23): 14430–14484.
- Guo X. and A. Facchetti. 2020. The Journey of Conducting Polymers from Discovery to Application, *Nature Materials*, 19: 922–928.
- Hailegnaw B., N.S. Sariciftci, and M.C. Scharber. 2020. Impedance Spectroscopy of Perovskite Solar Cells: Studying the Dynamics of Charge Carriers before and after Continuous Operation, *Phys Status Solidi A*, 217: 2000291–2000298. doi:10.1002/pssa.202000291.
- Halliday D., Resnick R., and Krane K.S. 1992. *Physics*, Fourth Edition, Volume Two, John Wiley & Sons, New York.
- Harikumar R., R. Prabu, and S. Raghavan. 2013. Electrical Impedance Tomography (EIT) and Its Medical Applications: A Review, *International Journal of Soft Computing and Engineering (IJSCE)*, 3: 193–198.

- Hariprakash B., S.K. Martha, and A.K. Shukla. 2003. Monitoring Sealed Automotive Lead-Acid Batteries by Sparse-Impedance Spectroscopy, *Proc Indian Acad Sci (Chem Sci)*, 115: 465–472.
- Harker F.R. and J.H. Maindonald. 1994. Changes in Cell Wall, Vacuole, and Membranes Detected Using Electrical Impedance Measurements, *Plant Phys*, 106: 165–171. <https://doi.org/10.1104/pp.106.1.165>.
- Hauff E.V. 2019. Impedance Spectroscopy for Emerging Photovoltaics, Published as Part of The Journal of Physical Chemistry Virtual Special Issue “Young Scientists”, *J Phys Chem C*, 123: 11329–11346. doi:10.1021/acs.jpcc.9b00892.
- Hayden R.I., C.A. Moyese, F.W. Calder, D.P. Crawford, and D.S. Fensom. 1969. Electrical Impedance Studies on Potato and Alfalfa Tissue, *J Exp Bot*, 20: 177–200.
- Helseth L.E. 2018. Electrical Impedance Spectroscopy of Multiwall Carbon Nanotube–PDMS Composites under Compression, *Mater Res Express*, 5: 105002–1050011.
- Heywang, W. 1961. Barium Titanate as a Semiconductor with Blocking Layers, *Solid-State Electron*, 3: 51–58.
- Heywang W. 1971. Semiconducting Barium Titanate, *Journal of Materials Science*, 6: 1214–1226.
- Hirschorn B., M.E. Orazem, B. Tribollet, V. Vivier, I. Frateur, and M. Musiani. 2010. Constant-Phase-Element Behaviour Caused by Resistivity Distributions in Films: I. Theory, *Journal of the Electrochemical Society*, 157: C452–C457.
- Hodge I.M., M.D. Ingram and A.R. West, 1976. Impedance and Modulus Spectroscopy of Polycrystalline Solid Electrolytes, *J Electroanal Chem*. 74: 125–143.
- Hsieh G., S.J. Ford, T.O. Mason, and L.R. Pederson. 1996a. Experimental Limitations in Impedance Spectroscopy: Part I. Simulation of Reference Electrode Artifacts in Three-Point Measurements, *Solid State Ionics*, 91: 191–201. doi:10.1016/S0167-2738(96)83019-0.
- Hsieh G., T.O. Mason, and L.R. Pederson. 1996b. Experimental Limitations in Impedance Spectroscopy: Part II. Electrode Artifacts in Three-Point Measurements on Pt/YSZ, *Solid State Ionics*, 91: 203–212. doi:10.1016/S0167-2738(96)83020-7
- Hsieh G., T.O. Mason, E.J. Garbocz, and L.R. Pederson. 1997. Experimental Limitations in Impedance Spectroscopy: Part III. Effect of Reference Electrode Geometry Position. *Solid State Ionics*, 96: 153–172. doi:10.1016/S0167-2738(97) 00073-8 www.britannica.com/science/virus accessed on 25 July 2022. www.genome.gov > genetics-glossary > Accessed 11 July 2022.
- Hughes D.G. and L. Pandey. 1984. Spurious Signals Caused by the Piezoelectric Ringing of NaN_2 in Pulsed NMR, *Journal of Magnetic Resonance*, 56: 428–442.
- Husain A., K. Kupwade-Patil, A.F. Al-Aibani, and M.F. Abdulsalam. 2017. In situ Electrochemical Impedance Characterization of Cement Paste with Volcanic Ash to Examine Early Stage of Hydration, *Constr Build Mater*, 133: 107–117.
- Hwang J.H., K.S. Kirkpatrick, T.O. Mason, and E.J. Garboczi. 1997. Experimental Limitations in Impedance Spectroscopy: Part IV. Electrode Contact Effects. *Solid State Ionics*, 98: 93–104. doi:10.1016/S0167-2738(97)00075-1.
- Idan A., J. Alter, M. Werbner, A. Ogungbile, M. Dessau, M. Gal-Tanamy, and S. Vernick. 2022. Rapid Electrochemical Immunodetection of SARS-CoV-2 Using a Pseudo-Typed Vesicular Stomatitis Virus Model, *Talanta*, 239: 123147–123148.
- Irvine J.T.S., D.C. Sinclair, and A.R. West. 1990a. Electroceramics: Characterization by Impedance Spectroscopy, *Adv Mater*, 2: 132–138.
- Irvine J.T.S., A.R. West, E. Amano, A. Huanosta, and R. Valenzuela. 1990b. Characterisation of Magnetic Materials by Impedance Spectroscopy, *Solid State Ionics*, 40/41: 220–223.

- Ishiwara H., M. Okuyama, and Y. Arimoto (eds). 2004. *Ferroelectric Random Access Memories, Fundamentals and Applications*, Topics in Applied Physics, Springer-Verlag, Heidelberg, Berlin, p 93.
- Ito T., H. Shirakawa, and S. Ikeda. 1974. Simultaneous Polymerization and Formation of Polyacetylene Film on the Surface of Concentrated Soluble Ziegler-Type Catalyst Solution, *J Polym Sci*, 12: 11–20.
- Jaiswal N., D. Kumar, S. Upadhyay, and O. Parkash. 2013. Ceria Co-doped with Calcium (Ca) and Strontium (Sr): A Potential Candidate as a Solid Electrolyte for Intermediate Temperature Solid Oxide Fuel Cells, *Ionics*, 20: 45–54. doi:10.1007/s11581-013-0936-8.
- Jaiswal N., K. Tanwar, R. Suman, D. Kumar, S. Uppadhya, and O. Parkash. 2019. A Brief Review on Ceria Based Solid Electrolytes for Solid Oxide Fuel Cells, *Journal of Alloys and Compounds*, 781: 984–1005.
- Jocsak I., G. Vegvari, and E. Vozary. 2019. Electrical Impedance Measurement on Plants: A Review with Some Insights to Other Fields, *Theor Exp Plant Physiol*, 31: 359–375. [https://doi.org/10.1007/s40626-019-00152-y\(01234](https://doi.org/10.1007/s40626-019-00152-y(01234).
- Joines W.T., Q.H. Liu, and Y.G. Ybarra. 2006. Electromagnetic Imaging of Biological Systems in Bioengineering and Biophysical Aspects of Electromagnetic Fields, In: *Handbook of Biological Effects of Electromagnetic Fields*, Third Edition, Frank S. (ed), Barnes and Ben Greenebaum, CRC Press, Boca Raton, p 422.
- Jona F. and G. Shirane. 1962. *Ferroelectric Crystals*, Pergamon Press, New York.
- Jonker G.H. 1967. Halogen Treatment of Barium Titanate Semiconductors, *Mat Res Bull*, 2: 401–407.
- Jonscher A.K. 1983. *Dielectric Relaxation in Solids*. Chelsea Dielectric Press, London.
- Kallel, A.Y., V. Petrychenko, and O. Kanoun. 2022. State-of-Health of Li-ion Battery Estimation Based on the Efficiency of the Charge Transfer Extracted from Impedance Spectra, *Appl Sci*, 12: 885. <https://doi.org/10.3390/app12020885>.
- Kanoun O. (ed). 2013. *Lecture Notes on Impedance Spectroscopy Measurement, Modeling and Applications*, CRC Press, Boca Raton.
- Kasap S.O. 2006. *Principles of Electronic Materials and Devices*, Third Edition, McGraw Hill, New York.
- Katare R.K. 1997. *Application of Impedance Spectroscopy in the study of Electronic Ceramics*, Ph.D. Thesis, Rani Durgavati University, Jabalpur.
- Katare R.K., L. Pandey, R.K. Dwivedi, O. Parkash, and D. Kumar. 1999. A Novel Approach Based on Impedance Spectroscopy for Measurement of Magnetic Permeability of Ceramics, *Indian Journal of Engineering and Materials Science*, 6(1): 34–42.
- Katare R.K., L. Pandey, O.P. Thakur, O. Parkash, and D. Kumar. 2003. Equivalent Circuit Model of $\text{Ca}_{1-x}\text{Y}_x\text{Ti}_{1-x}\text{Co}_x\text{O}_3$ Using Impedance Spectroscopy, *Modern Physics Letters B*, 17: 339–346.
- Katare R.K., L. Pandey, O.P. Thakur, O. Parkash, and D. Kumar. 2005. Impedance Spectroscopic Study of $\text{Ca}^{1-x}\text{Y}_x\text{Ti}_{1-x}\text{Co}_x\text{O}_3$ Ceramics Based Humidity Sensor, *International Journal of Modern Physics B*, 19: 1783–1791.
- Kaushik. D., M.N. Alias, and R. Brown. 1991. An Impedance Study of a Carbon Fiber/Vinyl Ester Composite, *Corrosion*, 47: 859.
- Kerner T.E., K.D. Paulsen, A. Hartov, S.K. Soho, and S.P. Poplack. 2002. Electrical Impedance Spectroscopy of the Breast: Clinical Imaging Results in 26 Subjects, *IEEE Transactions on Medical Imaging*, 21: 638–645.
- Khalil S.F., M.S. Mohhtar, and F. Ibrahim. 2014. The Theory and Fundamentals of Bioimpedance Analysis in Clinical Status Monitoring and Diagnosis of Diseases, *Sensors*, 14: 10895–10928.

- Khan M.Q. and K. Ahmad. 2020. Origin and Fundamentals of Perovskite Solar Cells in Recent Advances in Nanophotonics—Fundamentals and Applications, IntechOpen. doi: <http://dx.doi.org/10.5772/intechopen.94376>.
- Khoshnazar R. and Y. Shao. 2018. Characterization of Carbonation-Cured Cement Paste Using X-Ray Photoelectron Spectroscopy, *Constr Build Mater*, 168: 598–605.
- Kiew Lik-Voon, Chia-Yu Chang, Sheng-Yu Huang et al. 2021. Development of Flexible Electrochemical Impedance Spectroscopy-Based Biosensing Platform for Rapid Screening of SARS-CoV-2 Inhibitors, *Biosensors and Bioelectronics*, 183: 113213–1132110. <https://doi.org/10.1016/j.bios.2021.113213>.
- Kim H.C. and S.Y. Kim. 1995. Electrical Properties of Cement Paste Obtained from Impedance Spectroscopy, *J Mater Sci*, 30: 3768–3772.
- Kim Y-M, J-H Lee, and S-H Hong. 2003. Study of Alinite Cement Hydration by Impedance Spectroscopy, *Cem Concr Res*, 33: 299–304.
- Kingery W.D., H.K. Bowen, and D.R. Uhlmann. 1976. Introduction to Ceramics, Second Edition, John Wiley & Sons, New York.
- Kitamura Y., K. Toyoda, and B. Park. 2000. Electric Impedance Spectroscopy for Yogurt Processing, *Food Sci Technol Res*, 6: 310–313.
- Kittel C. 2005. Introduction to Solid State Physics, Eighth Edition, John Wiley & Sons, Hoboken, p 453.
- Kleitz, M., L. Dessemond, and M.C. Steil. 1995. Model for Ion-Blocking at Internal Interfaces in Zirconias, *Solid State Ionics*, 75: 107–115.
- Klemchuk P.P. 1990. Degradable Plastics: A Critical Review, *Polymer Degradation and Stability*, 27: 183–202.
- Knipper M., J. Parisi, K. Coakley, C. Waldauf, C.J. Brabec, and V. Dyakonov. 2007. Impedance Spectroscopy on Polymer-Fullerene Solar Cells, *Zeitschrift für Naturforschung A*, 62: 490–494.
- Kozhevnikov E., X.L. Hou, S.P. Qiao, Y.F. Zhao, C.F. Li, and W.M. Tian. 2016. Electrical Impedance Spectroscopy: A Potential Method for the Study and Monitoring of a Bone Critical-Size Defect Healing Process Treated with Bone Tissue Engineering and Regenerative Medicine Approaches, *Journal of Materials Chemistry B*, 4(16): 2757–2767. <https://doi.org/10.1039/C5TB02707A>.
- Kreyszig E. 1992. Advanced Engineering Mathematics, Fifth Edition, Willey Eastern Ltd, New Delhi.
- Kumar V., O.P. Thakur, L. Pandey, A.P. Guimaraes, A. Goel, O. Parkash, and D. Kumar. 2005. Modeling of Electrical Behavior of La_{0.7}Ca_{0.3}MnO₃ Ceramic Using Impedance Spectroscopy, *Modern Physics Letters B*, 19: 697–706.
- Kupwade-Patil K., S.D. Palkovic, A. Bumajdad, C. Soriano, and O. Buyukozturk. 2018. Use of Silica Fume and Natural Volcanic Ash as a Replacement to Portland Cement: Micro and Pore Structural Investigation Using NMR, XRD, FTIR and X-Ray Microtomography, *Constr Build Mater*, 158: 574–590.
- Kusche R., S. Kaufmann, and M. Ryschka. 2018. Dry Electrodes for Bioimpedance Measurements-Design, Characterization and Comparison, *Biomedical Physics & Engineering Express*, 5: 015001–0150013.
- Lanfredi, S. and A.C.M. Rodrigues. 1999. Impedance Spectroscopy Study of the Electrical Conductivity and Dielectric Constant of Polycrystalline LiNbO₃, *J Appl Phys*, 86: 2215–2219.
- Lang S.B., G.A. Stanciu, and S.G. Stanciu. 2011. Non-linear Characterizations of Surface Charge and Interfacial Morphology, In: *Biological Interactions with Surface Charge in Biomaterials*, Tofail S.A.M. (ed), RSC Publishing, Cambridge, UK, pp 45–56.

- Lario-García J. and R. Pallas-Areny. 2006. Constant-Phase Element Identification in Conductivity Sensors Using a Single Square Wave, *Sensors and Actuators*, A132: 122–128.
- Lark-Horovitz K. and V.A. Johnson. 1959. *Solid State Physics: Electrical, Magnetic, and Optical Properties*, New York and London, Academic Press.
- Lasserre P., B. Balansethupathy, V.J. Vezza, A. Butterworth, A. Macdonald, E.O. Blair, L. McAteer, S. Hannah, A.C. Ward, P.A. Hoskisson, A. Longmuir, S. Setford, E.C.W. Farmer, M.E. Murphy, H. Flynn, and D.K. Corrigan. 2022. SARS-CoV2 Aptasensors Based on Electrochemical Impedance Spectroscopy and Low-Cost Gold Electrode Substrates, *Anal Chem*, 94: 2126–2133.
- LevaBueno J., S.A. Peyman, and P.A. Millner. 2020. A Review on Impedimetric Immunosensors for Pathogen and Biomarker Detection, *Medical Microbiology and Immunology*, 209: 343–362.
- Lewis G.V., C.R.A. Catlow, and R.E.W. Casselton. 1985. PTCR Effect In BaTiO₃, *J Am Ceram Soc*, 68: 555–558.
- Li X., Z. Qin, H. Fu, T. Li, R. Peng, Z. Li, J.M. Rini, and X. Liu. 2021. Enhancing the Performance of Paper-Based Electrochemical Impedance Spectroscopy Nanobiosensors: An Experimental Approach, *Biosensors and Bioelectronics*, 177: 112672–112678.
- Li X., H. Zhu, K. Wang et al. 2010. Graphene-on-Silicon Schottky Junction Solar Cells, *Adv Mater*, 22: 2743–2748.
- Lines, M.E. and A.M. Glass. 1977. *Principles and Applications of Ferroelectrics and Related Materials*, Clarendon Press, Oxford.
- Lougheed E.C., S.R. Miller, B.D. Ripley, and R.A. Cline. 1981. Electrical Impedance of Damazonide- and Calcium-Treated McIntosh Apples, *Experientia*, 37: 835–836. <https://doi.org/10.1007/BF01985666>.
- Lvovich V.F. 2012. *Impedance Spectroscopy: Applications to Electrochemical and Dielectric Phenomena*, John Wiley & Sons, Hoboken.
- Macdonald J.R. 1987. *Impedance Spectroscopy, Emphasizing Solid Materials and Systems*, John Wiley & Sons, New York.
- Macdonald J.R. 2005 *Impedance Spectroscopy Theory, Experiment, and Applications*, Second edition, John Wiley & Sons, New Jersey.
- Madej D. 2020. A New Implementation of Electrochemical Impedance Spectroscopy (EIS) and Other Methods to Monitor the Progress of Hydration of Strontium Monoaluminate (SrAl₂O₄) Cement, *Journal of Thermal Analysis and Calorimetry*, 139: 17–28.
- Maiti H.S. and R.N. Basu. 1986. Complex Plane Impedance Analysis for Semiconducting Barium Titanate, *Mat Res Bull*, 21: 1107–1114.
- Mansfield F. 1993. Models for the Impedance Behaviour of Protective Coatings and Cases of Localized Corrosion, *Electrochimica Acta*, 38: 1891–1897.
- Mansfield F. 1995. Use of Electrochemical Impedance Spectroscopy for the Study of Corrosion Protection by Polymer Coatings, *J Appl Electrochemistry*, 25: 187–202.
- Marco Grossi M. and B. Riccò. 2017. Electrical Impedance Spectroscopy (EIS) for Biological Analysis and Food Characterization: A Review, *J Sens Sens Syst*, 6: 303–325.
- Markx G.H. and C.L. Davey. 1999. The Dielectric Properties of Biological Cells at Radiofrequencies: Applications in Biotechnology, Enzyme and Microbial Technology, 25: 161–171.
- Mason T.O., M.A. Campo, A.D. Hixson, and L.Y. Woo. 2002. Impedance Spectroscopy of Fiber-Reinforced Cement Composites, *Cement & Concrete Composites*, 24: 457–465.
- Matacena I., L. Lancellotti, N. Lisi, P.D. Veneri, P. Guerriero, and S. Daliento. 2020. Impedance Spectroscopy for the Characterization of the All-Carbon Graphene-Based Solar Cell, *Energies*, 13: 1908–1915. doi:10.3390/en13081908.

- McCafferty E. 2010. *Introduction to Corrosion Science*, Springer, New York.
- McCafferty E. and J.V. McArdle. 1995. *J Electrochem Soc.* 142: 1447–1453.
- McCarter W.J. 1996. The a.c. Impedance Response of Concrete during Early Hydration, *J Mater Sci*, 31: 6285–6292.
- McCarter, W.J., S. Garvin, and N. Bouzid. 1988. Impedance Measurements on Cement Paste, *J Mater Sci Lett*, 7: 1056–1057.
- McGivney D., D. Calvetti, and E. Somersalo. 2012. Quantitative Imaging with Electrical Impedance Spectroscopy, *Phys Med Biol*, 57: 7289–7302.
- Middlemiss L.A., A.J.R. Rennie, R. Sayers, and A.R. West. 2020. Characterisation of Batteries by Electrochemical Impedance Spectroscopy, 4th Annual CDT Conference in Energy Storage and Its Applications, Professor Andrew Cruden, 2019, 07-19, University of Southampton, U.K., *Energy Reports*, 6: 232–241.
- Miran Gaberšček. 2021. Understanding Li-Based Battery Materials via Electrochemical Impedance Spectroscopy, *Nature Communications*, 12: 6513–6516. <https://doi.org/10.1038/s41467-021-26894-5>.
- Mishra R., P. Chaitanya, A. Shukla, L. Pandey, O.P. Thakur, O. Parkash, and D. Kumar. 2013. On the Impedance Measurement of High Resistivity Materials by Using a Parallel Resistor in Two Probe Arrangement, *Trans Ind Ceram Soc*, 72: 261–264.
- Moqadam S.M., P.K. Grewal, Z. Haeri, P.A. Ingledew, K. Kohli, and F. Golnaraghi. 2018. Cancer Detection Based on Electrical Impedance Spectroscopy: A Clinical Study, *J Electr Bioimp*, 9: 17–23.
- Moulson A.J. and J.M. Herbert. 2003. *Electroceramics*, Second Edition. John Wiley & Sons, Chichester.
- Muders T., H. Luepschen, and C. Putensen. 2010. Impedance Tomography as a New Monitoring Technique, *Current Opinion in Critical Care*, 16: 269–275.
- Muller T.L., L.C. Ward, K.J. Plush, J.R. Pluske, D.N. D'Souza, W.L. Bryden, and R.J. van Barneveld. 2021. Use of Bioelectrical Impedance Spectroscopy to Provide a Measure of Body Composition in Sows, *Animal*, 15: 100156–100164.
- Muto N, H. Yanagida, T. Nakatsuji, M. Sugita, and Y. Ohtsuka. 1993. Preventing Fatal Fractures in Carbon-Fiber–Glass-Fiber-Reinforced Plastic Composites by Monitoring Change in Electrical Resistance, *J Am Ceram Soc*, 76 : 875–879.
- Najafi B., P. Bonomi, A. Casalegno, F. Rinaldi, and A. Baricci. 2020. Rapid Fault Diagnosis of PEM Fuel Cells through Optimal Electrochemical Impedance Spectroscopy Tests, *Energies*, 13: 3643–3662. doi:10.3390/en13143643.
- Nakajima Hironori and Tatsumi Kitahara. 2016. Real-Time Electrochemical Impedance Spectroscopy Diagnosis of the Marine Solid Oxide Fuel Cell, *Journal of Physics: Conference Series*, 745: 032149. doi:10.1088/1742-6596/745/3/032149.
- Namsheer K and C.S. Rout. 2021. Conducting Polymers: A Comprehensive Review on Recent Advances In Synthesis, Properties and Applications, *RSC Adv*, 11: 5659–5697.
- Naranjo-Hernández D., J. Reina-Tosina, L.M. Roa, G. Barbarov-Rostán, N. Aresté-Fosalba, A. Lara-Ruiz, P. Cejudo-Ramos, and F. Ortega-Ruiz. 2020. Smart Bioimpedance Spectroscopy Device for Body Composition Estimation, *Sensors*, 20: 70–97.
- Naranjo-Hernández D., J.R. Tosina, and M. Min, 2019, Fundamentals, Recent Advances, and Future Challenges in Bioimpedance Devices for Healthcare Applications, *Hindawi Journal of Sensors*, Volume 2019, Article ID 9210258, 42 pages. <https://doi.org/10.1155/2019/9210258>.
- Nasir N. and M.A. Ahmad. 2020. Cells Electrical Characterization: Dielectric Properties, Mixture, and Modeling Theories, *Hindawi Journal of Engineering*, Volume 2020, Article ID 9475490, 17 pages. <https://doi.org/10.1155/2020/9475490> Open access.

- NCERT Chemistry Part II, Text Book for Class XII, National Council for Educational Research and Training (NCERT). 2021–2022. ISBN 81-7450-716-7 (Part II), Sri Aurobindo Marg, New Delhi.
- NCERT Science, Textbook for Class IX, Chapter 5, 2020–2021. National Council of Educational Research and Training, ISBN 81-7450-492-3, Publication Division NCERT, Sri Aurobindo Marg, New Delhi.
- NCERT Science, Textbook for Class X, Chapter 6 (Life Processes), 2019, 2020-21. National Council of Educational Research and Training, ISBN 81-7450-636-5, Publication Division NCERT, Sri Aurobindo Marg, New Delhi.
- NCERT XII part I 2009.
- Newman J. 1996. Resistance for Flow of Current to a Disk. *J Electrochem Soc*, 113: 501–502.
- Nye J.F. 1985. *Physical Properties of Crystals: Their representation by tensors and matrices*, Clarendon Press, Oxford.
- Nye J.F. 2006. *Physical Properties of Crystals*, Clarendon Press, Oxford.
- O'hayre R., S.W. Cha, W.G. Colella, and F.B. Prinz. 2016. *Fuel Cell Fundamentals*. Third Edition. John Wiley & Sons, Hoboken.
- Oh S.H., B.I. Lee, E.J. Woo, S.Y. Lee, T.S. Kim, O. Kwon, and J.K. Seo. 2005. Electrical Conductivity Images of Biological Tissue Phantoms in MREIT. *Physiol Meas*, 26, S279–S288.
- Orazem M.E., I. Frateur, B. Tribollet, et al. 2013. Dielectric Properties of Materials Showing Constant-Phase-Element (CPE) Impedance Response, *Journal of the Electrochemical Society*, 160: C215–C225.
- Orazem M.E. and Tribollet B. 2008. *Electrochemical Impedance Spectroscopy*, John Wiley & Sons, Hoboken.
- Ortega J.M., I. Sanchez, and Miguel. 2017. Impedance Spectroscopy Study of the Effect of Environmental Conditions on the Microstructure Development of Sustainable Fly Ash Cement Mortars, *Materials*, 10: 1130–1145. doi:10.3390/ma10101130.
- Paine D.H., T. Repo, A.G. Taylor. 2001. Noninvasive Seed Quality Test by Impedance Spectrum Analysis, *Seed Technology*, 23: 187–192.
- Pan, H., R. Peto, Q.A. Karim, M. Alejandria et al. 2020. Repurposed Antiviral Drugs for COVID-19 –Interim WHO SOLIDARITY Trial Results, medRxiv. <https://doi.org/10.1101/2020.10.15.20209817>, Now published in *New England Journal of Medicine*. *N Engl J Med*, 2021384(6): 497–511. doi:10.1056/NEJMoa2023184.
- Pandey L. 1992. In Workshop on Use of Computers in Teaching Physics, Partly Sponsored by ICTP, Trieste, Italy, Jabalpur, Dec 3–9.
- Pandey L. and D.G. Hughes. 1984. Electrostatic Shield for the Suppression of Piezoelectric Ringing in Pulsed NMR, *Journal of Magnetic Resonance*, 56: 443–447.
- Pandey L., O. Parkash, R.K. Katare, and D. Kumar. 1995. Equivalent Circuit Models for Electronic Ceramics, *Bull Mater Sci*, 18: 563–576.
- Pandey L, O. Parkash, and D. Kumar. 1996. On Sample Holder Corrections in the Complex Impedance Analysis of Electronic Ceramics, *Indian Journal of Pure & Applied Physics*, 34: 28–33.
- Pandey L., R.K. Katare, O. Parkash, and D. Kumar. 1997. Evidence of Two Ferroelectric PTCR components in Valence Compensated Ceramic System $Ba_{1-x}La_xTi_{1-x}Co_xO_3$, *Bull Mater Sc*, 20: 933–947.
- Pandey L., R.K. Katare, O. Parkash, D. Kumar, and O.P. Thakur. 1998. Complex Impedance Analysis of Electronic Ceramics Showing Steeply Rising Impedance Pattern at Low Frequency, *Ind J Pure & Appl Physics*, 36: 228–235.

- Pandey S., D. Kumar, O. Parkash, and L. Pandey. 2017. Equivalent Circuit Models Using CPE for Impedance Spectroscopy of Electronic Ceramics, *Integrated Ferroelectrics*, 183: 141–163. doi:10.1080/10584587.2017.1376984.
- Pandey S. 2018. Structural, Electrical and Impedance Spectroscopic Studies on Sr²⁺, Fe³⁺ and Sn⁴⁺ doped BaTiO₃ Ceramics, Ph.D. Thesis, Indian Institute of Technology (Banaras Hindu University), Varanasi.
- Pandey S., O. Parkash, and D. Kumar. 2018a. Study of Sample–Electrode Interface in Ceramics by Using Impedance Spectroscopy, *International Journal of Scientific and Innovative Research*, 6(1): 43–52.
- Pandey S., O. Parkash, and D. Kumar. 2018b. Structural, Dielectric and Impedance Spectroscopic Studies on Fe Doped BaTiO₃, *Transactions of the Indian Ceramic Society*, 77(3): 127–131. doi:10.1080/0371750x.2018.1526653.
- Pandey S., D. Kumar, O. Parkash, and L. Pandey. 2019a. Impedance Spectroscopy: A Powerful Technique for Study of Electronic Ceramics, *Ceramic Materials – Synthesis, Characterization, Applications and Recycling*, Dolores Eliche Quesada, Luis Perez Villarejo and Pedro Sánchez Soto, IntechOpen, ISBN: 978-1-78985-774-0 doi:10.5772/intechopen.81398.
- Pandey S., O. Parkash, and D. Kumar. 2019b. Structural, Dielectric, Ferroelectric and Impedance Spectroscopic Studies on Ba_{1-x}Sr_xTiO₃ (0.15 < x < 0.35), *Modern Physics Letters B*, 33: 1950193. doi:10.1142/S0217984919501938.
- Peled A., J. Castro, W.J. Weiss. 2013. Atomic Force and Lateral Force Microscopy (AFM and LFM) Examinations of Cement and Cement Hydration Products. *Cem Concr Compos*, 36: 48–55.
- Perini N., A.R. Prado, C.M.S. Sad, E.V.R. Castro, and M.B.J.G. Freitas. 2012. Electrochemical Impedance Spectroscopy for in situ Petroleum Analysis and Water-in-Oil Emulsion Characterization, *Fuel*, 91: 224–228.
- Peters M.F., S.D. Lamore, L. Guo, C.W. Scott, and K.L. Kolaja. 2015. Human Stem Cell-Derived Cardiomyocytes in Cellular Impedance Assays: Bringing Cardiotoxicity Screening to the Front Line, *Cardiovasc Toxicol*, 15: 127–139. doi:10.1007/s12012-014-9268-9.
- Pournaras, A.V., M.I. Prodromidis, A.P. Katsoulidis, A.V. Badeka, D. Georgantelis, and M.G. Kontominas. 2008. Evaluation of Lacquered Tinplated Cans Containing Octopus in Brine by Employing X-Ray Microanalysis and Electrochemical Impedance Spectroscopy, *J. Food Eng.* 86: 460–464.
- Proskuryakov Y.Y., K. Durose, B.M. Taelea, and S. Oelting. 2007. Impedance Spectroscopy of Unetched CdTe/CdS Solar Cells—Equivalent Circuit Analysis, *Journal of Applied Physics*, 102: 024504–11.
- Proskuryakov Y.Y., K. Durose, M.K. Al Turkestani, I. Mora-Seró, G. Garcia-Belmonte, F. Fabregat-Santiago, J. Bisquert, V. Barrioz, D. Lamb, S.J.C. Irvine, and E.W. Jones. 2009. Impedance Spectroscopy Of Thin-Film CdTe/CdS Solar Cells under Varied Illumination, *Journal of Applied Physics*, 106: 044507-1-9.
- Qing M., H. Liang, J. Zhang, and H. Zhan. 2018. Impedance Spectroscopy Dependent Water Content Detection in Dynamic Oil-Water Emulsions, *AIP Advances*, 8: 105306–105309.
- The Radio Amateur's Handbook. 1968. By the Headquarters Staff of the American Radio relay League, Newington.
- Raistrick I.D., J. Ross Macdonald, and D.R. Franceschetti. 1987. Theory, In: *Impedance Spectroscopy, emphasizing solid materials and systems*, Macdonald J.R. Ed. John Wiley & sons, New York.
- Ramanavicius A., A. Finkelsteinas, H. Cesiulis, and A. Ramanaviciene. 2010. Electrochemical Impedance Spectroscopy of Polypyrrole Based Electrochemical Immunosensor, *Bioelectrochemistry*, 79: 11–16.

- Rashed M.Z., J.A. Kopechek, M.C. Priddy, K.T. Hamorsky, K.E. Palmer, N. Mittal, J. Valdez, J. Flynn, and S.J. Williams. 2021. Rapid Detection of SARS-CoV-2 Antibodies Using Electrochemical Impedance-Based Detector, *Biosensors and Bioelectronics*, 171: 112709. <https://doi.org/10.1016/j.bios.2020.112709>.
- Renna L.A., F.G. Blanc, and V. Giordani. 2020. Interface Modification of Lithium Metal Anode and Solid-State Electrolyte with Gel Electrolyte, *Journal of the Electrochemical Society*, 167: 070542.
- Repo T, D.H. Paine, and A.G. Taylor. 2002. Electrical Impedance Spectroscopy in Relation to Seed Viability and Moisture Content in Snap Bean (*Phaseolus vulgaris* L.), *Seed Science Research*, 12: 17–29.
- Richman D.D., R.J. Whitley, and F.G. Hayden. 2017. *Clinical Virology*, Fourth Edition, ASM Press, Washington.
- Riu P.J. 2004. Comments on “Bioelectrical Parameters of the Whole Human Body Obtained through Bioelectrical Impedance Analysis”, *Bioelectromagnetics*, 25: 69–71. <https://doi.org/10.1002/bem.10190>.
- Runyan W.R. 1975. *Semiconductor Measurements and Instrumentation*, McGraw Hill, New York.
- Ruoff A.L. 1973. *Materials Science*, Prentice Hall, Englewood Cliffs.
- Rusgrove J. and G. Woodward. 1981. *The Radio Amateur’s Handbook*, American Radio Relay League, Newington.
- Sadani K., L. Muthuraj, P. Nag, M. Fernandes, K. Kondabagil, C. Mukhopadhyay, and S. Mukherji. 2020. A Point of Use Sensor Assay for Detecting Purely Viral Versus Viral-Bacterial Samples, *Sensors and Actuators B: Chemical*, 322: 128562–128568.
- Sawyer C.B. and C.H. Tower. 1930. Rochelle Salt as a Dielectric, *Physical Review*, 35: 269–276.
- Saxena A. and Ashutosh Kumar Dubey. 2019a. Coupling of Living Cells with External Electrical Stimulation: A Computational Study, *Journal of Physics D: Applied Physics*, 52: 015401.
- Saxena A., S. Gupta., B. Singh, and A.K. Dubey. 2019b. Improved Functional Response of Spark Plasma Sintered Hydroxyapatite Based Functionally Graded Materials: An Impedance Spectroscopy Perspective, *Ceramics International*, 45: 6673–6683.
- Saxena A., D. Khare, S. Agrawal, A. Singh, and A.K. Dubey. 2021. Recent Advances in Materials Science: A Reinforced Approach toward Challenges against COVID-19, *Emergent Materials*, 4: 57–73. <https://doi.org/10.1007/s42247-021-00179-5>.
- Scandurra G., G. Tripodi, and A. Verzera. 2013. Impedance Spectroscopy for Rapid Determination of Honey Floral Origin, *J Food Eng*, 119: 738–743. <https://doi.org/10.1016/j.jfoodeng.2013.06.042>.
- Scarborough J.B. 1966. *Numerical Mathematical Analysis*, 6th Ed., Oxford & IBH Publishing Co., New Delhi.
- Schreiner S., J.D. Bronzino, and D.R. Peterson. 2016. *Medical Instruments and Devices, Principles and Practices*, CRC Press, Boca Raton, pp 1–28.
- Schwan H.P. 1957. *Electrical Properties of Tissue and Cell Suspensions*, *Advances in Biological and Medical Physics*, Vol 5, Academic Press, New York.
- Scott J.F. and Araujo C.A. Paz de., 1989. Ferroelectric Memories, *Science*, 246: 1400–1405.
- Scuderi C.A., T.O. Mason, and H.M. Jennings. 1991. Impedance Spectra of Hydrating Cement Pastes, *J Mater Sci*, 26: 349–353.
- Sergi G., M. De Rui, B. Stubbs, N. Veronese, and E. Manzato. 2016. Measurement of Lean Body Mass Using Bioelectrical Impedance Analysis: A Consideration of the Pros and Cons, *Aging Clin Exp Res.*, 29: 591–597. doi:10.1007/s40520-016-0622-6, published online 27 Aug 2016.

- Sharma D.K., K. Pareek, and A. Chowdhury. 2020. Investigation of Solar Cell Degradation Using Electrochemical Impedance Spectroscopy, *Int J Energy Res*, 2020: 1–10. doi:10.1002/er.5567 .
- Shirakawa H., E. Louis, A. MacDiarmid, C. Chiang, and A. Heeger. 1977. Synthesis of Electrically Conducting Organic Polymers: Halogen Derivatives of Polyacetylene, (CH)_x, *J Chem Soc Chem Commun*, 16: 578–580.
- Simpson R.E. 1974. *Introductory Electronics for Scientists and Engineers*, Allyn and Bacon, Boston.
- Sinclair D.C. and A.R. West 1989. Impedance and Modulus Spectroscopy of Semiconducting BaTiO₃ Showing Positive Temperature Coefficient of Resistance, *Journal of Applied Physics*, 66: 3850–3857. doi:10.1063/1.344049.
- Sinclair D.C. and A.R. West. 1994. Effect of Atmosphere on the PTCR Properties of BaTiO₃ Ceramics, *J Mater Sc*, 29(23): 6061–6068.
- Singh H. Hemanta and H. Basantakumar Sharma. 2020. Impedance Spectroscopy and Transport Properties of Polymer-Based Flexible Nanocomposites, *Solid State Communications*, 319: 114012–114025.
- Singh, T.U., S. Parida, M.C. Lingaraju, M. Kesavan, D. Kumar, and R.K. Singh. 2020. Drug Repurposing Approach to Fight COVID-19. *Pharmacological Reports*, 72: 1479–1508. <https://doi.org/10.1007/s43440-020-00155-6>.
- Soares J.C., A.C. Soares, M.K.S.C. Angelim, J.L. Proença-Modena, P.M. Moraes-Vieira, L.H.C. Mattoso, and O.N. Oliveira Jr. 2022. Diagnostics of SARS-CoV-2 Infection Using Electrical Impedance Spectroscopy with an Immunosensor to Detect the Spike Protein, *Talanta*, 239: 123076–123077.
- Squires G.L. 1976. *Practical Physics*, Second Edition, McGraw-Hill, London.
- Staehelein L.A. “Cell Wall”. *Encyclopedia Britannica*, 9 May 2019, www.britannica.com/science/cell-wall-plant-anatomy. Accessed 1 June 2022
- Stavriniidou E, M. Sessolo, B. Winther-Jensen, S. Sanaur, and G.G. Malliaras. 2014. A Physical Interpretation of Impedance at Conducting Polymer/Electrolyte Junctions, *AIP Advances*, 4: 017127.
- Stern M. and A.L. Geary. 1957. Electrochemical Polarization. I. Shape of Polarization Curves, *J Electrochem Soc*, 104: 56–63.
- Stupin D.D., E.A. Kuzina, A.A. Abelit, A. Emelyanov, D.M. Nikolaev, M.N. Ryazantsev, S.V. Koniakhin, and M.V. Dubina. 2021. Bioimpedance Spectroscopy: Basics and Applications, *ACS Biomater Sci Eng*, 7: 1962–1986.
- Sugiyama J., T. Hayashi T, and H. Horiuchi. 1989. Changes in Electrical Impedance of Prince Melon during Ripening. *Nippon Shokuhin Kogyo Gakkaishi*, 36: 424–427. https://doi.org/10.3136/nshkk1962.36.5_424.
- Suryanto B., W.G. McCarter, G. Starrs, and T.M. Chrisp. 2017. Characterization of Fly-ash Using Electrochemical Impedance Spectroscopy, *Procedia Engineering*, 171: 705–714.
- Szuster B, Z. Szcurek, D. Roj, A. Sobotnicki, and P. Kowalski. 2017. Bioimpedance Spectroscopy Monitoring – Design Challenges and Description of the Acquired Results, *Proc. 24th Intl Conf “Mixed Design of Integrated Circuits and Systems”*, June 22–24, Bydgoszcz, Poland.
- Tatara R., P. Karayaylali, Y. Yu, Y. Zhang, L. Giordano, F. Maglia, R. Jung, J.P. Schmidt, I. Lund, and Y. Shao-Horn. 2019. The Effect of Electrode-Electrolyte Interface on the Electrochemical Impedance Spectra for Positive Electrode in Li-Ion Battery, *J Electrochem Soc*, 166: A5090.
- Thakur O.P., D. Kumar, O. Parkash, and L. Pandey. 2004. Dielectric and Impedance Spectroscopic Behaviour of Alkali Oxide - Containing Glass Ceramics in the System [SrO.TiO₂]-[SiO₂.B₂O₃], *Journal of Ceramic Processing Research*, 5: 106–113.

- Thompson D. and Y. Lei. 2020. Mini Review: Recent Progress in RT-LAMP Enabled COVID-19 Detection, *Sens Actuators Rep*, 2: 100017–100019.
- Tofail S.A.M. and J. Bauer. 2016a. Electrically Polarized Biomaterials, *Adv Mater*, 28: 5470–5484.
- Tofail S.A.M. and J. Bauer. 2016b. Electrically Mediated Interactions at the Materials/Biology Interface, In: *Electrically Active Materials for Medical Devices*, Tofail, S.A.M. and Bauer J. (eds) Imperial College Press, London, UK, pp 1–18.
- Torrents J.M., T.O. Mason, and E.J. Garboczi. 2000. Impedance Spectra of Fiber-Reinforced Cement-Based Composites: A Modeling Approach, *Cem Concr Res*, 30: 585.
- Torrents J.M., T.O. Mason, A. Peled, S.P. Shah, and E.J. Garboczi. 2001. Analysis of the Impedance Spectra of Short Conductive Fiber-Reinforced Composites, *J Mater Sci*, 36: 4003–4012.
- Torres M.D.T., W.R. de Araujo, L.F. de Lima, A.L. Ferreira, and C. Fuente-Nunez. 2021. Low-Cost Biosensor for Rapid Detection of SARS-CoV-2 at the Point of Care Matter, 4: 2403–2416. <https://doi.org/10.1016/j.matt.2021.05.003>.
- Torres M.D.T., L.F. de Lima, A.L. Ferreira et al. 2022. Detection of SARS-CoV-2 with RAPID: A Prospective Cohort Study, *iScience*, 25: 104055. <https://doi.org/10.1016/j.isci.2022.104055>.
- Toyoda K. 1994. Impedance Spectroscopic Analysis in Agricultural Products in *Developments in Food Engineering, Part I*, Blackie, Glasgow/London, pp 143–145.
- Upadhyay S., 2013, High Temperature Impedance Spectroscopy of Barium Stannate, *BaSnO₃*, *Bull.Mater.Sci.*, 36(6):1019–1036.
- Vadhva P., J. Hu, M.J. Johnson, R. Stocker, M. Braglia, D.J.L. Brett, and A.J.E. Rettie. 2021. Electrochemical Impedance Spectroscopy for All-Solid-State Batteries: Theory, Methods and Future Outlook, *Chem Electro Chem*, 8: 1930–1947. doi.org/10.1002/celec.202100108.
- Van Vlack L.H. 1989. *Elements of Materials Science and Engineering*, Addison–Wesley Publishing Company, New York.
- Von Hippel A.R. 1954. *Dielectrics and Waves*, MIT Press, Cambridge, Massachusetts.
- Vostakola M.F. and B.A. Horri. 2021. Progress in Material Development for Low-Temperature Solid Oxide Fuel Cells: A Review, *Energies*, 14: 1280–1335. <https://doi.org/10.3390/en14051280>.
- Voza'ry E. and D. Horvath. 1998. Change in Impedance Parameters of Apple Slices during Drying Process, *IFAC Proc*, 31: 123–125. [https://doi.org/10.1016/S1474-6670\(17\)44042-0](https://doi.org/10.1016/S1474-6670(17)44042-0).
- Voza'ry E., P. La'szlo', and P. Sass. 1997. Effects of Storage on Electrical Impedance of Apple Tissues, 2nd European Biophysics Congress, Orle'ans, 13–17 July 1997.
- Voza'ry E., La'szlo' P., and Zsivanovits G. 1999. Impedance Parameter Characterizing Apple Bruise, *Ann N Y Acad Sci*, 873: 421–429. <https://doi.org/10.1111/j.1749-6632.1999.tb09491.x>.
- Wang C.A., Y. Huang, Y. Li, and Z. Zhang. 2000. Complex Impedance Analysis on Orientation Effect of Whiskers in Oriented SiC(w)/Si₃N₄ Composites, *J Amer Ceram Soc*, 83: 2689–2692.
- Wang L., J. Zhao, X. He et al. 2012. Electrochemical Impedance Spectroscopy (EIS) Study of LiNi_{1/3}Co_{1/3}Mn_{1/3}O₂ for Li-Ion Batteries, *Int J Electrochem Sci*, 7: 345–353.
- Wang S. and D.D.L. Chung. 1997. Self-Monitoring of Strain in Silicon Carbide Whisker Reinforced Silicon Nitride, *Smart Mater Struct*, 6: 199–203.
- Wang X. 2001. *Non-Destructive Characterisation of Structural Ceramics Using Impedance Spectroscopy*, Ph.D. Thesis, Brunel University.

- Wang X and D.D.L. Chung. 1997. Real-Time Monitoring of Fatigue Damage and Dynamic Strain in Carbon Fiber-Polymer Matrix Composite by Electrical Resistance Measurement, *Smart Mater Struct*, 6: 504–508.
- Wang X and D.D.L. Chung. 1998. Short Carbon Fiber Reinforced Epoxy Coating as a Piezoresistive Strain Sensor for Cement Mortar, *Sensors Actuators A*, 71: 208–212.
- Wang X and P. Xiao. 2002. Characterisation of Clay Sintering Process Using Impedance Spectroscopy, *Journal of the European Ceramic Society*, 22: 471–478.
- Wang Y., Y. Song, and Y. Xia. 2016. Electrochemical Capacitors: Mechanism, Materials, Systems, Characterization and Applications, *Chem Soc Rev*, 45: 5925–5950.
- Waser R. 1999. Modeling of Electroceramics: Applications and Prospects, *Journal of the European Ceramic Society*, 19: 655–664.
- Waser R. and Hagenbeck R. 2000. Grain Boundary in Dielectric And Mixed Conducting Ceramics, *Acta Mater*, 48: 797–825.
- Weaver G.M. and H.O. Jackson. 1966. Electrical Impedance, an Objective Index of Maturity in Peach, *Can J Plant Sci*, 46: 323–326.
- West A.R. and N. Hirose. 1995. Characterisation of Ferroelectric Materials by Impedance Spectroscopy, *Bol Soc Esp Cerám Vidrio*, 34 : 496–500.
- Westerhoff U., K. Kurbach, F. Lienesch, and M. Kurrat. 2016. Analysis of Lithium-Ion Battery Models Based on Electrochemical Impedance Spectroscopy, *Energy Technol*, 4: 1620–1630. doi:10.1002/ente.201600154.
- Willner I. and B. Willner. 2001. Biomaterials Integrated with Electronic Elements: En Route to Bioelectronics, *Trends Biotechnol*, 19: 222–230.
- Winie T., A.K. Arof, and S. Thomas (eds). 2020. *Polymer Electrolytes, Characterization Techniques and Energy Applications*, Wiley-VCH Verlag GmbH & Co, Weinheim, Germany.
- Woo L.Y., S. Wansom, A.D. Hixson, M.A. Campo, and T.O. Mason. 2003. A Universal Equivalent Circuit Model for the Impedance Response of Composites, *Journal of Materials Science*, 38: 2265–2270.
- Woo L.Y., S. Wansom, N. Ozyurt, B. Mu , S.P. Shah, and T.O. Mason. 2005. Characterizing Fiber Dispersion in Cement Composites Using AC-Impedance Spectroscopy, *Cement & Concrete Composites*, 27: 627–636.
- World Health Organization. 2022. WHO Coronavirus (COVID-19) Dashboard. www.nature.com/scitable/definition/virus-308/. Accessed 11 July 2022.
- Wu L., D. Peng, and L. Yong. 2016. Determination of the Transport Properties of Structural Concrete Using AC Impedance Spectroscopy Techniques, *Journal of Engineering*, 2016: 1–8.
- Yang L, M.L. Dong, Q. Ji, D. Bao, Z. Gang, and H.R. Zhen. 2021. Electrical Impedance Spectroscopy (EIS) in Plant Roots Research: A Review, *Plant Methods*, 17: 118, 25 pages.
- Yoo S.M., S.J. Yoon, J.A. Anta, H.J. Lee, P.P. Boix, and I. Mora-Sero. 2019. An Equivalent Circuit for Perovskite Solar Cell Bridging Sensitized to Thin Film Architectures, *Joule*, 3: 2535–2549.
- Zink M.D., F. König, S. Weyer, K. Willmes, S. Leonhardt, N. Marx, and A. Napp. 2020. Segmental Bioelectrical Impedance Spectroscopy to Monitor Fluid Status in Heart Failure, *Sci Rep*, 10: 3577–3589.
- Zink M.D., S. Weyer, K. Pauly, A. Napp et al. 2015. Feasibility of Bioelectrical Impedance Spectroscopy Measurement before and after Thoracentesis, *BioMed Research International*, Article ID 810797, 9 pages.

- Zywica R. and J.K. Banach. 2015. Simple Linear Correlation between Concentration and Electrical Properties of Apple Juice, *J Food Eng*, 158: 8–12. <https://doi.org/10.1016/j.jfoodeng.2015.02.012>.

USEFUL BOOKS AND WEBSITES

- Barsoukov E. and J. Ross Macdonald (eds). 2005, 2018. *Impedance Spectroscopy Theory, Experiment, and Applications, Third Edition*, John Wiley & Sons, Hoboken.
- The Basics of Electrochemical Impedance Spectroscopy, www.gamry.com/application-notes/EIS/basics-of-electrochemical-impedance-spectroscopy/. Accessed 12 September 2022.
- Brock J. (ed). 2017. *Electrochemical Impedance Spectroscopy Methods, Analysis and Research*, Nova Science Publishers, New York.
- Jonscher A.K. 1983. *Dielectric Relaxation in Solids*, Chelsea Dielectrics Press, London.
- Kanoun O. (ed). 2013. *Lecture Notes on Impedance Spectroscopy Measurement, Modeling and Applications*, CRC Press, Boca Raton.
- Lvovich V.F. 2012. *Impedance Spectroscopy: Applications to Electrochemical and Dielectric Phenomena*, John Wiley & Sons, Hoboken.
- Macdonald J. Ross (ed). 1987. *Impedance Spectroscopy Emphasizing Solid Materials and Systems*, John Wiley and Sons, New York.
- Orazem M.E. and B. Tribollet 2008. *Electrochemical Impedance Spectroscopy*, John Wiley & Sons, Hoboken.



Taylor & Francis

Taylor & Francis Group

<http://taylorandfrancis.com>

Index

A

AC response of an ideal capacitor 13
admittance 29
a general equivalent circuit model of a ceramic system 123
agriculture, food quality and Dairy 173
 α , β , δ and γ dispersions 171
alternating current 3, 8
a method to remove the electrode and cable contributions 116
Analysis of Experimental Data 109
angiotensin-converting enzyme 2 (ACE2) 198
anode 145
anodic and cathodic reactions 145
anodizing 152
a parallel combination of resistance R and inductor L 92
a parallel combination R_1 - L_1 connected in series with R_2 and L_2 97
apparatus for impedance spectra of bean seeds 176
a series combination of R and L 95
a series combination R_1 - L_1 - C_1 connected in parallel with C_2 101

B

battery 194; state of charge 195; state of health 195
battery diagnosis 194
bioceramics 159
bioimpedance spectroscopy 165
biological systems and medical diagnostics 162
bismuth ferrite and polyvinylidene fluoride (BFO-PVDF) nanocomposites 155, 157
body water estimation 165
bone critical size defects (CSD) 168–9
breast: cancer 167, 168; impedance measurements 168
brick-wall model 38–9, 123

C

carbonation behaviour of mortar 126
cathode 145
cell 174; wall 174; state 169; index 169
cement 124
cement-matrix composites 154
ceramic 38–39
ceramic-electrode interface behaviour 118
ceramics and glass ceramics 121
charging and discharging of a capacitor 4

clay 124
complex impedance analysis 28
complex non-linear least squares (CNLS) 44, 115, 226
complex plane plot 29
complex plane plots showing loops 102–4
complex relative permittivity 33
composites 153
concrete 126
conducting polymer 153
constant phase angle element (CPE) 49, 70, 109–15
corona viruses 197
corrosion 144; control 147; and electrochemistry 144, reaction 145
COVID-19 197, 198

D

data correction 44–7
degradation 144
delaminated area 151
depressed arc in the Z'' vs. Z' plot for parallel R-CPE equivalent circuit 72, 214
depressed semicircular Y'' vs. Y' plot 76
detection and differentiation of bacteria and virus 166
detection of SARS-CoV-2 using RAPID 200
dielectric permittivity ϵ 29, 49
dielectric relaxations 171
dispersed phase 154
displacive ferroelectrics 130
distribution in time constants 70

E

electric polarization (P) 130
electrical double layer 148
electrical impedance 8
electrical impedance tomography (EIT) 166
electrical potential 3
electro-ceramics 122
electrochemical cell 148
electrode effects 116
electrode potential 148
electrodes 42
electrolyte 147
electrotaxis 159
equation of the Z'' vs. Z' semi-circular arc for parallel RC model 36

equation of the Z'' vs. Z' semi-circular arc for parallel R-CPE model 72, 214
 equivalent circuit for an electrical double layer 149
 equivalent circuit for polymer-fullerene solar cell 155
 equivalent circuit for the frequency-switchable fiber coating model 161
 equivalent circuit models 30, 44, 49–108; of a ceramic 39
 equivalent circuit model for a polymer coated metal placed in aqueous media 151
 equivalent circuit model for the perovskite solar cell 191
 equivalent circuit model: a parallel combination R_2C_2 connected in series with parallel combination of R_1 , C_1 and CPE₁ 88
 equivalent circuit of a plant tissue 175
 equivalent circuit of an anodized coating 151
 equivalent circuit of electrochemical immunosensor 200
 erosion–corrosion 144
 estimation of durability of concrete structures 126
 experimental limitations and instrumental artefacts due to electrodes 116
 experimental measurements 41

F

ferroelectric domain reorganization 140
 ferroelectric hysteresis loop 131
 ferroelectrics and piezoelectrics 130
 fiber-switchable coating model 161
 fibre reinforced composites 160
 fly ash 126
 food quality and safety 179
 four-probe: setup 116; technique 43
 fractal electrode-electrolyte interface 119
 fruit during ripening 178
 fuel cells, solar cells and miscellaneous systems 180–2
 functionally graded materials (FGMs) 130

G

galvanic corrosion 147
 galvanostatic mode 117
 gas sensors 192
 getting the values of the components of the model 111–15
 glass 122
 glass-ceramic 122, 128
 glass ceramic-electrode system 118
 goodness of fit parameter χ^2 221
 grain–grain boundary–electrode system 116, 131
 grain and grain boundary 122
 ground and ground loops 3
 GW BASIC program 217

H

H₂S gas sensor 192, 193
 health of the tissue/plant 175
 Heywang model 132
 hints for developing equivalent circuit model 110
 hydrated cement 124
 hydrogen oxidation reaction (HOR) 181
 hydroxyapatite ($\text{Ca}_{10}(\text{PO}_4)_6(\text{OH})_2$)(HAP) 159
 hydroxyapatite (HA) 130

I

identification of cell state 169
 immittance functions 29
 immunosensors 199
 impedance 29, 121
 impedance: parallel RC circuit 25, 35, series RC circuit 18
 impedance of an ideal inductor 17
 impedance of the cell membrane 175
 impedance spectroscopy 28, 41
 impedance spectroscopy used to examine the quality of coatings packages 180
 impedance spectroscopy used to study yogurt processing 179
 impedance spectroscopy of rechargeable lithium ions batteries 195
 impedance values normalized to same sample dimensions 44–7
 impedance of an ideal capacitor 16
 IMPSPEC.BAS 227
 inference from depressed looking arc 110
 inference from shifted arc : M'' vs. M' plot 110; Z'' vs. Z' plot 110
 inference from steeply rising branch at high frequency side in M'' vs. M' plot 110
 Inference from steeply rising branch at low frequency side in Z'' vs. Z' plot 110
 inference from two clear semicircular arcs 110
 initial guesses in a complex non-linear least square (CNLS) 113
 interconversion of parallel and series RC circuits 208
 interface 147
 ITO 154

K

Kronig–Kramers relations 115

L

Li ion battery cell 153
 limiting values of Impedance of a parallel RC circuit 36
 linear least squares 115, 219

- linear portion in the Z'' vs. Z' 110
 liquid phase 124
 loss angle δ and loss tangent ($\tan \delta$) 32
 lumped components 31
 lumped equivalent circuit model 31
- M**
- M'' vs. M' plot, a steeply rising branch at high frequency side 58
 M'' vs. M' plot, shifted towards right 56
 magnetic domain reorganization 140
 magnetic: modulus M_{mag} 94; permeability μ 92; systems 139
 matrix 154
 mechanical vibrations of the piezoelectric 105
 metal packaging 179
 metal-solution interface equivalent circuit 149, 150
 model for study of biological tissues 66
 model involving resistance R and capacitance C in parallel 50
 model involving resistance R and capacitance C in series 53
 modelling 30, 31
 mortar 126
 multiwall carbon nanotube composites 158
- N**
- non-linear least squares 115, 219, 223
 non-ohmic 2
 NTCR (negative temperature coefficient of resistance) 132
 Nyquist plot 29
 Nyquist plots for different state of charge of rechargeable lithium ions batteries 195
- O**
- Ohm's law 1
 Ohmic 26
 order-disorder type ferroelectrics 130
 organic solar cells (OSCs) for photovoltaic modules 153
 oxidation 145
 oxygen reduction reaction (ORR) 181
 oxygen sensors 127
- P**
- P3HT 154
 parallel combination R_1 - C_1 in series with R_2 57
 parallel combination R_1 - C_1 in series with C_2 55
 parallel combination of R_1 , C_1 and CPE_1 in series with parallel R_2 C_2 88
 parallel combination of resistance R and constant phase angle element (CPE) 70
 parallel combination of resistance R and CPE 70
 parallel RC circuit 34
 parallel RC to series RC conversion and vice versa 208
 parallel R-CPE equivalent circuit gives a depressed arc in the Z'' vs. Z' a plot 210
 parallel resonance frequency f_p 106
 parallel R_p C_p circuit transformed into an equivalent series R_s C_s circuit 55
 PCBM 154
 P-E hysteresis 131
 PEDOT: PSS 154, 159
 permittivity 29
 perovskite solar cells (PSCs) 189
 perovskite SrTiO_3 129
 petroleum 192
 phase 13
 phase angle 15
 phase difference 13
 piezoelectric ceramic system $\text{Pb Zr}_{0.6}\text{Ti}_{0.4}\text{O}_3$ (PZT) 139
 piezoelectric material 105, 131
 plant tissue impedance 174
 plots for presence of at least two processes having time constants close to each other 59–64
 point of use disposable paper based impedimetric sensor 166
 polymer electrolyte 155
 polymers and composites 152
 potentiostatic mode 117
 power lost 3
 presence of a series CPE in the model 110
 program for creating Z'' vs. Z' plot 217
 PTCR (positive temperature coefficient of resistance) behaviour 118, 132
 PTCR behaviour of semiconducting BaTiO_3 ceramics 132
- Q**
- quality of coatings in lacquered tinplated cans 180
- R**
- radiation shielding concretes 125
 real-time accurate portable impedimetric detection prototype (RAPID 1.0) 200
 reduction 145
 refractories 122
 reinforced concrete 154
 repurpose the available drugs 201
 resistance R 1, 30
 right shift in: M'' vs. M' plot 110; Z'' vs. Z' plot 110

right shift in Y'' vs. Y' plot 100, 110
 right shifted semicircular Y'' vs. Y' arc 65
 root-mean-square ("rms") amplitude, V_{rms} 11
 Rusting 144

S

Sample-electrode contact behaviour for single phase and multiphase samples 118
 SARSCoV-2 198
 semicircular arc with changed sign of Z'' in Z'' vs. Z' plot 110
 separation of viable and non-viable snap bean seeds 176
 series combination of parallel R_1 -CPE₁ and parallel R_2 -CPE₂ 79
 series combination of parallel R_1C_1 , parallel R_2C_2 and CPE 83
 series combination of parallel R_1 -CPE₁, R_2 and CPE₂ 85
 series combination of R and CPE 75
 series R_1C_1 in parallel to R_2 64
 series R_1 - C_1 in parallel with series R_2 - C_2 and R_3 99
 series RC circuit 53
 series resonance frequency f_r 106
 simple equivalent circuit model for a fuel cell 184
 simulated immittance behaviours 49–108
 sintering 124
 skin cancer 167
 software IMPSPEC.BAS 115, 227
 solar cell 186
 solar cells degradation 188
 solenoidal coil 140
 solid oxide fuel cells (SOFC) 127
 solid-oxide fuel cell (SOFC) 183
 spectroscopic plots 28
 spreading resistance 161
 strontium aluminate hydrates 125
 strontium titanate borosilicate glass ceramics ($SrO.TiO_2-2SiO_2.B_2O_3$) 118
 strontium titanate glass ceramics 129
 structural cell changes during fruit ripening 173
 study of relaxation processes in tissues 171
 surface behaviour of electrodes 119

T

three-electrode setup 117
 three parallel RC networks connected in series 66
 time constant τ , 147
 tissue electrical equivalent circuit model 171
 tissue conductivity 164
 to distinguish between bruised and non-bruised apples 178
 transient response of a series RC circuit 19
 two parallel RC networks connected in series 59
 two parallel RL circuits connected in series 140
 two probe method 41, 116

U

uniform corrosion 147
 units of: L/R 27 207; RC 27 207; ωRC 27 208

V

valence compensated ceramic system $Ba_{1-x}La_xTi_xCo_xO_3$ 135
 viability of the stored seeds 176

W

warburg impedance 149, 214
 water of hydration 147
 working electrode 117

Y

Y'' vs. Y' plot for forearm 173
 Y'' vs. Y' plot, a depressed semicircular arc 76
 YIG (yttrium iron garnet) 140

Z

Z'' vs. Z' plot, a steeply rising branch at low frequency side 56
 Z'' vs. Z' plot shifted towards right 58
 Z'' vs. Z' plot, a straight line 76
 Z'' vs. Z' plot for a parallel R-CPE equivalent circuit 214
 Z'' vs. Z' plot showing a cross over from positive values of Z'' to negative values or vice versa 110
 Z'' vs. Z' plot, a straight line 76